Heteronuclear Metal Complexes Based on Compartmental Bridging Ligands for Dual-Modal Imaging

Bethany Crowston

A thesis submitted to the University of Sheffield in partial fulfilment of the requirements for the degree of Doctor of Philosophy

November 2018

The University of Sheffield

Department of Chemistry

Abstract

Heteronuclear metal complexes for dual-modal imaging

The design of dual- or multi-modal probes, in which two or more independent reporters are integrated into one unit, is an area of immense interest, as visualisation of biological matter can be enhanced enormously by sequentially exploiting the advantages of each detection mode. In particular, dual *optical/MRI* contrast agents are appealing, as the combination of a luminescent dye with an MRI-active unit within a single entity, produces a superior probe capable of imaging both the 'bigger picture' and the intricate detail within a cell. By combining the synergistic signals arising from both imaging modalities, images can be developed to reveal exquisite detail.

To this end, a series of water-soluble, heterometallic ruthenium(II)-based complexes based on compartmental bridging ligands have been synthesised for exploitation as dual-modal contrast agents. Incorporation of the commonly used MRI-active metal, Gd^{III}, into the probe design to produce multimetallic Ru^{II}-Gd^{III} hybrids has been investigated, as well as the relatively unexploited paramagnetic properties of Mn^{II} in Ru^{II}-Mn^{II} hybrids. Assessment of the concentration-normalised longitudinal relaxivity values (r_1) for each of the complexes has been undertaken, and the Ru^{II}-Gd^{III} hybrids have been evaluated as probes for cellular imaging.

Incorporation of the NIR-luminescent Ln^{III} ions, Yb^{III} and Nd^{III}, in place of the MRI-active metals Gd^{III} and Mn^{II}, has also provided a route to dual-modal optical/NIR imaging probes. Photoinduced energy-transfer from the photoactivated Ru^{II} centre has been shown to sensitise emission from the Ln^{III} ion, producing a dual-luminescent probe that has distinguishable emission, owing to the luminescent lifetimes of the two different metal centres being orders-of-magnitude apart.

Declaration

Except where specific references have been made to other sources, the work within this thesis is the original work of the author. It has not been submitted, in whole or in part, for any other degree.

Bethany Crowston

November 2018

iv

Acknowledgements

Firstly, I would like to thank my supervisor Prof. Mike Ward for the opportunity to study for my PhD under his expert guidance and support. I'm extremely grateful for all of his help and encouragement and for the opportunities he has given me. Thank you also to Prof. Julia Weinstein for her support and advice throughout my project, and to Julie and Jamie for their continued encouragement during my teaching responsibilities.

Thank you also to past and present members of the Ward group for their encouragement and their friendship throughout the last four years. Special thanks go to Liz for being an incredible mentor and for guiding me through my PhD with great words of wisdom, and also to Will for his help in the lab at the start of my PhD. And, of course, Jerry for being the ideas man and providing the tunes in the lab.

Many thanks go to all of the Chemistry Department members who facilitated my work, but in particular I'd like to thank Jon, Luke and Callum for their help in the tissue culture lab, and James for analysing my samples by TA and fitting the data for me. Thank you also to Sharon and Simon for analysing my samples in mass spec, and Sandra and Craig for helping me with NMR.

Finally, I'd like to thank all of my friends and family for supporting me over the last four years; it hasn't always been easy! I'm grateful to Charlotte for being my dancing buddy on nights out in Popworld, and to Paul for always cheering me up and supplying a bottle of fizz when the hard times are through. And last but certainly not least, I want to thank my wonderful mum for being the best role model anyone could ever ask for. She has encouraged me every step of the way and has always been there to pick me up when I'm down. I'm so lucky to have her unconditional love and support, and so this thesis is dedicated to her.

List of Abbreviations

2P-PDT: Two-photon-photodynamic therapy

2P-PLIM: Two-photon-phosphorescent lifetime imaging microscopy

3D-STED: Three-dimensional-stimulated emission depletion microscopy

A: Absorption

Å: Ångstrom

aq: Aqueous

a.u.: Arbitrary units

BET: Back-electron-transfer

bipy: 2,2-bipyridine

BODIPY: Boron-dipyrromethene

br: Broad

°C: Celsius

CDTA: Trans-1,2-diaminocyclohexane-N,N,N',N'-tetraacetic acid

CKD: Chronic kidney disease

cm: Centimetre

C^N: Monoanionic cyclometallating ligand

CORM: CO-releasing molecule

COSY: Homonuclear correlation spectroscopy

δ: Chemical shift

DAPI: 4',6-diamidino-2-phenylindole

DEPTQ: Distortionless enhancement by polarization transfer for quaternary centres

DMEM: Dulbecco's modified eagle medium

DMF: Dimethylformamide

DMSO: Dimethyl sulphoxide

DNA: Deoxyribonucleic acid

DOTA: 1,4,7,10-tetraazacyclododecane-1,4,7,10-tetraacetic acid

DPDP: Dipyridoxyl diphosphate

dppf: 1,1'-ferrocenediyl-bis(diphenylphosphine)

dppz: Dipyrido[3,2-*a*:2',3'-*c*]phenazine

dtbbipy: 4,4'-di-tert-butyl-2,2'-dipyridyl

DTPA: Diethylenetriaminepentaacetic acid

DTTA: Diethylenetriamine-N,N,N",N"-tetraacetate

ε: Extinction coefficient

Ec: Econazole

EDTA: Ethylenediaminetetraacetic acid

EMA: European Medicines Agency

ES⁺MS: Positive electrospray mass spectrometry

ES⁻MS: Negative electrospray mass spectrometry

Et: Ethyl

ET: Electron-transfer

EU: European Union

F: Fluorescence

FBS: Foetal bovine serum

FLIM: Fluorescent lifetime imaging microscopy

fs: Femtosecond

fwhm: Full width half maximum

g: Gram

h: Hour

H: Proton

HMBC: Heteronuclear multiple bond correlation

HOMO: Highest occupied molecular orbital

HOPO: Hydroxypyridonate

HPDO3A: 10-(2-hydroxypropyl)-1,4,7-tetraazacyclododecane-1,4,7-triacetic acid

HPLC: High performance liquid chromatography

HRMS: High resolution mass spectrometry

HSA: Human serum albumin

HSQC: Heteronuclear single quantum correlation

hv: Energy

Hz: Hertz

IC: Internal conversion

ICP-MS: Inductively coupled plasma-mass spectrometry

^{i}Pr: Isopropyl

ISC: Inter-system crossing

J: Joules

K: Kelvin

$k_{ex/q/et/EnT}$: Rate of (exchange/quenching/electron-transfer/energy-transfer)

kg: Kilogram

kHz: Kilohertz

$\lambda_{abs/em/ex}$: Wavelength (absorption/ emission/ excitation)

L: Litre

LLCT: Ligand-to-ligand charge transfer

Ln: Lanthanide

LUMO: Lowest unoccupied molecular orbital

M: Molar

max: Maximum

μ_B: Bohr magneton

MC: Metal-centred

Me: Methyl

mg: Milligram

MHz: Megahertz

mJ: Millijoule

µL: Microlitre

mL: Millilitre

MLCT: Metal-to-ligand charge transfer

µm: Micrometre

µM: Micromolar

µmol: Micromole

mm: Millimetre

mM: Millimolar

mmol: Millimole

mol: Mole

MRI: Magnetic resonance imaging

μs: Microsecond

ms: Millisecond

MSN: Mesoporous silica nanoparticles

MTT: 3-(4,5-dimethylthiazol-2-yl)-2,5-diphenyltetrazolium bromide

m/z: Mass over charge

N^C^N: Cyclometalating ligand

N^N: Polypyridyl

NBS: N-bromosuccinimide

NHS: National Health Service

NIR: Near-infrared

nm: Nanometre

NMR: Nuclear magnetic resonance

NMRD: Nuclear magnetic relaxation dispersion

ns: Nanosecond

NSF: Nephrogenic systemic fibrosis

ϕ: Quantum yield

P: Phosphorescence

PBS: Phosphate buffered solution

pbt: 2-(2-pyridyl)benzothiazole

PDT: Photodynamic therapy

PET: Positron emission tomography

PET: Photoinduced electron-transfer

PET-CT: Positron emission tomography–computed tomography

PET-MRI: Positron emission tomography–magnetic resonance imaging

PEnT: Photoinduced energy-transfer

Ph: Phenyl

phen: 1,10-phenanthroline

ph-phen: 5-phenyl-1,10-phenanthroline

PLIM: Phosphorescence lifetime imaging

ppm: Parts per million

ppy: Phenylpyridine

ps: Picosecond

PSII: Photosystem II

Py: Pyridine

PyC3A: N-picolyl-N,N',N'-trans-1,2-cyclohexylenediaminetriacetate

q: Hydration number

r_1: Concentration-normalised longitudinal relaxivity value

RGD: Arginylglycylaspartic acid

RMM: Relative molecular mass

RONs: Reactive oxygen and nitrogen species

ROS: Reactive oxygen species

rt: Room temperature

s: Second

S_0: Singlet ground state

S*: Singlet excited state

sh: Shoulder

solv: Solvent molecule

SPECT: Single-photon emission computed tomography

SPC: Single photon counting

SSIM: Saturated structured-illumination microscopy

STED: Stimulated emission depletion microscopy

τ: Lifetime

τ_q: Quenched lifetime

τ_M: Mean residence time

τ_R: Rotational correlation time

t: Time

T: Tesla

T_1: Longitudinal relaxation time

T*: Triplet excited state

TA: Transient absorption

TBAF: Tetra-*n*-butylammonium fluoride

TEM: Transmission electron microscopy

terpy: Terpyridine

TFA: Trifluoroacetic acid

THF: Tetrahydrofuran

TLC: Thin layer chromatography

TMSA: Trimethylsilylacetylene

tpphz: Tetrapyrido[3,2-*a*: 2′,3′-*c*: 3″,2″-*h*: 2″,3‴-*j*]phenazine

UV: Ultraviolet

v: Volume

V: Volts

Vis: Visible

Table of Contents

Chapter 1

Introduction

1.1) Biological Imaging

Biological imaging can be deemed to be one of the most important scientific discoveries of the 20th century due to the remarkable impact it has had on modern medicine. Since their inception, whole-body imaging modalities such as single-photon emission computed tomography (SPECT), positron emission tomography (PET) and magnetic resonance imaging (MRI) have become ubiquitous in medical diagnostics for detecting a wide variety of medical ailments[1–3]. In particular, numerous cancers can now be identified and treated more promptly[4,5]. However, the relatively low resolution and sensitivity associated with these techniques hinders their utility for imaging intricate detail at the cellular and subcellular level.

In contrast, when coupled with luminescence (a term that encompasses both fluorescence and phosphorescence), optical microscopy has superb sensitivity and resolution (*ca.* 200-250 nm). With the recent advancement of 'super-resolution' microscopy techniques[6] such as stimulated emission depletion microscopy (STED)[7] and saturated structured-illumination microscopy (SSIM), spatial resolution well below the limit imposed by the diffraction of light has also been realised (*ca.* 20-100 nm). As such, the visualisation of cellular level detail is now straightforward, and the possibility of monitoring the subcellular biological processes that are the basis of disease, rather than just imaging their end effects, has become a reality[8]. In this way, modern medicine has been revolutionised as more incidents of life-threatening medical conditions can be detected earlier, and the success of treatment can be more easily monitored.

This thesis will focus upon the utilisation of both MRI and optical microscopy in the field of biological imaging. In both cases the application of metal complexes as imaging agents will be reviewed, with select recent examples from the literature being highlighted. The relatively novel field of dual-modality imaging, in which two or more independent reporters are integrated into the same unit, will also be considered, with particular emphasis being placed upon mixed-metal complexes capable of acting as dual-modal probes that combine optical microscopy and MR imaging.

1.2) Magnetic Resonance Imaging

MRI has become a prominent imaging technique in clinical medicine due to its non-invasive nature and its versatility. Unlike other whole-body imaging modalities such as PET and X-ray, MRI does not use unpleasant radiochemicals or ionising radiation to produce an image, but rather relies on the principles of nuclear magnetic resonance (NMR) spectroscopy. This makes MRI a much softer and safer investigative procedure, and as such, its utilisation in medical diagnostics is rapidly accelerating. The NHS in England reported that the number of MRI examinations undertaken in 2017/2018 was 3.4 million, which was a growth of 59 % over a five-year period[9]. The technique is now routinely used to diagnose conditions of the central nervous system including multiple sclerosis[10] and Alzheimer's disease[11], as well as vascular abnormalities[12] and numerous types of cancer[13,14].

To produce a three-dimensional image of the area of the body under examination, MRI takes advantage of the water molecules that comprise the bulk of human tissue (average 65 %). Under normal conditions the spin angular momentum vectors of the protons on the water molecules are disordered and in random orientations (figure **1.01A**): however, when a strong magnetic field is applied the protons align their spins either in the direction of the magnetic field or against it. Nearly equal numbers of protons align in each direction and so the majority cancel each other out; however, a very small excess do not cancel, and it is these protons that MRI takes advantage of (figure **1.01B**). A pulsed radiofrequency current specific to hydrogen is applied to disrupt the alignment of the unmatched protons with the applied magnetic field, as they absorb the energy and flip their spins in a specific direction at a specific frequency of resonance known as the Larmor frequency (figure **1.01C**). As the radiofrequency field is removed the protons slowly relax back to their previous energy level (aligned with the applied magnetic field) and emit radio waves that are detected and converted into an image (figure **1.01D**).

Differentiation of the various tissues within the body occurs as a result of the water protons in different chemical environments taking different amounts of time to realign with the magnetic field (different relaxation rates), as well as the varying water densities within the tissues. However, signal intensities and sensitivity can be enhanced by administering a paramagnetic metal complex known as a *contrast enhancement agent*. The normal tumbling of these highly paramagnetic complexes produces an oscillating magnetic field, which

increases the rate at which the protons relax back to their ground state (aligned with the applied magnetic field), allowing the absorption of another photon more quickly. This produces brighter images and better contrast. The first such probe to be approved for human use in 1988 was a low molecular weight compound that utilised the unique magnetic properties of the Gd^{III} ion. Three decades on from this, a number of Gd^{III}-based agents are now commercially available, and approximately one in three MRI examinations undertaken each year involves the administration of a contrast agent.
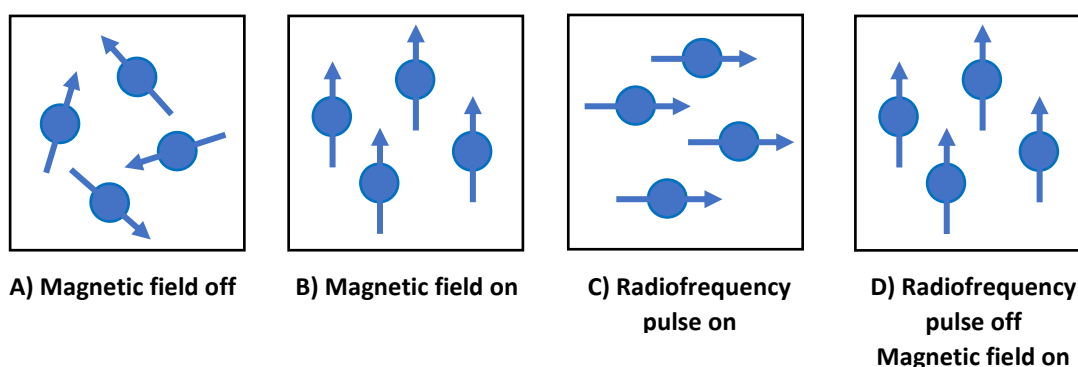
Figure 1.01: Simplified depiction of proton spin angular momentum vectors during an MRI examination. A) the magnetic field is off and the proton spins are in random orientations; B) a strong magnetic field is applied and an excess of the proton spins are aligned with the field; C) a pulsed radiofrequency current is applied and the proton spins flip out of alignment with the applied magnetic field; D) the radiofrequency pulse is removed and the proton spins return to their alignment with the applied magnetic field, releasing a detectable energy that is converted into an image

1.2.1) Gadolinium(III)-Based Contrast Agents

In the European Union there are currently eight Gd^{III}-based compounds approved for use as MRI contrast agents in humans by the European Medicines Agency (EMA)[15] (figure **1.02**). Gd^{III} is a perfect central metal ion for use in such agents, as it has seven unpaired electrons, and hence a high magnetic moment (7.94 μ_B), coupled with a long electron spin relaxation time (10^{-9} s) at the low magnetic field strengths used in MRI examinations (20-60 MHz). When combined, these properties help to shorten the longitudinal relaxation time (T_1) of water protons in tissues, which in turn enhances the relaxation rate ($1/T_1$). This generates greater contrast and a brighter image where the agent has distributed compared to areas where there is no contrast agent accumulation. Complexes of this kind are known as *positive*

contrast agents and their efficiency is assessed by their concentration-normalised longitudinal relaxivity value (r_1), defined as the increase in the relaxation rate of water protons per millimole of contrast agent ($mM^{-1} s^{-1}$). On average, the commercially available contrast agents have relaxivity values in the range $r_1 = 3.5$-4.8 $mM^{-1} s^{-1}$ (20 MHz, 25 °C, pH 8.5).

Conversely, there also exist *negative* contrast agents, which affect the transverse relaxation time (T_2) of water protons, and darken an image with increasing relaxation rates ($1/T_2$). Probes of this kind include superparamagnetic materials such as iron oxide nanoparticles[16,17], but this thesis will not consider them in any detail.
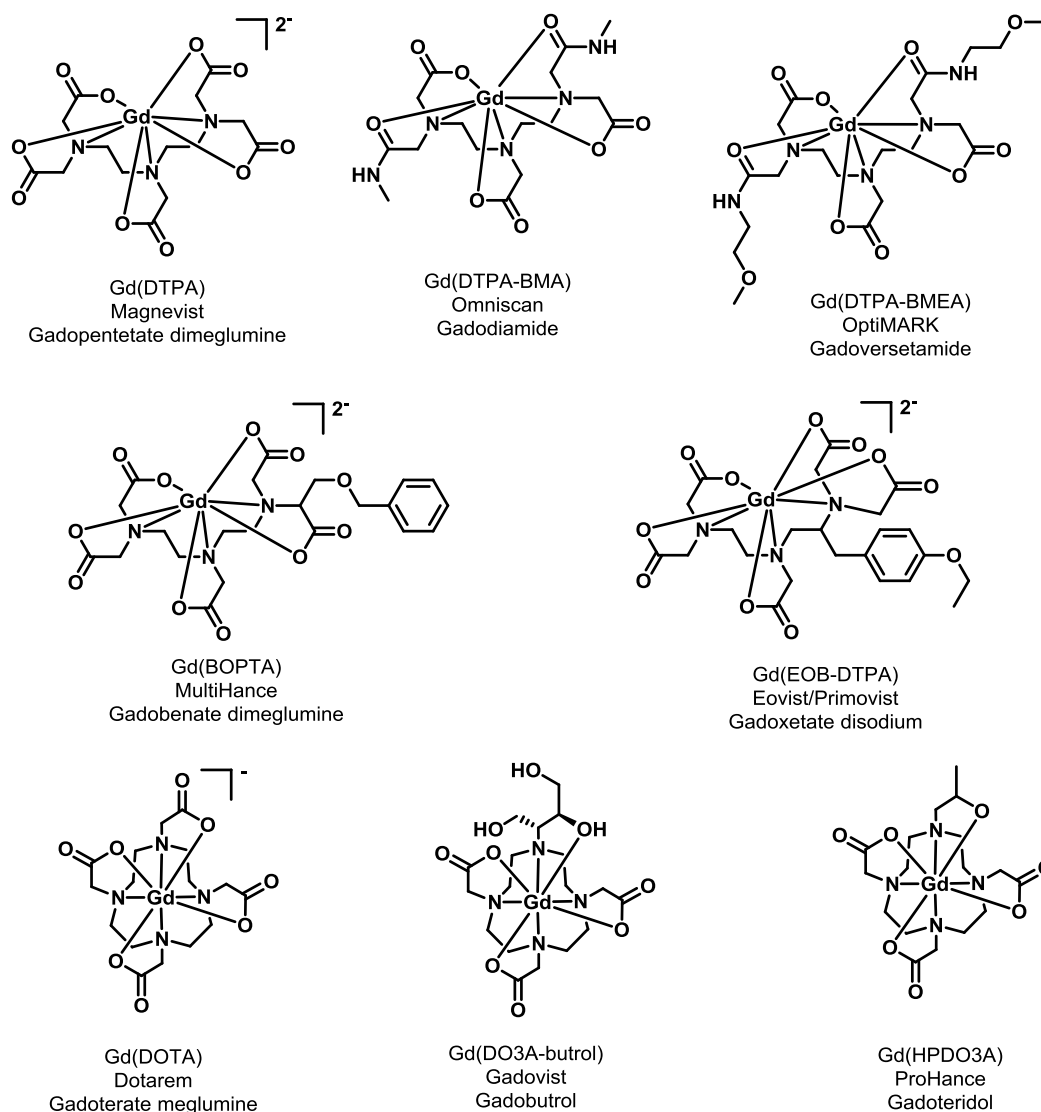
Figure 1.02: Structures of the eight commercially available Gd^III-based MRI contrast agents approved for use in humans

Although the Gd^{III} ion has excellent properties for use in T_1-weighted MRI examinations, free Gd^{III} ions are highly toxic *in vivo*. The radius of the Gd^{III} ion is similar to that of the Ca^{II} ion, which can have unfortunate effects if transmetallation occurs. Ca^{II}-mediated signalling can be disrupted and kinetically and thermodynamically stable Gd^{III}-based complexes can accumulate in the body, causing toxic effects. In rare circumstances, Gd^{III}-based contrast agents have been linked to the onset of nephrogenic systemic fibrosis (NSF) in patients with renal impairment[18,19]. This is a severe and potentially fatal syndrome that involves the formation of excess fibrous connective tissue in internal organs and the skin.

To prevent toxicity from free metal ions, the Gd^{III} ion is tightly bound within a chelating ligand based on a polyaminocarboxylate motif. The high coordination number of the Gd^{III} ion allows eight coordination bonds to be made to nitrogen and oxygen donor atoms, which ensures excellent kinetic and thermodynamic stability of the compound *in vivo*. Three of the commercially approved agents currently in use are based on macrocyclic structures, which, on average, tend to have higher stability constants than those structures comprised of acyclic motifs. These more stable macrocyclic structures (Dotarem, Gadovist and ProHance) tend to be linked to less toxic effects when used for *in vivo* imaging.

1.2.1.1) Relaxivity Enhancement of Gadolinium(III)-Based Contrast Agents

The aim of administering a contrast agent during an MRI examination is to maximise the concentration-normalised longitudinal relaxivity value (r_1) of the water protons, as the higher a relaxivity value achieved, the better the contrast of the image, and the more detail that can be observed. If relaxivity values of the order of r_1 = 100-200 $mM^{-1} s^{-1}$ were to be realised, the contrast of the image would be such that more sensitive molecular imaging could be carried out. Higher relaxivity values would also allow lower concentrations of the contrast agent to be administered, which would help to abate the toxic effects that free Gd^{III} ions have *in vivo*.

In order to design a new generation of improved Gd^{III}-based contrast agents with higher relaxivity values per millimole of agent, a number of parameters need to be optimised[20]. The hydration of the central Gd^{III} ion (q value) and the distance between the water protons and the unpaired electron spin (r) play a key role in the relaxivity achievable by a contrast agent. At least one water molecule needs to be bound to the Gd^{III} metal centre at

any given time, which is facilitated by the octadentate chelating ligands described previously. They guarantee that one of the nine coordination sites on the Gd[III] ion will be vacant for a water molecule to bind, which helps to improve the relaxivity, as the distance between the paramagnetic metal centre and the water proton is reduced. A rapid exchange rate between the water molecules bound to the Gd[III] centre and the surrounding bulk water molecules (k_{ex}) helps to improve the relaxivity value even further, as turnover rates on the microsecond timescale ensure that each Gd[III] ion can relax a large number of protons on water molecules over a shorter period of time.

Increasing the number of water molecules that can bind to the paramagnetic metal centre at any given time will also improve upon the relaxivity values achievable by a contrast agent; however, this may affect the complex integrity *in vivo* if the Gd[III] ion makes less coordination bonds to the stabilising chelate. A hydroxypyridonate (HOPO)-based chelating ligand circumvented this issue (figure **1.03**), as a high relaxivity value was measured for the complex (7.7 mM^{-1} s^{-1}, 20 MHz, 25 °C, pH 8.5) (attributed to the *two* water molecules bound to the Gd[III] centre), yet high stability of the complex was still reported even though only six coordination bonds were made to the metal centre[21]. The probe design was such that the energy barrier between the intermediate tris(aqua) complex and the observed bis(aqua) complex was low, which reduced the mean residence time of the bound water molecules in the first coordination sphere (τ_M).
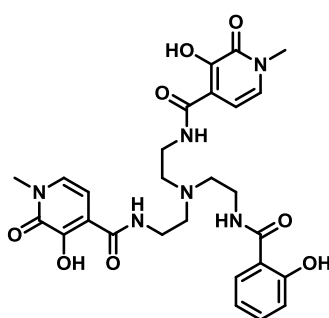
Figure 1.03: Structure of a hydroxypyridonate-based ligand for an MRI contrast agent with high stability and two coordinated water molecules

A final key aspect of a contrast agent's design to be optimised for high relaxivity values is the tumbling rate of the species, which is characterised by the rotational correlation time (τ_R). Larger complexes with high molecular weights have been shown to boast higher relaxivity values in comparison to smaller complexes, as the larger size encourages slower rotation in solution. This slower tumbling rate of the larger paramagnetic complexes produces an

oscillating magnetic field, which has components closer to the Larmor frequency for hydrogen, and so the rate at which the water protons relax back to their ground state (aligned with the applied magnetic field) is increased. This allows absorption of another photon more quickly compared to the smaller complexes, and hence the relaxivity value for the larger complexes is increased in comparison. Strategies such as incorporating Gd[III] ions into nanoparticles[22] have been used effectively to reduce the rotational correlation time, as well as tethering the paramagnetic metal centre to a rigid macromolecule[23]. When coupled with a luminescent metal centre this also produces probes capable of dual-modal optical/MR imaging that will be discussed in detail later in this thesis (section **1.4.1**).

1.2.2) Manganese(II)-Based Contrast Agents

The Gd[III] ion is currently the most prevalent paramagnetic metal centre used in contrast agents for T_1-weighted MRI examinations, but originally the Mn[II] ion was considered for the role due to its amenable physical properties. The ion was initially discounted for *in vivo* imaging on toxicity grounds; however, recently, with the design of better stabilising chelating ligands, Mn[II]-based contrast agents, including those based on nanoparticles[24,25] and macromolecules[26,27], are once again being considered as Gd[III]-free alternatives[28]. Gd[III]-based contrast agents have been shown to have toxic effects when administered *in vivo*, especially in patients with impaired renal function. As some 14 % of the US population is affected by chronic kidney disease (CKD), the development of a safer probe that is compatible with imaging the kidney would have a large impact on modern medicine.

Comparable to the Gd[III] ion, high spin Mn[II] has a number of physical properties that make it an efficient ion for use in MRI. It has five unpaired electrons and hence a high spin quantum number (s = 5/2), a long electronic relaxation time, and fast water exchange kinetics. Unlike Gd[III], however, Mn[II] is also a biologically relevant ion as it is a natural constituent of cells, being involved in mitochondrial function. This makes Mn[II] a suitable ion for imaging mitochondria-rich organs such as the kidney, as the greater the density of mitochondria in a cell, the higher the level of Mn[II] uptake, and the better contrast seen in the image.

Free Mn[II] ions are still toxic to the human body, however, and overexposure can lead to a neurodegenerative disorder known as 'manganism', whose symptoms resemble those of Parkinson's disease. Only one commercially available Mn[II]-based contrast agent has ever been

approved for use in humans, known as mangafodipir trisodium (Mn-DPDP) or Teslascan® (**1**, figure **1.04**), but it was removed from the EU market in 2010 over concerns for its toxicity in patients, as the complex was found to partially dissociate *in vivo*. It is worth noting, however, that free Mn^{II} ions have an efficient elimination pathway through the hepatobiliary system, which free Gd^{III} ions do not have, and so accumulation and toxicity is not as severe an issue for Mn^{II}-based contrast agents as they are for complexes with Gd^{III} as the paramagnetic ion.

Macrocycle-based ligand structures have shown excellent stability with Gd^{III} ions, however, their use with Mn^{II} ions is flawed. The d-block Mn^{II} ion has a smaller ionic radius than the lanthanide Gd^{III} ion and so can make fewer coordination bonds. This is an issue when using macrocyclic ligands, as they saturate the metal coordination, which prohibits a water co-ligand from binding. This produces an impasse, whereby improving the *in vivo* stability of the Mn^{II}-based complex has detrimental effects on its relaxivity efficiency[29]. For this reason, alternative acyclic ligand types are now being considered.
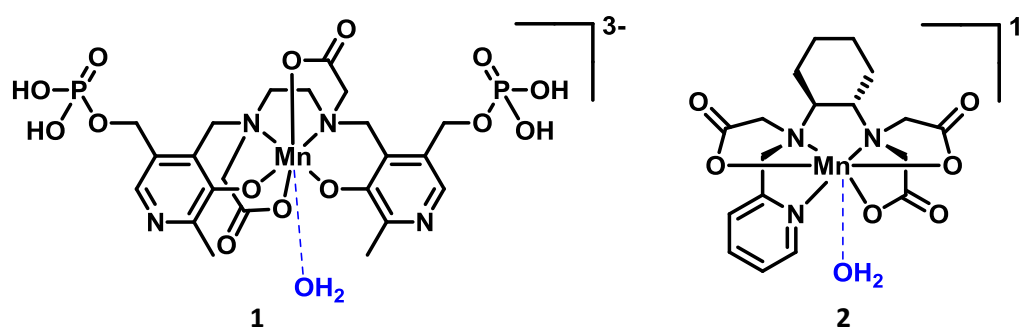
Figure 1.04: Structures of Mn^{II}-based MRI contrast agents

One such alternative from Caravan and co-workers[30] is the hexadentate acyclic ligand PyC3A (N-picolyl-N,N',N'-trans-1,2-cyclohexylenediaminetriacetate) (**2**, figure **1.04**), which showed high stability compared to the commercial contrast agents Magnevist® (Gd^{III}-based) (figure **1.02**) and Teslascan® (Mn^{II}-based). When challenged with 25 mole equivalents of Zn^{II} (pH 6.0, 37 °C), the PyC3A ligand was 20-fold more resistant to metal ion displacement than the diethylenetriaminepentaacetic acid (DTPA) ligand in Magnevist®, and it was also found to be $> 10^5$ times more stable at pH 7.4 than the dipyridoxyl diphosphate ligand (DPDP) in Teslascan®.

The complex also demonstrated excellent properties when tested as an MRI contrast agent *in vivo*. When administered to mice (60 μmol/kg) the agent was > 99 % eliminated by a

mixed renal/hepatobiliary pathway within 24 hours, and when administered to baboons (0.01 mmol/kg) the agent's high stability was enduring, as analysis of blood and urine samples revealed excretion of the agent intact[31]. The relaxivity value measured in bovine blood plasma (r_1 = 3.8 mM^{-1} s^{-1}) was also comparable to both acyclic and macrocyclic commercial Gd^{III}-based agents (Magnevist®, r_1 = 4.1 mM^{-1} s^{-1}; Dotarem®, r_1 = 3.6 mM^{-1} s^{-1}) under identical conditions (60 MHz, 37 °C, pH 7.4), which was attributed to the fast water exchange rate of the water co-ligand (k_{ex} = 1.0 x 10^8 s^{-1}, 37 °C).

A further benefit arising from the design of the PyC3A ligand was the potential to easily modify the structure by straightforwardly substituting the N-pyridyl donor constituent. A short, cyclic peptide shown to have high selectivity for fibrin (the main component of a blood clot) was used to link four Mn^{II}-PyC3A units together, in order to create a complex capable of molecular imaging of thrombosis. No loss of stability was noted with the synthetic modification, and due to the larger size and slower molecular rotation of the complex in solution, the per Mn^{II} ion relaxivity value in pH 7.4 buffer was increased four-fold compared to the smaller, parent complex (r_1 = 8.5 mM^{-1} s^{-1} and r_1 = 2.1 mM^{-1} s^{-1}, respectively).

As research continues to resolve the issue of poor kinetic and thermodynamic stability of Mn^{II}-based contrast agents, whilst improving upon the relaxivity values achievable by the paramagnetic central ion, it becomes more of a possibility that soon the Gd^{III}-based commercial agents will be supplemented with less toxic Mn^{II} alternatives.

1.3) Optical Microscopy

In comparison to the whole-body imaging technique of MRI, optical microscopy has a resolution capable of elucidating detail at the cellular level. As most diseases and cancerous tissues begin at the molecular level, the ability to monitor the biological processes that are the basis of these life-threatening illnesses is extremely important for their earlier detection and treatment. Cells are transparent and colourless, however, and so extracting any kind of detailed image of their morphology is difficult without help from a differential cell stain. Luminescent dyes are widely used for this purpose in optical microscopy as they provide excellent sensitivity and resolution, and many dyes have been designed to target specific biomolecules[32] and chemical species[33]. Indeed, one of the key features of a cancerous tumour is oxygen deprivation (hypoxia)[34], and so a luminescent probe that shows sensitivity to oxygen *via* changes in emission intensity and lifetime can be used to monitor the oxygen levels in living cells to assess their health status[8,35]. Three key organic compounds fluorescein, rhodamine and BODIPY (figure **1.05**) tend to form the foundation of such agents.
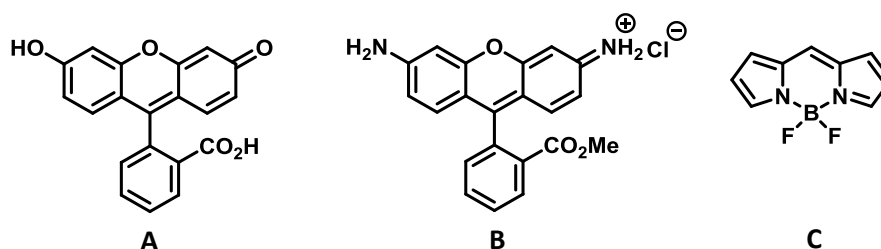
Figure 1.05: Structures of the common organic fluorophores which form the foundation of many optical microscopy imaging agents. **A**) fluorescein, **B**) rhodamine, **C**) BODIPY

Such fluorescent imaging agents allow biological entities and their processes to be tracked, with the view of tracing molecular abnormalities in particular. This is not a straightforward undertaking, however, with several requirements for an effective probe needing to be met. To be even considered for application as a bioimaging agent, a luminophore must first pass a few suitability tests related to its solubility and stability, toxicity, and uptake and localisation *in vitro*.

When entering a biological environment it is essential that the probe remains intact in order to avoid any cytotoxic effects, and it should be photochemically stable when irradiated with light to avoid any unwanted dissociation. The probe should also be resilient to

photobleaching, although an exception to this stipulation is light-activated drug-delivery systems which require ligands to be photolabile in order to have therapeutic effects[36]. With regards to solubility, a probe should readily dissolve into a biologically appropriate solvent such as a buffer solution to aid their cellular uptake, and should remain in solution indefinitely to avoid unwanted leaching out of the cell. The ability to cross lipophilic cell membranes and barriers is also a desired trait of the probe, with the additional feature of specific localisation in a site of interest such as lysosomes[37] or mitochondria[38] being preferred.

Although fluorescent organic dyes have found great utility in optical imaging, their effectiveness is not without flaws. The short emission lifetimes of the probes permits the unwanted interference of autofluorescence from endogenous biomolecules, and synthetic modification of the probe to tailor the absorption and emission properties is not straightforward. To try and combat these issues, research into the use of phosphorescent transition-metal coordination compounds as non-invasive probes has recently increased in popularity[39,40]. Most probes tend to be based on a mid-to-late-transition metal with a d^6 low-spin octahedral electronic configuration. The kinetic inertness of these heavy metal complexes abates their toxicity towards biological matter due to the low rate of ligand exchange, and many such complexes have long-lived and well known luminescence from metal-to-ligand-charge-transfer (MLCT) excited states.

1.3.1) Metal Complexes as Cellular Imaging Agents

Metal complexes possess additional attractive features for use in biological imaging to those detailed above, but when discussing the benefits of using metal-based complexes as emissive probes it first seems pertinent to briefly detail the mechanism by which the complexes absorb and emit radiation. This can be described with a simplified Jablonski diagram (figure **1.06**).

On absorption of a photon, an electron in the chromophore is promoted into a higher energy orbital, taking the molecule from the ground state (S_0) to an excited singlet state (S*). This is a fast, spin-allowed process typically a few femtoseconds in duration. Due to the combination of a low-oxidation d^6 metal centre with π-acceptor ligands such as 2,2'-bipyridine, this state usually has MLCT character and displays a strong absorption coefficient (*ca.* 10^4 M^{-1} cm^{-1}). From the many electronic levels of this excited state, the chromophore can either re-emit this photon as fluorescence (τ = nanoseconds) or can undergo inter-system

crossing (ISC) to an excited triplet state (T*, usually ^{3}MLCT). This process is slower than absorption (typically femtoseconds to nanoseconds in duration) as it violates the spin selection rule, but it is facilitated by spin orbit coupling due to the presence of a heavy metal atom with a high spin-orbit coupling constant, ζ. Emission from the ^{3}MLCT energy level results in longer-lived phosphorescence (τ = microseconds or longer) due to the formally spin-forbidden nature (i.e. $\Delta S \neq 0$) of this radiative transition. It is this emission from the ^{3}MLCT state with long decay lifetimes, as well as several other ideal characteristics, which make metal complexes superior to probes that are purely organic in nature for application in cellular imaging.
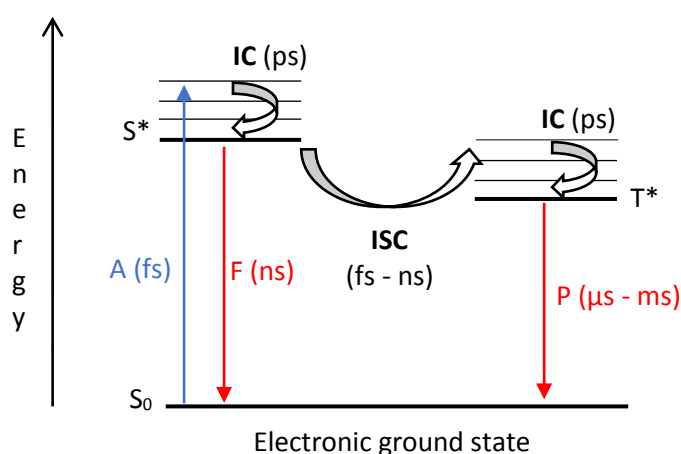
Figure 1.06: A simplified Jablonski diagram illustrating the transitions between electronic states of a metal complex for the processes of fluorescence and phosphorescence. Coloured and block arrows represent radiative and non-radiative processes, respectively. (A = absorption, F = fluorescence, P = phosphorescence, S_0 = singlet ground state, S* = singlet excited state, T* = triplet excited state, IC = internal conversion, ISC = inter-system crossing, fs, ps, ns, µs, ms = femto-, pico- nano-, micro- and milli-second)

One of the most useful features of phosphorescent transition-metal complexes is that colour tuning across the visible spectrum is particularly straightforward with the judicious choice of ligand. Fine-control of the absorption and emission properties of the complex is also made possible by simply attaching electron-withdrawing or -donating groups to the ligand periphery. This means that metal complexes can be designed to absorb and emit in the 'biological optical window' (λ = 650-950 nm), where the absorption of light by most biomolecules in tissues is the lowest[41]. The use of longer wavelength light to excite metal complexes also has the benefit of being less photodamaging to cells during imaging, and can penetrate tissue to increased depths compared to higher energy radiation. This is in stark

comparison to organic fluorophores where such straightforward synthetic modification is unlikely. Tailoring the excitation wavelength to be anywhere other than the UV-visible region of the electromagnetic spectrum is therefore difficult, and consequently most organic fluorophores are often characterised by the unwanted interference of autofluorescence from endogenous biomolecules[42]; an effect made worse by the fact that this cannot be removed by time-gating as the probe fluorescence is also short-lived.

As was noted previously, emission from metal complexes is usually long-lived due to the heavy metal atom with a high spin-orbit coupling constant, ζ, facilitating ISC, which harvests a high triplet quantum yield following photoexcitation. Emission lifetimes are two to three orders-of-magnitude longer than those of organic entities, and as such, phosphorescence from the metal-based probe can be distinguished from the cell's shorter-lived autofluorescence by time-gated detection (figure **1.07**)[38]. A time delay of a few tens of nanoseconds between the excitation pulse and detection of the signal allows for the decay of any background fluorescence. This makes it possible to isolate the desired signal only, giving an enhanced signal-to-noise ratio and very low detection limits. This attribute is also particularly advantageous when using phosphorescence lifetime imaging (PLIM) to study metal complexes *in vitro.*
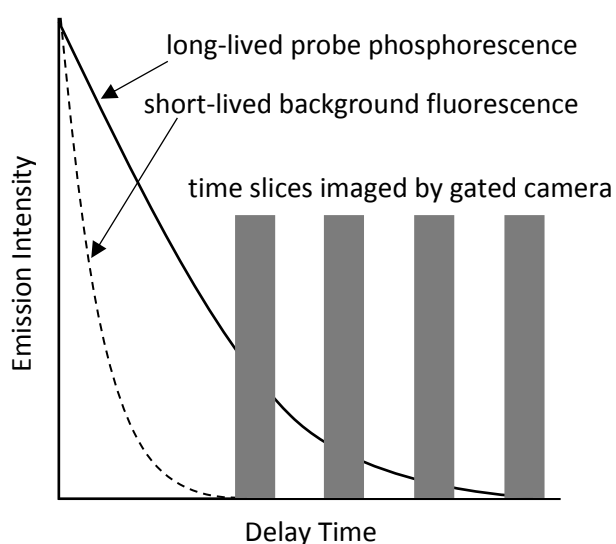

Figure 1.07: Illustration of the concept of time-gating in order to distinguish a desired signal from short-lived background autofluorescence in a cell

The fact that emission originates from a ^{3}MLCT state in heavy metal complexes, which is a different state from that which was excited in the first place, means that overlap of the absorption and emission spectra is small due to the large energy difference between the two energy levels. This is a particular problem with organic fluorophores, which normally absorb into, and emit from, the same S_1 excited state, quite often leading to self-absorption and hence quenching of luminescence.

A final benefit of using metal complexes as phosphorescent probes is that the long-lived excited state has more time to interact with dissolved molecular oxygen in solution, which is useful for a number of reasons. Firstly, the phosphorescence lifetime of the metal-based probe is sensitive to the concentration of oxygen in the surrounding environment, which is a property that can be exploited for phosphorescent lifetime imaging (PLIM). An image is produced based on the differential excited-state decay rates of the probe due to differences in the concentration of oxygen inside a cell, which can be used to detect hypoxic tissues such as cancerous tumours. Secondly, phosphorescent probes interacting with dissolved molecular oxygen results in the formation of singlet oxygen ($^1\Delta_g$ state), which is highly reactive towards biomolecules and leads to phototoxicity. This forms the basis of the use of heavy metal complexes therapeutically in photodynamic therapy (PDT)[43]. Both of these topics will be touched upon later in this thesis.

The current developments in using metal complexes as biological probes for luminescence imaging and therapeutic applications will now be assessed. In particular, emphasis will be placed upon Ru^{II}-based complexes and the progress made over the last decade. Other d-block metal complexes will also be briefly considered including those based on Re^I, Ir^{III}, and Pt^{II}. As the topic area is rather broad and rich with cutting-edge research, only select recent examples are included.

1.3.2) Ruthenium(II)-Based Cellular Imaging Agents

The archetypal Ru^{II} complex, [Ru(bipy)$_3$]$^{2+}$ (where 'bipy' denotes the ligand 2,2'-bipyridine), is well-studied and has ideal photophysical properties for luminescent imaging. Due a combination of the low-oxidation state d^6 metal centre with 2,2'-bipyridine π-acceptor ligands, the lowest excited state of the complex has {Ru$^{II}\rightarrow\pi^*_{(N^\wedge N)}$} MLCT character. ISC from the initially-generated singlet excited state to the triplet manifold is fast, owing to

the heavy atom effect, and therefore, phosphorescence from the ^{3}MLCT state is usually the main radiative decay mechanism. This leads to long emissive lifetimes ($\tau > 500$ ns)[44], which are beneficial for time-gated detection in PLIM, for example, whereby cellular autofluorescence can be excluded. The complex has limited cell permeability, however, which restricts its application as a *cellular* imaging probe. As such, the vast majority of reported Ru^{II}-based cellular imaging agents tend to be based around the [Ru(N^N)$_3$]$^{2+}$ core (figure **1.08**), in which at least one of the polypyridyl (N^N) ligands has been modified to bestow improved cell permeation properties.
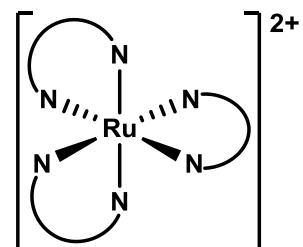
Figure 1.08: The core structure of Ru^{II} cellular imaging agents. (N^N = polypyridyl)

Good examples of this are the well-known molecular 'light-switch' complexes [Ru(bipy)$_2$(dppz)]$^{2+}$ (where 'dppz' denotes the ligand dipyrido[3,2-a:2',3'-c]phenazine) (**3**, figure **1.09**) and [(phen)$_2$Ru(tpphz)Ru(phen)$_2$]$^{4+}$ (where 'tpphz' denotes the ligand tetrapyrido[3,2-a: 2',3'-c: 3'',2''-h: 2''',3'''-j]phenazine) (**4**, figure **1.09**), which both contain extended N^N ligands capable of binding to nuclear DNA[45,46]. The complexes are non-emissive at room temperature in water, but display intense luminescence when bound to double-helical DNA due to shielding of the phenazine nitrogen atoms from any hydrogen-bonded water molecules, which act as quenchers. This remarkable behaviour allows for sensitive probing of the DNA environment, as the intensity and the maximum energy of the photoluminescence responds to subtle changes in the DNA helix structure.

3   **4**
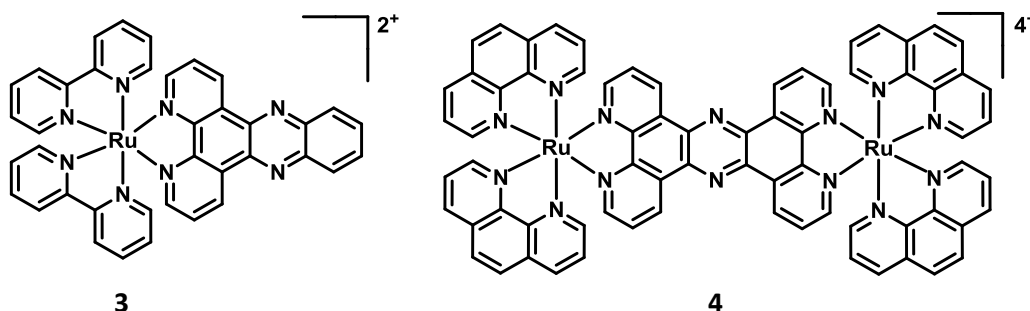
Figure 1.09: Examples of Ru^{II}-based complexes that target the nucleus of a cell by binding to DNA

Due to its excellent light-harvesting properties, compound **4** from Thomas and co-workers has lent itself to a number of different modalities for imaging cellular DNA. As its emission is fairly long-lived ($\tau > 160$ ns), the complex was investigated as the first example of

a transition-metal-based cellular DNA probe using two-photon phosphorescent lifetime imaging microscopy (2P-PLIM)[47]. The luminescence lifetime was orders-of-magnitude longer than conventional fluorescent lifetime imaging microscopy (FLIM), allowing for complete removal of any interfering autofluorescence from endogenous fluorophores and leading to high levels of sensitivity from a cellular DNA probe. The complex has also shown excellent potential as a super-resolution probe[48]; imaging both mitochondria and DNA when used alongside SSIM and STED imaging techniques. In particular, 3D-STED images of nuclear DNA were produced with unprecedented resolution. Furthermore, as the complex consists of two electron-dense metal centres and is kinetically unreactive, along with its Os[II] analogue[49], it has also been used to produce high-resolution images of cellular DNA through the non-light-based imaging technique of transmission electron microscopy (TEM).

As well as imaging nuclear DNA[50], Ru[II]-based luminescent dyes are also being developed as potential anti-cancer therapeutic agents[51,52]. In comparison to commonly used platinum-based compounds such as cisplatin, Ru[II]-based compounds have been shown to cause fewer and less severe side effects, which may in part be due to their improved suitability towards physiological conditions such as slow ligand exchange in water.

One way in which anti-cancer properties are bestowed upon a Ru[II]-based complex is to adorn the probe with an already established anti-cancer drug (**5**-**6**, figure **1.10**). Not only can the luminescence from the metal centre act as a monitor for drug localisation, but the pharmacokinetic and pharmacodynamic properties of the parent drug can also be improved upon as the metal complex aids in cellular uptake. Recently, a luminescent and photolabile Ru[II] complex, [Ru(phen)$_2$Ec$_2$]Cl$_2$ (**5**, figure **1.10**), was developed as a dual cellular imaging agent and a light-activated drug-delivery system by attaching two econazole molecules (an imidazole-based drug currently being investigated for oral and intravenous applications in the treatment of cancer[53]) to a [Ru(phen)$_2$]$^{2+}$ core[36].
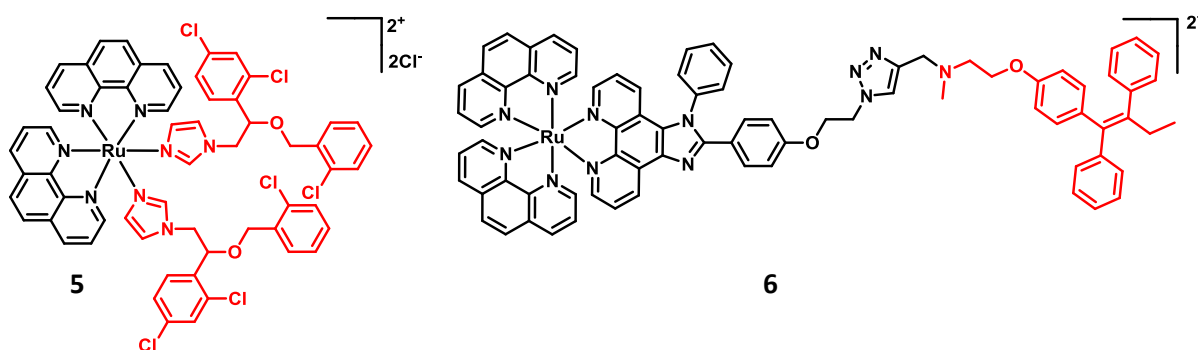
Figure 1.10: Examples of Ru^{II}-based complexes linked to anti-cancer drugs (highlighted in red)

The probe accumulated in the cytoplasm of both live and fixed DLD-1 colon carcinoma cells (20 µM, 4 hours, 37 °C), with red luminescence being observed under physiological conditions in the dark (figure **1.11a**). This confirmed that no ligand exchange occurred under these conditions, as the corresponding photoactivated complex, in which one of the econazole ligands has been photocleaved, is non-luminescent. Upon increasing irradiation times with green light (λ_{ex} = 520 nm), however, a decrease in emission intensity was observed (figure **1.11a**), indicating the selective cleavage of a metal-drug bond to produce free econazole and [Ru(phen)$_2$Ec(H$_2$O)]$^{2+}$.
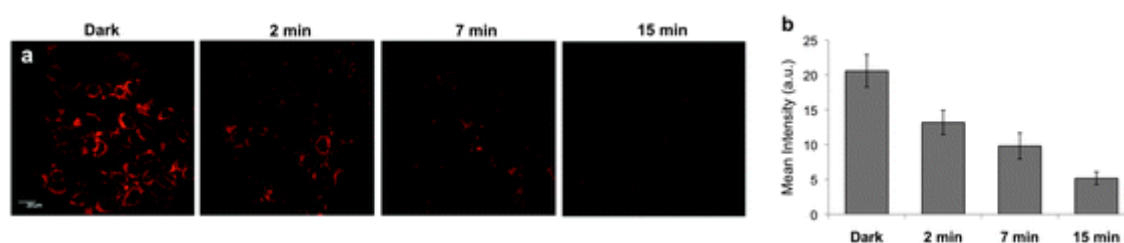
Figure 1.11: a) Confocal luminescence microscopy images of DLD-1 cells treated with **5** and irradiated with light for different time periods. (Scale bar = 20 µm); b) Mean luminescence intensities of cell samples after light treatment. (Reproduced with permission from ref. 36. Copyright (2015) Royal Society of Chemistry)

To measure the cytotoxicity of the prodrug, various tumour cell lines were incubated with the complex for 24 hours and then irradiated with light for 15 minutes. Cell viability studies revealed a significant increase in cytotoxicity upon irradiation with green light, compared to control cells that were left in the dark and those incubated with just the parent drug econazole nitrate.

This work demonstrated the promise that metal-complex-based, light-activated drug delivery shows for the improved transport of drugs. Their prodrug forms can be supplied in fairly high concentrations and their localisation monitored by luminescence, whilst they are physiologically inert in the dark and only selectively toxic to cells upon irradiation with light.

Ru^{II} polypyridyl complexes can lack selectivity for cancerous cells, however, being taken up equally well by healthy cells, leading to unwanted phototoxicity to normal tissue. Therefore, substituting the complexes with targeting groups that are known to bind to receptors in cancerous cells can guide the probes to selectively accumulate in unhealthy tissues. One such [Ru(phen)$_2$(N^N)]$^{2+}$ probe was tethered to a tamoxifen molecule (**6**, figure **1.10**), which is known to competitively bind to oestrogen receptors in breast cancer cells[54]. This blocks the effect of oestrogen on these receptors and stops the encouragement of cancerous cell growth by initiating programmed cell death. The Ru^{II} metal centre was shown to be an efficient phosphorescent guide and producer of singlet oxygen ($^1O_2$) under two-photon irradiation ($\lambda_{ex} = 830$ nm), which makes the probe a candidate for use in PDT. Reactive oxygen species (ROS) such as $^1O_2$ are highly cytotoxic; damaging intracellular biomolecules and ultimately instigating cell death. If carefully controlled, this generation of ROS can be used to treat a small abnormal area of tissue without the need for surgery.

Compared to a control molecule not adorned with a tamoxifen unit, compound **6** demonstrated enhanced cellular uptake and two-photon photodynamic therapy (2P-PDT) abilities in MCF-7 breast cancer cells, whereas little uptake and phototoxicity was demonstrated in non-cancerous cell lines (HL-7702 and COS-7) (figure **1.12**). The tamoxifen moiety was confirmed as the key mediator for uptake of the complex into the breast cancer cells, as a competition experiment with an oestrogen receptor inhibitor led to suppressed uptake of the probe. Cell viabilities of *ca.* 90 % were measured with increasing concentrations of compound **6** in the dark, however, a reduction in the viability of MCF-7 cells by 99 % was achieved with a probe concentration of only 16 µM when the cells were irradiated. This demonstrated that like other 2P-PDT agents, cytotoxicity could be selectively 'switched-on' through irradiation with light, but that also selective uptake into unhealthy breast cancer cells could be orchestrated by tethering the Ru^{II} probe to an oestrogen-receptor targeting molecule (tamoxifen). This leads the way to a new design of 2P-PDT agents, whereby healthy tissue will remain unaffected by treatment.
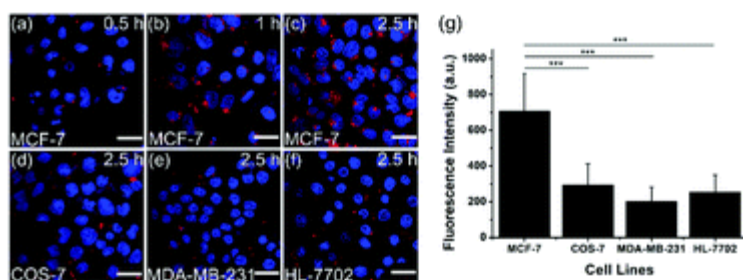
Figure 1.12: Confocal luminescence microscopy images of MCF-7 cells treated with **6** for a) 0.5 h, b) 1 h, and c) 2.5 h; d) COS-7 cells incubated with **6** for 2.5 h; e) MDA-MB-231 cells incubated with **6** for 2.5 h; f) HL-7702 cells incubated with **6** for 2.5 h. The nucleus was stained with Hoechst 33342 (λ_{ex}: 405 nm, λ_{em}: 430–470 nm) and **6** (λ_{ex}: 488 nm, λ_{em}: 570–630 nm) (Scale bar = 30 μm). g) Fluorescence intensity of **6** in different cells after 2.5 h incubation. (Reproduced with permission from ref. 54. Copyright (2018) Royal Society of Chemistry)

1.3.3) Other D-Block Metal Cellular Imaging Agents

Progress in developing luminescent Re^I complexes as cellular imaging agents has occurred steadily since Coogan and co-workers first reported their potential in 2007[55]. The archetypal structure for such complexes is that of *fac*-[Re(CO)$_3$(N^N)X]$^{n+}$ (figure **1.13**), where N^N is a polypyridyl ligand such as 2,2'-bipyridine or 1,10-phenanthroline, and X is a monodentate ancillary ligand such as a halide or substituted pyridine.

In general, complexes of this nature exhibit intense and fairly long-lived luminescence (τ > 200 ns), usually in the lower-energy region of the visible spectrum and typically from a ^{3}MLCT {$Re^I \rightarrow \pi^*_{(N^N)}$} state[56]. Tuning of both absorption and emission energies is, therefore, made facile by the introduction of electron-withdrawing or electron-donating groups onto the polypyridyl ligand, leading to a blue- or red-shift in energy, respectively. Conversely, studies have shown that modification of the spectator ligand, X, only produces small changes to the photophysical behaviour of the complexes[57]. This presents the opportunity to tailor the uptake and localisation properties of the complexes[58] without compromising the desired luminescent properties of the probe. The inherent versatility that comes from the easy synthetic modification of the ancillary ligand, X, also allows Re^I complexes to be designed with the intention of sensing particular entities that may indicate certain health problems. For example, the ability to sense certain
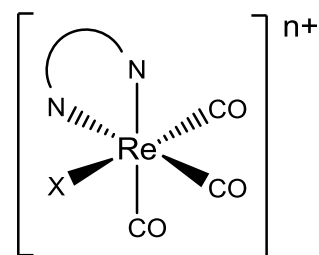
Figure 1.13: The core structure of Re^I cellular imaging agents. (N^N = polypyridyl, X = halide or pyridyl)

sugars[59] (glucose in particular) can aid in the tracking of rapidly growing cancer cells due to their propensity to catabolize glucose at high rates.

In addition to the useful properties bestowed on Re[I] complexes by the polypyridyl and ancillary ligands, the three carbon monoxide (CO) ligands give rise to potential anti-cancer properties[60]. CO-releasing molecules (CORMs) have shown excellent promise when used to deliver moderate doses of toxic CO gas to cancerous cells, as the ensuing disruption to mitochondrial function induces cell death. However, target selectivity and dosage control are hard to orchestrate in most cases. Luminescent Re[I] compounds that are photoactivatable are, therefore, incredibly useful as *photo*-CORMs, as the photoinduced release of CO ligands can be carefully controlled by irradiation, and the localisation of the probe and degree of CO delivery can be monitored by luminescence microscopy.

A 2-(2-pyridyl)benzothiazole (pbt) Re[I] complex (**7a**, figure **1.14**) entrapped in the pores of mesoporous silica nanoparticles (MSNs) displayed luminescence 'turn-off' upon irradiation with low-power UV light, due to the resulting Re[I] complex being non-luminescent upon photoinduced release of one of the CO ligands[61]. This property was used to monitor the CO-induced cell death in MDA-MB-231 (human breast cancer) cells incubated with the Re[I]-loaded MSNs, as the orange intracellular luminescence was diminished upon the photoinduced release of a CO ligand. Replacing the ancillary ligand with a water molecule (**7b**, figure **1.14**) produced a Re[I] photo-CORM that not only displayed orange emission (λ_{em} = 605 nm) 'turn-off', but also exhibited blue luminescence 'turn-on' (a 200 nm blue-shift) upon complete loss of *all three* CO ligands (figure **1.15**)[62]. Again, tracking of the CO-induced cell death in MDA-MB-231 cells incubated with the Re[I] complex was achieved by monitoring the progressive loss of orange luminescence, but this time the concomitant gain of blue luminescence from the free pbt ligand was used to signal the end point in CO delivery.

$X = P(C_6H_5)_3$ **(a)**
H_2O **(b)**

7
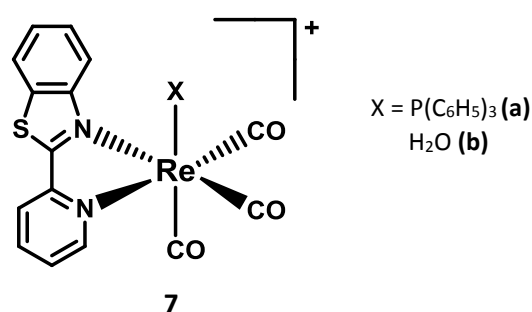
Figure 1.14: Examples of photoactivatable CO-releasing (photo-CORM) Re[I] complexes
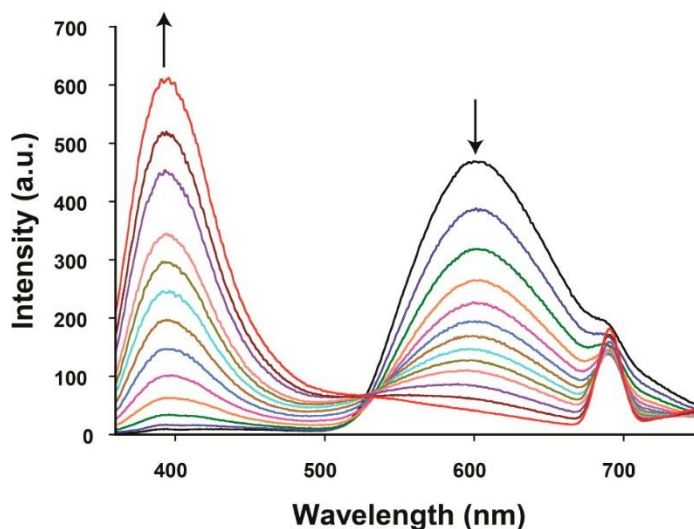
Figure 1.15: Time-resolved luminescence traces of **7b** in acetonitrile upon exposure to low-power UV illumination at two minute intervals. (Reproduced with permission from ref. 62. Copyright (2016) American Chemical Society)

In the case of Ir[III]-based probes, heteroleptic complexes of the type [Ir(C^N)$_2$(N^N)]$^+$ (figure **1.16**) are the most widely investigated, where C^N is a monoanionic cyclometalating ligand such as 2-phenylpyridine (ppy) or 2,4-difluorophenylpyridine (dfppy) and N^N is a polypyridyl ligand such as 2,2'-bipyridine or 1,10-phenanthroline[63]. Density functional theory calculations have shown that the highest occupied molecular orbital (HOMO) in these complexes is composed of the Ir[III] d-orbitals and the π-orbitals of the phenyl rings, whereas the lowest unoccupied molecular orbital (LUMO) is localised on the heterocyclic rings of the cyclometalated ligands[64]. Although the polypyridyl ligand is not directly involved in the lowest excited state, it can affect the excited-state energy by adjusting the electron density at the metal centre[65]. As a result of this, emission from Ir[III] compounds is tuneable across the visible spectrum from blue to red, and emission lifetimes ranging from nanoseconds to milliseconds can be achieved.
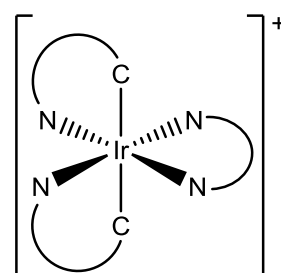
Figure 1.16: The core structure of Ir[III] cellular imaging agents. (N^N = polypyridyl, C^N = cyclometalated ligand)

The bis-cyclometalated nature of the compounds also offers distinct advantages when considering the complexes as imaging agents. The overall formal charge of the complex is lower (+1 rather than +3 in [Ir(N^N)$_3$]$^{3+}$ complexes), which bestows good cellular uptake

properties on the complex, as lower-charged compounds pass across cell membranes more readily than those with higher charges. The lipophilicity associated with the cyclometalated core also aids the transport of the complexes into the cell structure; however, it does seem to hinder control over specificity of localisation. Finally, the σ-donating character of the ligands raises the energy of the metal-centred orbitals. This improves their ability to participate in the excited-state of the complex, leading to high triplet-state conversion efficiencies and an increase in the radiative rate constant[66]. As such, Ir[III]-based complexes are often used to monitor the oxygen concentration in cells and *in vivo*, as molecular oxygen with a triplet ground state efficiently quenches the phosphorescence from the Ir[III] triplet-excited-state *via* energy-transfer. This change in emission intensity and lifetime from the Ir[III] centre provides a means to quantify the oxygen concentration wherever the probe is localised.

A deprivation of adequate oxygen supply, known as hypoxia, can affect gene expression and can greatly accelerate the progression of tumour growth. At the other extreme, an excess of molecular oxygen (hyperoxia) can cause increased levels of reactive oxygen and nitrogen species (RONs), which can affect the central nervous system. A quantitative detection method for the levels of oxygen *in vivo* is, therefore, an extremely important tool for the earlier detection of these diseases. Exploiting the luminescence properties of an Ir[III] complex provides a non-invasive method that can be used alongside imaging techniques such as PLIM. In general, most probes have been designed to detect hypoxic conditions[8,67]; however, one recently reported dual-phosphorescent Ir[III]-based probe from Lo and co-workers sequentially imaged both hypoxia and hyperoxia (**8**, figure **1.17**)[68].

8
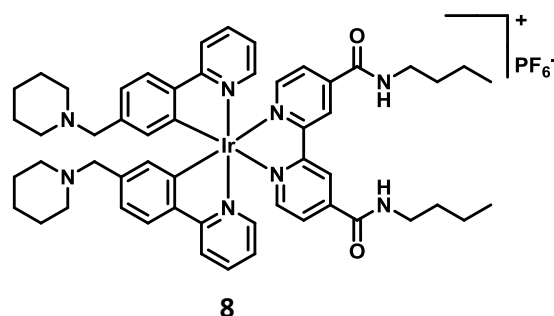
Figure 1.17: A dual-phosphorescent Ir[III] probe for sequential imaging of hypoxic and hyperoxic conditions

The complex in question displayed naked-eye distinguishable green, orange and red emission in aqueous buffer solution under three different oxygen concentrations – hypoxic (N_2 atmosphere), normoxic (air) and hyperoxic (O_2 atmosphere), respectively (figure **1.18**). This emission sensitivity to oxygen concentration was reproduced when the probe was incubated (5 µM, 2h) with three different cell types (HeLa, HepG2, and 3T3) under low (5 %) and high (50 %) oxygen environments, as the green luminescence was predominant under the hypoxic conditions, and red luminescence under the hyperoxic environment. This demonstration of spectral response to intracellular oxygen concentration from a single small molecule opens the door to more easily diagnosing abnormal molecular oxygen levels *in vivo* that are the underlying cause of many diseases.
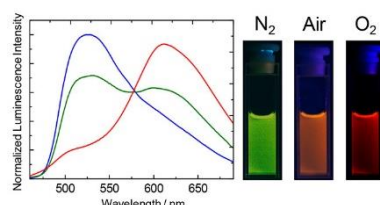
Figure 1.18: Luminescence spectrum of **8** in PBS/MeOH (9:1, *v:v*) under N_2 (blue), air (green), and O_2 (red) atmospheres and photographs of **8** upon excitation by a UV lamp. (Reproduced with permission from ref. 68. Copyright (2018) American Chemical Society)

Unlike the d^6 metals Ir^{III}, Ru^{II} and Re^I that adopt a distorted octahedral arrangement, Pt^{II} is a d^8 metal ion and prefers to assume a 4-coordinate square planar configuration. The metal has found widespread use in the chemotherapeutic agents cisplatin, carboplatin and oxaliplatin (figure **1.19**), which stop cancer cells from multiplying by forming covalent Pt-DNA crosslinks. However, the evolution of resistant cell lines and the lack of control over specific localisation leading to non-cancerous cell death are issues needing to be addressed with these chemotherapeutic agents. For this reason new Pt^{II}-based complexes are currently being investigated for use in PDT, as the toxicity can be controlled by light-activation, significantly reducing damage to healthy tissues[69,70].
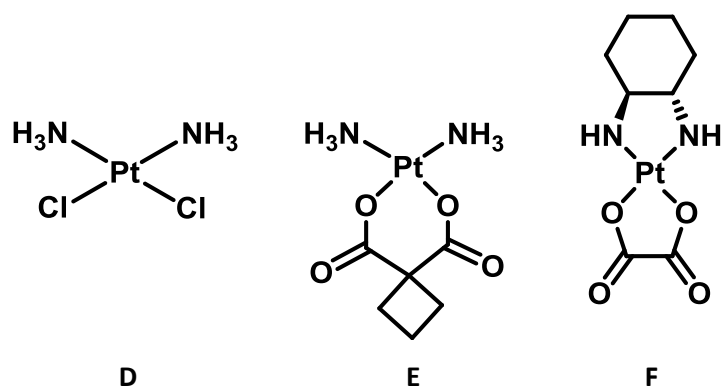
Figure 1.19: Structures of Pt^{II}-based chemotherapeutic drugs.
D) cisplatin, E) carboplatin and F) oxaliplatin

One such example was based on a methyl-substituted, cyclometalating N^C^N ligand (**9**, figure **1.20**)[71]. The complex demonstrated excellent light toxicity in several cancerous cell lines (HeLa, SW480 and EJ) as well as in the cisplatin-resistant bladder cancer cell line, EJ-R, at low concentrations (0.1–1 µM) and low doses of visible light (λ_{ex} = 405 nm, 3.6 J cm^{-2}).

9
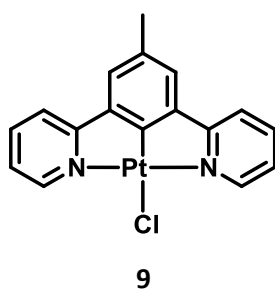
Figure 1.20: An example of a cyclometalated
Pt^{II}-based PDT agent

1.4) Dual-Modality Imaging

Collectively, the arsenal of imaging techniques available covers the complete spectrum of diagnostic eventualities: from imaging tumours in larger three-dimensional systems (MRI, PET, X-ray), down to tracing microscopic abnormalities inside a cell (optical). However, it remains the case that no individual technique reigns supreme with regards to suitability for all applications. Each method suffers from an inherent limitation, such as poor resolution or lack of sensitivity, restricting its ability to interrogate all aspects of structure and function[72].

This issue is not a trivial one to resolve, however, as the simple combination of two separate probes is not a practical option. Co-localisation in an area of interest is unlikely as identical bio-distribution is difficult to engineer. The design of dual- or multi-modal probes, in which two or more independent reporters are integrated into one unit, is therefore an area of immense interest. Identical pharmacokinetics are guaranteed as the probes are tethered together through chemical bonds, and the visualisation of biological matter can be enhanced enormously by simultaneously exploiting the advantages of each detection mode. By combining the synergistic signals arising from both imaging modalities, images can be developed to reveal exquisite detail.

A combined positron emission tomography–computed tomography (PET-CT) scanner[73] has already established the evolution of medical diagnosis, with hybrid PET-MRI scanners[74] following suit just this decade. Data from both devices can be taken sequentially and superimposed to form a single image. The amalgamation of data from the two separate sources allows both accurate diagnosis of health issues such as cancer, but also the facile monitoring of the success of treatment. A drawback to such systems, however, is that they still require the use of both ionising radiation and unpleasant radiochemicals. For this reason, research into multi-modal probes finds itself favouring optical microscopy/MRI hybrids, as both techniques are relatively mild towards biological matter in comparison. Interest has grown to such an extent recently that this combination now finds itself in the pre-clinical phase[75].

1.4.1) Dual Optical/MR Imaging Agents

Optical imaging has excellent sensitivity and resolution compared to MRI, but the depth of tissue penetration it can achieve is only in the millimetre range. In contrast, MRI can image optically opaque systems. The practicality of utilising luminescence is, therefore, limited to cellular and subcellular level imaging; quite complementary to the capability of MRI to image whole bodies/organs. It therefore stands to reason that when a luminescent dye and an MRI-active unit are combined into a single, dual-modal entity, a superior probe will be produced; not only capable of imaging the 'bigger picture', but also capable of delving into the intricate detail within a cell.

There are many interesting approaches described in the literature of ways in which these two modes of imaging have been integrated into a single probe. The simplest method is the attachment of small organic fluorophores to the pendant arms of the already established MRI contrast agents (figure **1.02**)[76–78]. Although this practice appears to be effective, with the design of biologically relevant porphyrin-Gd[III] amalgams being reported[79], in the majority of cases the issue of interfering background autofluorescence still remains a fundamental flaw that needs to be addressed. Larger organic systems such as quantum dots[80,81] and nanoparticles[82] functionalised with Gd[III]-chelates have also been described.

Luminescent Ln[III] ions – mostly Eu[III] and Tb[III] (both of whom emit in the visible region of the electromagnetic spectrum) – have also been extensively exploited in the design of dual-modal probes. A distinct chelating structure is usually loaded with either a magnetic Gd[III] ion or a photoluminescent Ln[III] ion and then mixtures of the two probes administered[83]. Parallel bio-distributions are hypothesised in this case due to the isostructural nature of the probes and the chemical similarity of the Ln[III] ions. A distinct challenge with this method, however, is the opposing requirements that each Ln[III] ion has with regards to coordinating water molecules. To obtain an efficient contrast agent for MR imaging purposes, coordination of a water molecule to the Gd[III] ion is essential. For the purposes of optical imaging, however, coordination of a water molecule is deleterious to the luminescence of the Ln[III] ion. Hence a 'Catch-22' situation is created that is particularly difficult to resolve. However, recent advances using Tb[III][84,85] or Dy[III][86] as both the magnetic unit and the photoluminescent unit has proven successful, as well as linking multiple [Gd(DOTA)]- (commercial Dotarem®) chelates to the surface of NaGdF$_4$:Yb[III],Tm[III] upconverting nanoparticles[87].

This thesis will focus upon the strategy of combining a photoluminescent transition-metal moiety with a magnetic Gd^{III} unit. Gd^{III} has already been shown to act as an efficient contrast agent for MRI (section **1.2.1**) due to its seven unpaired electrons and high paramagnetic relaxivity[15,88], and so the vast majority of literature in this area involves this particular Ln^{III} ion. However, there has been a recent report of integrating MnO$_2$ nanosheets with [Ru(bipy)$_3$][PF$_6$]$_2$ to produce an optical/MRI dual-modal probe that takes advantage of the paramagnetic properties of the Mn^{II} ion[89].

The incorporation of a luminescent transition-metal ion into the design helps to overcome many of the issues encountered with the previous attempts at producing dual-modal probes, due to the many advantageous properties that metal complexes possess when applied to biological imaging (section **1.3.1**). Numerous d-block metals have been utilised[90–93], however, this thesis will place particular emphasis on d-f hybrids utilising the luminescent properties of a Ru^{II} metal centre, and will briefly survey potential dual-modal optical/MRI complexes based on Re^{I}, Ir^{III} and Pt^{II} as well.

1.4.1.1) Ruthenium(II)-Gadolinium(III) Heteropolymetallic Complexes

Integrating Ru^{II} metal centres into the design of dual-modal optical/MRI probes is a judicious choice, as these complexes exhibit excellent light-harvesting abilities as well as the propensity to emit luminescence towards the red (and more biologically penetrative) end of the visible spectrum. The first such reported example utilised two terpyridine-based ligands adorned with diethylenetriamine-N,N,N'',N''-tetraacetate (DTTA) polycarboxylates at the 4'-positions to bind two MRI-active Gd^{III} ions (**10**, figure **1.21**)[94]. The relaxivity value measured for this dual-modal RuGd$_2$ probe was r_1 = 7.8 mM^{-1} s^{-1} per Gd^{III} ion (20 MHz, 37 °C), which is higher than the commercial MRI agents under the same experimental conditions (r_1 = 3.8-4.0 mM^{-1} s^{-1} per Gd^{III} ion).

This increase in proton relaxivity was attributed to a number of factors. Firstly, the water co-ligand exchange rate (measured for the Fe^{II} analogue) was faster than that of the commercial agent Magnevist® ([Gd(DTPA)]$^{2-}$) (k_{ex} = (5.1 ± 0.3) x 10^6 s^{-1} and k_{ex} = (3.3 ± 0.2) x 10^6 s^{-1}, respectively) due to the presence of two water molecules bound to each of the Gd^{III} centres (one more than the commercial agent). Secondly, the larger size of the complex and

the rigidity of the terpyridine ligands contributed to slowing the rotational correlation time of the probe in solution (τ_R = 410 ± 10 ps).

Unfortunately, enhancing the rigidity of the complex by directly linking the Gd[III] binding site to the terpyridine ligand had a negative effect on the stability of the complex. The basicity of the electron lone-pair on the central nitrogen atom on the DTTA ligand was reduced by the electron-withdrawing nature of the aromatic ligand, making Gd[III] dissociation *in vivo* more likely in comparison to the commercial MRI agents. Utilisation of the terpyridine ligands also had a negative effect on the luminescent properties of the dual-modal probe, as the Ru[II] centre was not emissive at room temperature in water (as has been found with the parent compound, [Ru(terpy)$_2$]$^{2+}$)[95]. This is due to thermal quenching of the lowest energy ^{3}MLCT excited-state by non-radiative decay of the low-lying triplet metal-centred (^{3}MC) state.
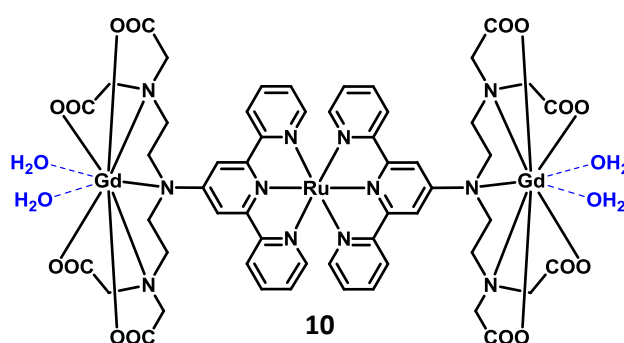
Figure 1.21: An example of a combined Ru[II]-Gd[III]$_2$ dual-modal optical/MR imaging agent

A second reported Ru[II]-Gd[III] heteropolymetallic complex from the Parac-Vogt group also utilised an acyclic motif for binding the MRI-active Gd[III] ion, however, in this example the [Gd(DTPA)] chelate was straddled by two luminescent [Ru(bipy)$_2$(ph-phen)]$^{2+}$ units (**11**, figure **1.22**)[96]. In this case, the relaxivity value measured in water was r_1 = 7.0 mM^{-1}s^{-1} (20 MHz, 37 °C), increasing to r_1 = 14.3 mM^{-1}s^{-1} (20 MHz, 37 °C) when measured in a 4 % solution of human serum albumin (HSA). This confirmed that the probe was making non-covalent interactions to the protein, as the mobility of the MRI agent was reduced, which led to the longitudinal relaxation rate doubling in value.
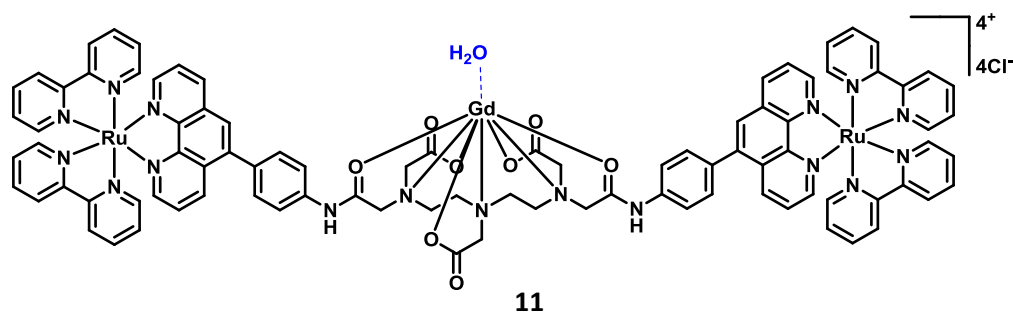
Figure 1.22: An example of a combined Ru$^{II}_2$-Gd^{III} dual-modal optical/MR imaging agent

Although the relaxivity value measured in water was an improvement on the parent [Gd(DTPA)]$^{2-}$ MRI agent, it was hampered by the slow water exchange rate brought about by a long residence time of the bound water molecule in the first coordination sphere (τ_M = 808 ± 34 ns). The stability of the complex to Gd^{III} dissociation was also not considered for the purposes of *in vivo* imaging. The luminescence behaviour of the [Ru$_2$Gd]$^{4+}$ dual-modal probe was an improvement on the terpyridine-based RuGd$_2$ complex (**10**), however. Upon excitation into the ^{1}MLCT absorption band at λ_{ex} = 440 nm, the complex displayed bright red emission in water (λ_{em} = 550-850 nm, centred at λ_{em} = 620 nm, ϕ = 4.7 %), which was long-lived (τ = 540 ns).

As the acyclic Gd^{III} chelates have been found to have reduced stability with regards to Gd^{III} dissociation *in vivo*, a number of recently published Ru^{II}-Gd^{III} potential dual-modal probes have chosen to use the more stable macrocyclic [Gd(DOTA)] motif for binding the MRI-active metal centre (figure **1.23**).
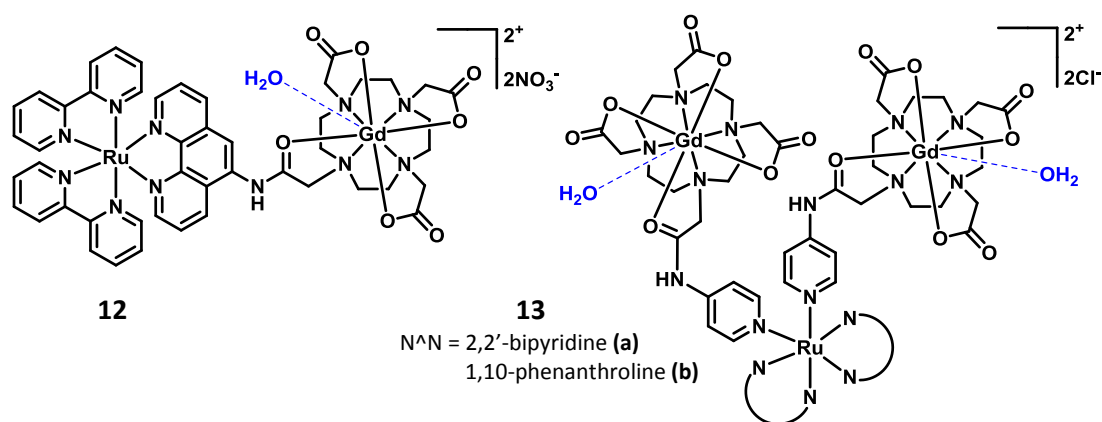
Figure 1.23: Examples of combined Ru^{II}-Gd^{III} dual-modal optical/MR imaging agents with macrocyclic Gd^{III} binding sites

The first example was a simple bimetallic [RuGd]$^{2+}$ complex based on a central [Ru(bipy)$_2$(phen)]$^{2+}$ core (**12**, figure **1.23**)[97], which had a measured relaxivity value in water of r$_1$ = 4.7 mM^{-1} s^{-1} (20 MHz). This value is marginally improved upon compared to that of the commercial agent [Gd(DOTA)]$^-$, due to the [RuGd]$^{2+}$ probe's higher molecular weight reducing its rotational correlation time, however, there is no indication of the experimental temperature which makes it difficult to accurately compare the values. To evaluate the probe's MRI capabilities *in vivo* it was administered to a Kunming mouse (0.2 mL, 2 mM). Bladder contrast enhancement was detected five minutes after injection, continued for up to six hours, and then returned to zero after 22 hours. This is likely due to the excretion of the probe; however, no experimental procedures were carried out to quantify this.

When tested as a luminescent marker the probe also showed promising activity. In PBS buffer at pH 7.4 the ^{1}MLCT absorption maximum was found to be λ_{abs} = 450 nm. Upon excitation in to this band, a typical luminescence profile was recorded for the [Ru(bipy)$_2$(phen)]$^{2+}$ core with an emission maximum centred at λ_{em} = 605 nm and a lifetime of τ = 688 ns. Incubation of the probe (10 μM, 15 minutes, 37 °C) in human liver carcinoma cells (HepG2) led to clear intracellular luminescence detectable in the nuclear region and the cytoplasm, with minimal cytotoxicity being observed (cell viabilities were > 90 % even with probe concentrations of up to 100 μM). Incubation of the probe in the small crustacean, *Daphnia magna*, confirmed its successful application to *in vivo* imaging.

Further trimetallic [RuGd$_2$]$^{2+}$ complexes in which the luminescent centre was either [Ru(bipy)$_2$]$^{2+}$ or [Ru(phen)$_2$]$^{2+}$ (**13a-b**, figure **1.23**)[98,99] were also reported for their potential as dual-modal optical/MR imaging agents. Introduction of the Gd^{III} chelates was achieved by coordination of pendant pyridine rings (on substituted DOTA ligands) to the two vacant binding sites on the Ru^{II} metal centre.

The relaxivity values measured for the complexes were modest (r$_1$ = 5.8 mM^{-1} s^{-1} and r$_1$ = 6.2 mM^{-1} s^{-1} per Gd^{III} ion, respectively) (20 MHz, 37 °C, pH 7.4, PBS), but both were an improvement upon the value for the parent [Gd(DOTA)]$^-$ complex (r$_1$ = 3.4 mM^{-1} s^{-1}) under the same experimental conditions. When measured in the presence of a 4.5 % HSA solution, both of the complexes displayed enhanced relaxivity values (r$_1$ = 14.3 mM^{-1} s^{-1} and r$_1$ = 15.4 mM^{-1} s^{-1} per Gd^{III} ion, respectively) due to the non-covalent interactions between the probe and the protein, which slow down the molecular tumbling in solution.

The probes demonstrated typical luminescent properties for the $[Ru(bipy)_2]^{2+}$ and $[Ru(phen)_2]^{2+}$ central units, with ^{1}MLCT absorption maxima at λ_{abs} = 480 nm, and emission maxima in the region of λ_{em} = 590-595 nm when measured in 0.1 M Tris-HCl buffer at pH 7.4 and room temperature. When incubated with HeLa cells (50 µM, 24 h, 37 °C), both $[RuGd_2]^{2+}$ imaging agents showed high cytotoxic properties (cell viabilities between 46.0-19.5 %) at relatively low concentrations of the probes due to the promotion of apoptosis (programmed cell death). This suggests that rather than being potential dual-modal *imaging* agents, the probes may be useful as therapeutic *anti-cancer* agents.

1.4.1.2) Other D-Block Metal-Gadolinium(III) Heteropolymetallic Complexes

Re^I metal centres are good candidates to be the luminescent component of a dual-modal optical/MRI probe, as the metal tolerates a comprehensive range of synthetic possibilities. In theory, the formation of bio-conjugates and more complicated architectures is facile due to the ease in which the labile chloride ligand on the central Re^I atom can be substituted. Its chemistry is also analogous to that of ^{99m}Tc^I, the most commonly used radioisotope in medicine. As such, dual-modal imaging probes integrating Re^I centres can also be thought of as prospective dual-modal MRI/SPECT probes as well[100]. As a result of these attractive qualities, one of the first examples of a d-f dual probe was a Re^I-Gd^{III} complex[101].

A $[Re(bipy)(CO)_3]^+$ core was attached to a $[Gd(DOTA)]$ chelate through a pyridine spacer unit (**14**, figure **1.24**). When excited in the near-UV (λ_{ex} = 337 nm), the lifetime of the Re^I ^{3}MLCT emission (λ_{em} = 600 nm, water) was improved upon greatly compared to the parent complex $[Re(bipy)(CO)_3Cl]$ (τ = 240 ns and τ < 10 ns, respectively)[102] because of the substitution of the chloride ligand with an N-bound pyridyl group. This longer luminescence lifetime would allow for the efficient gating of any background autofluorescence if the probe were to be used as a luminescent dye.

The relaxivity value measured in water was large at high frequency values (r_1 = 8.6 mM^{-1} s^{-1}, 500 MHz), which was attributed to a dihydrate coordination state and most likely a high water exchange rate as a result of this. When measured in PBS, the relaxivity value decreased (r_1 = 3.9 mM^{-1} s^{-1}, 500 MHz), however, as a consequence of phosphate anions competitively binding to the Gd^{III} ion and reducing the number of water molecules bound to the paramagnetic centre. This may be an issue for use of the probe *in vivo* as many biological entities may cause this detrimental effect to occur.
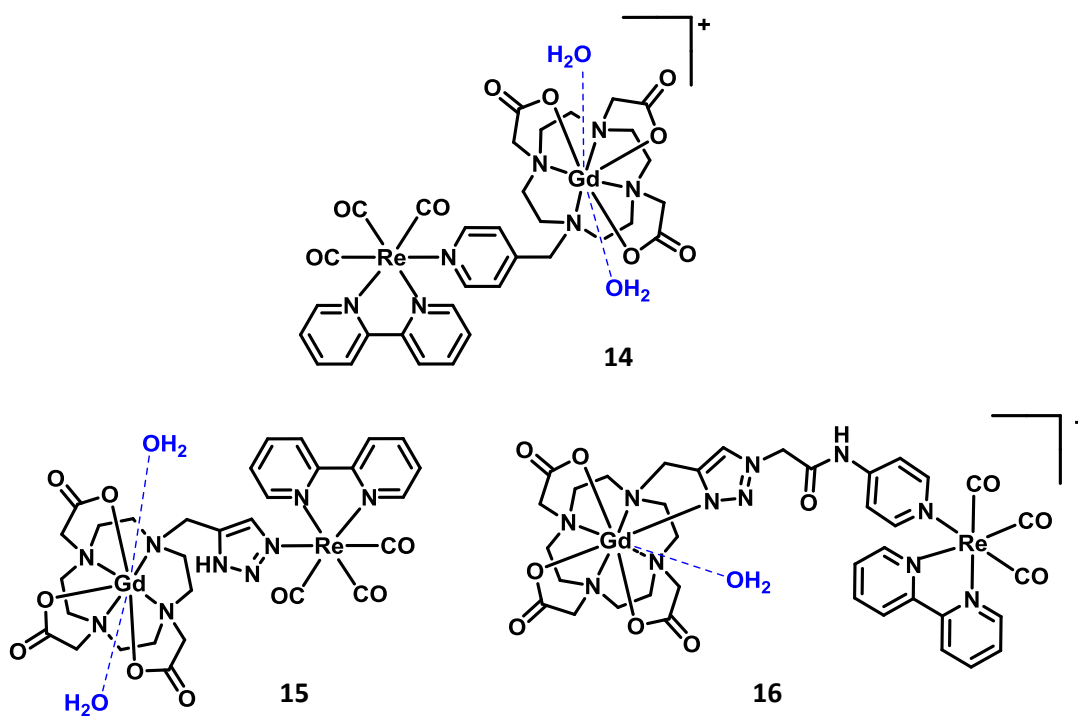
Figure 1.24: Examples of combined Re^I-Gd^{III} dual-modal optical/MR imaging agents

Later examples from the same group[103] addressed this issue and highlighted the importance that judicious design of the spacer ligand between the two metal centres has on the dual-modal imaging abilities of a probe. Simple [Gd(DOTA)] complexes were synthesised in which the Re^I and Gd^{III} binding sites were bridged by differing ligands containing triazole units (**15**-**16**, figure **1.24**). In complex **15** the triazole unit bridges both of the metal centres. This direct coordination of the Re^I centre to the triazole unit reduced the donor ability of the other nitrogen atoms in the ring, and as such an equilibrium existed in which the triazole unit was either coordinated or uncoordinated to the Gd^{III} ion, leaving a vacant site available for a second water molecule to bind. In complex **16**, however, the Re^I centre was separated from the triazole unit by an alkyl spacer and so an octadentate Gd^{III} chelate was favoured, leaving only one vacant binding site available for a water molecule.

Upon photoexcitation (λ_{ex} = 337 nm), both complexes displayed similar Re^I ^{3}MLCT-based emission profiles in water (λ_{em} = 600 nm, $\tau \approx$ 110 ns), however, the different coordination environment at the Re^I centres affected the relaxometric properties of the two probes. Complex **15** showed an increased relaxivity value (r_1 = 5.3 ± 0.5 mM^{-1} s^{-1}) compared to complex **16** (r_1 = 4.2 ± 0.4 mM^{-1} s^{-1}) when measured in water under the same experimental conditions (7 T, 37 °C, pH 7.4); most likely due to an increased hydration number (q = 2) in complex **15**. However, when measured in PBS, the extra vacant coordination site in complex

15 left the probe susceptible to competitive phosphate anion binding and the relaxivity value decreased greatly (r_1 = 3.2 ± 0.3 mM^{-1} s^{-1}). The relaxivity value for complex **16** was found to be phosphate-independent (r_1 = 4.1 ± 0.4 mM^{-1} s^{-1}) as the coordinated triazole unit shielded the Gd^{III} centre from the anion.

This work demonstrated that dual-modal imaging systems should ideally comprise two well-separated imaging components within a single assembly. Increasing the hydration state around the paramagnetic centre was also shown to be a double-edged sword, as although the relaxivity value of the probe was initially improved, it left the probe vulnerable to competitive binding of unwanted anions, which had a detrimental effect on the relaxivity value achieved.

The combined imaging proficiencies of Ir^{III} and Gd^{III} components have largely been unexplored thus far despite Ir^{III} complexes being well documented as effective luminescent probes (section **1.3.3**). An initial bimetallic [IrGd]$^+$ example (**17**, figure **1.25**) showed impressive dual abilities when applied to both MR imaging of murine livers and photoluminescent staining of KB (human nasopharyngeal epidermal carcinoma) and L02 (human normal hepatocyte) cell lines, however[104].
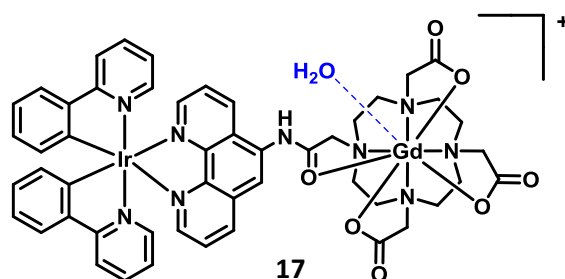
Figure 1.25: An example of a combined Ir^{III}-Gd^{III} dual-modal optical/MR imaging agent

The relaxivity value in saline solution was measured as r_1 = 3.4 mM^{-1} s^{-1} (128 MHz, 25 °C), which is quite a low value, but one difficult to compare to current mononuclear contrast agents without measuring them under the same experimental conditions. The low relaxivity value did not hamper the MRI abilities of compound **17** *in vivo*, however, as successful assessment was carried out in mice. The probe was administered (100 µL, 0.05 mM per kg of body weight) and the T_1 contrast enhancement monitored at 30, 55 and 85 minutes. After 30 minutes brighter contrast was observed due to accumulation of the probe in the liver (figure

1.26B), which then slowly decreased until it had returned after 85 minutes to the levels of pre-contrast agent administration (figure **1.26D**). Comparing analyses of tissue samples taken from both an injected mouse and a control mouse (injected with PBS buffer only), no tissue damage, inflammation or lesions were found, instilling confidence in the low toxicity of the probe. Bio-distribution studies did show, however, that the concentration of free Gd^{III} ions was often quite high in certain organs, questioning the stability of the [Gd(DOTA)] unit in this case.
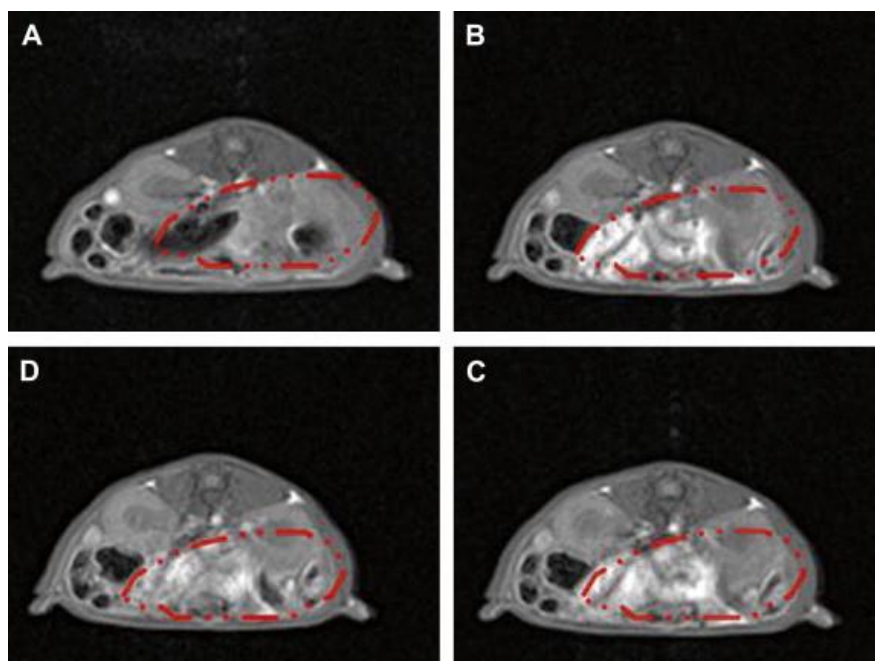
Figure 1.26: Progressive MR images of the liver from a male mouse administered with **17** (100 µL, 0.05 mM per kg of body weight): A) pre-injection, B) 30 min, C) 55 min, and D) 85 min after intravenous injection. (Reproduced with permission from ref. 104. Copyright (2012) Elsevier)

Under photoexcitation at λ_{ex} = 405 nm in water, compound **17** displayed typical Ir^{III}-based luminescence centred at λ_{em} = 560 nm, with a quantum yield of 1.4 %. When incubated with both KB and L02 cell lines (20 µM, 30 minutes, 37 °C, PBS), the probe was found to localise in the mitochondria (confirmed with co-localisation experiments with MitoTracker® complexes Janus Green B and Red CM-H2XRos) (figure **1.27**), which was attributed to the positive charge on the complex. Cytotoxicity MTT experiments revealed that L02 cells showed low viability (< 75 %) compared to the KB cancer cells (> 90 %) when incubated with compound **17** at high concentrations (> 50 µM, 24h, 37 °C).

Overall the probe showed excellent promise when applied to both aspects of biological imaging sequentially, however, the relaxivity value reported was regrettably rather low. This could be a product of the saturated skeleton permitting free rotation of the Gd[III] chelate independently of the Ir[III] moiety, hence hindering the desired slow molecular tumbling in solution.
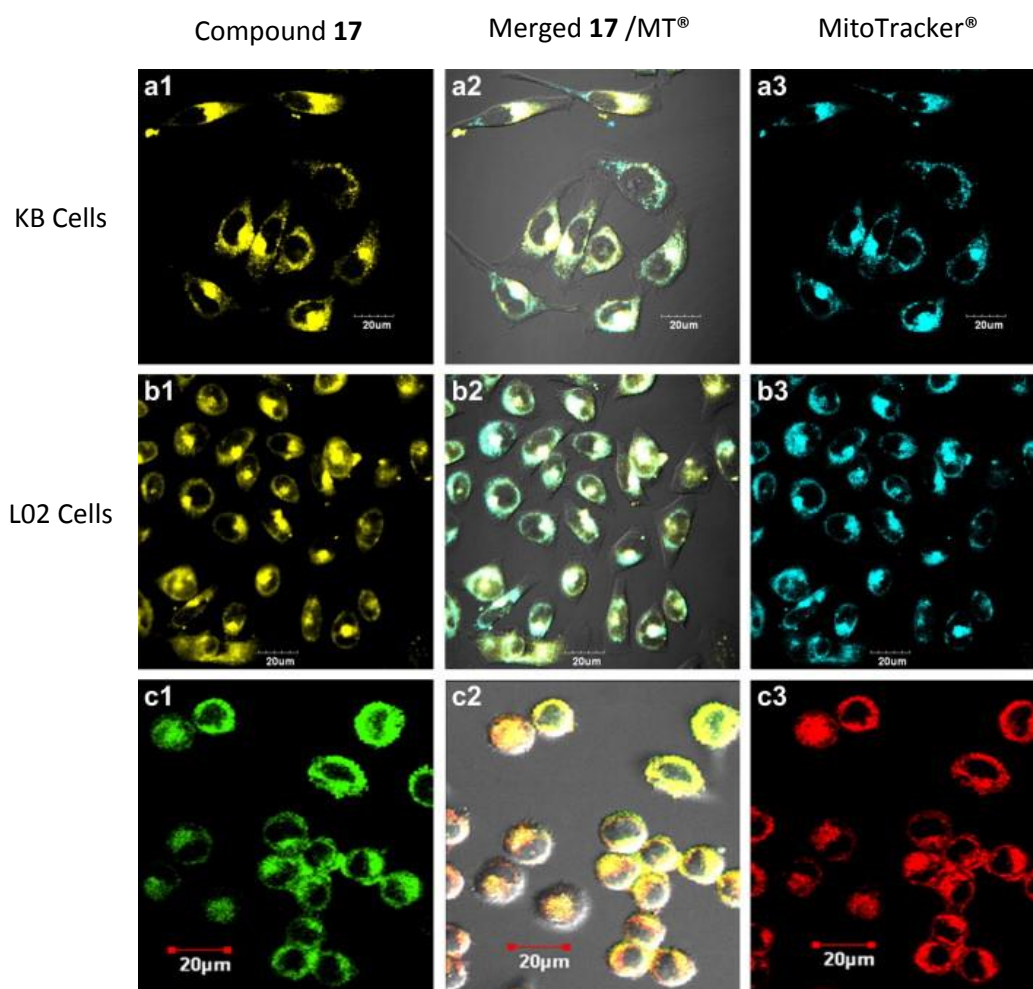
Figure 1.27: Confocal images of KB cells (a1–a3) and L02 cells (b1–b3) co-incubated with **17** (20 μM) and MitoTracker® probes in PBS for 30 min at 37 °C. a1, b1 and c1 show **17**-labelled mitochondria (λ_{ex} = 405 nm), a3 and b3 show Janus green B labelled mitochondria (λ_{ex} = 488 nm), c3 shows MitoTracker® Red CM-H2XRos labelled mitochondria (λ_{ex} = 543 nm). The overlapped merged images are shown in a2, b2 and c2. (Reproduced with permission from ref. 104. Copyright (2012) Elsevier)

Attaching a luminescent Pt[II] centre to an MRI-active Gd[III] centre is an attractive undertaking, as not only would the probe have dual-modal imaging capabilities, but the Pt[II] unit may also have therapeutic properties such as those of the common anti-cancer drug, cisplatin[105]. Production of such a probe, capable of both diagnostic and therapeutic capabilities, would transform the real-time monitoring of cancer treatment[106]. However, imparting water-solubility to such Pt[II]-Gd[III] hybrids has proven difficult, and as a consequence, only one example has so far been reported, by the Pope group (**18**, figure **1.28**)[107].

The probe in question consisted of a [Gd(DOTA)] chelating structure tethered to a cyclometalated Pt[II] complex *via* a pendant pyridine donor. The relaxivity value measured in water was $r_1 = 7.1$ mM^{-1} s^{-1} (30 MHz, 37 °C, pH 6.7), which was consistent with a hydration state of $q = 1$. Upon photoexcitation in to the ^{1}MLCT absorption band ($\lambda_{ex} = 425$ nm) in aqueous solution, visible luminescence was observed ($\lambda_{em} = 617$ nm) with a lifetime of $\tau = 59$ ns, although this value was quenched in comparison to the cyclometalated Pt[II] unit on its own ($\tau = 116$ ns). The emission occurred in the red (more biologically penetrative) end of the electromagnetic spectrum, which helps to avoid luminescence from endogenous biomolecules during imaging; however, the lifetime of the luminescence would be rather short for use in time-gated imaging. Luminescent imaging studies with MCF-7 cells revealed that the complex was not well taken up, but this may have been as a consequence of the probe's neutral charge or its amphiphilic nature.
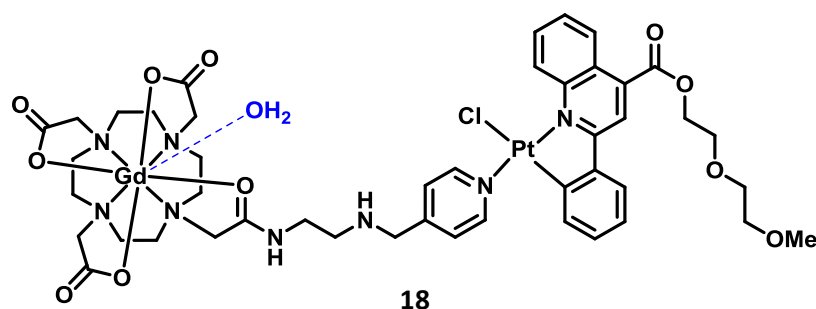
Figure 1.28: An example of a combined Pt[II]-Gd[III] dual-modal optical/MR imaging agent

1.4.1.3) 'Metallostar' Heteropolymetallic Complexes

Dual-modal optical/MRI probes described thus far have typically been bi- or tri-metallic in nature – comprising one luminescent d-block metal centre and one or two MRI-active Gd[III] centre(s) – and have tended to have respectable relaxivity values consistent with

their low molecular weights. Increased relaxivity values have been realised, however, through the design of *'metallostars'* – supramolecular heteropolymetallic structures that have both large molecular weights and low internal flexibilities. The design tends to consist of multiple Gd^{III} chelates surrounding a d-block metal centre, which leads to a high density of paramagnetic ions (and numerous vacant coordination sites for binding of water molecules) confined to a small molecular volume.

The first reported example of such an entity was generated by Desreux and co-workers[108,109] in their search for an improved MRI contrast agent. When mixed with Fe^{II} ions, phenanthroline derivatives of [Gd(DOTA)] self-assembled into a tetranuclear $[FeGd_3]^{2+}$ system (**19**, figure **1.29**). A relaxivity measurement of 12.2 mM^{-1} s^{-1} per Gd^{III} ion (20 MHz, 37 °C) was achieved, which was a threefold improvement from the Gd^{III} chelate on its own.

Livramento and co-workers[110–112] extended this work further by assembling three 2,2'-bipyridyl ligands, each with the capacity to chelate two Gd^{III} ions, around a central Fe^{II} ion. The large size and rigidity of the $[FeGd_6]^{4-}$ entity (**20**, M = Fe, figure **1.29**), combined with six MRI-active Gd^{III} centres within one structure, resulted in a substantial relaxivity value of 27.0 mM^{-1} s^{-1} (4.5 mM^{-1} s^{-1} per Gd^{III} ion, 20 MHz, 25 °C). *In vivo* MRI feasibility experiments conducted on mice showed that the signal enhancement was approximately four times higher with the 'metallostar' species than with the commercial contrast agent [Gd(DOTA)]⁻.

19   **20**
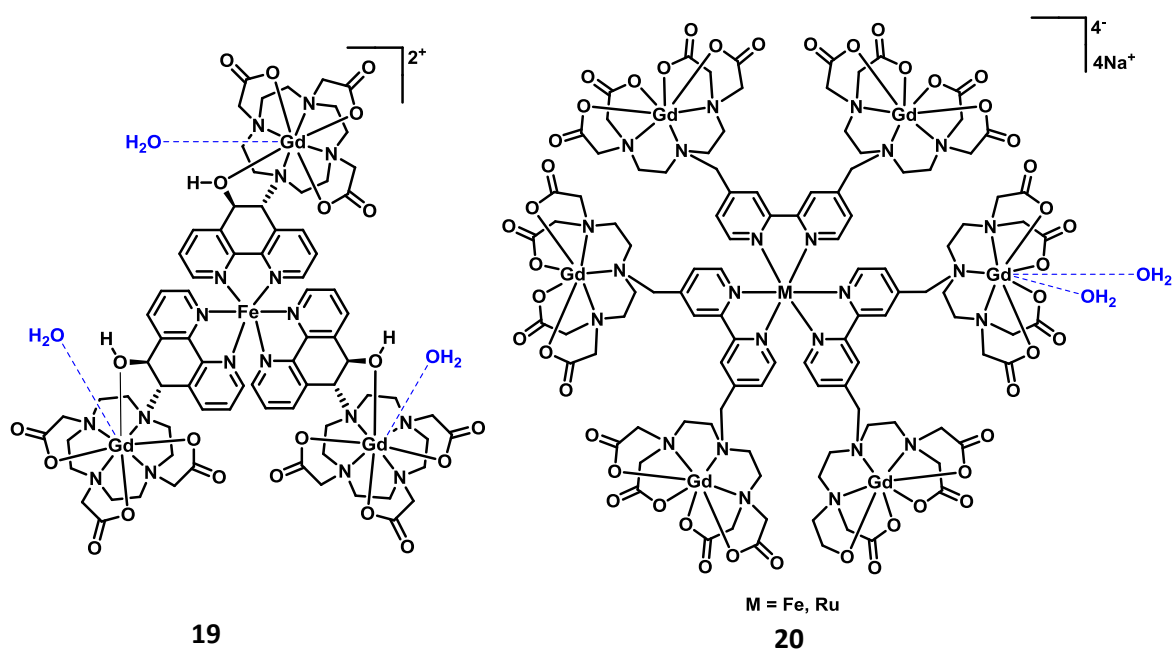
Figure 1.29: Examples of d-f polymetallic 'metallostar' assemblies

The potential for these systems to behave as dual-modal optical/MRI probes was not explored, however, until Bünzli and co-workers[113] introduced a photoactive $[Ru(bipy)_3]^{2+}$ core to produce an isostructural $[RuGd_6]^{4-}$ complex (**20**, M = Ru, figure **1.29**). Not only did this bestow improved kinetic and thermodynamic stability onto the 'metallostar' when in biological media compared to the Fe^{II} analogue, but the issues of autofluorescence and biodegradation were also circumvented. Photoexcitation of the $[Ru(bipy)_3]^{2+}$ core at λ_{ex} = 450 nm produced a broad emission band between λ_{em} = 550-850 nm at room temperature in doubly-distilled water, and the relaxivity value measured for the $[RuGd_6]^{4-}$ complex was similar to that of the Fe^{II} analogue at approximately 5.5 $mM^{-1} s^{-1}$ per Gd^{III} ion (60 MHz, 25 °C).

Although this large, heptametallic structure showed excellent potential for use as a dual-modal probe, since its publication there have been limited reports of similar d-f heterometallic complexes of this size. Other *tetranuclear* 'metallostars' using both Ru^{II} and Gd^{III} ions have been reported, however, with the design of complexes able to specifically label particular biomolecules beginning to be explored[99, 114–116].

Parac-Vogt and co-workers[114] reported of a $[RuGd_3]^-$ 'metallostar' consisting of a central Ru^{II} ion surrounded by three 1,10-phenanthroline ligands linked to DTPA-moieties *via* amide bonds (**21a**, figure **1.30**). The rigidity of the ligands, and the introduction of three Gd^{III} centres (each with a hydration state of q = 1), helped to produce a large relaxivity value of r_1 = 12.0 $mM^{-1} s^{-1}$ per Gd^{III} ion (20 MHz, 37 °C). When measured in a 4 % HSA solution no increase in this value was observed, however, indicating that the complex made no interactions with the protein. The complex also showed appropriate photophysical properties for use in optical microscopy: upon excitation into the Ru^{II}-based ^1MLCT band at λ_{ex} = 450 nm, red emission centred around λ_{em} = 610 nm was produced, with a good quantum yield of luminescence compared to other Ru^{II}-Gd^{III} hybrids (ϕ = 4.8 %).

A $[RuGd_3]^{5+}$ 'metallostar' based on the same $[Ru(phen)_3]^{2+}$ photoactive core was reported by the same group (**21b**, figure **1.30**) as the first example of a tissue-selective dual-modal contrast agent[115]. The probe had three RGD peptides linked to macrocyclic [Gd(DOTA)] chelates, which enabled it to detect $\alpha_v\beta_3$-integrin-expressing tissues. Upon binding of the RGD-peptide to the integrin, local immobilisation of the contrast agent occurred, which resulted in a slower tumbling rate in solution. This improved the agent's relaxivity, and hence the contrast of the image, allowing for facile detection of the tissues expressing the particular integrin (which are often cancerous).
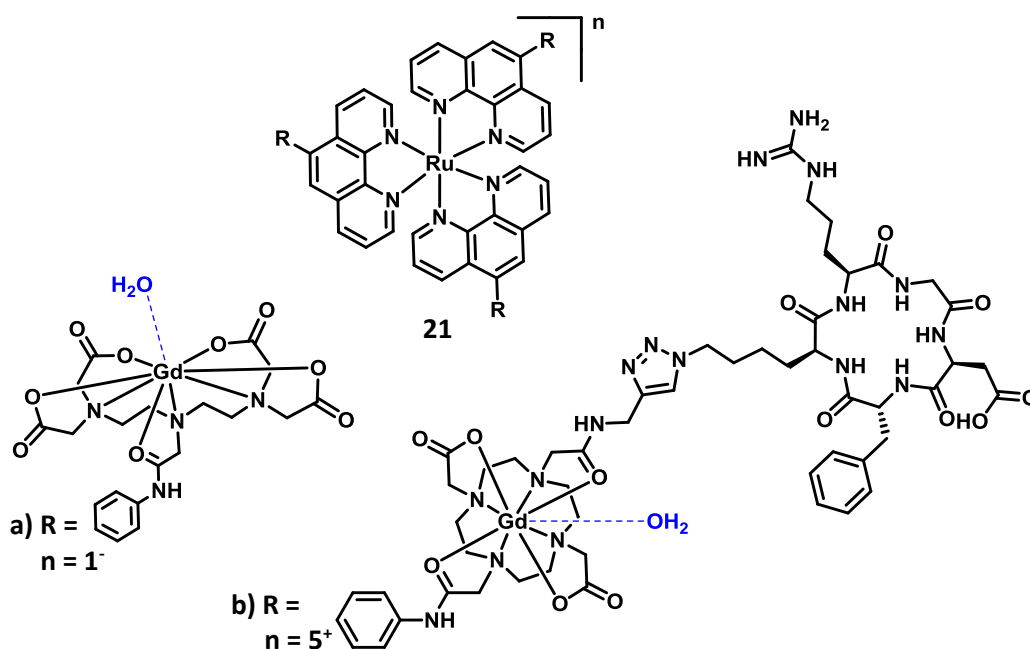
Figure 1.30: Examples of tetranuclear Ru^{II}-Gd^{III} 'metallostar' assemblies

The relaxivity value measured for the probe in water was $r_1 = 9.7$ mM^{-1} s^{-1} (20 MHz, 37 °C), which was fairly low for a probe of this size ($\tau_R = 469 \pm 11$ ps), however. This was attributed to a slow water-exchange rate ($\tau_M = 850 \pm 1$ ns) as a result of the two amide bonds near the Gd^{III} centres. The probe's photoluminescent properties redeemed its use as an imaging agent, however, as a typical Ru^{II}-based emission profile was observed with a fair luminescence quantum yield ($\phi = 4.7$ %). The emission was also long-lived ($\tau = 804 \pm 6$ ns) and was detectable in the NIR region as well as the visible, making the probe an ideal candidate for both luminescence and MRI detection of $\alpha_v\beta_3$-integrin-expressing tissues.

Subsequent terpyridine-based [RuGd$_3$] 'metallostar' species reported displayed vastly different levels of success when appraised for their dual-modal optical/MR imaging abilities (figure **1.31**). In the case where the Ru^{II} ion was bound to 2,2'-bipyridine units linked to pyridine-bis(iminodiacetate) Gd^{III} chelates[116] (**22**, figure **1.31**), the photoluminescent properties of the probe were typical. Upon photoexcitation at $\lambda_{ex} = 472$ nm in water at pH 7.4, red emission was observed ($\lambda_{em} = 660$ nm) with a luminescence quantum yield of $\phi = 2.6$ %. However, when the d-block metal core was [Ru(terpy)]$^{2+}$ (**23**, figure **1.31**)[99], the probe was non-luminescent at room temperature in water, impairing its use as a probe for optical microscopy. When incubated with HeLa cells (50 μM, 24 h, 37 °C), compound **23** did show high cytotoxic properties (cell viabilities of 16.5 %) due to the promotion of programmed cell

death, which suggests that the probe may be more useful as a therapeutic *anti-cancer* agent rather than a dual-modal *imaging* agent.

The relaxivity value measured for the [Ru(bipy)$_3$]$^{2+}$-based probe (**22**) also exceeded that of the [Ru(terpy)]$^{2+}$-based probe (**23**) (r_1 = 17.0 mM^{-1} s^{-1} and 7.5 mM^{-1} s^{-1} per Gd^{III} ion, respectively, 20 MHz, 37 °C). This was due to the superior design of the former probe over the latter. The rigid, highly conjugated design of compound **22** resulted in a particularly slow tumbling rate in solution (τ_R = 252 ps) as the whole molecule rotated as one large entity. The saturated linkers in compound **23**, however, allowed the different metal centres to rotate independently of one another, leading to a reduced tumbling rate. Utilisation of the [Gd(DTPA)] acyclic chelate in compound **22** compared to the macrocyclic [Gd(DOTA)] chelate in compound **23** also had a marked effect on the values measured, due to the difference in hydration state of the two complexes. Compound **22** had two vacant coordination sites, and as such the residence lifetime of the Gd^{III}-coordinated water molecules was very short (τ_M = 77.5 ns). In comparison, the macrocyclic chelate allowed only *one* water molecule to bind to the Gd^{III} centre (being octadentate), which will have resulted in a reduced residence lifetime and, therefore, a lower relaxivity value. No consideration for the *in vivo* stability of the two complexes was made, however, and so although the reduced chelate coordination in compound **22** increased the q value, it may also have facilitated unwanted leaching of the Gd^{III} ion.
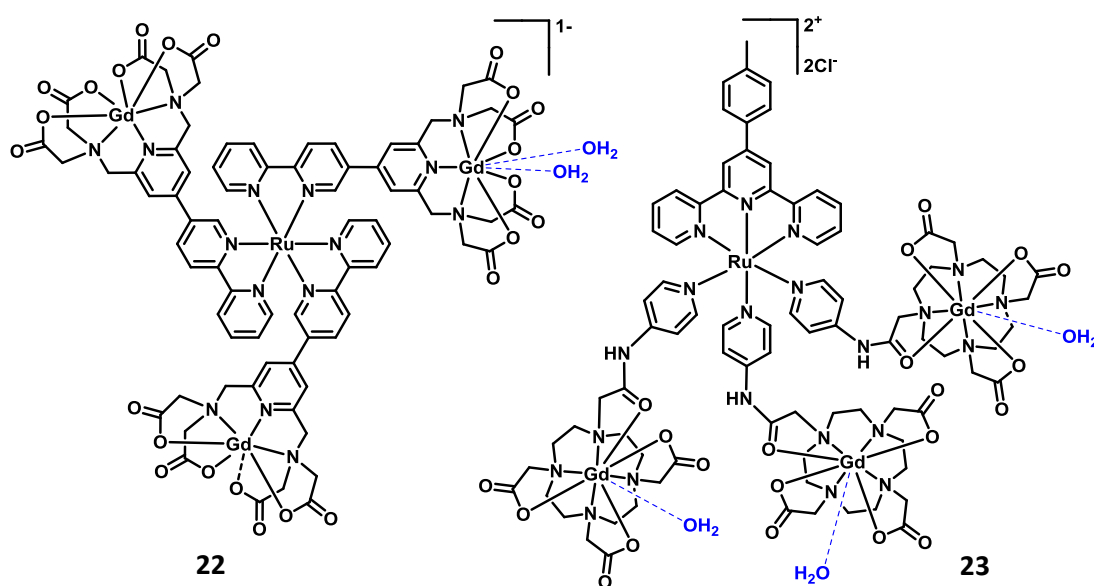
Figure 1.31: Examples of tetranuclear Ru^{II}-Gd^{III} 'metallostar' assemblies

1.5) Summary

Phosphorescent transition-metal complexes, particularly those based on the d^6 metal ions Ru^{II}, Re^{I} and Ir^{III}, have shown extensive applicability to luminescent imaging as both individual probes for optical microscopy, and when coupled with MRI-active Gd^{III} ions to afford potential dual-modal optical/MRI contrast agents. This is in part due to the excellent light-harvesting and emitting abilities of the metal centres, and in part due to their amenability towards effective cellular staining.

The heavy metal atom facilitates ISC from the initially-generated singlet excited-state to a triplet excited-state manifold, and as such, long-lived phosphorescence is the main radiative decay mechanism for the majority of the reported probes. This enables imaging techniques such as PLIM to completely remove interference arising from autofluorescence of endogenous biomolecules, providing high resolution and sensitivity. The ease of synthetically modifying the metal complexes also opens up the possibility of controlling the phosphorescence energy, facilitating the tuning of emission to be anywhere in the UV-visible-NIR region of the electromagnetic spectrum. This is particularly advantageous in cellular imaging, as the complexes can be designed to absorb and emit in the 'biological optical window' (λ_{em} = 650-950 nm), where competing absorption from most biomolecules in tissues is the lowest. Control of cellular localisation is also possible through judicious synthetic modification of the ligand architecture.

A number of luminescent metal complexes are now being rationally designed to have additional therapeutic applications, such as photoactivatable Re^{I} photo-CORMS that can be selectively photoinduced to deliver toxic CO gas to cancerous cells, and numerous PDT agents that bear no cytotoxicity until irradiated. In these cases, the luminescence from the metal centre has a dual function; allowing the visual monitoring of the localisation of the probe, as well as inducing cytotoxic effects.

With regards to probes for dual-modal optical/MR imaging, in which two independent reporters are integrated into one unit, progress in developing these relatively novel contrast agents is steady. Incorporation of a luminescent metal centre into the probe is proving facile due to the wealth of new transition-metal complexes currently being reported. However, extracting the full potential from the MRI-active aspect of the probe is proving a challenge. Ideally, the paramagnetic Gd^{III} ion needs to be securely ensconced within a

polyaminocarboxylate chelating structure, whilst leaving a high number of vacant coordination sites for the crucial binding of water molecules, without compromising the complex's stability and facilitating the leaching of toxic Gd^{III} ions *in vivo*. So far, however, an increase in vacant coordination sites to improve relaxivity has led to the competitive binding of unwanted anions such as phosphate, which has interrupted coordination of water molecules, and thereby reduced the relaxivity values achieved. In some cases an increased number of vacant sites around the Gd^{III} centre has improved the mean residence time of the water molecule in the first coordination sphere, however, which is having a positive impact on the relaxivity values attainable.

The main current stumbling block that still needs to be addressed with regards to dual-modal optical/MR imaging, however, is the discrepancy between the working concentrations of the two independent probes. Luminescence gives a response over a subnanomolar to micromolar concentration range, but MRI contrast enhancement is likely to be poor at submicromolar concentrations. In theory, lower concentrations of an MRI contrast agent can be administered if relaxivity values of the order of $r_1 = 100\text{-}200$ mM^{-1} s^{-1} are attained. Larger complexes with high molecular weights have been shown to boast higher relaxivity values in comparison to smaller complexes, as the larger size encourages slower rotation in solution. Attempts to address this issue have begun with the synthesis of supramolecular heteropolymetallic structures known as 'metallostars', as they have large molecular weights, low internal flexibilities and a high density of paramagnetic ions confined to a small molecular volume. The relaxivity values attained by these complexes are in the order of $r_1 = 30\text{-}50$ mM^{-1} s^{-1}, and so they are ideal candidates for investigation and improvement as dual-modal optical/MRI contrast agents.

1.6) Research Objectives

The main endeavour of this work is to design and synthesise new heterometallic complexes for exploitation as potential dual-modal optical/MRI contrast agents. In particular, the transition metal ruthenium(II) has been selected as the luminescent component of the probe due to its excellent record as a cellular imaging agent. The metal exhibits long-lived phosphorescence in the 'biological optical window', and has proven amenability for use in biological imaging, with low cytotoxicity being reported in the majority of cases. Synthetic modification of the archetypal $[Ru(bipy)_3]^{2+}$ complex is also facile and provides entry to a wealth of rationally designed structures.

Incorporation of the commonly used MRI-active metal Gd^{III} into the probe design to produce multimetallic Ru^{II}-Gd^{III} hybrids will be investigated, as well as the relatively unexploited paramagnetic properties of Mn^{II} in Ru^{II}-Mn^{II} hybrids. Ideally, improving the rigidity and increasing the molecular weight of these multimetallic arrays will see an improvement in measured relaxivity values, which in turn will hopefully lower the current working concentrations of the MRI-active component and make dual-modal probes a more realistic target for clinical applications. To this end, a systematic increase in the number of MRI-active metal centres in the dual-modal probes will be investigated, starting with simple bimetallic structures and culminating in the design and synthesis of a $[RuGd_6]^{4-}$ 'metallostar' entity.

Incorporation of the NIR-luminescent Ln^{III} ions, Yb^{III} and Nd^{III}, in place of the MRI-active metals Gd^{III} and Mn^{II}, also provides a route to dual-modal optical/NIR imaging probes. Energy-transfer from the photoactivated Ru^{II} centre can sensitise emission from the Ln^{III} ion, producing a dual-luminescent probe that has distinguishable emission owing to the luminescent lifetimes of the two different metal centres being orders-of-magnitude apart.

1.7) References

1   C. P. S. Blanken, E. S. Farag, S. M. Boekholdt, T. Leiner, J. Kluin, A. J. Nederveen, P. van Ooij and R. N. Planken, *J. Magn. Reson. Imaging*, 2018, **48**, 318–329.

2   P. Bonnitcha, S. Grieve and G. Figtree, *Free Radic. Biol. Med.*, 2018, **126**, 296–312.

3   V. Valotassiou, J. Malamitsi, J. Papatriantafyllou, E. Dardiotis, I. Tsougos, D. Psimadas, S. Alexiou, G. Hadjigeorgiou and P. Georgoulias, *Ann. Nucl. Med.*, 2018, 1–11.

4   V. Cuccurullo, G. D. Di Stasio and L. Mansi, *World J. Nucl. Med.*, 2018, **17**, 70–78.

5   M. Karpuz, M. Silindir-Gunay and A. Y. Ozer, *Cancer Biother. Radiopharm.*, 2018, **33**, 39–51.

6   M. Lakadamyali, *ChemPhysChem*, 2014, **15**, 630–636.

7   G. Vicidomini, P. Bianchini and A. Diaspro, *Nat. Methods*, 2018, **15**, 173–182.

8   X. Zheng, X. Wang, H. Mao, W. Wu, B. Liu and X. Jiang, *Nat. Commun.*, 2015, **6**, 5834.

9   NHS England (2018, July 19), *Diagnostic Imaging Dataset 2017-18 Data*, retrieved from https://www.england.nhs.uk/statistics/wp-content/uploads/sites/2/2018/07/Provisional-Monthly-Diagnostic-Imaging-Dataset-Statistics-2018-07-19.pdf [accessed 2018, Sept 28).

10   U. W. Kaunzner and S. A. Gauthier, *Ther. Adv. Neurol. Disord.*, 2017, **10**, 247–261.

11   E. G. Kehoe, J. P. McNulty, P. G. Mullins and A. L. W. Bokde, *Biomark. Med.*, 2014, **8**, 1151–1169.

12   F. Bonneville, *Diagn. Interv. Imaging*, 2014, **95**, 1145–1150.

13   S. Sankineni, M. Osman and P. L. Choyke, *Biomed Res. Int.*, 2014, Article ID 590638.

14   P. S. N. van Rossum, A. L. H. M. W. van Lier, I. M. Lips, G. J. Meijer, O. Reerink, M. van Vulpen, M. G. E. H. Lam, R. van Hillegersberg and J. P. Ruurda, *Clin. Radiol.*, 2015, **70**, 81–95.

15   Z. Zhou and Z.-R. Lu, *Wiley Interdiscip. Rev. Nanomedicine Nanobiotechnology*, 2013, **5**, 1–18.

16   A. Gramoun, L. A. Crowe, L. Maurizi, W. Wirth, F. Tobalem, K. Grosdemange, G. Coullerez, F. Eckstein, M. I. Koenders, W. B. Van den Berg, H. Hofmann and J.-P. Vallée, *Arthritis Res. Ther.*, 2014, **16**, R131.

17   J. Sharkey, P. J. Starkey Lewis, M. Barrow, S. M. Alwahsh, J. Noble, E. Livingstone, R. J. Lennen, M. A. Jansen, J. G. Carrion, N. Liptrott, S. Forbes, D. J. Adams, A. E. Chadwick, S. J. Forbes, P. Murray, M. J. Rosseinsky, C. E. Goldring and B. K. Park, *Cytotherapy*, 2017, **19**, 555–569.

18   T. Grobner, *Nephrol. Dial. Transplant.*, 2006, **21**, 1104–1108.

19   P. Marckmann, L. Skov, K. Rossen, A. Dupont, M. B. Damholt, J. G. Heaf and H. S. Thomsen, *J. Am. Soc. Nephrol.*, 2006, **17**, 2359–2362.

20   J. Lohrke, T. Frenzel, J. Endrikat, F. C. Alves, T. M. Grist, M. Law, J. M. Lee, T. Leiner, K. C. Li, K. Nikolaou, M. R. Prince, H. H. Schild, J. C. Weinreb, K. Yoshikawa and H. Pietsch, *Adv. Ther.*, 2016, **33**, 1–28.

21   S. M. Cohen, J. Xu, E. Radkov, K. N. Raymond, M. Botta, A. Barge and S. Aime, *Inorg. Chem.*, 2000, **39**, 5747–5756.

22   D. Ni, W. Bu, E. B. Ehlerding, W. Cai and J. Shi, *Chem. Soc. Rev.*, 2017, **46**, 7438–7468.

23   M. Botta and L. Tei, *Eur. J. Inorg. Chem.*, 2012, **2012**, 1945–1960.

24   Z. Zhen and J. Xie, *Theranostics*, 2012, **2**, 45–54.

25   J. Xiao, X. M. Tian, C. Yang, P. Liu, N. Q. Luo, Y. Liang, H. B. Li, D. H. Chen, C. X. Wang, L. Li and G. W. Yang, *Sci. Rep.*, 2013, **3**, 3424.

26   D. Pan, S. D. Caruthers, A. Senpan, A. H. Schmieder, S. A. Wickline and G. M. Lanza, *Wiley Interdiscip. Rev. Nanomedicine Nanobiotechnology*, 2011, **3**, 162–173.

27   M. Kueny-Stotz, A. Garofalo and D. Felder-Flesch, *Eur. J. Inorg. Chem.*, 2012, **2012**, 1987–2005.

28   D. Pan, A. H. Schmieder, S. A. Wickline and G. M. Lanza, *Tetrahedron*, 2011, **67**, 8431–8444.

29   B. Drahoš, I. Lukeš and É. Tóth, *Eur. J. Inorg. Chem.*, 2012, **2012**, 1975–1986.

30   E. M. Gale, I. P. Atanasova, F. Blasi, I. Ay and P. Caravan, *J. Am. Chem. Soc.*, 2015, **137**, 15548–15557.

31   E. M. Gale, H.-Y. Wey, I. Ramsay, Y.-F. Yen, D. E. Sosnovik and P. Caravan, *Radiology*, 2018, **286**, 865–872.

32   J. A. Thomas, *Chem. Soc. Rev.*, 2015, **44**, 4494–4500.

33   T. D. Ashton, K. A. Jolliffe and F. M. Pfeffer, *Chem. Soc. Rev.*, 2015, **44**, 4547–4595.

34   M. Hockel and P. Vaupel, *JNCI J. Natl. Cancer Inst.*, 2001, **93**, 266–276.

35   T. Yoshihara, Y. Yamaguchi, M. Hosaka, T. Takeuchi and S. Tobita, *Angew. Chemie*, 2012, **124**, 4224–4227.

36   N. Karaoun and A. K. Renfrew, *Chem. Commun.*, 2015, **51**, 14038–14041.

37   Y. Han, M. Li, F. Qiu, M. Zhang and Y.-H. Zhang, *Nat. Commun.*, 2017, **8**, 1307.

38   Q. Zhao, C. Huang and F. Li, *Chem. Soc. Rev.*, 2011, **40**, 2508–2524.

39   V. Fernández-Moreira, F. L. Thorp-Greenwood and M. P. Coogan, *Chem. Commun.*, 2010, **46**, 186–202.

40   E. Baggaley, J. A. Weinstein and J. A. G. Williams, *Coord. Chem. Rev.*, 2012, **256**, 1762–1785.

41   J. Frangioni, *Curr. Opin. Chem. Biol.*, 2003, **7**, 626–634.

42   M. Y. Berezin and S. Achilefu, *Chem. Rev.*, 2010, **110**, 2641–2684.

43   L. K. McKenzie, I. V. Sazanovich, E. Baggaley, M. Bonneau, V. Guerchais, J. A. G. Williams, J. A. Weinstein and H. E. Bryant, *Chem. Eur. J.*, 2017, **23**, 234–238.

44   A. Juris, V. Balzani, F. Barigelletti, S. Campagna, P. Belser and A. von Zelewsky, *Coord. Chem. Rev.*, 1988, **84**, 85–277.

45   A. E. Friedman, J. C. Chambron, J. P. Sauvage, N. J. Turro and J. K. Barton, *J. Am. Chem. Soc.*, 1990, **112**, 4960–4962.

46   M. R. Gill, J. Garcia-Lara, S. J. Foster, C. Smythe, G. Battaglia and J. A. Thomas, *Nat. Chem.*, 2009, **1**, 662–667.

47   E. Baggaley, M. R. Gill, N. H. Green, D. Turton, I. V Sazanovich, S. W. Botchway, C. Smythe, J. W. Haycock, J. A. Weinstein and J. A. Thomas, *Angew. Chem. Int. Ed.*, 2014, **53**, 3367–3371.

48   S. Sreedharan, M. R. Gill, E. Garcia, H. K. Saeed, D. Robinson, A. Byrne, A. Cadby, T. E. Keyes, C. Smythe, P. Pellett, J. Bernardino de la Serna and J. A. Thomas, *J. Am. Chem. Soc.*, 2017, **139**, 15907–15913.

49   A. Wragg, M. R. Gill, C. J. Hill, X. Su, A. J. H. M. Meijer, C. Smythe and J. A. Thomas, *Chem. Commun.*, 2014, **50**, 14494–14497.

50   V. Brabec and J. Kasparkova, *Coord. Chem. Rev.*, 2018, **376**, 75–94.

51   F. E. Poynton, S. A. Bright, S. Blasco, D. C. Williams, J. M. Kelly and T. Gunnlaugsson, *Chem. Soc. Rev.*, 2017, **46**, 7706–7756.

52   J. Liu, C. Zhang, T. W. Rees, L. Ke, L. Ji and H. Chao, *Coord. Chem. Rev.*, 2018, **363**, 17–28.

53 Y.-S. Ho, C.-H. Wu, H.-M. Chou, Y.-J. Wang, H. Tseng, C.-H. Chen, L.-C. Chen, C.-H. Lee and S.-Y. Lin, *Food Chem. Toxicol.*, 2005, **43**, 1483–1495.

54 X. Zhao, M. Li, W. Sun, J. Fan, J. Du and X. Peng, *Chem. Commun.*, 2018, **54**, 7038–7041.

55 A. J. Amoroso, M. P. Coogan, J. E. Dunne, V. Fernández-Moreira, J. B. Hess, A. J. Hayes, D. Lloyd, C. Millet, S. J. A. Pope and C. Williams, *Chem. Commun.*, 2007, 3066–3068.

56 V. Balzani and S. Campagna, Eds., *Photochemistry and Photophysics of Coordination Compounds II*, Springer Berlin Heidelberg, Berlin, Heidelberg, 2007, vol. 281.

57 L. Sacksteder, A. P. Zipp, E. A. Brown, J. Streich, J. N. Demas and B. A. DeGraff, *Inorg. Chem.*, 1990, **29**, 4335–4340.

58 R. G. Balasingham, M. P. Coogan and F. L. Thorp-Greenwood, *Dalton Trans.*, 2011, **40**, 11663–11674.

59 K. Yin Zhang, K. Ka-Shun Tso, M.-W. Louie, H.-W. Liu and K. K.-W. Lo, *Organometallics*, 2013, **32**, 5098–5102.

60 L. C.-C. Lee, K.-K. Leung and K. K.-W. Lo, *Dalt. Trans.*, 2017, **46**, 16357–16380.

61 I. Chakraborty, S. J. Carrington, J. Hauser, S. R. J. Oliver and P. K. Mascharak, *Chem. Mater.*, 2015, **27**, 8387–8397.

62 S. J. Carrington, I. Chakraborty, J. M. L. Bernard and P. K. Mascharak, *Inorg. Chem.*, 2016, **55**, 7852–7858.

63 K. K.-W. Lo, S. P.-Y. Li and K. Y. Zhang, *New J. Chem.*, 2011, **35**, 265–287.

64 T. Sajoto, P. I. Djurovich, A. Tamayo, M. Yousufuddin, R. Bau, M. E. Thompson, R. J. Holmes and S. R. Forrest, *Inorg. Chem.*, 2005, **44**, 7992–8003.

65 Z. Chen, Z. Bian and C. Huang, *Adv. Mater.*, 2010, **22**, 1534–1539.

66 J. A. G. Williams, A. J. Wilkinson and V. L. Whittle, *Dalt. Trans.*, 2008, 2081.

67 J. R. Shewring, A. J. Cankut, L. K. McKenzie, B. J. Crowston, S. W. Botchway, J. A. Weinstein, E. Edwards and M. D. Ward, *Inorg. Chem.*, 2017, **56**, 15259–15270.

68 K. Y. Zhang, P. Gao, G. Sun, T. Zhang, X. Li, S. Liu, Q. Zhao, K. K.-W. Lo and W. Huang, *J. Am. Chem. Soc.*, 2018, **140**, 7827–7834.

69 K. Mitra, C. E. Lyons and M. C. T. Hartman, *Angew. Chemie Int. Ed.*, 2018, **57**, 10263–10267.

70 L. K. McKenzie, H. E. Bryant and J. A. Weinstein, *Coord. Chem. Rev.*, 2018. *In Press, Corrected Proof, Available online 19 April 2018*

71   R. E. Doherty, I. V. Sazanovich, L. K. McKenzie, A. S. Stasheuski, R. Coyle, E. Baggaley, S. Bottomley, J. A. Weinstein and H. E. Bryant, *Sci. Rep.*, 2016, **6**, 22668.

72   A. R. Kherlopian, T. Song, Q. Duan, M. A. Neimark, M. J. Po, J. K. Gohagan and A. F. Laine, *BMC Syst. Biol.*, 2008, **2**, 74.

73   D. W. Townsend, *Semin. Ultrasound, CT MRI*, 2008, **29**, 232–235.

74   H. Jadvar and P. M. Colletti, *Eur. J. Radiol.*, 2014, **83**, 84–94.

75   E. J. Sutton, T. D. Henning, S. Boddington, S. Demos, C. Krug, R. Meier, J. Kornak, S. Zhao, R. Baehner, S. Sharifi and H. Daldrup-Link, *Mol. Imaging*, 2010, **9**, 278–290.

76   A. Mishra, R. Mishra, S. Gottschalk, R. Pal, N. Sim, J. Engelmann, M. Goldberg and D. Parker, *ACS Chem. Neurosci.*, 2014, **5**, 128–137.

77   P. Verwilst, S. Park, B. Yoon and J. S. Kim, *Chem. Soc. Rev.*, 2015, **44**, 1791–1806.

78   E.-J. Kim, S. Bhuniya, H. Lee, H. M. Kim, W. S. Shin, J. S. Kim and K. S. Hong, *ACS Appl. Mater. Interfaces*, 2016, **8**, 10266–10273.

79   J. Luo, L.-F. Chen, P. Hu and Z.-N. Chen, *Inorg. Chem.*, 2014, **53**, 4184–4191.

80   G. J. Stasiuk, S. Tamang, D. Imbert, C. Poillot, M. Giardiello, C. Tisseyre, E. L. Barbier, P. H. Fries, M. de Waard, P. Reiss and M. Mazzanti, *ACS Nano*, 2011, **5**, 8193–8201.

81   Y. Shi, Y. Pan, J. Zhong, J. Yang, J. Zheng, J. Cheng, R. Song and C. Yi, *Carbon N. Y.*, 2015, **93**, 742–750.

82   S. Liu, P. Zhang, S. R. Banerjee, J. Xu, M. G. Pomper and H. Cui, *Nanoscale*, 2015, **7**, 9462–9466.

83   E. Debroye and T. N. Parac-Vogt, *Chem. Soc. Rev.*, 2014, **43**, 8178–8192.

84   M. Harris, S. Carron, L. Vander Elst, S. Laurent, R. N. Muller and T. N. Parac-Vogt, *Chem. Commun.*, 2015, **51**, 2984–2986.

85   M. Harris, S. Carron, L. Vander Elst, S. Laurent and T. N. Parac-Vogt, *Eur. J. Inorg. Chem.*, 2015, **2015**, 4572–4578.

86   M. Harris, L. Vander Elst, S. Laurent and T. N. Parac-Vogt, *Dalt. Trans.*, 2016, **45**, 4791–4801.

87   S. Carron, Q. Y. Li, L. Vander Elst, R. N. Muller, T. N. Parac-Vogt and J. A. Capobianco, *Dalton Trans.*, 2015, **44**, 11331–11339.

88   D. V Hingorani, A. S. Bernstein and M. D. Pagel, *Contrast Media Mol. Imaging*, 2015, **10**, 245–265.

89   W. Shi, B. Song, W. Shi, X. Qin, Z. Liu, M. Tan, L. Wang, F. Song and J. Yuan, *ACS Appl. Mater. Interfaces*, 2018, **10**, 27681–27691.

90   W.-S. Li, J. Luo and Z.-N. Chen, *Inorg. Chem. Commun.*, 2011, **14**, 1898–1900.

91   X. Zhang, X. Jing, T. Liu, G. Han, H. Li and C. Duan, *Inorg. Chem.*, 2012, **51**, 2325–2331.

92   J. Luo, W.-S. Li, P. Xu, L.-Y. Zhang and Z.-N. Chen, *Inorg. Chem.*, 2012, **51**, 9508–9516.

93   G. Dehaen, S. V. Eliseeva, K. Kimpe, S. Laurent, L. Vander Elst, R. N. Muller, W. Dehaen, K. Binnemans and T. N. Parac-Vogt, *Chem. Eur. J.*, 2012, **18**, 293–302.

94   J. Costa, R. Ruloff, L. Burai, L. Helm and A. E. Merbach, *J. Am. Chem. Soc.*, 2005, **127**, 5147–5157.

95   J. R. Kirchhoff, D. R. McMillin, P. A. Marnot and J. P. Sauvage, *J. Am. Chem. Soc.*, 1985, **107**, 1138–1141.

96   G. Dehaen, P. Verwilst, S. V. Eliseeva, S. Laurent, L. Vander Elst, R. N. Muller, W. M. De Borggraeve, K. Binnemans and T. N. Parac-Vogt, *Inorg. Chem.*, 2011, **50**, 10005–10014.

97   W. Shi, B. Song, M. Tan, Z. Ye, J. Yuan, J. Yuan, J. A. Piper, K. Binnemans, T. N. Parac-Vogt, G. Lee, M. Swihart, P. Prasad, J. Robert and E. Benoist, *RSC Adv.*, 2015, **5**, 96525–96531.

98   A. Nithyakumar and V. Alexander, *Dalton Trans.*, 2015, **44**, 17800–17809.

99   A. Nithyakumar and V. Alexander, *New J. Chem.*, 2016, **40**, 4606–4616.

100   J.-A. Park, J. Y. Kim, H.-K. Kim, W. Lee, S. M. Lim, Y. Chang, T.-J. Kim and K. M. Kim, *ACS Med. Chem. Lett.*, 2012, **3**, 299–302.

101   T. Koullourou, L. S. Natrajan, H. Bhavsar, S. J. A. Pope, J. Feng, J. Narvainen, R. Shaw, E. Scales, R. Kauppinen, A. M. Kenwright and S. Faulkner, *J. Am. Chem. Soc.*, 2008, **130**, 2178–2179.

102   S. J. A. Pope, B. J. Coe and S. Faulkner, *Chem. Commun.*, 2004, 1550–1551.

103   M. Tropiano, C. J. Record, E. Morris, H. S. Rai, C. Allain and S. Faulkner, *Organometallics*, 2012, **31**, 5673–5676.

104   H. Yang, L. Ding, L. An, Z. Xiang, M. Chen, J. Zhou, F. Li, D. Wu and S. Yang, *Biomaterials*, 2012, **33**, 8591–8599.

105   Y.-P. Ho, S. C. F. Au-Yeung and K. K. W. To, *Med. Res. Rev.*, 2003, **23**, 633–655.

106   Z. Zhu, X. Wang, T. Li, S. Aime, P. J. Sadler and Z. Guo, *Angew. Chemie Int. Ed.*, 2014, **53**, 13225–13228.

107 O. J. Stacey, A. J. Amoroso, J. A. Platts, P. N. Horton, S. J. Coles, D. Lloyd, C. F. Williams, A. J. Hayes, J. J. Dunsford and S. J. A. Pope, *Chem. Commun.*, 2015, **51**, 12305–12308.

108 V. Comblin, D. Gilsoul, M. Hermann, V. Humblet, V. Jacques, M. Mesbahi, C. Sauvage and J. F. Desreux, *Coord. Chem. Rev.*, 1999, **185–186**, 451–470.

109 J. Paris, C. Gameiro, V. Humblet, P. K. Mohapatra, V. Jacques and J. F. Desreux, *Inorg. Chem.*, 2006, **45**, 5092–5102.

110 J. B. Livramento, E. Tóth, A. Sour, A. Borel, A. E. Merbach and R. Ruloff, *Angew. Chem. Int. Ed.*, 2005, **44**, 1480–1484.

111 J. B. Livramento, A. Sour, A. Borel, A. E. Merbach and E. Tóth, *Chem. Eur. J*, 2006, **12**, 989–1003.

112 J. B. Livramento, C. Weidensteiner, M. I. M. Prata, P. R. Allegrini, C. F. G. C. Geraldes, L. Helm, R. Kneuer, A. E. Merbach, A. C. Santos, P. Schmidt and E. Tóth, *Contrast Media Mol. Imaging*, **1**, 30–39.

113 L. Moriggi, A. Aebischer, C. Cannizzo, A. Sour, A. Borel, J.-C. G. Bünzli and L. Helm, *Dalton Trans.*, 2009, 2088–2095.

114 G. Dehaen, S. V. Eliseeva, P. Verwilst, S. Laurent, L. Vander Elst, R. N. Muller, W. De Borggraeve, K. Binnemans and T. N. Parac-Vogt, *Inorg. Chem.*, 2012, **51**, 8775–8783.

115 P. Verwilst, S. V. Eliseeva, L. Vander Elst, C. Burtea, S. Laurent, S. Petoud, R. N. Muller, T. N. Parac-Vogt and W. M. De Borggraeve, *Inorg. Chem.*, 2012, **51**, 6405–6411.

116 A. Boulay, C. Deraeve, L. Vander Elst, N. Leygue, O. Maury, S. Laurent, R. N. Muller, B. Mestre-Voegtlé and C. Picard, *Inorg. Chem.*, 2015, **54**, 1414–1425.

Chapter 2

Synthesis and Photophysical Properties of Scaffolds for Dual-Modal Imaging Agents

2.1) Previous Work in the Ward Group

Mixed d-f metal complexes, in which a luminescent d-block metal centre (namely Ir[III]) sensitises visible luminescence from a lanthanide ion (Eu[III] and Tb[III]) *via* d→f energy-transfer, have been an area of interest in the Ward group for a number of years[1,2]. The Ir[III]-Gd[III] analogues were initially synthesised as control compounds due to the absence of Ir→Gd energy-transfer; however, these complexes are of interest in their own right due to the potential they hold as dual-modal imaging agents. The photoluminescent Ir[III] centre can be exploited for luminescent imaging, whereas the magnetic Gd[III] centre is an MRI-active reporter (**24**, figure **2.01**).

The kinetic lability of the Gd[III] ion binding site within the previously published complexes makes them unsuitable candidates for dual-modal imaging agents, however; as free, solvated Gd[III] ions have been shown to be highly toxic within the human body[3]. Careful consideration of the Gd[III] chelate structure was necessary, therefore, to improve upon the design of the probes and to provide confidence in their integrity when used for *in vitro* imaging.
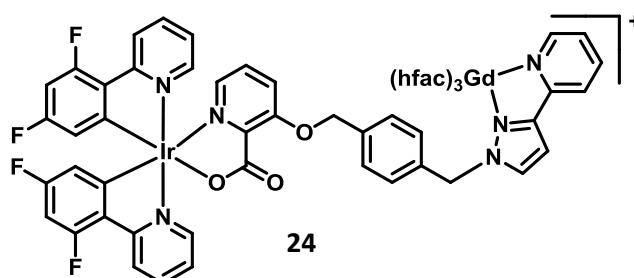
Figure 2.01: An example of a previously synthesised Ir[III]-Gd[III] complex with a labile Gd[III] binding site

The mixed d-f metal complexes were modified to incorporate the Gd[III] chelates DOTA and DTPA (**25**-**26**, figure **2.02**), which are already approved for commercial use as MRI contrast agents (figure **1.02**), as these polyaminocarboxylate binding sites provide high kinetic and thermodynamic stability in aqueous media[1,4]. Indeed, when one equivalent of a competing DOTA ligand was added to a 0.1 mM sample of compound **26** (Eu[III] analogue) in water, no significant changes to the sensitised Eu[III]-based emission profile were seen. If the competing ligand had stripped the Eu[III] ion from the chelate, a decrease in the Eu[III]-based emission intensity would have been recorded.

A further characteristic of the original Ir^{III}-Gd^{III} probe design that is sub-optimal for their application as dual-modal optical/MR imaging agents, was the presence of saturated linkers in the carbon skeleton between the two metal complex centres (**25**, figure **2.02**). These permit independent rotation of the two different metal centres, which could be deleterious to the probe's success as an MRI contrast agent, as the rotational correlation time (τ_R) of the Gd^{III} centre would be shortened by the ability of that unit to rotate independently. Installing an element of rigidity into the ligand architecture with an acetylenic connector (**26**, figure **2.02**) helps to slow down the tumbling rate of the Gd^{III} complex unit in solution, as the entire structure now rotates as one large entity. This gives longer rotational correlation times which, in turn, should improve the relaxivity values achievable by the dual-probe. Indeed, an unusually high relaxivity value of $r_1 = 11.9$ mM^{-1} s^{-1} (20 MHz, 37 °C) was measured for the low molecular weight compound **26**, which is comparable to that of a probe that contains more than one Gd^{III} centre[5].
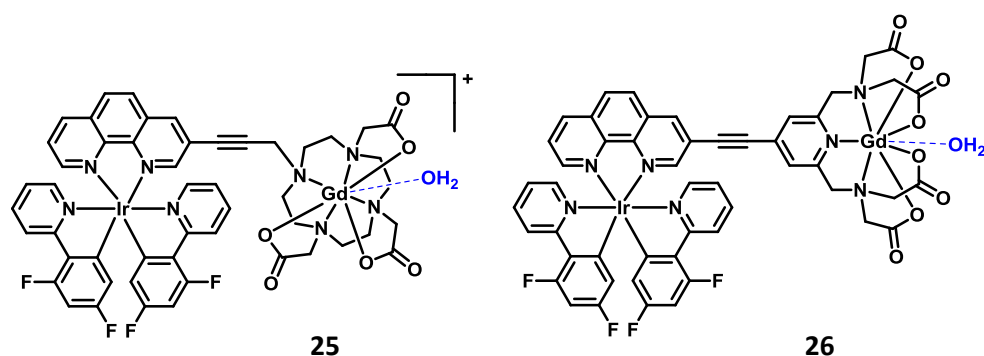
Figure 2.02: Examples of previously prepared dinuclear dual-modal Ir^{III}-Gd^{III} probes[1,4]

In further studies, the alkyne-bridged **IrGd** dinuclear structure (**26**) was extended to incorporate a second Gd^{III} chelate[6] (**27**, figure **2.03**). In principle, the relaxivity value measured for this trinuclear **IrGd₂** species should have improved upon the value measured for the dinuclear **IrGd** species, as its larger size means it tumbles even more slowly in solution. The increased number of Gd^{III} centres in the trinuclear **IrGd₂** analogue should also have doubled the number of vacant coordination sites for water molecules to bind compared to the dinuclear **IrGd** structure. However, the addition of a further Gd^{III} centre resulted in an unprecedented lower relaxivity value being measured for the trinuclear **IrGd₂** probe when both complexes were measured in a H_2O/DMSO (95:5, *v:v*) mixture ($r_1 = 14.0$ mM^{-1} s^{-1} and $r_1 = 12.6$ mM^{-1} s^{-1} (20 MHz, 37 °C) for **IrGd** and **IrGd₂**, respectively). The unexpected lower r_1

value measured for the trinuclear **IrGd₂** species was ascribed to the compound's poor solubility in water, which may have induced aggregation in solution leading to the hydration state of the Gd^{III} centres being affected.

27
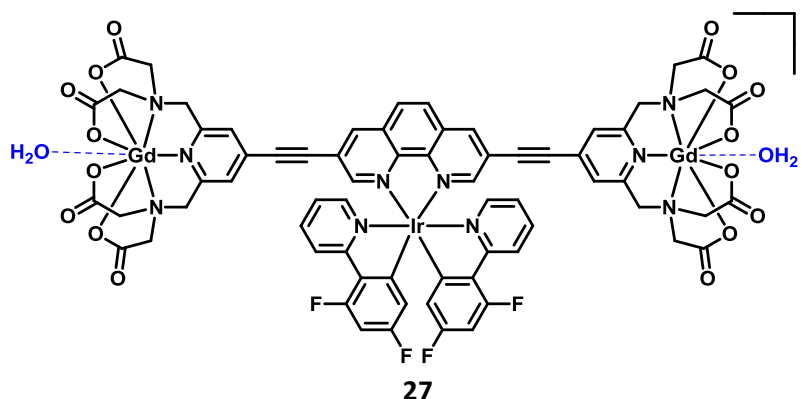
Figure 2.03: A trinuclear dual-modal Ir^{III}-Gd^{III}₂ species

To expand upon this work, and to navigate around the issue of lack of water solubility for the trinuclear **IrGd₂** probe, ruthenium(II) bis(2,2'-bipyridine)-based analogues of the two irdium-based acetylene-bridged optical/MR imaging agents (**26** and **27**) have been synthesised. As ruthenium-based complexes have shown excellent promise as water-soluble, non-toxic optical microscopy agents (section **1.3.2**), and as potential dual-modal optical/MRI probes (section **1.4.1.1**), replacing the hydrophobic iridium centre with a ruthenium centre as the emissive unit was an obvious next step. In an attempt to extend the series of acetylene-bridged dual-probes even further, the synthesis of a larger **RuGd₆** 'metallostar' species (section **1.4.1.3**) has also been undertaken (**Ru-Alkyne-Metallostar-Gd**, figure **2.04**).

As a final endeavour, the linking unit's contribution to the relaxivity values measured has been investigated by modification of the dinuclear probe design to include a triazole linker in place of the acetylene bridge (**Ru-Triazole-Dyad-Gd**, figure **2.04**). The synthesis, characterisation and photophysical properties of these ruthenium-based scaffolds, without the MRI-active metal centre bound, will be presented in this chapter.

Ru-Alkyne-Metallostar-Gd   **Ru-Triazole-Dyad-Gd**
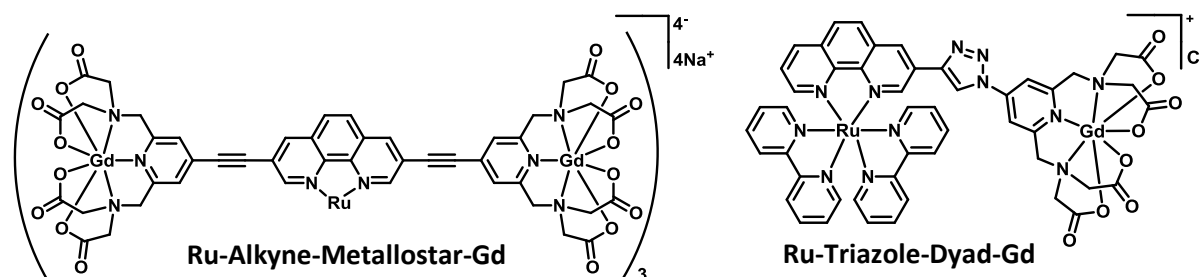
Figure 2.04: Structures of new optical/MRI dual-modal imaging agents synthesised

2.2) An Alkyne-Bridged Scaffold for a Dinuclear Dual-Modal Imaging Agent

2.2.1) Synthesis and Characterisation

Upon removal of the metal ion in the polyaminocarboxylate binding site, retrosynthetic analysis of the target dinuclear **RuM** (M = Gd, Mn, Zn, Yb, Nd) species yielded synthons **A(dyad)** and **B** (scheme **2.01**). With the alkyne substituent in place at the 4-position of the pyridine-based chelate **B**, a complementary halogen on the 1,10-phenanthroline ligand on synthon **A(dyad)** was necessary to take advantage of the robust Sonogashira[7] coupling reaction to form the crucial carbon-carbon bond. The ruthenium metal centre was incorporated into the complex before attempting the coupling reaction to block the binding site of the 3-bromo-1,10-phenanthroline ligand[8,9]. This circumvented any issues arising from the Cu[I] ions preferentially binding to the phenanthroline ligand instead of participating in the Sonagashira catalytic cycle, and allowed for a 'chemistry-on-complex' approach, which has been proven successful in similar synthetic endeavours[10]. The syntheses of these two synthons will now be briefly detailed. Full experimental details can be found in chapter **6**.
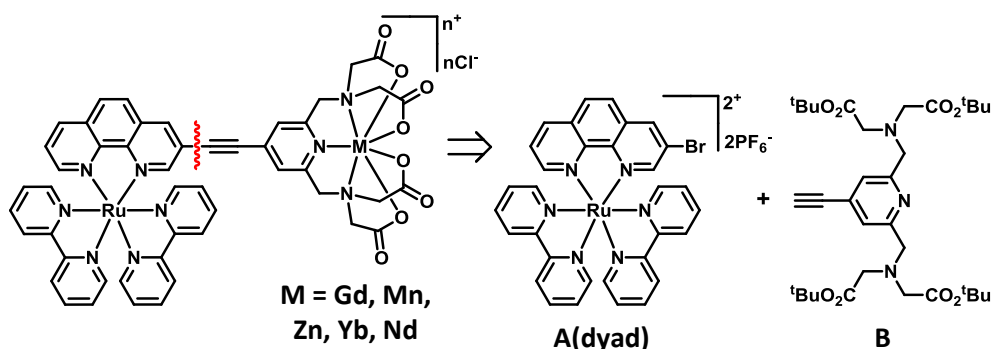
Scheme 2.01: Retrosynthetic analysis of the monosubstituted alkyne-bridged scaffold

The synthesis of synthon **A(dyad)** was achieved in two steps following literature preparations (scheme **2.02**). At first, 1,10-phenanthroline monohydrochloride monohydrate was subjected to bromination, to yield a mixture of both 3-bromo-1,10-phenanthroline and 3,8-dibromo-1,10-phenanthroline, which were separated by column chromatography[11]. Substitution at these positions is desired as the most intense electronic transitions occur along this long axis of the compound, providing high levels of electronic delocalisation without interfering with coordination to the Ru[II] centre (it has been noted that substitution at the 2,9-positions can render complexes photolabile[12]). Introduction of the ruthenium(II) bis(2,2'-

bipyridine) centre was achieved through the straightforward mixing of 3-bromo-1,10-phenanthroline with *cis*-bis(2,2'-bipyridine)-dichloro-ruthenium hydrate[13] in methanol. The mixture was heated at reflux for eight hours before the addition of saturated KPF_6 solution induced precipitation of the product. The solid was dissolved in dichloromethane and washed with water to produce the pure compound (verified by ^1H NMR spectroscopy) in near quantitative yield.
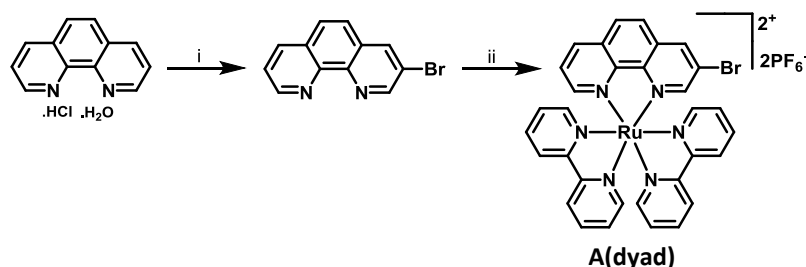
Scheme 2.02: Synthetic route to synthon **A(dyad)**. i) $PhNO_2$, Br_2, 130-140 °C, 3h; ii) MeOH, $Ru(bipy)_2Cl_2.2H_2O$, reflux, 8h

The synthesis of synthon **B** was achieved in five steps following modified literature preparations (scheme **2.03**), with positive electrospray mass spectrometry (ES^+MS) and ^1H NMR spectroscopy verifying the successful isolation of each synthetic target. At first, commercially available 4-hydroxy-2,6-dimethylpyridine was brominated at the 4-position using phosphorus pentabromide[14]. The resulting 4-bromo-2,6-dimethylpyridine was then converted to the bis(bromomethyl) compound using N-bromosuccinimide (NBS), catalytic benzoyl peroxide and UV irradiation to initiate the radical reaction[15]. Installation of the crucial tertiary-butyl protected pendant 'arms' of the metal chelate was achieved through a substitution reaction with di-(tert-butyl)-iminodiacetate[16], and then a straightforward Sonogashira reaction with trimethylsilylacetylene (TMSA) introduced the trimethylsilyl-protected alkyne group at the 4-position of the pyridine ring. Deprotection of the trimethylsilyl group to reveal the free alkyne was carried out in THF using tetra-*n*-butylammonium fluoride (TBAF), but as the deprotection was performed *in situ* before reacting synthon **B** on further, no characterisation data were recorded for this species.
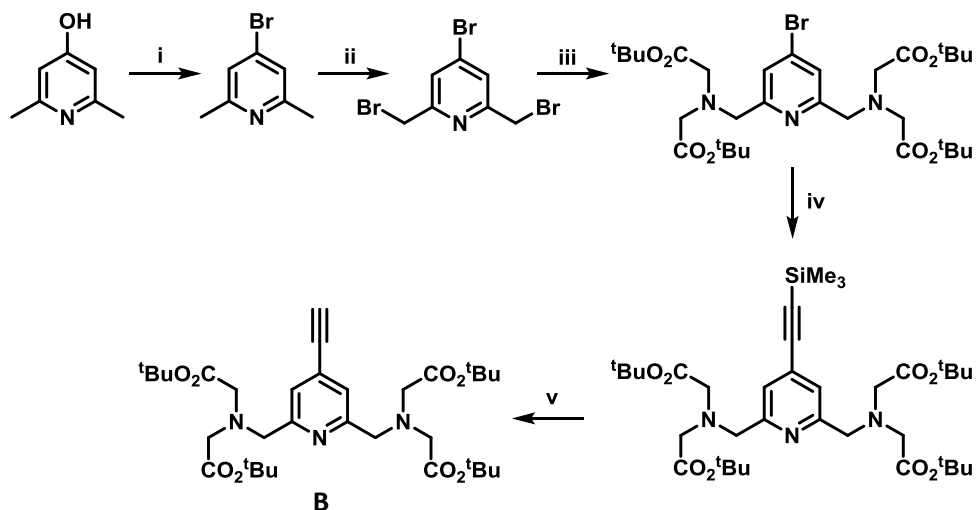
Scheme 2.03: Synthetic route to synthon **B**. i) $CHCl_3$, PBr_5, reflux, 3h; melt, 120 °C, 16h; ii) $CHCl_3$, NBS, benzoyl peroxide (cat.), reflux, 48h, hυ; THF, diethyl phosphite, $^iPr_2NEt$, rt, 5h, Ar; iii) MeCN, di-tert-butyl iminodiacetate, Na_2CO_3, rt, 24h; iv) $^iPr_2NH$, TMSA, $Pd(PPh_3)_2Cl_2$, CuI, PPh_3, 83 °C, 24h, Ar; v) THF, TBAF, rt, 16h

With the successful synthesis of synthons **A(dyad)** and **B**, a Sonogashira coupling reaction between the two entities was performed to produce the **Ru-Alkyne-Dyad-Ester** species (scheme **2.04**). One equivalent of synthon **A(dyad)** was mixed with copper iodide and one ninth of an equivalent of the palladium catalyst [1,1′-bis(diphenylphosphino)ferrocene]dichloropalladium(II) ((dppf)$PdCl_2$) in an anhydrous mixture of DMF and diisopropylamine (5:1, *v:v*). In a separate flask, two equivalents of synthon **B** were dissolved in the same solvent system. Both flasks were deoxygenated with argon for thirty minutes, before the solution of synthon **B** was added dropwise with constant stirring to the other reagents. The reaction was left stirring under argon at room temperature for sixteen hours, before a crude mass spectrum confirmed the successful coupling of the two synthons. A molecular ion peak at m/z = 604.7 was observed for the $[M − 2PF_6]^{2+}$ ion of the **Ru-Alkyne-Dyad-Ester** species, and a peak at m/z = 337.0 for the $[M − 2PF_6]^{2+}$ ion of synthon **A(dyad)** was not present. Purification was achieved on silica gel (200-300 mesh) to afford **Ru-Alkyne-Dyad-Ester** in a moderate yield (50 %).
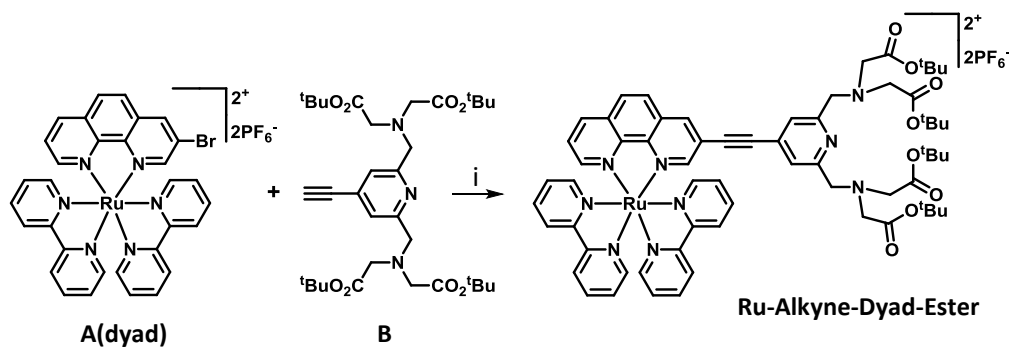
Scheme 2.04: Synthetic route to **Ru-Alkyne-Dyad-Ester**.
i) DMF: $^{i}Pr_2NH$ (5:1, *v:v*), (dppf)PdCl$_2$, CuI, rt, 16h, Ar

The successful purification of **Ru-Alkyne-Dyad-Ester** was verified using ^{1}H NMR spectroscopy (figure **2.05**) and high-resolution mass spectrometry (HRMS) (appendix **2.01**). The aromatic region of the ^{1}H NMR spectrum (400 MHz, d_6-acetone) integrates to the expected twenty-five protons, with the singlet at δ = 7.61 ppm corresponding to the H^3/H^5 protons on the pyridine ring, and the remaining signals tallying to a combination of the three N^N ligands. In the aliphatic region there are singlet peaks at δ = 1.45 ppm, δ = 3.49 ppm and δ = 4.00 ppm integrating as 36, 8 and 4 protons, respectively, which represent the protons on the pendant 'arms' of the metal chelate. The residual solvent peak for acetone can be seen at δ = 2.05 ppm, and the two signals at δ = 2.78 ppm and δ = 2.82 ppm can be ascribed to HOD and H$_2$O, respectively.
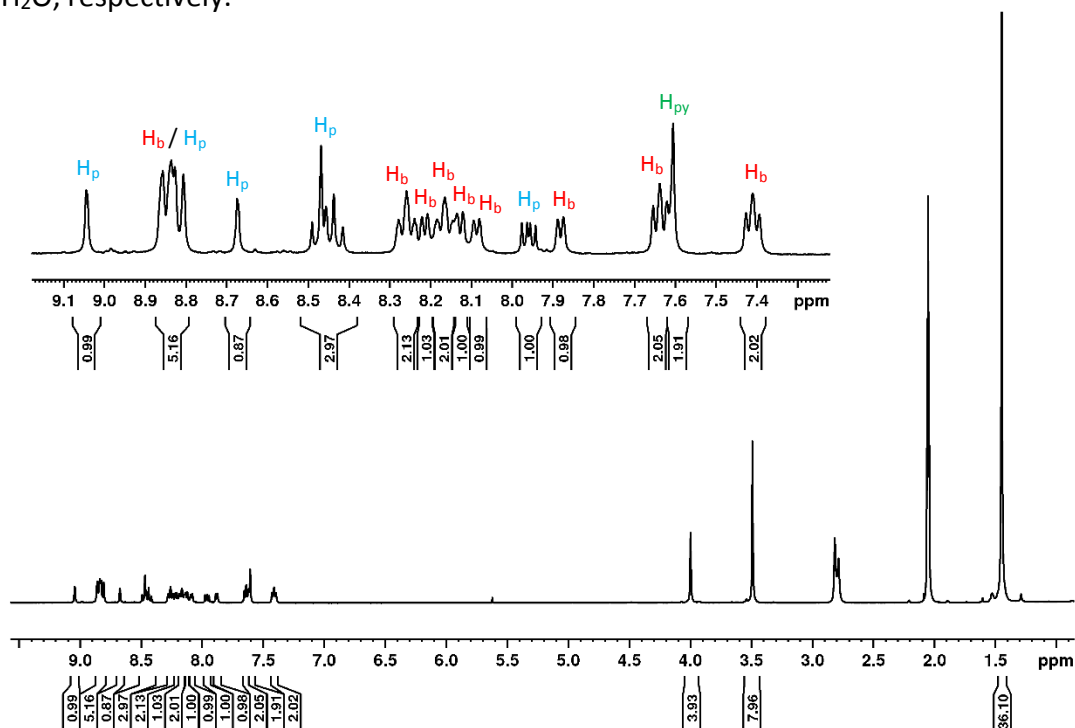
Figure 2.05: ^{1}H NMR spectrum (d_6-acetone, 400 MHz) of **Ru-Alkyne-Dyad-Ester** at 298 K.
(H$_b$ = proton on bipyridine ligand, H$_p$ = proton on phenanthroline ligand,
H$_{py}$ = proton on pyridine ring)

The calculated m/z value for the $[M - 2PF_6]^{2+}$ ion in the high-resolution mass spectrum (604.7316) tallied well with the value observed (604.7318), with the isotope pattern matching that expected for the Ru^{II} ion.

With convincing evidence for the successful synthesis of **Ru-Alkyne-Dyad-Ester**, the final step in the synthetic route towards the alkyne-bridged scaffold for a dinuclear dual-modal probe was to remove the tertiary-butyl protecting groups on the pendant 'arms' of the pyridine-based chelate. This produced an environment in which the MRI-active metal ions could bind (scheme **2.05**) and was achieved by stirring **Ru-Alkyne-Dyad-Ester** in dichloromethane with trifluoroacetic acid (TFA) for eighteen hours at room temperature. Repeated washings were used to remove the TFA, before the compound was dissolved in the minimum amount of methanol and precipitated with an excess of diethyl ether. The solid was then collected by centrifugation and dried under a stream of nitrogen to yield the compound in nearly quantitative yield. Again, ^{1}H NMR spectroscopy (figure **2.06**) and HRMS (appendix **2.02**) were used to verify the successful synthesis and purity of **Ru-Alkyne-Dyad-Acid**.
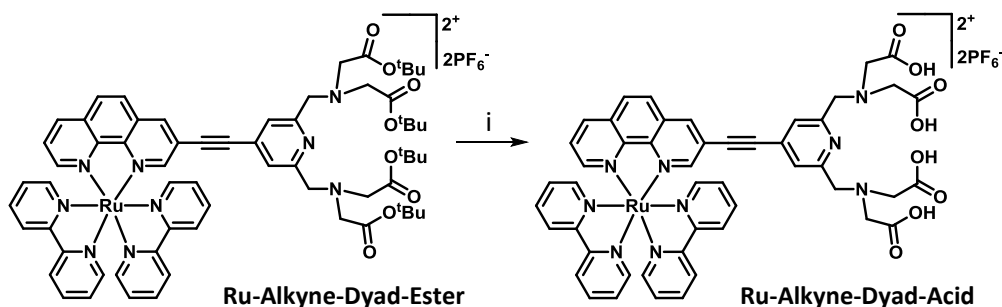
Scheme 2.05: Synthetic route to **Ru-Alkyne-Dyad-Acid**. i) CH_2Cl_2, TFA, rt, 18h

The calculated m/z value for the $[M - 2PF_6]^{2+}$ ion in the high-resolution mass spectrum was 492.6055 and the observed value was 492.6056, with the isotope pattern matching that expected for the Ru^{II} ion. In the aliphatic region of the ^{1}H NMR spectrum (500 MHz, d_6-DMSO, 303 K), there are two sharp singlets at $\delta = 3.46$ ppm and $\delta = 3.94$ ppm, which can be assigned to the protons on the pendant 'arms' of the pyridine-based chelate. The large peak at $\delta = 1.45$ ppm seen in the spectrum for **Ru-Alkyne-Dyad-Ester** is no longer present, which verifies the successful removal of the tertiary-butyl protecting groups, but a signal for the carboxylic acid protons is not visible due to hydrogen-deuterium exchange with the bulk solvent. The signal at $\delta = 2.50$ ppm is the residual solvent peak for DMSO, and the broad signals for H_2O and HOD are at $\delta = 3.33$ ppm and $\delta = 3.30$ ppm, respectively. In the aromatic region there are several

integrals that tally to the twenty-five protons expected, with the singlet at δ = 7.56 ppm corresponding to the two equivalent H^3/H^5 protons on the pendant pyridine ring. A two-dimensional ^1H-^1H NMR correlation spectrum (500 MHz, d_6-DMSO, 303 K) (appendix **2.03**) was used in conjunction with the one-dimensional ^1H NMR spectrum to assign the protons on the 1,10-phenanthroline ligand and the 2,2'-bipyridine ligands, respectively.
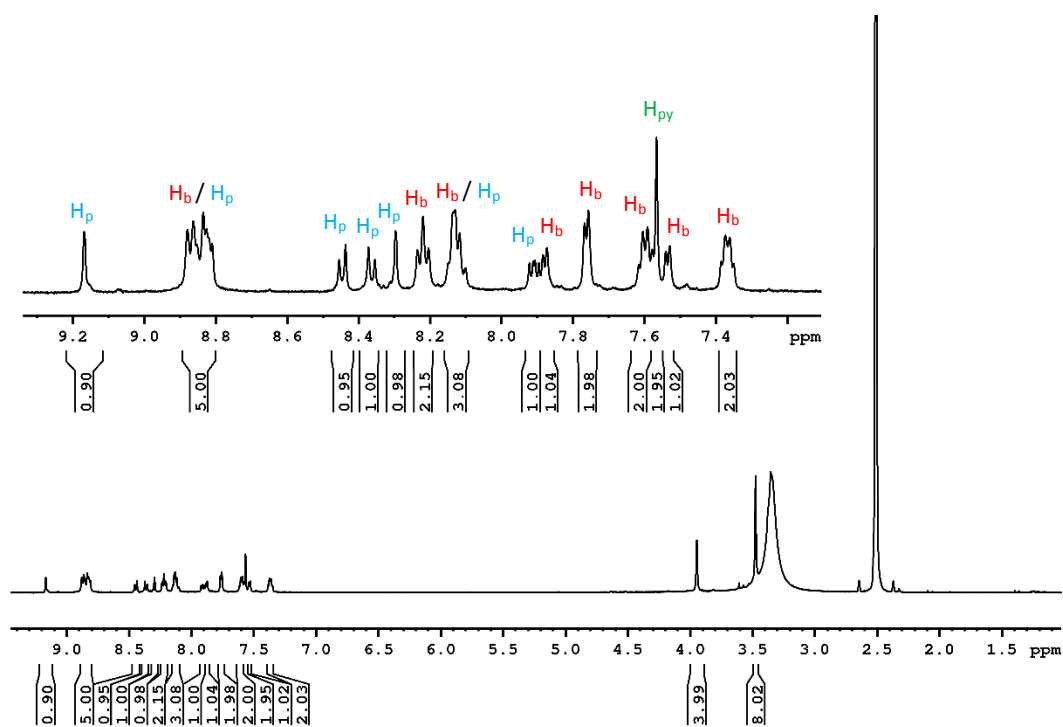
Figure 2.06: ^1H NMR spectrum (d_6-DMSO, 500 MHz) of **Ru-Alkyne-Dyad-Acid** at 303 K.
(H_b = proton on bipyridine ligand, H_p = proton on phenanthroline ligand,
H_{py} = proton on pyridine ring)

2.2.2) Photophysical Properties

UV/Vis absorption spectra were recorded in several solvents for both **Ru-Alkyne-Dyad-Ester** and **Ru-Alkyne-Dyad-Acid**, and extinction coefficients were measured in acetonitrile for **Ru-Alkyne-Dyad-Ester** and in water for **Ru-Alkyne-Dyad-Acid**. Emission profiles and lifetimes of emission were recorded for both compounds (including as a frozen glass at 77 K), and the quantum yield of emission was measured for **Ru-Alkyne-Dyad-Acid** against $[Ru(bipy)_3]Cl_2.6H_2O$ in aerated water. Finally, excitation spectra were measured in each solvent.

2.2.2.1) UV/Vis Absorption

UV/Vis absorption profiles for **Ru-Alkyne-Dyad-Ester** and **Ru-Alkyne-Dyad-Acid** were recorded in EtOH/MeOH *(4:1, v:v)* (figure **2.07a**) and acetonitrile (figure **2.07b**) at 298 K. No discernible differences between the two compounds can be seen in either of the solvents, demonstrating that the tertiary-butyl protecting groups on the metal chelate have a negligible effect on the ground state absorption properties.

When comparing the spectra for **Ru-Alkyne-Dyad-Ester** and **Ru-Alkyne-Dyad-Acid** to that of the parent $[Ru(bipy)_2(phenBr)]^{2+}$ compound, and to a previously published compound with extended conjugation along the phenanthroline ligand[10], $([\{Ru(bipy)_2(phen)\}_2C\equiv C]^{4+})$ (table **2.01**), it can be seen that the spectra have similar features. Both **Ru-Alkyne-Dyad-Ester** and **Ru-Alkyne-Dyad-Acid** show an intense absorption band in the UV region ($\lambda_{abs} < 300$ nm) similar to $[Ru(bipy)_2(phenBr)]^{2+}$, which can be assigned as the $\pi\rightarrow\pi^*$ transition centred on the bipyridine ligands. The weaker band centred around $\lambda_{abs} = 325$ nm, therefore, must be the $\pi\rightarrow\pi^*$ transition centred on the phenanthroline backbone. Comparing these absorption values to those of $[\{Ru(bipy)_2(phen)\}_2C\equiv C]^{4+}$ shows similar red-shifting of the $\pi\rightarrow\pi^*$ transition on the extended phenanthroline ligand in comparison to the $\pi\rightarrow\pi^*$ transition on the bipyridine ligands. Finally, it can be seen that both complexes have a broad absorption spanning the range $\lambda_{abs} = 375\text{-}550$ nm, with the maximum centred around $\lambda_{abs} = 440$ nm. These are the ^{1}MLCT absorptions associated with both the 2,2'-bipyridine and 1,10-phenanthroline ligands, overlapping in energy.
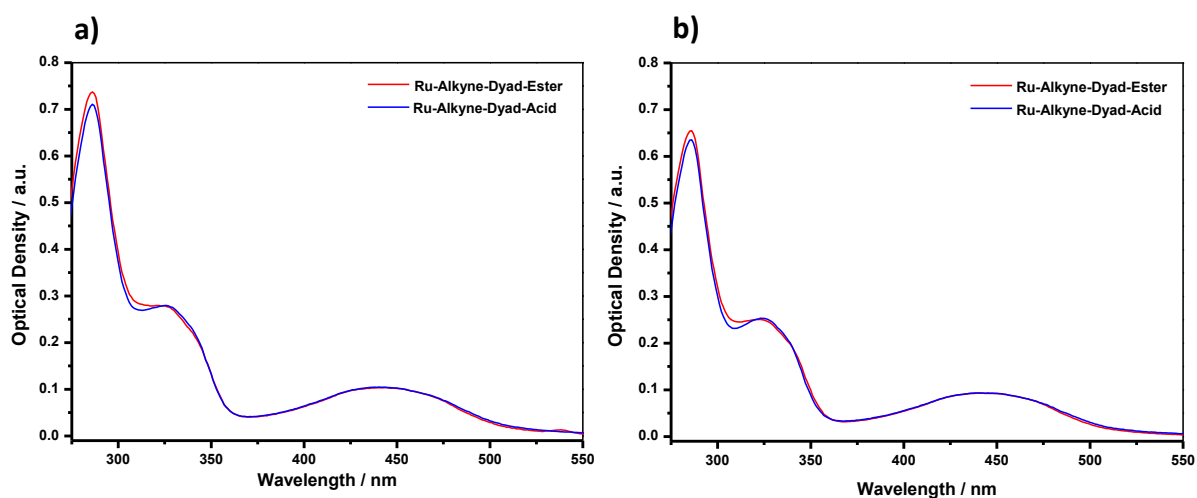
Figure 2.07: Normalised (at $\lambda_{abs} = 440$ nm) UV/Vis absorption spectra of **Ru-Alkyne-Dyad-Ester** (red) and **Ru-Alkyne-Dyad-Acid** (blue) at 298 K. a) EtOH/MeOH (4:1, *v:v*), and b) MeCN

Table 2.01: UV/Vis absorption data for **Ru-Alkyne-Dyad-Ester** and **Ru-Alkyne-Dyad-Acid** at 298 K. [a]Data taken from ref. 10.

Compound	Solvent	λ_{abs} (nm) [ε (x 10^4 M^{-1} cm^{-1})]
[a][Ru(bipy)$_2$(phenBr)]$^{2+}$	MeCN	272 [6.6], 286 [6.5], 448 [1.5]
[a][{Ru(bipy)$_2$(phen)}$_2$C≡C]$^{4+}$	MeCN	286 [14], 342 [4.3], 356 [2.5], 440 [2.5]
Ru-Alkyne-Dyad-Ester	CH$_2$Cl$_2$	287, 329 (sh), 445 (br)
	EtOH/MeOH (4:1, *v:v*)	286, 321 (sh), 442 (br)
	MeCN	286 [88], 321 (sh) [39], 444 (br) [14]
	THF	287, 323 (sh), 442 (br)
	DMF	288, 322 (sh), 449 (br)
Ru-Alkyne-Dyad-Acid	EtOH/MeOH (4:1, *v:v*)	286, 325 (sh), 441 (br)
	MeOH	286, 325 (sh), 441 (br)
	MeCN	286, 324 (sh), 444 (br)
	H$_2$O	285 [12], 325 (sh) [5.5], 442 (br) [1.6]
	DMF	288, 325 (sh), 447 (br)

2.2.2.2) Emission

Luminescence profiles and the lifetime of the luminescence decay for **Ru-Alkyne-Dyad-Ester** and **Ru-Alkyne-Dyad-Acid** were recorded in several aerated solvents (table **2.02**), but profiles in EtOH/MeOH (4:1, *v:v*) at 298 K and 77 K (figure **2.08a**) and acetonitrile (figure **2.08b**) will be reviewed for comparison purposes.

Upon excitation into the ^{1}MLCT absorption bands at λ_{ex} = 440-445 nm, both complexes in each solvent at 298 K produce broad and featureless emission profiles. This is typical for [Ru(bipy)$_2$(N^N)]$^{2+}$-based compounds, indicating spin-forbidden ^{3}MLCT {Ru^{II}→π*$_{(N^N)}$} transitions. The emission is centred around λ_{em} = 645 nm, with **Ru-Alkyne-Dyad-Acid** having a red-shift in its emission maximum (~10 nm) compared to **Ru-Alkyne-Dyad-Ester**. These values are, in turn, both red-shifted in comparison to the parent complex [Ru(bipy)$_2$(phen)]$^{2+}$ in acetonitrile (table **2.02**) due to the extended π-network along the phenanthroline backbone. The lowest unoccupied molecular orbitals (LUMO) on **Ru-Alkyne-Dyad-Ester** and **Ru-Alkyne-Dyad-Acid** have been stabilised and, therefore, the energy of the emission maxima have been lowered, as has been seen for similar complexes with extended conjugation[17].

The broad and featureless profiles observed at 298 K changed to include more vibrational structure when the emission was measured as a frozen glass at 77 K for both compounds. The main emission band blue-shifted (~30 nm) and two less intense shoulders

appeared on the lower-energy side. This small blue-shift is consistent with the charge-transfer state no longer being stabilised by the fast solvent reorganisation that occurs at 298 K. The solvent dipoles are immobile on the timescale of the excited-state at 77 K and so cannot respond to the electronic configuration change that occurs upon an excitation. This also has an effect on the luminescence decay lifetimes, which are on a microsecond timescale for both complexes at 77 K, compared to a nanosecond timescale when measured at 298 K.
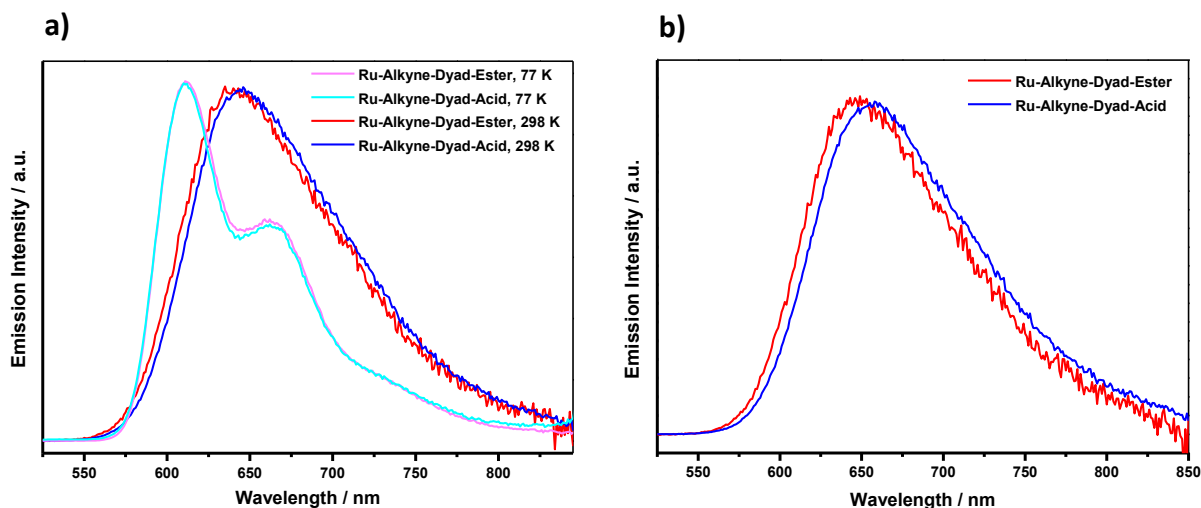
Figure 2.08: Normalised (at λ_{em} = max intensity), corrected emission spectra in aerated solvents. a) **Ru-Alkyne-Dyad-Ester** (magenta, 77 K, λ_{ex} = 440 nm, and red, 298 K, λ_{ex} = 445 nm) and **Ru-Alkyne-Dyad-Acid** (cyan, 77 K, and blue, 298 K, λ_{ex} = 445 nm for both) in EtOH/MeOH (4:1, *v:v*); b) **Ru-Alkyne-Dyad-Ester** (red) and **Ru-Alkyne-Dyad-Acid** (blue) in MeCN at 298 K (λ_{ex} = 445 nm)

The luminescence decay lifetimes recorded in aerated acetonitrile and EtOH/MeOH (4:1, *v:v*) at 298 K were *ca.* τ = 250 ns, which were of similar magnitude to the lifetime of the luminescence from the conjugated dinuclear complex [{Ru(bipy)$_2$(phen)}$_2$C≡C]$^{4+}$ compound in acetonitrile (table **2.02**) and are typical for spin-forbidden ^{3}MLCT {Ru^{II}→π*$_{(N\wedge N)}$} transitions. The luminescence quantum yield value (ϕ) for **Ru-Alkyne-Dyad-Acid** was calculated to be ϕ = 0.020 when measured against [Ru(bipy)$_3$]Cl$_2$.6H$_2$O[18] as a standard in aerated water at 298 K, which is quite low in comparison to the original **IrGd** compound (**26**) (ϕ = 0.040)[4].

Table 2.02: Luminescence data for **Ru-Alkyne-Dyad-Ester** and **Ru-Alkyne-Dyad-Acid** in aerated solvents. [a]Data taken from ref. 17.

Compound	Solvent	$\lambda_{em}^{298\,K}$ (nm) [$\lambda_{em}^{77\,K}$ (nm)]	$\tau^{298\,K}$ (ns) [$\tau^{77\,K}$ (µs)]
[a][Ru(bipy)$_2$(phen)]$^{2+}$	MeCN	610	147
[a][{Ru(bipy)$_2$(phen)}$_2$C≡C]$^{4+}$	MeCN	648	225
Ru-Alkyne-Dyad-Ester	CH$_2$Cl$_2$	627	571
	EtOH/MeOH (4:1, *v:v*)	640 [611, 660 (sh) 711 (sh)]	275 [6.2]
	MeCN	647	240
	THF	659	296
	DMF	664	294
Ru-Alkyne-Dyad-Acid	EtOH/MeOH (4:1, *v:v*)	646 [611, 662 (sh) 706 (sh)]	232 [5.8]
	MeOH	653	226
	MeCN	658	241
	H$_2$O	661	341
	DMF	664	241

Excitation spectra recorded at λ_{em} = 630 nm in aerated EtOH/MeOH (4:1, *v:v*) at 298 K for both **Ru-Alkyne-Dyad-Ester** and **Ru-Alkyne-Dyad-Acid** were overlaid with UV/Vis absorption spectra recorded in the same solvent (figure **2.09**). A good match between the spectra can be seen, which is a clear indication that the emission observed for both complexes occurs as a result of absorption in to the ^{1}MLCT band.
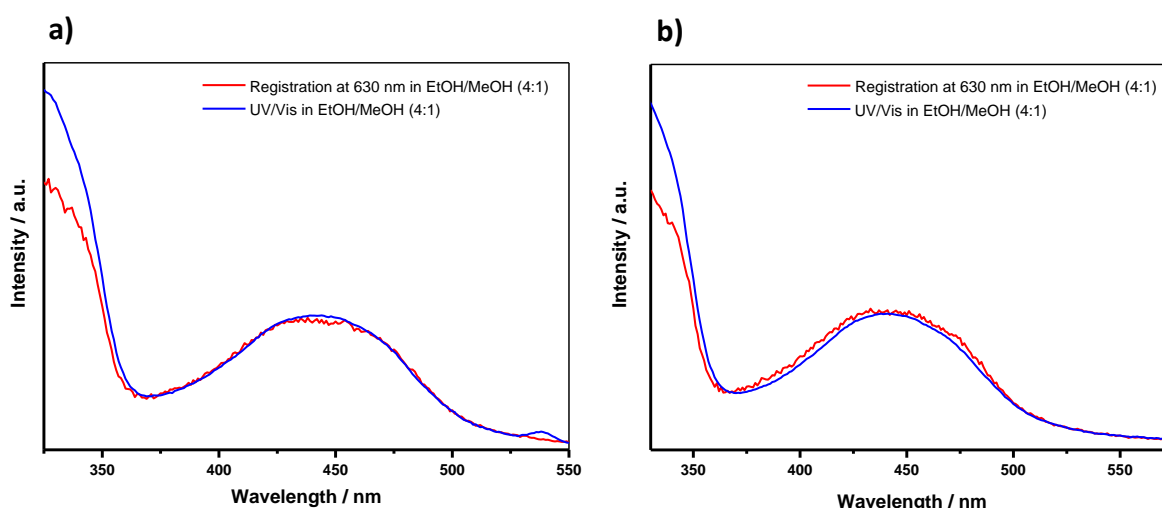
Figure 2.09: Normalised (at λ = 440 nm) spectra in aerated EtOH/MeOH (4:1, *v:v*) at 298 K. Corrected excitation spectra at λ_{em} = 630 nm (red) and UV/Vis spectra (blue) of a) **Ru-Alkyne-Dyad-Ester** and b) **Ru-Alkyne-Dyad-Acid**

2.3) An Alkyne-Bridged Scaffold for a Trinuclear Dual-Modal Imaging Agent

2.3.1) Synthesis and Characterisation

To extend the dual-modal imaging potential of the dinuclear **RuGd** species, a 3,8-disubstituted phenanthroline scaffold around the central Ru^{II} unit has also been synthesised as a basis for trinuclear **RuGd$_2$** complexes. It was postulated that the increase in length along the rigid backbone should reduce the rotational correlation time of the molecule in solution even further, which in turn should improve the relaxivity values that can be achieved.

Retrosynthetic analysis of this compound yielded similar synthons to those for the monosubstituted phenanthroline scaffold (scheme **2.01**), however, for synthon **A(triad)** the phenanthroline ligand is brominated at both the 3- and 8-positions to allow for a coupling reaction at both sides of the scaffold. Synthesis of this synthon is parallel to the monosubstituted analogue (scheme **2.02**), but starting from 3,8-dibromo-1,10-phenanthroline instead.
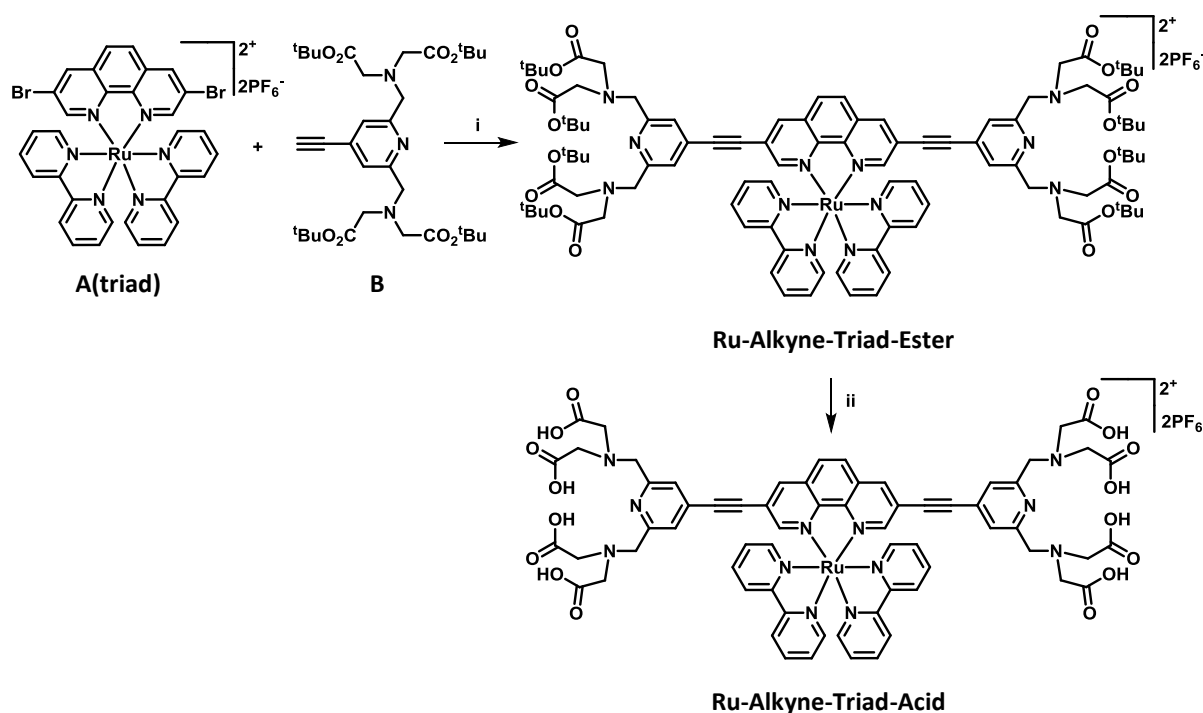
Scheme 2.06: Synthetic route to **Ru-Alkyne-Triad-Acid**. i) DMF: ^{i}Pr$_2$NH (5:1, *v:v*), (dppf)PdCl$_2$, CuI, rt, 40h, Ar; ii) CH$_2$Cl$_2$, TFA, rt, 18h

Coupling of the synthons through a Sonogashira reaction was exactly analogous to the synthesis of the monosubstituted phenanthroline scaffold (scheme **2.06i**), although a further two equivalents of synthon **B** were added after sixteen hours of reaction time, as some of the

intermediate monosubstituted scaffold entity was detected by ES⁺MS. Stirring at room temperature for a further twenty-four hours was necessary to drive the reaction to completion to produce **Ru-Alkyne-Triad-Ester** in a slightly reduced yield (45 %) compared to **Ru-Alkyne-Dyad-Ester** (50 %).

The ^{1}H NMR spectrum (400 MHz, d_6-acetone) (figure **2.10**) shows the expected singlet peaks at δ = 1.45 ppm, δ = 3.49 ppm and δ = 3.99 ppm for the protons on the polyaminocarboxylate binding site. Compared to the monosubstituted phenanthroline scaffold, the peaks all integrate to twice the number of protons (72, 16 and 8, respectively), as there are now two chelate centres on the compound. The aromatic region is also simpler for **Ru-Alkyne-Triad-Ester** as there is now twofold symmetry in the molecule (a C_2 axis). The singlet peak at δ = 7.56 ppm equates to the four equivalent H^3/H^5 protons on the two pendant pyridine rings, and the singlet at δ = 8.48 ppm corresponds to the H^5/H^6 phenanthroline protons. The final four protons on the phenanthroline ligand manifest as doublet signals at δ = 8.67 ppm and δ = 9.05 ppm (with a low coupling value of J = 1.9 Hz), and the integrals of the remaining six signals in the aromatic region combine to the expected sixteen protons on the two 2,2'-bipyridine ligands.

Figure 2.10: ^{1}H NMR spectrum (400 MHz, d_6-acetone) of **Ru-Alkyne-Triad-Ester** at 298 K.
(H_b = proton on bipyridine ligand, H_p = proton on phenanthroline ligand,
H_{py} = proton on pyridine ring)

Further characterisation was achieved with HRMS (appendix **2.04**), with the calculated and the actual *m/z* values found for the $[M - 2PF_6]^{2+}$ ion tallying well (912.4067 and 912.4073, respectively).

Removal of the tertiary-butyl groups using TFA to reveal the deprotected **Ru-Alkyne-Triad-Acid** compound was achieved in an identical fashion to the monosubstituted phenanthroline scaffold (scheme **2.06ii**). ^{1}H NMR spectroscopy in D_2O (figure **2.11**) was used to characterise the complex, and two-dimensional ^{1}H-^{1}H correlation spectroscopy (appendix **2.05**) was used to identify each signal. The 1,10-phenanthroline ligand protons appear as three singlet peaks equating to two protons each at δ = 8.25 ppm, δ = 8.35 ppm and δ = 8.74 ppm, with the majority of the bipyridine signals residing further upfield in comparison. The H^3/H^5 protons of the pendant pyridine rings appear as a singlet at δ = 7.69 ppm, and the pendant 'arms' of the chelate produce singlets at δ = 4.16 ppm and δ = 4.74 ppm. The residual H_2O signal occurs as a large peak at δ = 4.79 ppm. Overall, the NMR peaks appear broad and lack structure compared to those for **Ru-Alkyne-Triad-Ester**, possibly due to a combination of aggregation by π-stacking of the hydrophobic regions of the molecules in solution, and slow molecular tumbling in the more viscous solvent, D_2O.
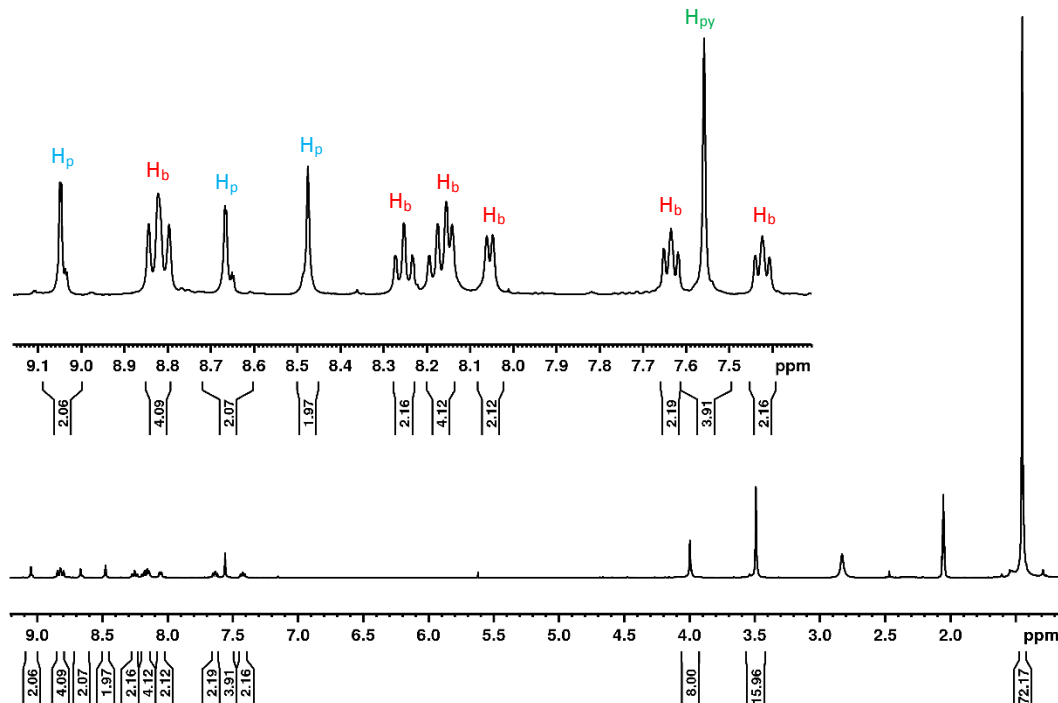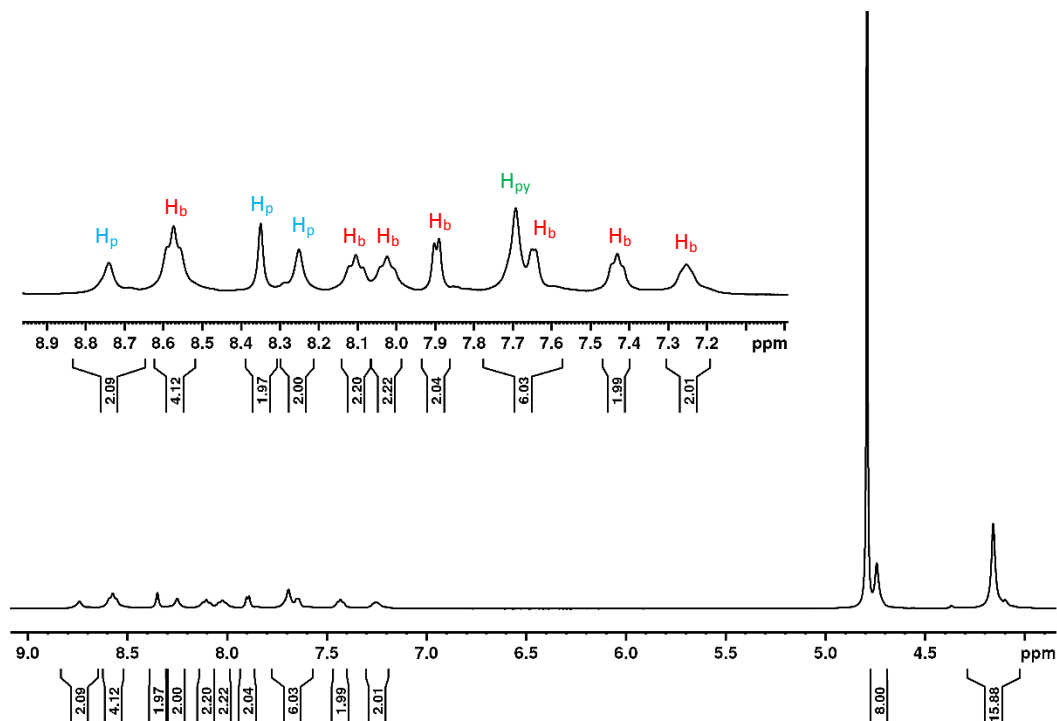

Figure 2.11: ^{1}H NMR spectrum (400 MHz, D_2O) of **Ru-Alkyne-Triad-Acid** at 298 K.
(H_b = proton on bipyridine ligand, H_p = proton on phenanthroline ligand,
H_{py} = proton on pyridine ring)

A high-resolution mass spectrum (appendix **2.06**) also confirms successful isolation of the **Ru-Alkyne-Triad-Acid** species with a detected *m/z* value of 688.1568 for the $[M - 2PF_6]^{2+}$ ion agreeing well with the calculated *m/z* value, 688.1563.

2.3.2) Photophysical Properties

UV/Vis absorption spectra were recorded in several solvents for both **Ru-Alkyne-Triad-Ester** and **Ru-Alkyne-Triad-Acid**, and extinction coefficients were measured in acetonitrile for **Ru-Alkyne-Triad-Ester** and in water for **Ru-Alkyne-Triad-Acid**. Emission profiles and lifetimes of emission were recorded for both compounds (including as a frozen glass at 77 K for **Ru-Alkyne-Triad-Ester**), and the quantum yield of emission was measured for **Ru-Alkyne-Triad-Acid** against [Ru(bipy)$_3$]Cl$_2$.6H$_2$O in aerated water. Finally, excitation spectra were measured in each solvent.

2.3.2.1) UV/Vis Absorption

UV/Vis absorption profiles for **Ru-Alkyne-Triad-Ester** and **Ru-Alkyne-Triad-Acid** recorded in EtOH/MeOH (4:1, *v:v*) can be compared (figure **2.12a**). Both spectra have a similar structure, with an intense peak centred around λ_{abs} = 350 nm for the π→π* transition on the phenanthroline backbone, and two less intense peaks in the region λ_{abs} = 375-550 nm, which are the distinct ^{1}MLCT absorptions for the two different N^N ligands.
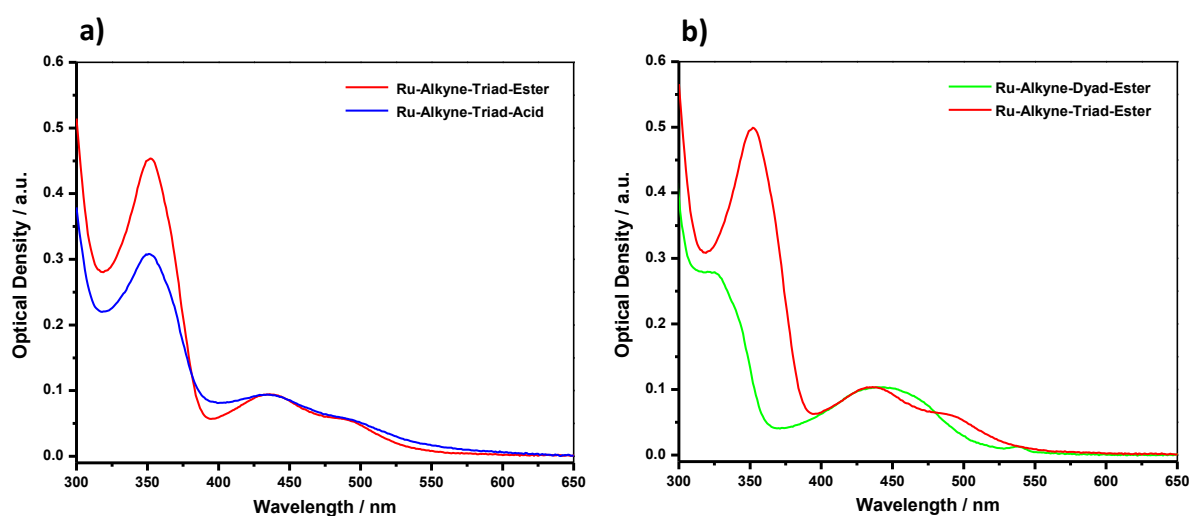
Figure 2.12: Normalised (at λ_{abs} = 435 nm) UV/Vis absorption spectra in EtOH/MeOH (4:1, *v:v*) at 298 K. a) **Ru-Alkyne-Triad-Ester** (red) and **Ru-Alkyne-Triad-Acid** (blue); b) **Ru-Alkyne-Dyad-Ester** (green) and **Ru-Alkyne-Triad-Ester** (red)

When comparing the spectrum for **Ru-Alkyne-Triad-Ester** to **Ru-Alkyne-Dyad-Ester**, the effect of increasing the conjugation along the phenanthroline backbone by adding a second pendant metal chelate can be seen (figure **2.12b**). The $\pi \rightarrow \pi^*$ transition on the phenanthroline ligand is much more intense in **Ru-Alkyne-Triad-Ester**, and it has red-shifted by ~30 nm compared to **Ru-Alkyne-Dyad-Ester**, in which the phenanthroline ligand is only monosubstituted. The [1]MLCT absorption for the phenanthroline ligand has also red-shifted in the disubstituted phenanthroline species and now appears as a distinct shoulder ($\lambda_{abs} = 480$ nm) at lower energy than the [1]MLCT absorption for the two bipyridine ligands, which itself appears unaffected by the addition of a second metal chelate. These spectral changes are corroborated by a previously published compound with extended conjugation along the phenanthroline ligand[12], [Ru(dtbbipy)$_2$(3,8-pyC≡Cphen)]$^{2+}$ (table **2.03**).

Table 2.03: UV/Vis absorption data for **Ru-Alkyne-Triad-Ester** and **Ru-Alkyne-Triad-Acid** at 298 K. [a]Data taken from ref. 12.

Compound	Solvent	λ_{abs} (nm) [ε (x10^3 M^{-1} cm^{-1})]
[a][Ru(dtbbipy)$_2$(3,8-pyC≡Cphen)]$^{2+}$	CH$_2$Cl$_2$	287 [11], 371 [6.8], 440 [1.9], 502 [1.1]
Ru-Alkyne-Triad-Ester	CH$_2$Cl$_2$	357, 437, 476 (sh)
	EtOH/MeOH (4:1, *v:v*)	352, 436, 476 (sh)
	MeCN	351 [56], 437 [14], 476 (sh) [9.3]
	DMF	352, 439, 480 (sh)
	THF	355, 437, 481 (sh)
Ru-Alkyne-Triad-Acid	EtOH/MeOH (4:1, *v:v*)	350, 434, 476 (sh)
	MeOH	351, 434, 481 (sh)
	H$_2$O	349 [46], 434 [6.5], 485 (sh) [3.7]
	DMF	355, 439, 484 (sh)

2.3.2.2) Emission

Luminescence profiles and the lifetime of the luminescence decay for **Ru-Alkyne-Triad-Ester** and **Ru-Alkyne-Triad-Acid** were recorded in several aerated solvents (table **2.04**), but profiles in EtOH/MeOH (4:1, *v:v*) at 298 K and 77 K (figure **2.13a**) will be reviewed for comparison purposes.

Upon excitation in to the ^{1}MLCT absorption band at λ_{ex} = 435 nm, both complexes produce broad and featureless emission profiles at 298 K indicating spin-forbidden ^{3}MLCT {Ru^{II}→π*$_{(N^\wedge N)}$} transitions. The emission is centred around λ_{em} = 680 nm, with **Ru-Alkyne-Triad-Acid** having a red-shift in its emission maximum (~5-10 nm) compared to **Ru-Alkyne-Triad-Ester**. When frozen as a glass at 77 K, the luminescence profile for **Ru-Alkyne-Triad-Ester** transformed to include more vibrational structure, with two less intense shoulders appearing at lower energy, and the main emission band (the 0-0 transition) blue-shifted by ~30 nm compared to the emission in fluid solution. The reason for this (rigidochromism) was discussed earlier. Unfortunately, **Ru-Alkyne-Triad-Acid** had limited solubility in EtOH/MeOH (4:1, *v:v*) and an emission spectrum at 77 K could not be measured.

Again, the effect of increasing the conjugation along the phenanthroline backbone by adding a second pendant metal chelate can be seen when comparing the luminescence profiles of **Ru-Alkyne-Dyad-Ester** and **Ru-Alkyne-Triad-Ester** (figure **2.13b**). At both 298 K and 77 K in EtOH/MeOH (4:1, *v:v*), the emission maximum for **Ru-Alkyne-Triad-Ester** is red-shifted by 35 nm compared to **Ru-Alkyne-Dyad-Ester**.
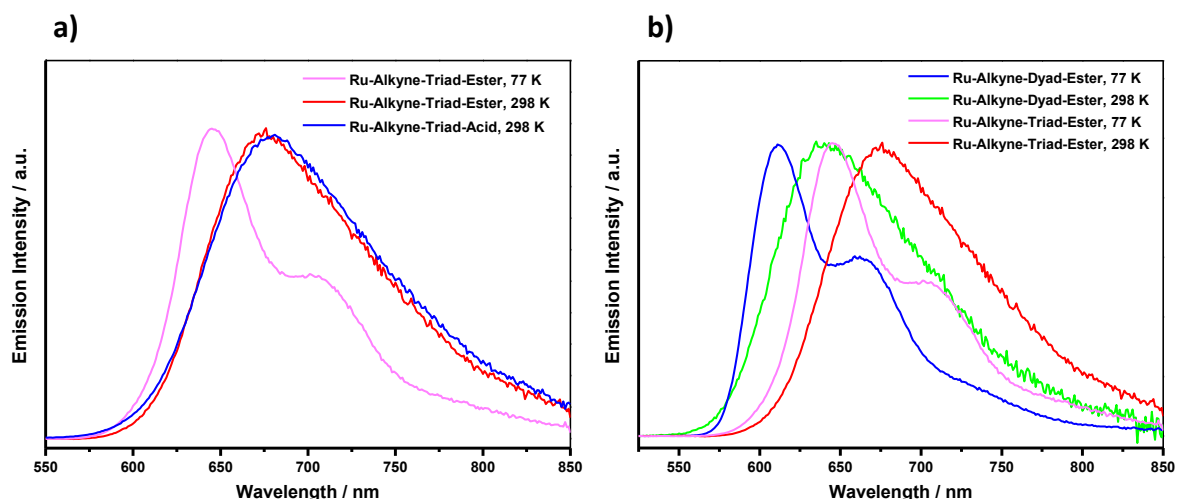
Figure 2.13: Normalised (at λ_{em} = max intensity), corrected emission spectra in aerated EtOH/MeOH (4:1, *v:v*) at 298 K and as a glass at 77 K. a) **Ru-Alkyne-Triad-Ester** (magenta, 77 K and red, 298 K, λ_{ex} = 435 nm for both) and **Ru-Alkyne-Triad-Acid** (blue, 298 K, λ_{ex} = 435 nm); b) **Ru-Alkyne-Dyad-Ester** (blue, 77 K and green, 298 K, λ_{ex} = 440 nm for both) and **Ru-Alkyne-Triad-Ester** (magenta, 77 K and red, 298 K, λ_{ex} = 435 nm for both)

The luminescence decay lifetime in aerated solvent at 298 K for **Ru-Alkyne-Triad-Ester** was *ca.* τ = 300 ns, reducing to *ca.* τ = 250 ns for **Ru-Alkyne-Triad-Acid**, due to the carboxylic acid groups quenching the luminescence more than the tertiary-butyl groups. When measured as a frozen glass at 77 K, the decay lifetime recorded for **Ru-Alkyne-Triad-Ester** was τ = 3.8 μs, which is reduced compared to **Ru-Alkyne-Dyad-Ester** (τ = 6.2 μs). This effect is also reflected in the luminescence quantum yield value (φ) of **Ru-Alkyne-Triad-Acid**, which was calculated to be φ = 0.006 when measured against $[Ru(bipy)_3]Cl_2.6H_2O$[18] as a standard in aerated water at 298 K. This value is significantly reduced compared to **Ru-Alkyne-Dyad-Acid** (φ = 0.020), illustrating the deleterious effect that the extra substitution in **Ru-Alkyne-Triad-Acid** has on the emission intensity.

Table 2.04: Luminescence data for **Ru-Alkyne-Triad-Ester** and **Ru-Alkyne-Triad-Acid** in aerated solvents. [a]Data taken from ref. 12.

Compound	Solvent	$\lambda_{em}^{298\,K}$ (nm) $[\lambda_{em}^{77\,K}$ (nm)]	$\tau_1, \tau_2^{298\,K}$ (ns) $[\tau^{77\,K}$ (μs)]	A_1, A_2 (%)
[a]$[Ru(dtbbipy)_2(3,8-pyC\Xi Cphen)]^{2+}$	CH_2Cl_2	657	591	--
Ru-Alkyne-Triad-Ester	CH_2Cl_2	662	650	--
	EtOH/MeOH (4:1, *v:v*)	676 [645, 701 (sh), 742 (sh)]	284 [3.8]	--
	MeCN	683	271	--
	DMF	702	280	--
	THF	706	306	--
Ru-Alkyne-Triad-Acid	EtOH/MeOH (4:1, *v:v*)	681	273, 49	95, 5
	MeOH	691	235, 120	98, 2
	H_2O	697	209, 102	26, 74
	DMF	702	259, 49	87, 13

Excitation spectra recorded at λ_{em} = 660 nm in aerated EtOH/MeOH (4:1, *v:v*) at 298 K for both **Ru-Alkyne-Triad-Ester** and **Ru-Alkyne-Triad-Acid** were overlaid with UV/Vis absorption spectra recorded in the same solvent (figure **2.14**). A good match between the spectra can be seen, which is a clear indication that the emission observed for both complexes occurs as a result of absorption in to the [1]MLCT band.
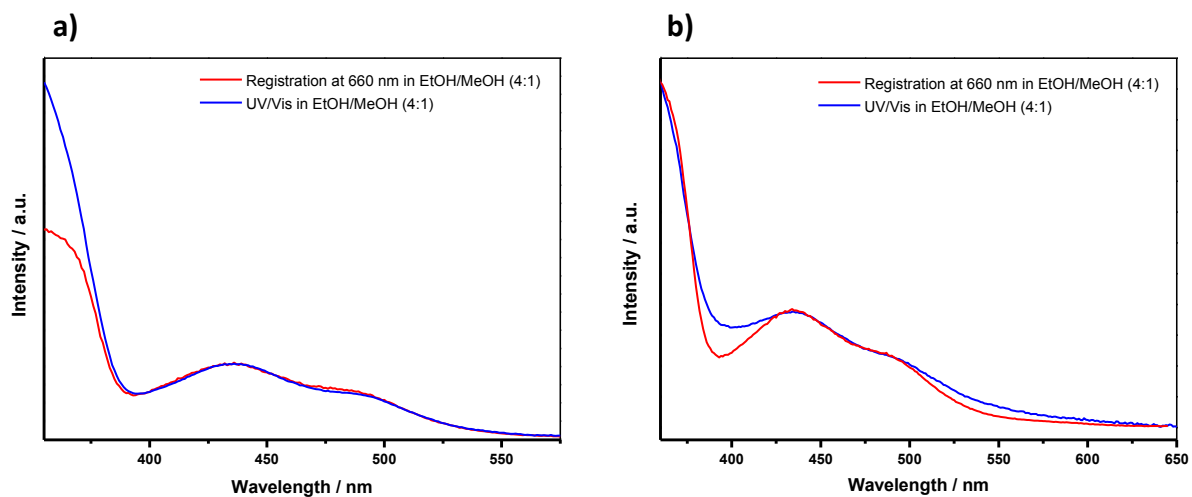
Figure 2.14: Normalised (at λ = 435 nm) spectra in aerated EtOH/MeOH (4:1, *v:v*) at 298 K. Corrected excitation spectra at λ$_{em}$ = 660 nm (red) and UV/Vis spectra (blue) of a) **Ru-Alkyne-Triad-Ester** and b) **Ru-Alkyne-Triad-Acid**

2.4) An Alkyne-Bridged Scaffold for a 'Metallostar' Dual-Modal Imaging Agent

2.4.1) Synthesis and Characterisation

As the synthetic route developed proved amenable to producing both a monosubstituted and disubstituted phenanthroline scaffold around the central Ru[II] unit, the same method was used to synthesise a larger 'metallostar' entity capable of binding six MRI-active metal centres (figure **2.15**).
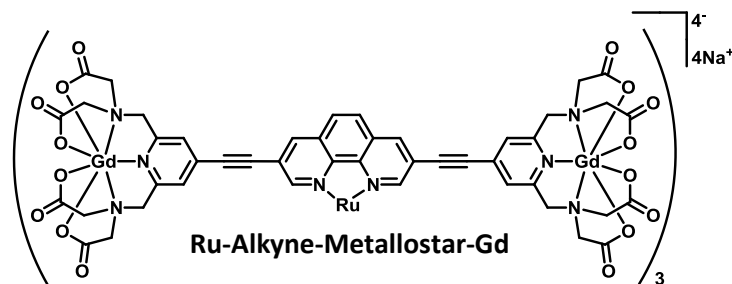
Figure 2.15: A 'metallostar' dual-modal Ru[II]-Gd[III]$_6$ species

Previously, 'metallostars' have been made by a convergent approach in which the pre-prepared ligands, with the MRI-active metal centre already bound, are assembled around the central luminescent metal centre by mixing the components in a 3:1 ratio[19–21]. However, in this example, the central ruthenium complex component was synthesised first, before the insertion of the Gd[III] metal centres.

Retrosynthetic analysis of the targeted 'metallostar' species produced synthons very similar to the previous scaffolds (scheme **2.01**), including 4-ethynyl-2,6-disubstituted pyridine (synthon **B**) and a ruthenium centre surrounded by brominated 1,10-phenanthroline ligands to take advantage of the Sonogashira coupling reaction (synthon **A(metallostar)**). In this case, to allow introduction of six pendant metal chelates, the Ru[II]-based synthon was tris(3,8-dibromo-1,10-phenanthroline)Ru(II) hexafluorophosphate (scheme **2.07**). Two equivalents of 3,8-dibromo-1,10-phenanthroline were heated with ruthenium(III) chloride trihydrate in DMF to produce bis(3,8-dibromo-1,10-phenanthroline)Ru(II)-dichloride hydrate, which was subsequently heated with a further equivalent of 3,8-dibromo-1,10-phenanthroline in ethylene glycol to produce the final synthon, **A(metallostar)**. Purification was achieved by column chromatography and was verified by ^{1}H NMR spectroscopy and HRMS.
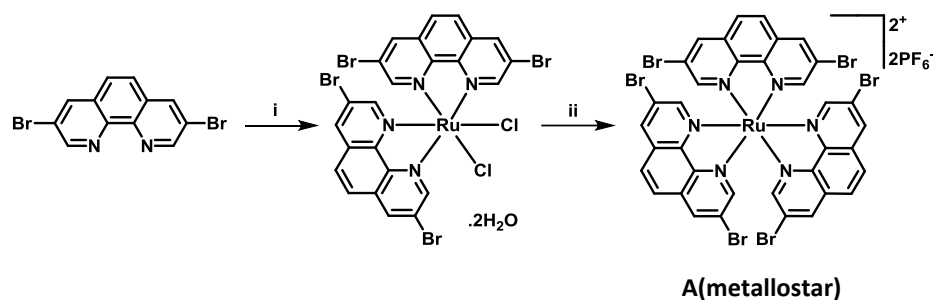
Scheme 2.07: Synthetic route to synthon **A(metallostar)**. i) DMF, $RuCl_3.3H_2O$, LiCl, reflux, 7h; ii) ethylene glycol, 3,8-dibromo-1,10-phenanthroline, 120 °C, 16h

Synthesis of the **Ru-Alkyne-Metallostar-Ester** species was achieved by subjecting synthon **A(metallostar)** to six independent Sonogashira reactions with synthon **B** (scheme **2.08i**). Initially, twelve equivalents of synthon **B** were added to a deoxygenated solution of synthon **A(metallostar)**, $(dppf)PdCl_2$ and copper iodide dissolved in an anhydrous mixture of DMF and triethylamine (5:1, *v:v*). The solution was stirred at room temperature for sixteen hours, before a further twelve equivalents of synthon **B** were added. The resulting solution was left stirring for seven days before the crude product was extracted and purified by column chromatography on silica gel (200-300 mesh), and then by size-exclusion chromatography on Sephadex® LH-20. A low yield was finally achieved (15 %), but this was due to incomplete conversion of the starting material to the fully-substituted product. Some of the equivalents of synthon **B** were lost to the competing Glaser reaction in which two alkyne groups coupled to a di-yne in the presence of copper iodide. Addition of further equivalents of synthon **B** may help to overcome this issue and avoid the partially-substituted entities in the future.

Successful isolation of **Ru-Alkyne-Metallostar-Ester** was confirmed by ES+MS (appendix **2.07**), as a molecular ion peak at *m/z* = 2168.6 for the $[M - 2PF_6]^{2+}$ species was recorded with the typical Ru^{II} ion isotope pattern. The ^1H NMR spectrum (figure **2.16**, 400 MHz, d_6-acetone) is very simple as the compound only has seven different proton environments due to the symmetry in the molecule. The peaks are also broad as the molecule is very large and tumbles slowly in solution.
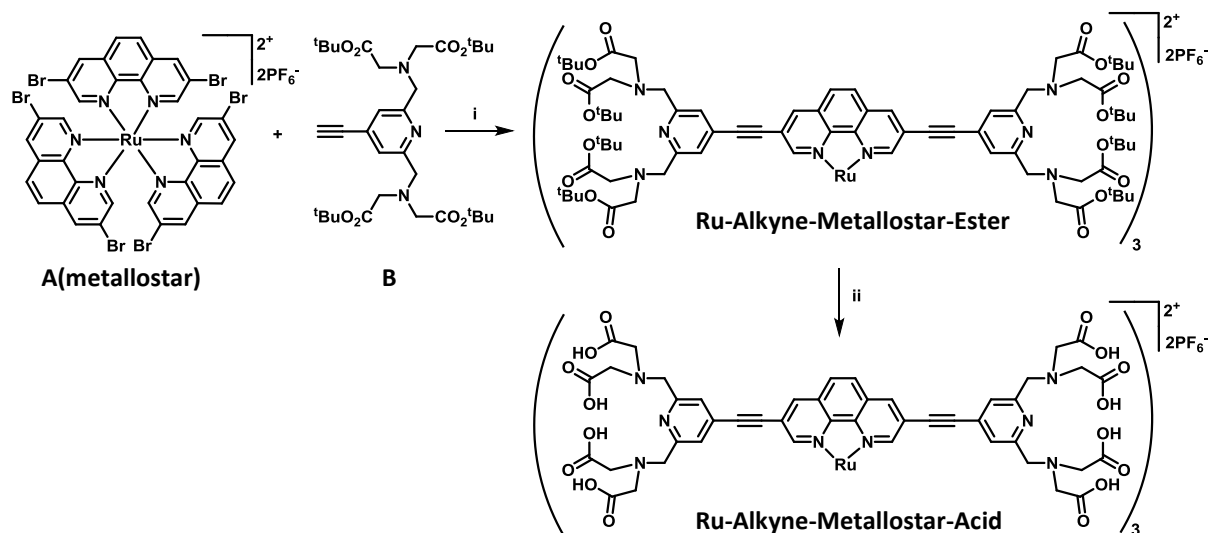
Scheme 2.08: Synthetic route to **Ru-Alkyne-Metallostar-Acid**. i) DMF: NEt$_3$ (5:1, *v:v*), (dppf)PdCl$_2$, CuI, rt, 8 days, Ar; ii) CH$_2$Cl$_2$, TFA, rt, 18h

A singlet at δ = 1.41 ppm integrating to *ca.* 216 protons accounts for the twenty-four tertiary-butyl groups on the six polyaminocarboxylate chelates, and the remaining two singlets in the aliphatic region at δ = 3.45 ppm and δ = 3.96 ppm represent the two proton environments on the chelate 'arms'. The residual solvent peak is present at δ = 2.05 ppm and a broad peak at δ = 2.84 ppm is due to H$_2$O and HOD in the solvent. In the aromatic region there are 4 broad singlets at δ = 7.55 ppm, δ = 8.49 ppm, δ = 8.81 ppm and δ = 9.06 ppm integrating as 12, 6, 6 and 6 protons, respectively. The peak at δ = 7.55 ppm characterises the twelve equivalent H^3/H^5 protons on the pendant pyridine rings, whilst the other three singlets represent the three proton environments on the phenanthroline ligands.

As the ^{1}H NMR spectrum is so simple due to the high symmetry of the complex, to provide further evidence of successful synthesis, a DEPTQ ^{13}C NMR spectrum (figure **2.17**, 500 MHz, 1,1,2,2-tetrachloroethane-d_2) was also recorded to help assign the carbon environments. The large, negative peak at δ = 73.78 ppm is the residual solvent peak for 1,1,2,2-tetrachloroethane and the remaining sixteen peaks are for the different carbon environments. There are eleven negative peaks which correspond to the nine quaternary carbon atoms and the two CH$_2$ environments, with the remaining five positive signals corresponding to the CH and CH$_3$ environments. Further precise assignment of each individual carbon environment (appendix **2.08**) was achieved using a two-dimensional HSQC spectrum (appendix **2.09**) and a two-dimensional HMBC spectrum (appendix **2.10**).
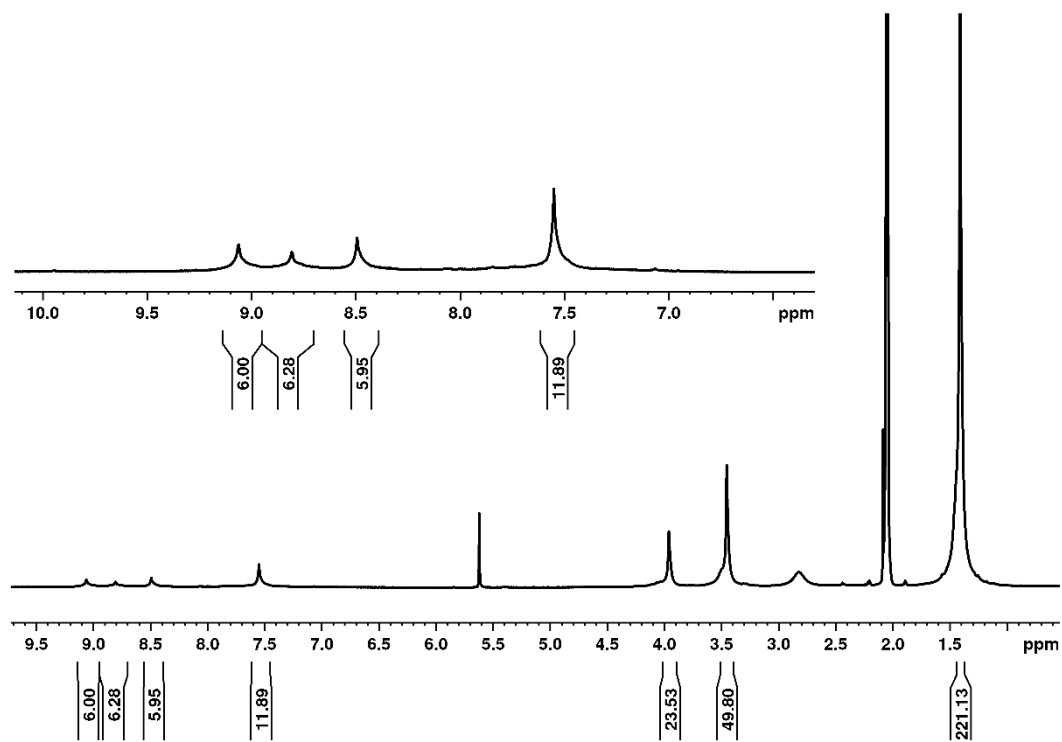
Figure 2.16: ^{1}H NMR spectrum (400 MHz, d_6-acetone) of **Ru-Alkyne-Metallostar-Ester** at 298 K
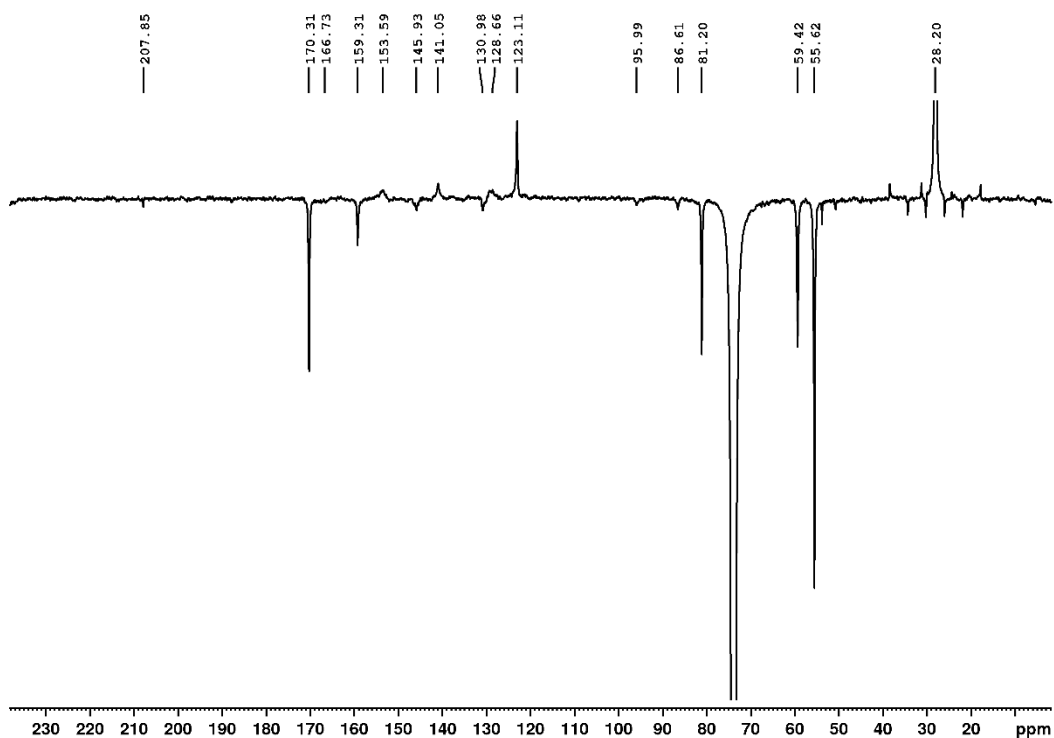
Figure 2.17: DEPTQ ^{13}C NMR spectrum (500 MHz, 1,1,2,2-tetrachloroethane-d_2)
of **Ru-Alkyne-Metallostar-Ester** at 298 K

Removal of the tertiary-butyl protecting groups to produce the **Ru-Alkyne-Metallostar-Acid** compound was achieved in an analogous way to the previous synthetic routes (scheme **2.08ii**). **Ru-Alkyne-Metallostar-Ester** was stirred in dichloromethane and TFA, and then washed repeatedly to remove the TFA. The product was then dissolved in the minimum amount of methanol and precipitated by addition of an excess of diethyl ether. The solid was collected by centrifugation and dried under a stream of nitrogen to yield the compound in near quantitative yield. However, once the residual TFA had been removed, the resulting **Ru-Alkyne-Metallostar-Acid** solid was insoluble in all solvents unless the pH was adjusted using base. This was most likely due to the substantial number of carboxylic acid groups dominating the exterior of the compound.

^{1}H NMR spectroscopy (figure **2.18,** 500 MHz, D_2O, pD 4.38) was used to verify the successful synthesis and purity of **Ru-Alkyne-Metallostar-Acid**, although the pD of the D_2O solution had to be adjusted to pD 4.38 to ensure complete dissolution of the solid. The singlets at δ = 3.82 ppm and δ = 4.57 ppm are representative of the polyaminocarboxylate chelate protons, but unfortunately the residual H_2O peak at δ = 4.79 ppm partially overlaps with the signal at δ = 4.57 ppm. There are also unknown impurity peaks at δ = 3.26 ppm and between δ = 3.55-3.63 ppm, which partially overlap with the broad signal at δ = 3.82 ppm. The signals in the aromatic region have become even broader in comparison to those in the spectrum for **Ru-Alkyne-Metallostar-Ester** and have overlapped. The peak integrating to twelve protons at δ = 7.54 ppm most likely represents the H^3/H^5 protons on the six pendant pyridine rings, with the phenanthroline protons making up the remaining signals.

Again, a DEPTQ ^{13}C NMR spectrum (figure **2.19,** 500 MHz, D_2O, pD 4.38) was recorded to characterise the carbon environments in the compound (appendix **2.11**), aided by a two-dimensional HSQC spectrum (appendix **2.12**). The signals are weak in the spectrum because of the low concentration of the NMR sample due to its limited solubility, but fourteen peaks can be identified for the different carbon environments. The spectrum is similar to that for **Ru-Alkyne-Metallostar-Ester**, although the positive peak at δ = 28.2 ppm and the negative peak at δ = 81.2 ppm are no longer present, as they represented the carbon atoms in the tertiary-butyl groups that have now been removed.
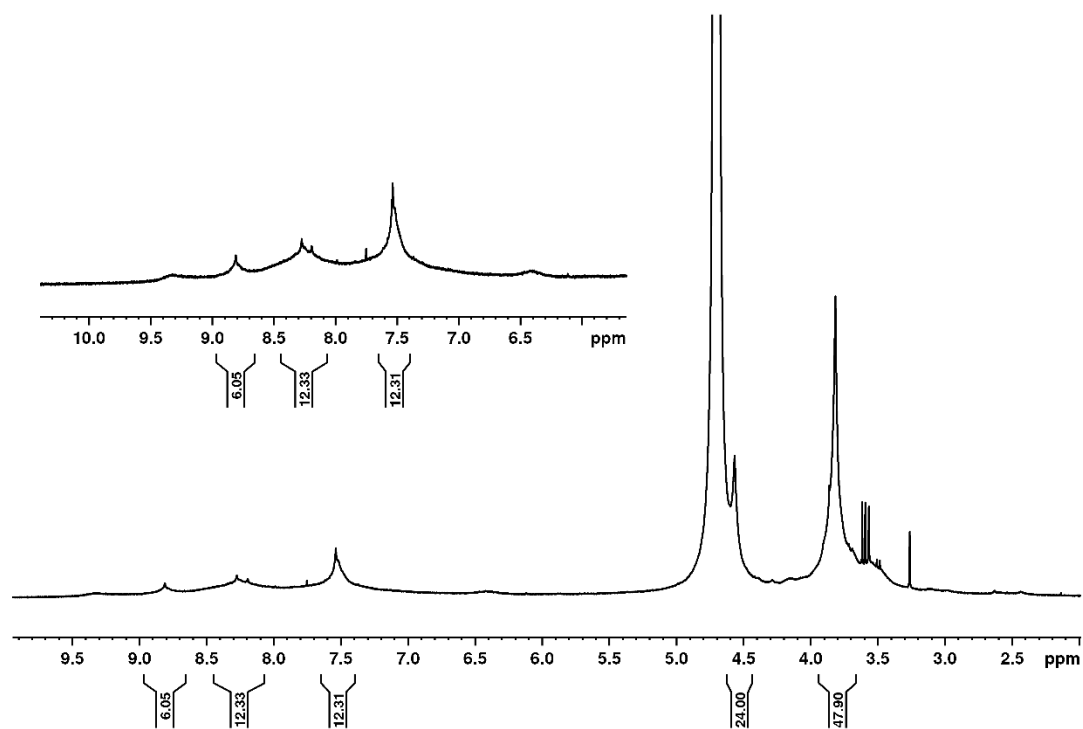
Figure 2.18: ^{1}H NMR spectrum (500 MHz, D$_2$O, pD 4.38) of **Ru-Alkyne-Metallostar-Acid** at 298 K
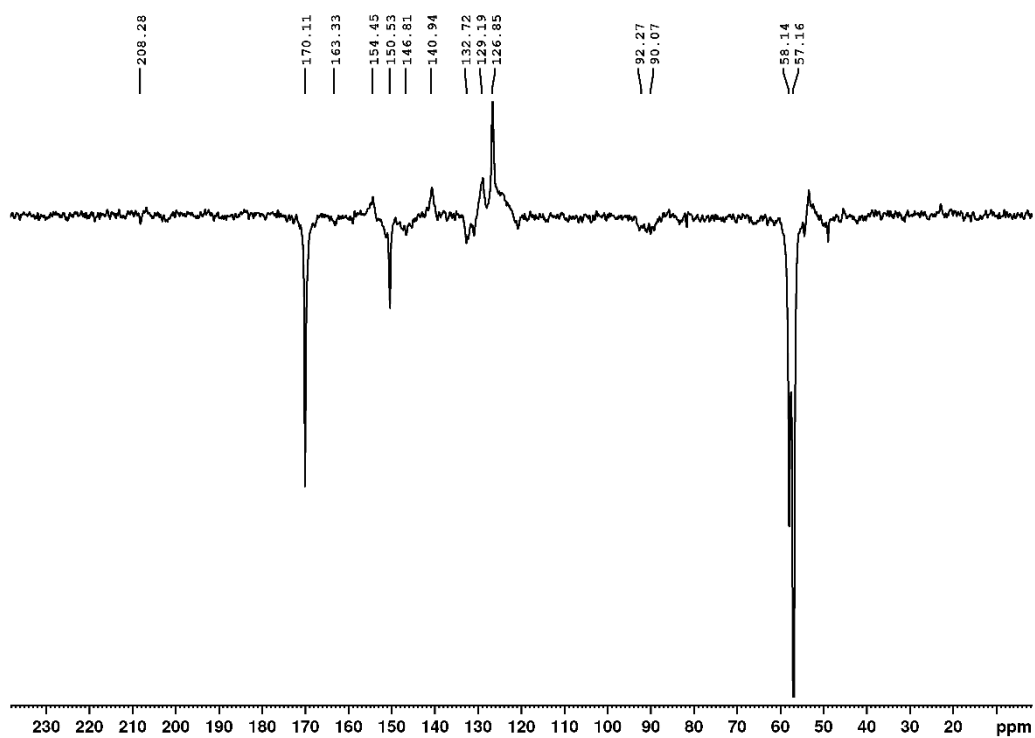
Figure 2.19: DEPTQ ^{13}C NMR spectrum (500 MHz, D$_2$O, pD 4.38) of
Ru-Alkyne-Metallostar-Acid at 298 K

2.4.2) Photophysical Properties

UV/Vis absorption spectra were recorded in several solvents for **Ru-Alkyne-Metallostar-Ester** and in water at pH 9 for **Ru-Alkyne-Metallostar-Acid**. Emission profiles and lifetimes of emission were recorded for both compounds (including as a frozen glass at 77 K for **Ru-Alkyne-Metallostar-Ester**), and the quantum yield of emission was measured for **Ru-Alkyne-Metallostar-Acid** against $[Ru(bipy)_3]Cl_2.6H_2O$ in aerated water. Finally, excitation spectra were measured in each solvent.

2.4.2.1) UV/Vis Absorption

The UV/Vis absorption profile for **Ru-Alkyne-Metallostar-Ester** was recorded in EtOH/MeOH (4:1, *v:v*) (figure **2.20a**) and the profile for **Ru-Alkyne-Metallostar-Acid** was recorded in water at pH 9 (figure **2.20b**). The two spectra are similar, with an intense peak centred around λ_{abs} = 350 nm for the $\pi \rightarrow \pi^*$ transition on the phenanthroline ligands, and a less intense peak in the region λ_{abs} = 480 nm, which is the ^{1}MLCT absorption on the phenanthroline ligands.
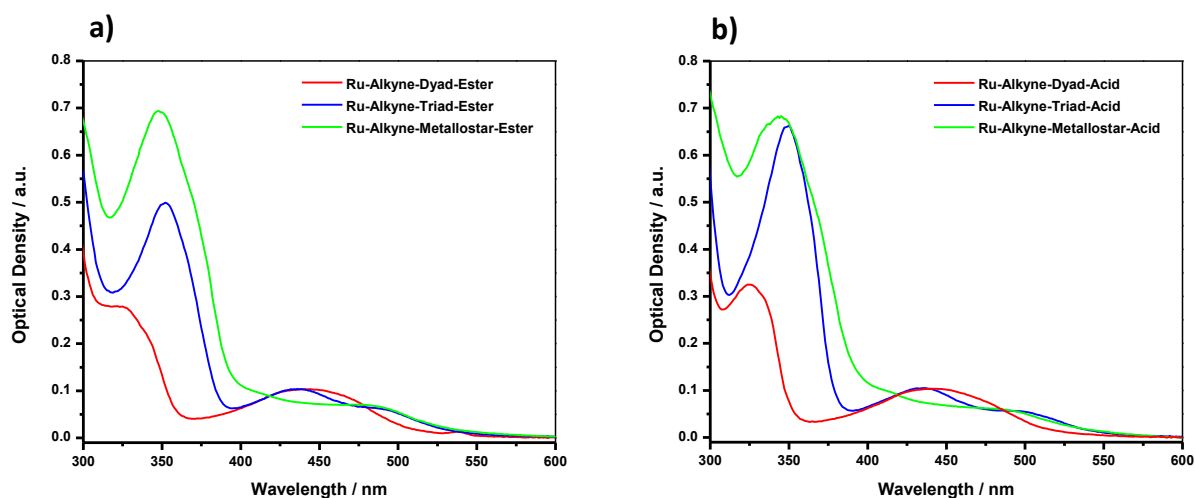
Figure 2.20: Normalised UV/Vis absorption spectra at 298 K. a) **Ru-Alkyne-Dyad-Ester** (red), **Ru-Alkyne-Triad-Ester** (blue) and **Ru-Alkyne-Metallostar-Ester** (green) in EtOH/MeOH (4:1, *v:v*); b) **Ru-Alkyne-Dyad-Acid** (red), **Ru-Alkyne-Triad-Acid** (blue) and **Ru-Alkyne-Metallostar-Acid** (green, pH 9) in H_2O

When comparing the spectra for the 'metallostar' species to the spectra for the monosubstituted and disubstituted phenanthroline scaffolds in both solvents (figure **2.20**), the consequences of the progressive changes to the N^N ligands around the ruthenium core can clearly be seen. Moving from the monosubstituted phenanthroline scaffold to the disubstituted phenanthroline scaffold increased the intensity of the $\pi \rightarrow \pi^*$ transition on the phenanthroline ligand (λ_{abs} = 320-350 nm), and also red-shifted the λ_{max} value by ~30 nm, which is maintained in the 'metallostar' species as the phenanthroline ligand structure is the same. Between λ_{abs} = 400-550 nm, the [1]MLCT absorptions also change sequentially to reflect the nature of the ligands surrounding the ruthenium core. The monosubstituted phenanthroline scaffold has a broad, featureless absorption, as the transitions on the two different N^N ligands overlap. This transforms to include a red-shifted shoulder peak (λ_{abs} = 480 nm) in the profile for the disubstituted phenanthroline scaffold, which is the [1]MLCT absorption for the more conjugated phenanthroline ligand. Again, this is maintained in the spectrum for the 'metallostar' species, and the absorption assigned to the [1]MLCT on the bipyridine ligands (λ_{abs} = 440 nm) is no longer present.

Comparing the absorption data to a previously published 'metallostar' species (**20**, figure **1.29**, Eu analogue, M = Ru)[20] shows similar trends (table **2.05**), although the ligands are bipyridine-based in the literature rather than phenanthroline-based and so each absorption is blue-shifted in comparison.

Table 2.05: UV/Vis absorption data for **Ru-Alkyne-Metallostar-Ester** and **Ru-Alkyne-Metallostar-Acid** at 298 K. [a]Data taken from ref. 20.

Compound	Solvent	λ_{abs} (nm)
[a]**RuEu$_6$ (20)**	H_2O	293, 330 (sh), 360 (sh), 450
Ru-Alkyne-Metallostar-Ester	CH_2Cl_2	352, 369 (sh), 475
	EtOH/MeOH (4:1, *v:v*)	348, 362 (sh), 475
	MeCN	347, 365 (sh), 478
	THF	351, 374 (sh), 484
	DMF	348, 363 (sh), 489
Ru-Alkyne-Metallostar-Acid	H_2O (pH 9)	289, 344, 367 (sh), 480

2.4.2.2) Emission

Luminescence profiles and the lifetime of the luminescence decay were recorded in several aerated solvents for **Ru-Alkyne-Metallostar-Ester** and in water at pH 9 for **Ru-Alkyne-Metallostar-Acid** (table **2.06**). Profiles in EtOH/MeOH (4:1, *v:v*) at 77 K (figure **2.21a**) and in water (figure **2.21b**) will be reviewed for comparison purposes.

Upon excitation in to the ^{1}MLCT absorption band at λ_{ex} = 480-485 nm, both complexes produce broad and featureless emission profiles at 298 K, centred around λ_{em} = 640-650 nm. When frozen as a glass at 77 K, the luminescence profile for **Ru-Alkyne-Metallostar-Ester** displays the usual changes with more vibrational structure on the low energy side of the main (0-0) emission band, which has blue-shifted (~20 nm) due to rigidochromism. When comparing the 'metallostar' species to the monosubstituted and disubstituted phenanthroline scaffolds at 77 K (figure **2.21a**), it can be seen that the emission maximum for the 'metallostar' species is red-shifted compared to the monosubstituted phenanthroline scaffold, but blue-shifted in comparison to the disubstituted phenanthroline scaffold. This is similar for the acid-derivatives in water (figure **2.21b**), however, in this case the 'metallostar' species has the highest energy emission maximum.
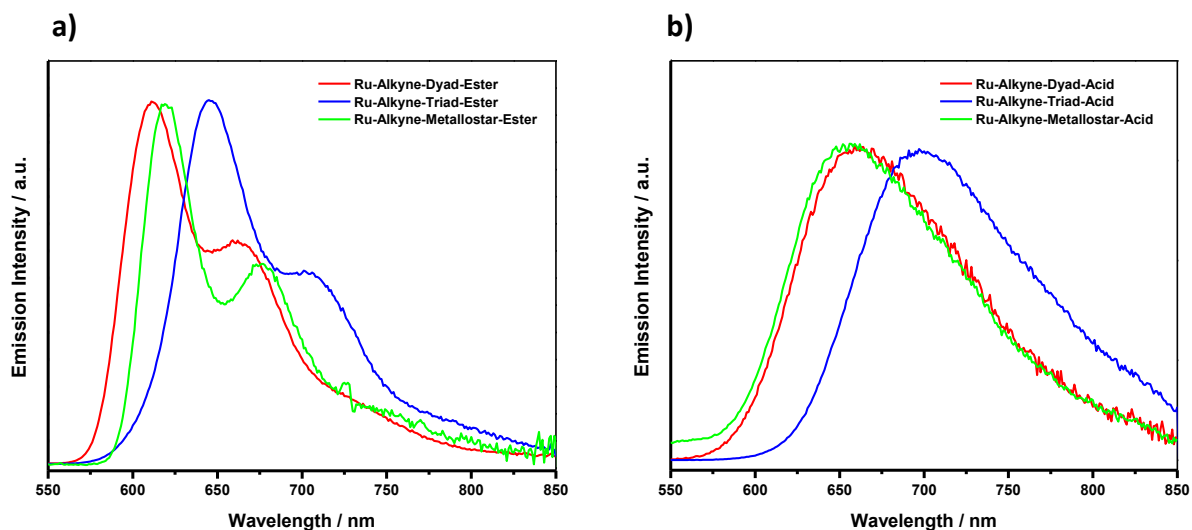
Figure 2.21: Normalised (at λ_{em} = max intensity), corrected emission spectra in aerated solvents.
a) **Ru-Alkyne-Dyad-Ester** (red, λ_{ex} = 440 nm), **Ru-Alkyne-Triad-Ester** (blue, λ_{ex} = 435 nm) and **Ru-Alkyne-Metallostar-Ester** (green, λ_{ex} = 485 nm) in EtOH/MeOH (4:1, *v:v*) at 77 K;
b) **Ru-Alkyne-Dyad-Acid** (red, λ_{ex} = 440 nm), **Ru-Alkyne-Triad-Acid** (blue, λ_{ex} = 435 nm) and **Ru-Alkyne-Metallostar-Acid** (green, λ_{ex} = 480 nm, pH 9) in H$_2$O at 298 K

The time-resolved luminescence decay profiles recorded for both the ester-protected and carboxylic acid derivatives of the 'metallostar' species were complex and were all fitted with triexponential decays. Typically, two longer lifetimes (*ca.* τ = 300-600 ns) were the main components, with one much shorter lifetime (*ca.* τ = 50 ns) making up 2 % of the overall decay. Such complex behaviour could arise from aggregation in solution.

Table 2.06: Luminescence data for **Ru-Alkyne-Metallostar-Ester** and **Ru-Alkyne-Metallostar-Acid** in aerated solvents. [a]Data taken from ref. 20.

Compound	Solvent	$\lambda_{em}^{298\,K}$ (nm) [$\lambda_{em}^{77\,K}$ (nm)]	$\tau_1, \tau_2, \tau_3^{298\,K}$ (ns) [$\tau_1, \tau_2, \tau_3^{77\,K}$ (ns)]	A_1, A_2, A_3 (%)
[a]**RuEu$_6$ (20)**	H$_2$O	625, 660 (sh) [584, 625, 680 (sh)]	--	--
Ru-Alkyne-Metallostar-Ester	CH$_2$Cl$_2$	620	785, 338, 52	71, 27, 2
	EtOH/MeOH (4:1, *v:v*)	643 [619, 676 (sh)]	660, 384, 43 [5063, 1111, 145]	21, 77, 2 [97, 2, 1]
	MeCN	651	435, 147, 34	59, 38, 3
	THF	659	696, 370, 50	60, 38, 2
	DMF	668	492, 291, 36	86, 12, 2
Ru-Alkyne-Metallostar-Acid	H$_2$O (pH 9)	656	457, 25, 8	78, 8, 14

The luminescence quantum yield value (ϕ) of **Ru-Alkyne-Metallostar-Acid** was calculated to be ϕ = 0.003 when measured against [Ru(bipy)$_3$]Cl$_2$.6H$_2$O[18] as a standard in aerated water at 298 K. This value is reduced compared to the analogous monosubstituted and disubstituted phenanthroline scaffolds (ϕ = 0.020 and 0.006, respectively), illustrating the deleterious effect the extra substitution on the phenanthroline ligands has on the emission intensity.

An excitation spectrum (λ_{em} = 635 nm) recorded in aerated EtOH/MeOH (4:1, *v:v*) at 298 K for **Ru-Alkyne-Metallostar-Ester** was overlaid with a UV/Vis absorption spectrum recorded in the same solvent (figure **2.22a**). A good match between the spectra can be seen, which is a clear indication that the emission observed for the complex occurs as a result of absorption in to the [1]MLCT band.
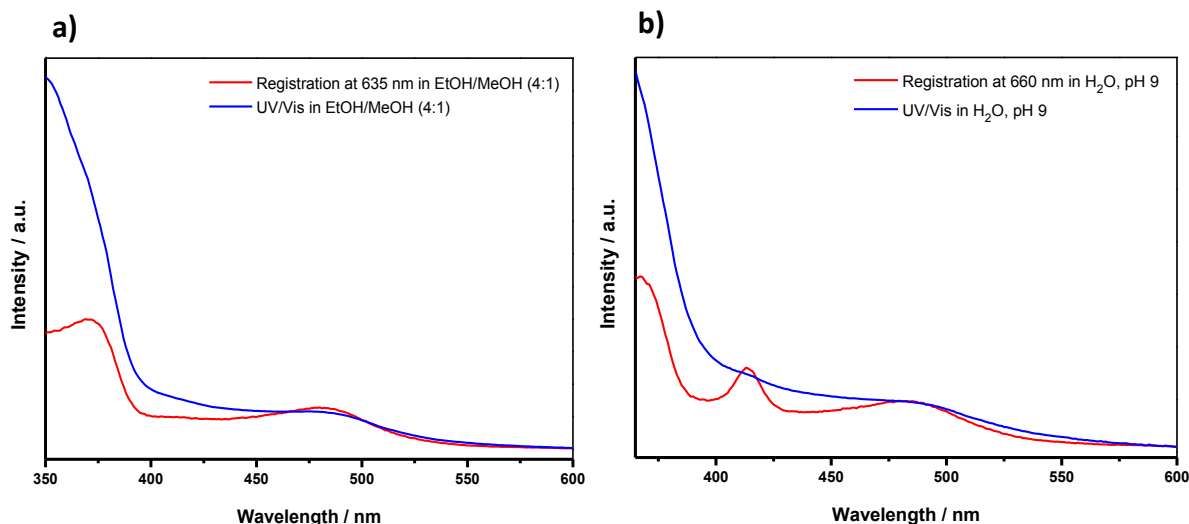
Figure 2.22: Normalised (at λ = 480 nm) spectra in aerated solvents at 298 K. Corrected excitation spectra (red) and UV/Vis spectra (blue) of a) **Ru-Alkyne-Metallostar-Ester** (EtOH/MeOH (4:1, *v:v*), λ_{em} = 635 nm) and b) **Ru-Alkyne-Metallostar-Acid** (H_2O, pH 9, λ_{em} = 660 nm)

A similar comparison of the excitation spectrum (λ_{em} = 660 nm) and the UV/Vis absorption spectrum for **Ru-Alkyne-Metallostar-Acid** recorded in aerated water at pH 9 and at 298 K, reveals different results, however (figure **2.22b**). The excitation spectrum has the same basic shape as the UV/Vis spectrum apart from a new peak at λ = 415 nm. A luminescence profile recorded at λ_{ex} = 415 nm (figure **2.23a**) revealed a similar emission band centred around λ_{em} = 650 nm compared to the profile recorded at λ_{ex} = 480 nm, but also showed more structure with a more pronounced shoulder peak emerging at λ_{em} = 705 nm. An excitation spectrum recorded at λ_{em} = 705 nm (figure **2.23b**) is similar to the excitation spectrum recorded at λ_{em} = 660 nm but does still not match the UV/Vis spectrum.

This evidence suggests that the compound may have aggregated in solution due to its limited solubility in water. This is further supported by the lifetime of the luminescence decay in water at pH 9 (τ_1 = 457 ns, τ_2 = 25 ns, τ_3 = 8 ns) not tallying with the expected trend. Compared to **Ru-Alkyne-Dyad-Acid** and **Ru-Alkyne-Triad-Acid** (τ = 341 ns and τ = 209 ns, respectively), the main lifetime component (τ = 457 ns) in **Ru-Alkyne-Metallostar-Acid** is longer-lived. As the quantum yield value measured for **Ru-Alkyne-Metallostar-Acid** is reduced in intensity compared to its less-substituted counterparts, it would be expected that the lifetime value measured would also have reduced by the same magnitude.
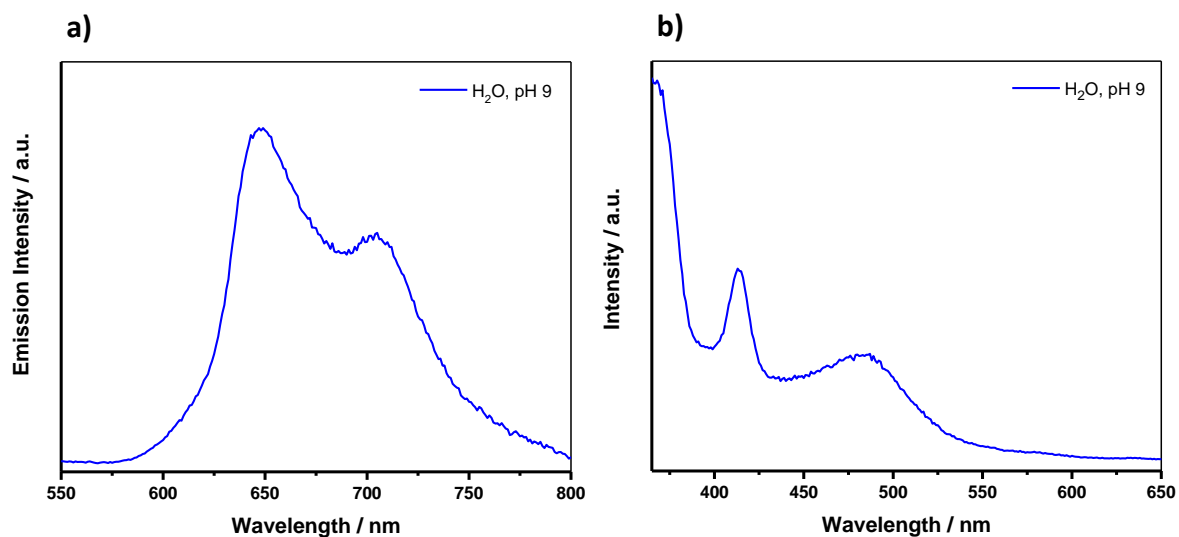
Figure 2.23: Corrected spectra of **Ru-Alkyne-Metallostar-Acid** in aerated H_2O (pH 9) at 298 K. a) Emission (λ_{ex} = 415 nm), b) Excitation (λ_{em} = 705 nm)

2.5) A Triazole-Bridged Scaffold for a Dinuclear Dual-Modal Imaging Agent

2.5.1) Synthesis and Characterisation

With the successful production of a series of alkyne-bridged scaffolds based on ruthenium(II) bis(2,2'-bipyridine) cores for potential dual-modal optical/MR imaging agents, the spacer unit in each pendant 'arm', separating the Ru[II] core from the pendant binding site for Gd[III], was then modified to a triazole entity to assess its effect on the relaxivity value measured for a dinuclear framework.

Retrosynthetic analysis of this alternative triazole-bridged scaffold produced synthons **C** and **D** (scheme **2.09**) with functional groups in place to utilise an azide/alkyne, copper-catalysed 'click' reaction[22,23]. An azide group was attached to the pyridine-based chelate (**D**) and an alkyne substituent was attached to the 1,10-phenanthroline ligand on synthon **C**, as there was no precedent in the literature for connecting an azide group directly to a 1,10-phenanthroline unit.
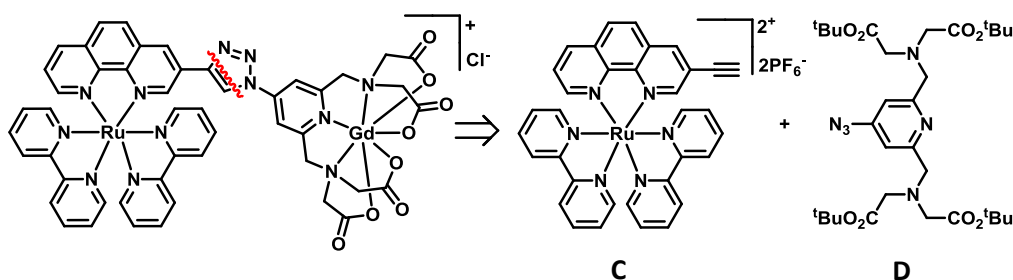
Scheme 2.09: Retrosynthetic analysis of the monosubstituted triazole-bridged scaffold

The most straightforward route to synthon **C** was considered to be the simple modification of synthon **A** by reacting it with TMSA in a Sonogashira reaction (scheme **2.10**, **route A**). Removal of the trimethylsilyl protecting group proved challenging, however, as the ruthenium centre decomposed under various reaction conditions. Using milder bases in the reaction, and also changing the alkyne reactant to (triisopropylsilyl)acetylene and 2-methyl-3-butyn-2-ol proved unsuccessful remedies to the problem, as decomposition was still encountered. A second route to the synthon was, therefore, designed, in which the alkyne substituent was attached to the 1,10-phenanthroline ligand *before* the ruthenium(II) bis(2,2'-bipyridine) centre was bound (scheme **2.10**, **route B**).
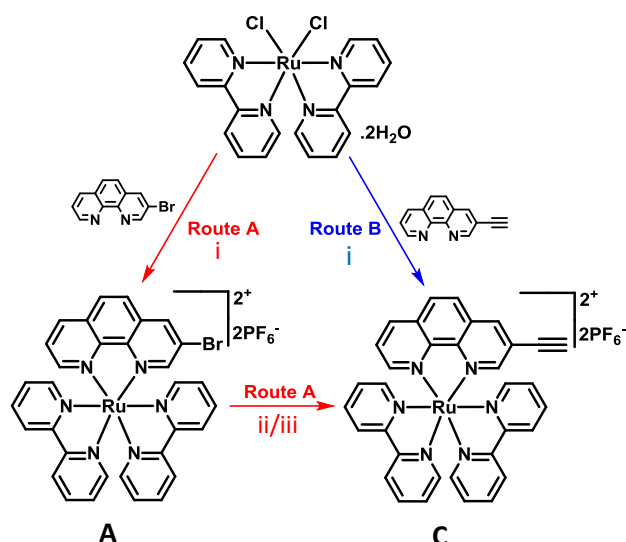
Scheme 2.10: The two routes attempted in the synthesis of synthon **C**.
Route A: i) MeOH, reflux, 8h; ii) DMF: NEt$_3$ (3:1, *v:v*), TMSA, 3d, Ar; iii) THF, TBAF, rt, 16h
Route B: i) MeOH, reflux, 8h

Starting from 3-bromo-1,10-phenanthroline, synthon **C** was successfully synthesised in three steps following literature preparations (scheme **2.11**). The trimethylsilyl-protected alkyne substituent was attached to the phenanthroline core by reacting 3-bromo-1,10-phenanthroline with TMSA in the presence of Pd(PPh$_3$)$_2$Cl$_2$ and copper iodide in THF:NEt$_3$ (2:1, *v:v*)[24]. Deprotection of the trimethylsilyl group to reveal the free alkyne was achieved using potassium carbonate in a MeOH:THF mixture (2:1, *v:v*)[25], and then coordination to the ruthenium(II) bis(2,2'-bipyridine) centre was accomplished by refluxing the ligand with *cis*-bis(2,2'-bipyridine)-dichloro-ruthenium hydrate[13] in methanol. ^{1}H NMR spectroscopy and ES[+]MS were used to characterise each compound.
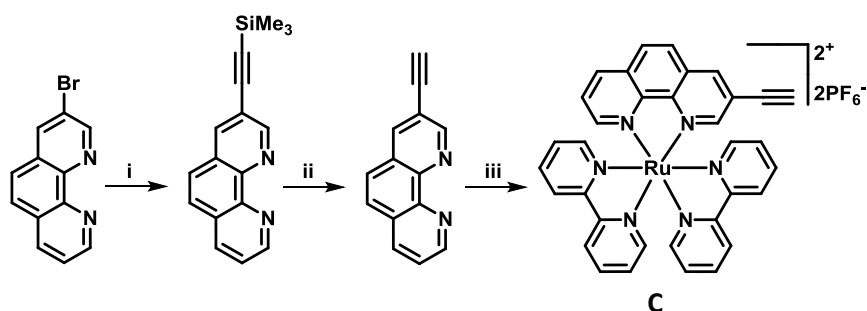
Scheme 2.11: Synthetic route to synthon **C**. i) THF: NEt$_3$ (2:1, *v:v*), Pd(PPh$_3$)$_2$Cl$_2$, CuI, TMSA, 70 °C, 24h, Ar; ii) MeOH: THF (2:1, *v:v*), K$_2$CO$_3$, rt, 6h; iii) MeOH, Ru(bipy)$_2$Cl$_2$.2H$_2$O, reflux, 6h

The synthesis of synthon **D** proved simple, as it was constructed from a previously synthesised compound in one step following a literature preparation[26] (scheme **2.12**). 4-bromo-2,6-disubstituted pyridine was reacted with sodium azide in DMF at 100 °C for two days in the presence of a phase transfer catalyst, tetrabutylammonium hydrogensulphate, to improve the solubility of the azide in the organic solvent. A good yield of 73 % was achieved, and purity was verified by ^{1}H NMR spectroscopy and ES$^+$MS.

4-bromo-2,6-disubstituted pyridine   **D**
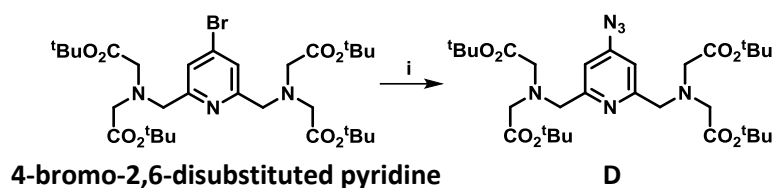
Scheme 2.12: Synthetic route to synthon **D**. i) DMF, NaN$_3$, ^{t}Bu$_4$NHSO$_4$, 100 °C, 48 h, Ar

With the successful syntheses of both synthons **C** and **D**, the copper-catalysed 'click' reaction between the two species was attempted using the method described in a literature preparation[26] (scheme **2.13**). The two synthons were dissolved in deoxygenated, anhydrous acetonitrile with copper iodide (10 mol %) as the source of Cu^I ions. Heating at reflux under an argon atmosphere for 24 hours proved effective, as a molecular ion peak at m/z = 626.2 was observed for the [M − 2PF$_6$]$^{2+}$ ion of the **Ru-Triazole-Dyad-Ester** species in an ES$^+$ mass spectrum. A low yield of the desired compound was eventually recovered from the reaction, however, as the main product was found to be the Glaser-coupled dimeric compound (figure **2.24**). A ^{1}H NMR spectrum of this side-product appeared similar to the ^{1}H NMR spectrum of synthon **C**; however, an ES$^+$ mass spectrum (appendix **2.13**) revealed an ion pattern for a species with a charge of 4$^+$, demonstrating that there are two ruthenium(II) bis(2,2'-bipyridine) centres in this compound.

C   **D**   **Ru-Triazole-Dyad-Ester**
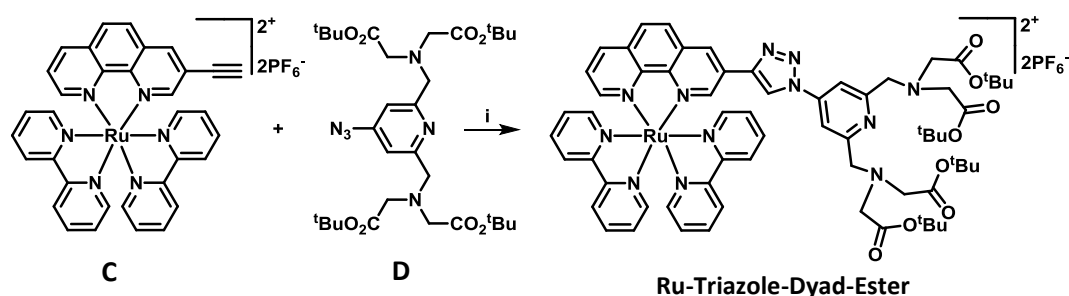
Scheme 2.13: Synthetic route to **Ru-Triazole-Dyad-Ester**.
i) MeCN, CuI, reflux, 24 h, Ar

In future preparations of the **Ru-Triazole-Dyad-Ester** species, using more equivalents of synthon **D** may help to avoid the unwanted Glaser coupling reaction. Unlike the usual conditions for a copper-catalysed 'click' reaction, careful removal of all traces of oxygen may also help to deter the competing reaction.
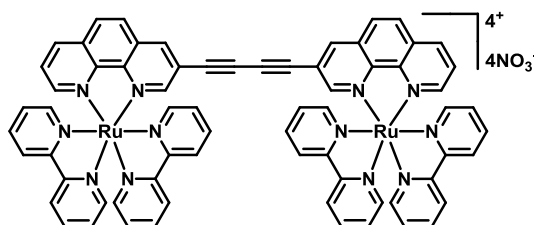
Figure 2.24: Unwanted Glaser-coupled side-product from the synthetic route to **Ru-Triazole-Dyad-Ester**

Characterisation of the **Ru-Triazole-Dyad-Ester** species was achieved with HRMS (appendix **2.14**) and ^{1}H NMR spectroscopy (figure **2.25**). The calculated and actual m/z values found for the $[M - 2PF_6]^{2+}$ ion agreed well (626.2393 and 626.2401, respectively) and the ^{1}H NMR spectrum (d_6-acetone, 400 MHz) confirmed the successful isolation of the pure product.
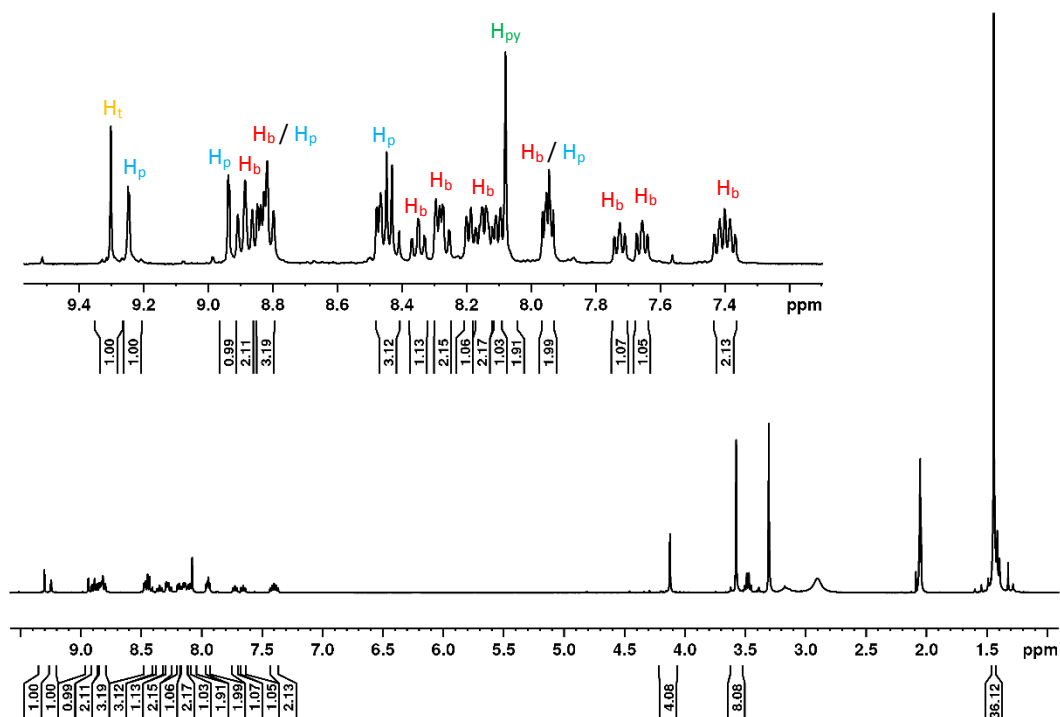
Figure 2.25: ^{1}H NMR spectrum (d_6-acetone, 400 MHz) of **Ru-Triazole-Dyad-Ester** at 298 K. (H_b = proton on bipyridine ligand, H_p = proton on phenanthroline ligand, H_{py} = proton on pyridine ring, H_t = proton on triazole ring)

The aromatic region integrates to the twenty-six protons expected. The deshielded singlet at δ = 9.29 ppm corresponds to the triazole ring proton, the singlet at δ = 8.09 ppm corresponds to the two pendant pyridine ring protons H^3 and H^5, and the remaining signals are from the three N^N ligands. In the aliphatic region, there are characteristic signals for the pendant metal chelate protons (three singlets at δ = 1.45 ppm, δ = 3.57 ppm and δ = 4.12 ppm, integrating to 36, 8 and 4 protons, respectively) and the remaining signals are for residual solvent.

Removal of the tertiary-butyl groups to reveal the **Ru-Triazole-Dyad-Acid** compound was achieved in an identical fashion to the alkyne analogue using TFA in dichloromethane (scheme **2.14**).

Ru-Triazole-Dyad-Ester   **Ru-Triazole-Dyad-Acid**
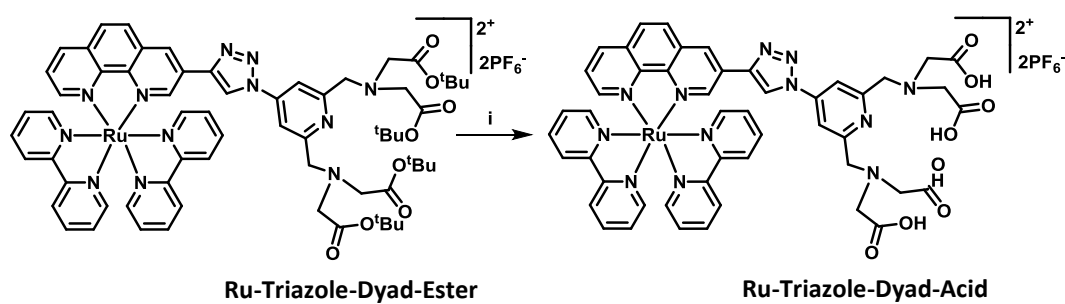
Scheme 2.14: Synthetic route to **Ru-Triazole-Dyad-Acid**. i) CH$_2$Cl$_2$, TFA, rt, 18h

The *m/z* value of the main signal found in the HRMS (appendix **2.15**) was 514.1141, which was a good match for the calculated *m/z* value for the $[M - 2PF_6]^{2+}$ ion, 514.1162. A ^{1}H NMR spectrum (figure **2.26**) in d_6-DMSO shows all of the expected peaks for the compound, but due to a combination of aggregation of the molecules in solution, and slow molecular tumbling, the signals appear broad, even with the sample heated to 373 K.

In the aromatic region there are a number of signals arising from protons on the three N^N ligands, plus the two equivalent H^3/H^5 protons on the pendant pyridine ring and the triazole proton. In the aliphatic region the residual DMSO peak manifests as a large peak at δ = 2.50 ppm, and there are two signals representing the chelate 'arms' of **Ru-Triazole-Dyad-Acid** at δ = 3.53 ppm and δ = 4.09 ppm. Unfortunately, water in the sample appears as a broad peak between δ = 3.40-3.90 ppm, which distorts the integration value for the signal at δ = 3.53 ppm to ten protons rather than the correct value of eight.
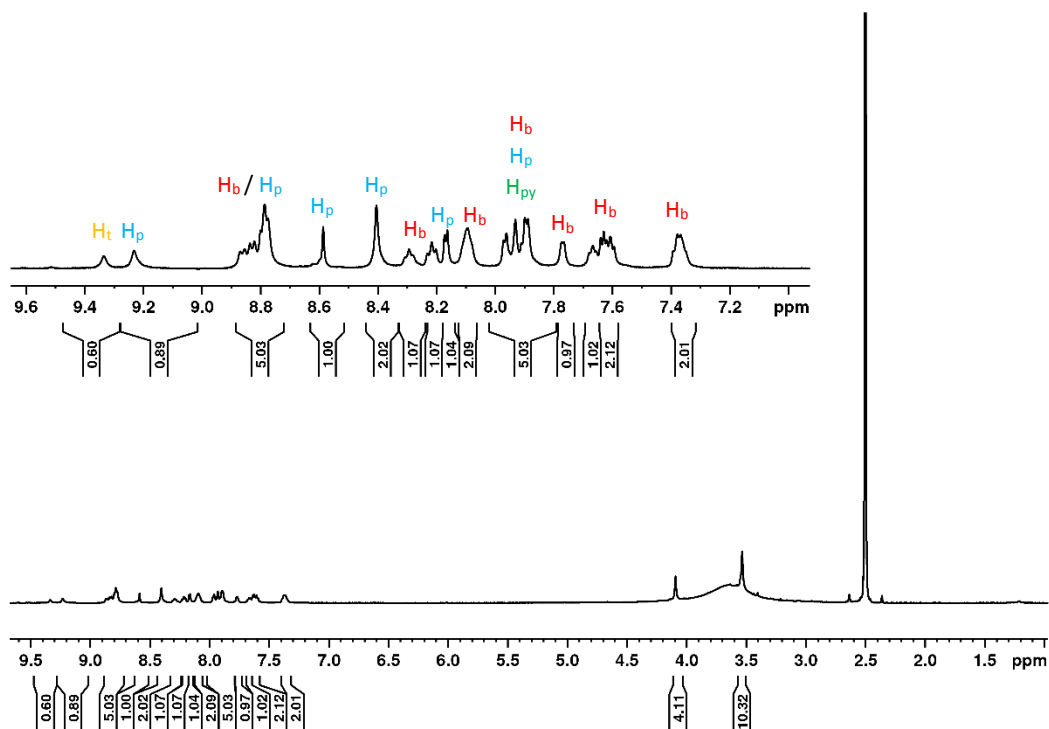
Figure 2.26: ^{1}H NMR spectrum (d_6-DMSO, 500 MHz) of **Ru-Triazole-Dyad-Acid** at 373 K.
(H_b = proton on bipyridine ligand, H_p = proton on phenanthroline ligand,
H_{py} = proton on pyridine ring, H_t = proton on triazole ring)

2.5.2) Photophysical Properties

UV/Vis absorption spectra were recorded in several solvents for both **Ru-Triazole-Dyad-Ester** and **Ru-Triazole-Dyad-Acid**, and an extinction coefficient was measured for **Ru-Triazole-Dyad-Acid** in water. Emission profiles and lifetimes of emission were recorded for both compounds (including as a frozen glass at 77 K), and the quantum yield of emission was measured for **Ru-Triazole-Dyad-Acid** against [Ru(bipy)$_3$]Cl$_2$.6H$_2$O in aerated water. Finally, excitation spectra were measured in each solvent.

2.5.2.1) UV/Vis Absorption

UV/Vis absorption profiles for **Ru-Triazole-Dyad-Ester** and **Ru-Triazole-Dyad-Acid** were recorded in several solvents (table **2.07**), but spectra in EtOH/MeOH (4:1, *v:v*) will be reviewed for comparison purposes (figure **2.27a**). Both spectra have a similar structure, with an intense peak centred around λ_{abs} = 285 nm for the $\pi{\rightarrow}\pi^*$ transition on the bipyridine ligand and a less intense shoulder peak at λ_{abs} = 310 nm for the $\pi{\rightarrow}\pi^*$ transition on the

phenanthroline ligand. Two less intense peaks overlapping in the region λ_{abs} = 375-550 nm are the ^{1}MLCT absorptions for the two different types of N^N ligand.
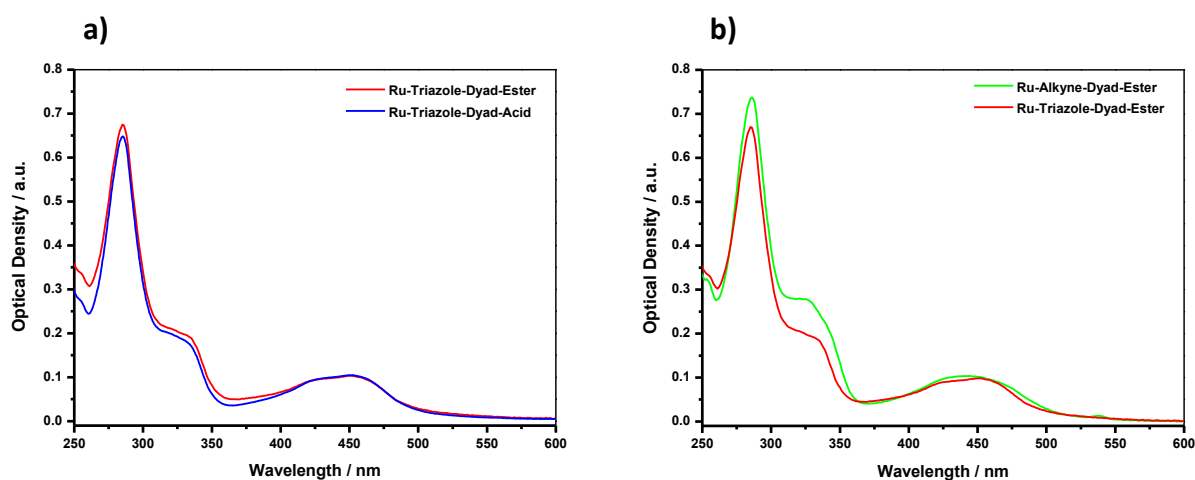
Figure 2.27: Normalised (at λ_{abs} = 450 nm) UV/Vis absorption spectra in EtOH/MeOH (4:1, *v:v*) at 298 K. a) **Ru-Triazole-Dyad-Ester** (red) and **Ru-Triazole-Dyad-Acid** (blue); b) **Ru-Alkyne-Dyad-Ester** (green) and **Ru-Triazole-Dyad-Ester** (red)

Table 2.07: UV/Vis absorption data for **Ru-Triazole-Dyad-Ester** and **Ru-Triazole-Dyad-Acid** at 298 K. [a]Data taken from ref. 10.

Compound	Solvent	λ_{abs} (nm) [ε (x10^4 M^{-1} cm^{-1})]
[a][Ru(bipy)$_2$(phenBr)]$^{2+}$	MeCN	272 [6.6], 286 [6.5], 448 [1.5]
Ru-Triazole-Dyad-Ester	CH$_2$Cl$_2$	287, 323 (sh), 434, 456 (sh)
	EtOH/MeOH (4:1, *v:v*)	285, 313 (sh), 433, 451 (sh)
	MeCN	284, 318 (sh), 437, 451 (sh)
	THF	287, 321 (sh), 442, 456 (sh)
	DMF	287, 322 (sh), 438, 456 (sh)
Ru-Triazole-Dyad-Acid	EtOH/MeOH (4:1, *v:v*)	285, 312 (sh), 428, 451 (sh)
	MeOH	285, 314 (sh), 431, 450 (sh)
	MeCN	285, 309 (sh), 427, 449 (sh)
	H$_2$O	282 [35], 309 (sh) [12], 428 [5.0], 451 (sh) [5.4]
	DMF	288, 315 (sh), 439, 454 (sh)

When comparing the spectrum for **Ru-Triazole-Dyad-Ester** to that of **Ru-Alkyne-Dyad-Ester**, it can be seen that changing the phenanthroline ligand substituent has negligible effect on the UV/Vis spectrum shape (figure **2.27b**). The π→π* transition on the phenanthroline ligand (λ_{abs} = 310 nm) is slightly more intense in the alkyne-containing species compared to

the triazole-containing one, and the ^{1}MLCT absorption bands (λ_{abs} = 375-550 nm) for the two different N^N ligands are easier to distinguish in the triazole-bridged analogue, although they still overlap with each other.

2.5.2.2) Emission

Luminescence profiles and the lifetime of the luminescence decay for **Ru-Triazole-Dyad-Ester** and **Ru-Triazole-Dyad-Acid** were recorded in several aerated solvents (table **2.08**), but profiles in EtOH/MeOH (4:1, *v:v*) at 298 K and 77 K (figure **2.28a**) will be reviewed for comparison purposes.

Upon excitation in to the ^{1}MLCT absorption band at λ_{ex} = 450 nm, both complexes produce broad and featureless emission profiles at 298 K indicating spin-forbidden ^{3}MLCT {Ru^{II}→π*$_{(N^N)}$} transitions. The emission is centred around λ_{em} = 620-625 nm, which is red-shifted when compared to the parent complex [Ru(bipy)$_2$(phen)]$^{2+}$ in acetonitrile (table **2.08**), as the increased conjugation along the phenanthroline ligand in the **Ru-Triazole-Dyad** compounds stabilise the LUMO energy level and lowers the emission energy.

The emission observed was temperature dependent, as the maximum energy blue-shifted from λ_{em} = 620-625 nm at 298 K to λ_{em} = 585 nm in a frozen glass at 77 K for both compounds. The luminescence profiles also transformed to include more vibrational structure, with two less intense shoulder peaks appearing on the low-energy side of the main 0-0 transition.

The effect of changing the phenanthroline ligand substitution from an alkyne linker to a triazole linker is more obvious in the luminescence profiles compared to the UV/Vis spectra (figure **2.28b**). At both 298 K and 77 K in EtOH/MeOH (4:1, *v:v*), the emission maximum for **Ru-Triazole-Dyad-Ester** is blue-shifted by ~25 nm compared to **Ru-Alkyne-Dyad-Ester**.

The luminescence decay lifetimes recorded for both **Ru-Triazole-Dyad-Ester** and **Ru-Triazole-Dyad-Acid** are similar in all solvents to those recorded for the alkyne-bridged analogues and are typical for [Ru(bipy)$_2$(N^N)]$^{2+}$ compounds. This similarity in luminescence intensity is also reflected in the luminescence quantum yield values (φ) for the two monosubstituted phenanthroline structures, which were calculated to be φ = 0.023 and φ = 0.020 for **Ru-Triazole-Dyad-Acid** and **Ru-Alkyne-Dyad-Acid**, respectively. This indicates that

the addition of a triazole-bridge does not have a significant quenching effect on the ruthenium-based luminescence.
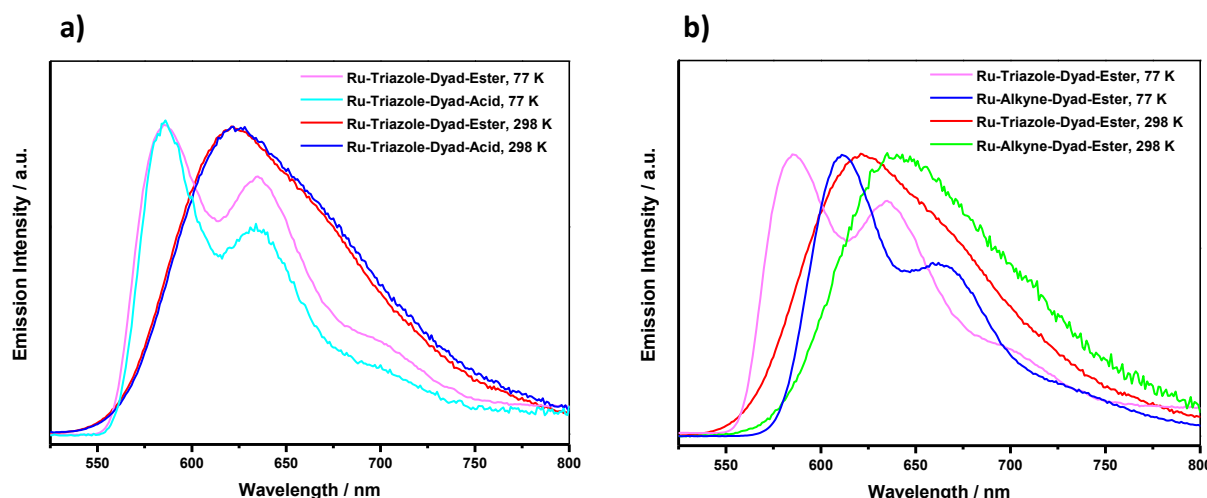
Figure 2.28: Normalised (at λ_{em} = max intensity), corrected emission spectra in aerated EtOH/MeOH (4:1, *v:v*) at 298 K and as a glass at 77 K. a) **Ru-Triazole-Dyad-Ester** (magenta, 77 K and red, 298 K, λ_{ex} = 450 nm for both) and **Ru-Triazole-Dyad-Acid** (cyan, 77 K and blue, 298 K, λ_{ex} = 450 nm for both); b) **Ru-Triazole-Dyad-Ester** (magenta, 77 K and red, 298 K, λ_{ex} = 450 nm for both) and **Ru-Alkyne-Dyad-Ester** (blue, 77 K and green, 298 K, λ_{ex} = 440 nm for both)

Table 2.08: Luminescence data for **Ru-Triazole-Dyad-Ester** and **Ru-Triazole-Dyad-Acid** in aerated solvents. [a]Data taken from ref. 17.

Compound	Solvent	$\lambda_{em}^{298\,K}$ (nm) [$\lambda_{em}^{77\,K}$ (nm)]	$\tau_1, \tau_2^{298\,K}$ (ns) [$\tau_1, \tau_2^{77\,K}$ (µs)]	A_1, A_2 (%)
[a]**[Ru(bipy)₂(phen)]²⁺**	MeCN	610	147	--
Ru-Triazole-Dyad-Ester	CH₂Cl₂	611	233	--
	EtOH/MeOH (4:1, *v:v*)	621 [585, 635, 681 (sh)]	229 [7.4]	--
	MeCN	624	201	--
	THF	638	203	--
	DMF	634	263	--
Ru-Triazole-Dyad-Acid	EtOH/MeOH (4:1, *v:v*)	623 [586, 634, 675 (sh)]	232 [7.2, 0.95]	-- [93, 7]
	MeOH	627	216, 35	95, 5
	MeCN	626	170	--
	H₂O	631	543	--
	DMF	636	255, 32	96, 4

Excitation spectra recorded in aerated EtOH/MeOH (4:1, *v:v*) at 298 K for both **Ru-Triazole-Dyad-Ester** (λ_{em} = 620 nm) and **Ru-Triazole-Dyad-Acid** (λ_{em} = 610 nm) were overlaid with UV/Vis absorption spectra recorded in the same solvent (figure **2.29**). A good match between the spectra can be seen, which is a clear indication that the emission observed for both complexes occurs as a result of absorption in to the ^{1}MLCT band.
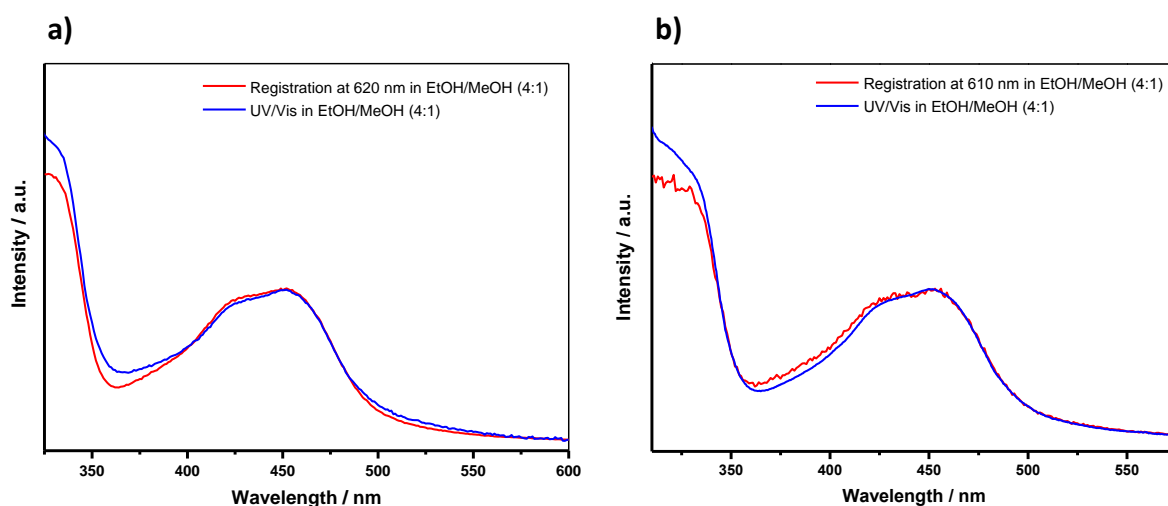
Figure 2.29: Normalised (at λ = 450 nm) spectra in aerated EtOH/MeOH (4:1, *v:v*) at 298 K. Corrected excitation spectra (red) and UV/Vis spectra (blue) of a) **Ru-Triazole-Dyad-Ester** (λ_{em} = 620 nm) and b) **Ru-Triazole-Dyad-Acid** (λ_{em} = 610 nm)

2.6) Summary

The scaffolds for bis(2,2-bipyridine)ruthenium(II)-based analogues of previously studied iridium-based dinuclear and trinuclear acetylene-bridged complexes have been introduced, and their syntheses detailed. The key step in the overall reaction scheme was a Sonogashira reaction between a ruthenium(II) bis(2,2-bipyridine)-based compound with a pendant bromine atom, and a tertiary-butyl protected polyaminocarboxylate chelate bearing a pendant terminal alkyne group, which was achieved with moderate success (45-50 %). Full characterisation of both the tertiary-butyl protected entity, and the resultant carboxylic acid compound upon removal of the tertiary-butyl groups, was achieved with ^{1}H NMR spectroscopy and high-resolution mass spectrometry for both the monosubstituted and disubstituted phenanthroline scaffolds.

A larger 'metallostar' species, with the potential to chelate six MRI-active metal centres for each luminescent ruthenium centre, based on alkyne spacers between peripheral sites and the core [Ru(phen)$_3$]$^{2+}$ unit, was also synthesised in a low yield (15 %). In this case, successful synthesis was achieved by subjecting the starting ruthenium centre to six independent Sonogashira coupling reactions. The **Ru-Alkyne-Metallostar-Ester** species showed good solubility in a wide range of solvents, however, upon removing the tertiary-butyl protecting groups, the resulting compound containing twenty-four carboxylic acid groups on the exterior surface was insoluble in all solvents except aqueous base. Full characterisation of the ester-protected and carboxylic acid complexes was achieved with ^{1}H and ^{13}C NMR spectroscopy and ES$^+$MS.

Finally, the probe design was modified to include a triazole linking unit in place of the acetylene bridge to assess the linker's importance in improving relaxivity values. The monosubstituted phenanthroline scaffold was successfully synthesised by taking advantage of the robust alkyne/azide, copper-catalysed 'click' reaction, however, a competing Glaser coupling between two alkyne substituents had a detrimental effect on the overall yield, reducing it to 20 %. Full characterisation of both the ester-protected compound and the carboxylic acid chelate was achieved through ^{1}H NMR spectroscopy and high-resolution mass spectrometry.

UV/Vis absorption spectra for the series of scaffolds showed typical bands for [Ru(N^N)$_3$]$^{2+}$ compounds. Intense absorptions in the UV region (λ_{abs} < 400 nm) were ascribed

to the $\pi \rightarrow \pi^*$ transitions centred on the two different N^N ligands, and weaker bands between λ_{abs} = 400-550 nm characterised the ^{1}MLCT absorptions. Increasing the conjugation along the compound's backbone on progressing from a monosubstituted to a disubstituted phenanthroline ligand, and then to a 'metallostar' species, was clearly seen in the spectra as both the $\pi \rightarrow \pi^*$ transition on the phenanthroline ligand and the ^{1}MLCT absorption red-shifted. Changing the phenanthroline substitution from an alkyne-bridged ligand to a triazole-bridged ligand had negligible effect on the UV/Vis absorption properties of the monosubstituted phenanthroline scaffold.

Increasing the number of pendant metal chelating centres surrounding the luminescent Ru^{II} core, at which MRI-active metal ions could bind, was deleterious to the luminescent properties of the scaffolds, however. Upon progressing from one pendant 'arm' to two and then (in the 'metallostar') six pendant alkyne 'arms', the quantum yield of luminescence compared to [Ru(bipy)$_3$]Cl$_2$.6H$_2$O in aerated water decreased from ϕ = 0.020 and ϕ = 0.023, to ϕ = 0.006 and then to ϕ = 0.003. As the compounds need to display bright luminescence in their capacity as probes for optical microscopy, this is obviously a drawback; however, a solution to this problem may be to increase the concentration of the probes when utilising their luminescence for imaging. As the difference between the two working concentrations of current luminescent probes and MRI contrast agents is large, increasing the concentration needed for the optical microscopy aspect of the dual-modal probe may help to overcome this disparity.

Excitation spectra overlaid with UV/Vis absorption spectra for all of the compounds have the same shape, as the fluorescence intensity is proportional to the absorption. This gives a good indication that the complexes are pure and do not form aggregates in the ground state. This is not the case for **Ru-Alkyne-Metallostar-Acid**, however, whose spectra do not match due to the limited solubility of the compound in all solvents which may cause aggregation in solution.

2.7) Future Work

To continue this work further, it would be interesting to extend the triazole-bridged scaffold to include a disubstituted (potentially **RuGd$_2$** trinuclear) and a 'metallostar' (potentially **RuGd$_6$**) species, and to change the luminescent metal centre to Ir^{III}. This may help to overcome the solubility issues that were found with the **Ru-Alkyne-Metallostar-Acid** compound and the original **IrGd$_2$** (**27**) compound, as the triazole-bridged analogue will have more sites available for protonation.

2.8) References

1   E. Baggaley, D.-K. Cao, D. Sykes, S. W. Botchway, J. A. Weinstein and M. D. Ward, *Chem. Eur. J.*, 2014, **20**, 8898–8903.

2   D. Sykes, A. J. Cankut, N. M. Ali, A. Stephenson, S. J. P. Spall, S. C. Parker, J. A. Weinstein and M. D. Ward, *Dalton Trans.*, 2014, **43**, 6414–6428.

3   J. G. Penfield and R. F. Reilly, *Nat. Clin. Pract. Nephrol.*, 2007, **3**, 654–668.

4   A. Jana, E. Baggaley, A. Amoroso and M. D. Ward, *Chem. Commun.*, 2015, **51**, 8833–8836.

5   E. Debroye and T. N. Parac-Vogt, *Chem. Soc. Rev.*, 2014, **43**, 8178–8192.

6   A. Jana, B. J. Crowston, J. R. Shewring, L. K. McKenzie, H. E. Bryant, S. W. Botchway, A. D. Ward, A. J. Amoroso, E. Baggaley and M. D. Ward, *Inorg. Chem.*, 2016, **55**, 5623–5633.

7   K. Sonogashira, Y. Tohda and N. Hagihara, *Tetrahedron Lett.*, 1975, **16**, 4467–4470.

8   A. J. Pallenberg, K. S. Koenig and D. M. Barnhart, *Inorg. Chem.*, 1995, **34**, 2833–2840.

9   J. Suffert and R. Ziessel, *Tetrahedron Lett.*, 1991, **32**, 757–760.

10   D. Tzalis and Y. Tor, *J. Am. Chem. Soc.*, 1997, **119**, 852–853.

11   D. Tzalis, Y. Tor, F. Salvatorre and S. Jay Siegel, *Tetrahedron Lett.*, 1995, **36**, 3489–3490.

12   M. Karnahl, S. Krieck, H. Görls, S. Tschierlei, M. Schmitt, J. Popp, D. Chartrand, G. S. Hanan, R. Groarke, J. G. Vos and S. Rau, *Eur. J. Inorg. Chem.*, 2009, **2009**, 4962–4971.

13   B. P. Sullivan, D. J. Salmon and T. J. Meyer, *Inorg. Chem.*, 1978, **17**, 3334–3341.

14   H. Li, J. Tatlock, A. Linton, J. Gonzalez, T. Jewell, L. Patel, S. Ludlum, M. Drowns, S. V Rahavendran, H. Skor, R. Hunter, S. T. Shi, K. J. Herlihy, H. Parge, M. Hickey, X. Yu, F. Chau, J. Nonomiya and C. Lewis, *J. Med. Chem*, 2009, **52**, 1255–1258.

15   J.-L. Chen, X. Wang, F. Yang, C. Cao, G. Otting and X.-C. Su, *Angew. Chem. Int. Ed.*, 2016, **55**, 13744–13748.

16   H. Takalo, P. Pasanen, J. Kankare, K. Undheim, G. Wittman, L. Gera, M. Bartók, I. Pelczer and G. Dombi, *Acta Chem. Scand.*, 1988, 42b, 373–377.

17   E. C. Glazer, D. Magde and Y. Tor, *J. Am. Chem. Soc.*, 2005, **127**, 4190–4192.

18   K. Nakamaru, *Bull. Chem. Soc. Jpn.*, 1982, **55**, 2697–2705.

19   J. B. Livramento, E. Tóth, A. Sour, A. Borel, A. E. Merbach and R. Ruloff, *Angew. Chem. Int. Ed.*, 2005, **44**, 1480–1484.

20   L. Moriggi, A. Aebischer, C. Cannizzo, A. Sour, A. Borel, J.-C. G. Bünzli and L. Helm, *Dalton Trans.*, 2009, 2088–2095.

21   G. Dehaen, S. V. Eliseeva, P. Verwilst, S. Laurent, L. Vander Elst, R. N. Muller, W. De Borggraeve, K. Binnemans and T. N. Parac-Vogt, *Inorg. Chem.*, 2012, **51**, 8775–8783.

22   V. V. Rostovtsev, L. G. Green, V. V. Fokin and K. B. Sharpless, *Angew. Chem. Int. Ed.*, 2002, **41**, 2596–2599.

23   C. W. Tornøe, C. Christensen and M. Meldal, *J. Org. Chem.*, 2002, **67**, 3057–3064.

24   Y. Fan, L.-Y. Zhang, F.-R. Dai, L.-X. Shi and Z.-N. Chen, *Inorg. Chem.*, 2008, **47**, 2811–2819.

25   J. Ponce, J. Aragó, I. Vayá, J. G. Magenti, S. Tatay, E. Ortí and E. Coronado, *Eur. J. Inorg. Chem.*, 2016, **2016**, 1851–1859.

26   C. S. Bonnet, F. Buron, F. Caillé, C. M. Shade, B. Drahoš, L. Pellegatti, J. Zhang, S. Villette, L. Helm, C. Pichon, F. Suzenet, S. Petoud and É. Tóth, *Chem. Eur. J.*, 2012, **18**, 1419–1431.

2.9) Appendices
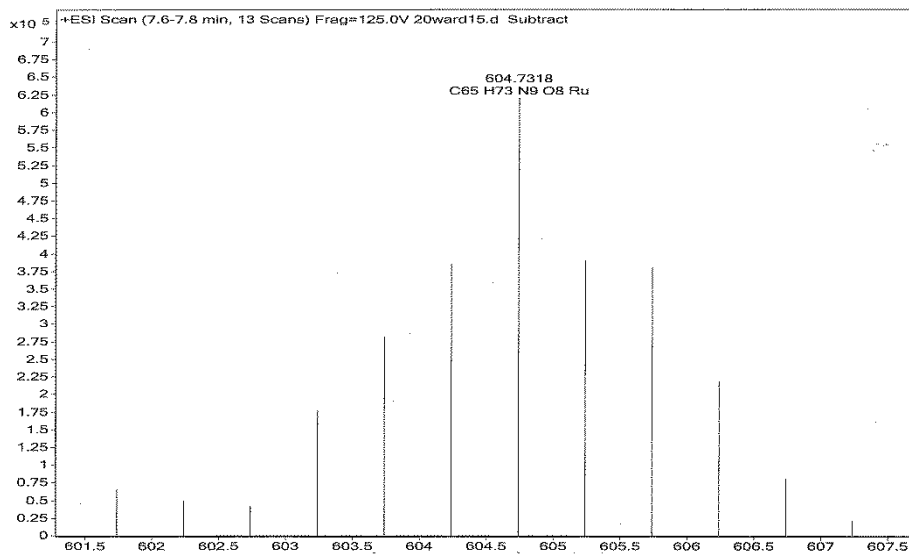
Appendix 2.01: High-resolution mass spectrum of **Ru-Alkyne-Dyad-Ester**.
Calculated for $[C_{65}H_{73}N_9O_8Ru]^{2+}$, 604.7316.
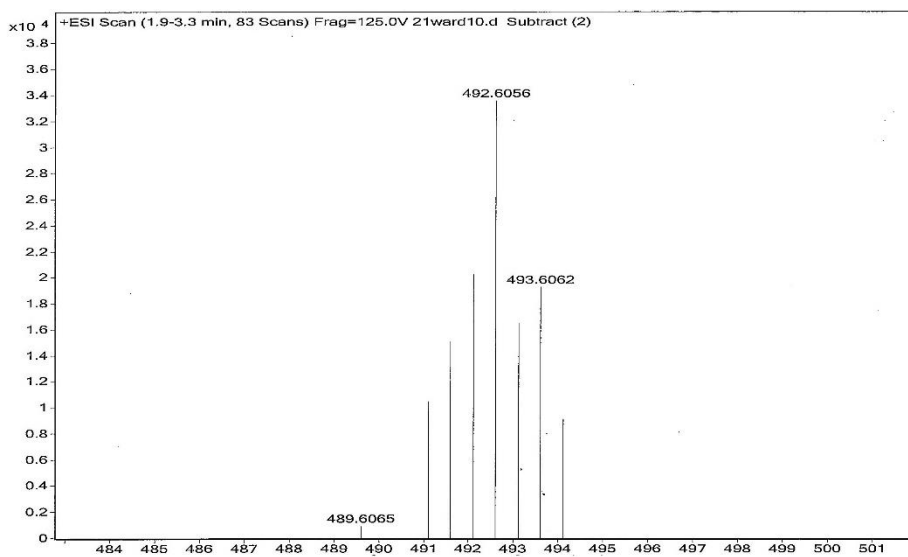
Appendix 2.02: High-resolution mass spectrum of **Ru-Alkyne-Dyad-Acid**.
Calculated for $[C_{49}H_{41}N_9O_8Ru]^{2+}$, 492.6055.
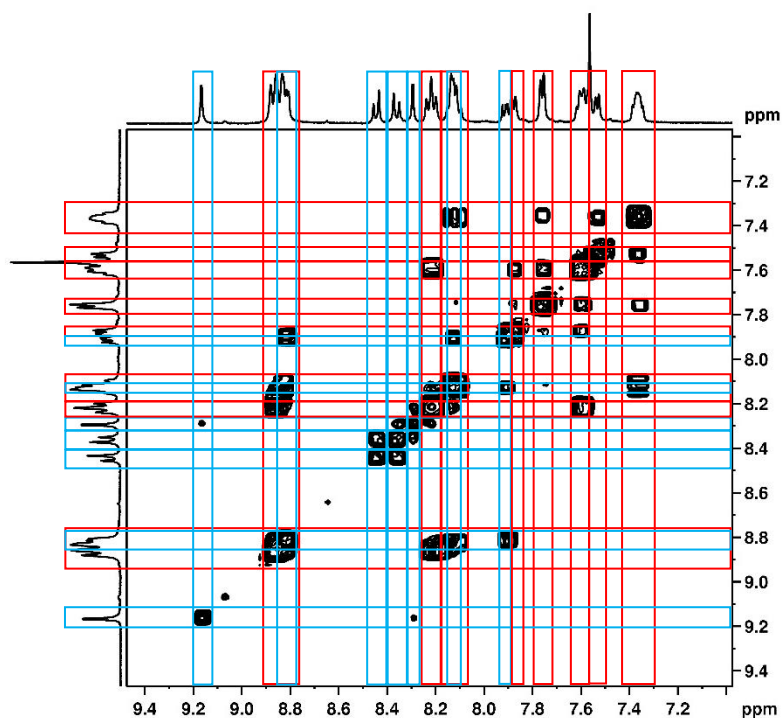
Appendix 2.03: The aromatic region of an annotated ^{1}H-^{1}H correlation NMR spectrum (500 MHz, d_6-DMSO) for **Ru-Alkyne-Dyad-Acid** at 303 K. (Red lines = protons on bipyridine ligand, blue lines = protons on phenanthroline ligand)
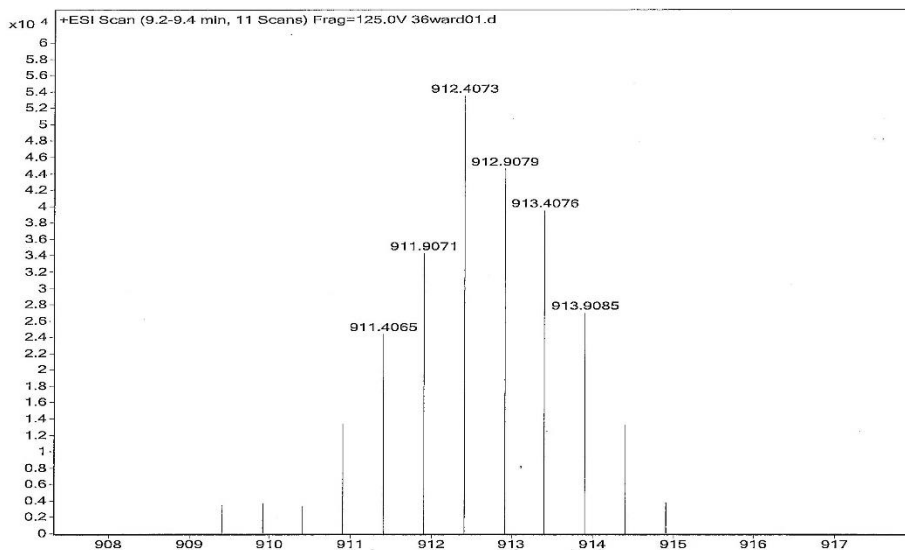
Appendix 2.04: High-resolution mass spectrum of **Ru-Alkyne-Triad-Ester**. Calculated for $[C_{98}H_{122}N_{12}O_{16}Ru]^{2+}$, 912.4067.
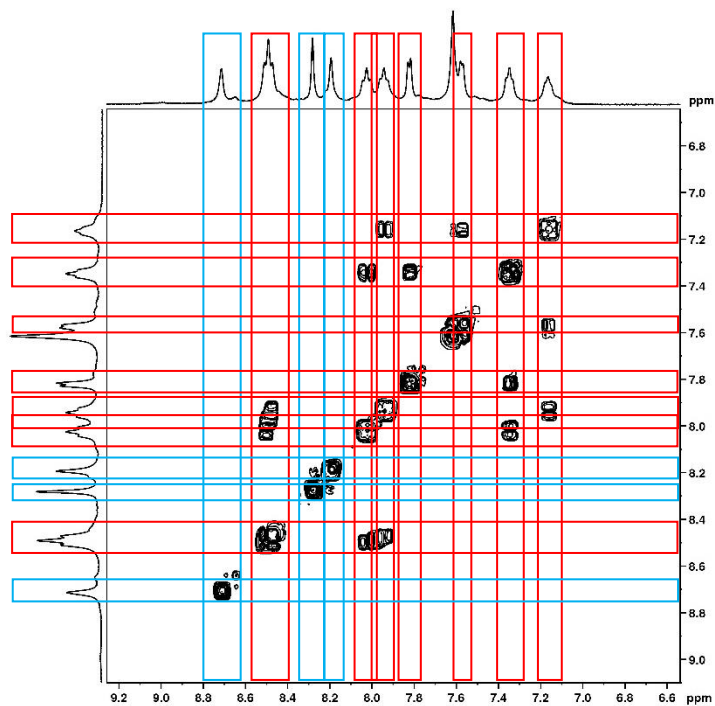
Appendix 2.05: The aromatic region of an annotated ^{1}H-^{1}H correlation NMR spectrum (400 MHz, D$_2$O) for **Ru-Alkyne-Triad-Acid** at 298 K. (Red lines = protons on bipyridine ligand, blue lines = protons on phenanthroline ligand)
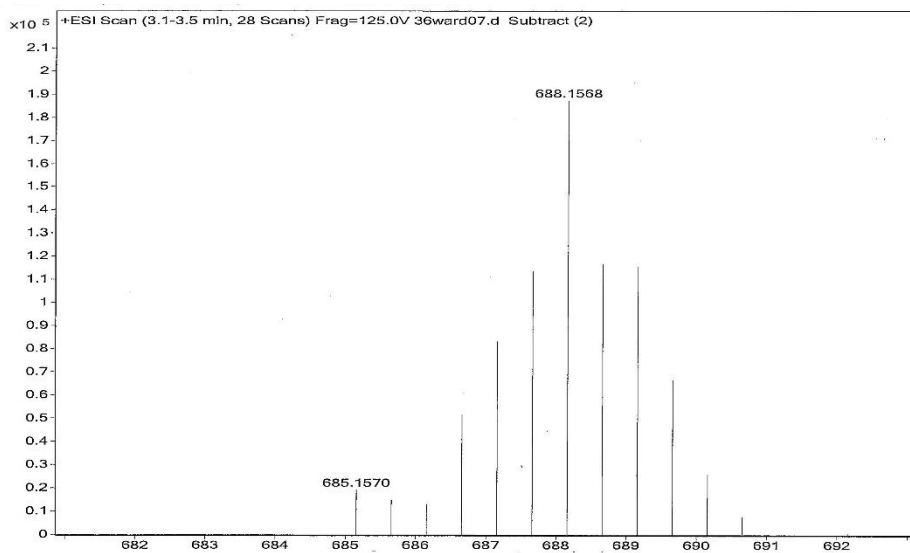
Appendix 2.06: High-resolution mass spectrum of **Ru-Alkyne-Triad-Acid**. Calculated for [C$_{66}$H$_{58}$N$_{12}$O$_{16}$Ru]$^{2+}$, 688.1563.
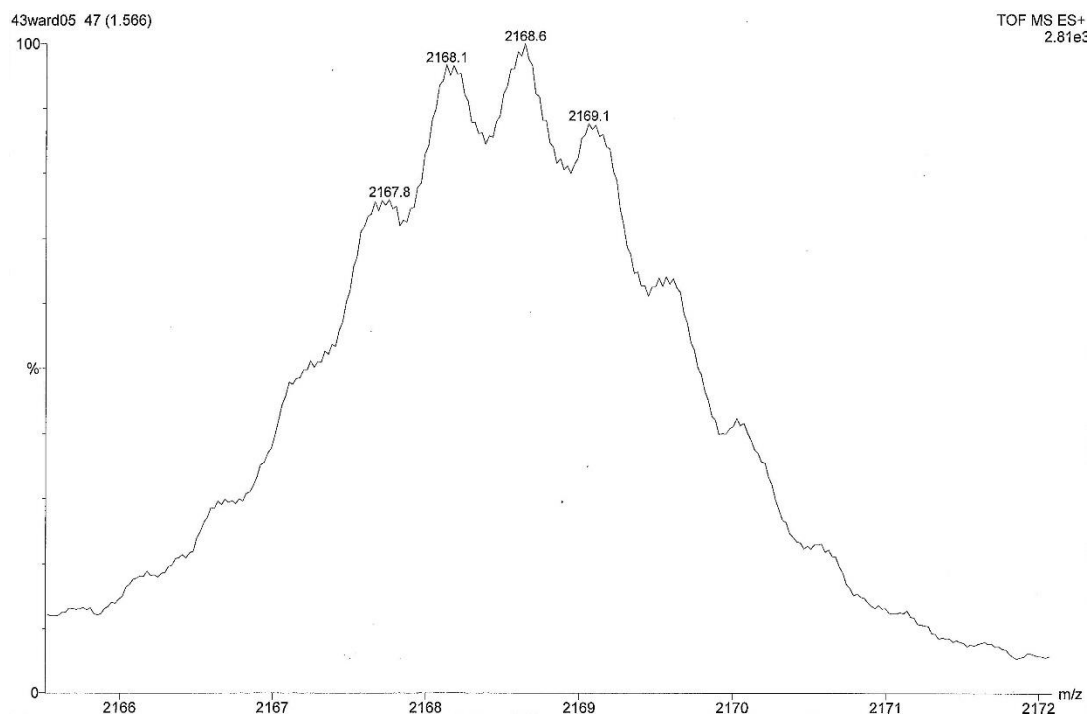
Appendix 2.07: Mass spectrum of **Ru-Alkyne-Metallostar-Ester**

Appendix 2.08: Table of NMR assignments (500 MHz, 1,1,2,2-tetrachloroethane-d_2) for **Ru-Alkyne-Metallostar-Ester**
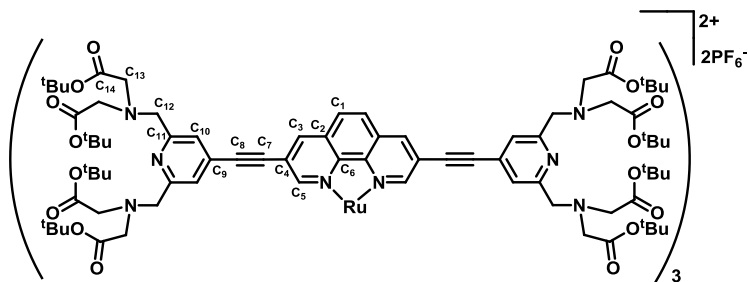
Carbon Number	Proton Shift (ppm)	Carbon Shift (ppm)
C1	8.01	153.6
C2		145.9
C3	8.83	141.0
C4		166.7
C5	8.34	128.7
C6		131.0
C7		86.6
C8		96.0
C9		170.3
C10	7.55	123.1
C11		159.4
C12	3.92	59.4
C13	3.41	55.6
C14		207.8
C(C$\underline{\text{H}}_3$)$_3$	1.41	28.2
$\underline{\text{C}}$(CH$_3$)$_3$	1.41	81.2
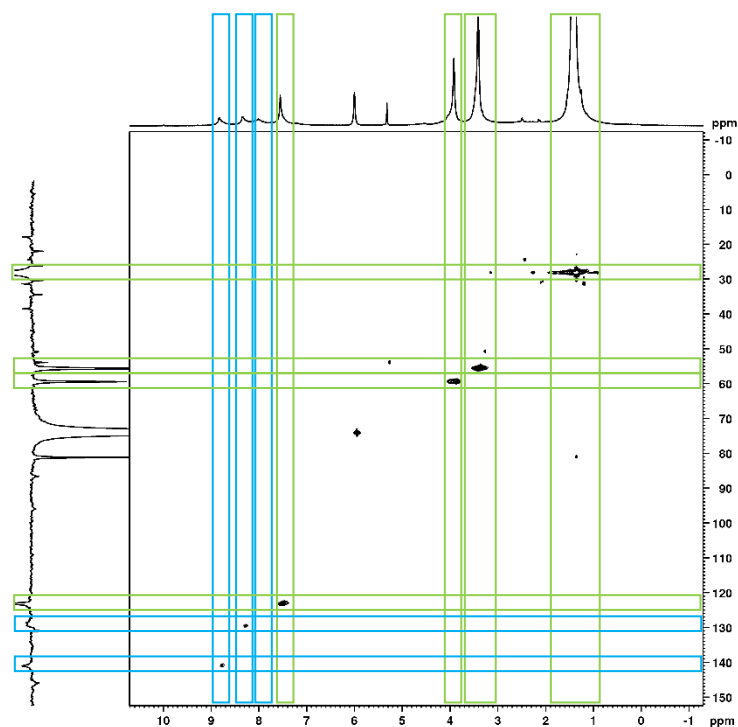
Appendix 2.09: ^{1}H-^{13}C correlation (HSQC) NMR spectrum (500 MHz, 1,1,2,2-tetrachloroethane-d_2) of **Ru-Alkyne-Metallostar-Ester** at 298 K. (Green lines = correlation on pyridine chelate, blue lines = correlation on phenanthroline ligand)
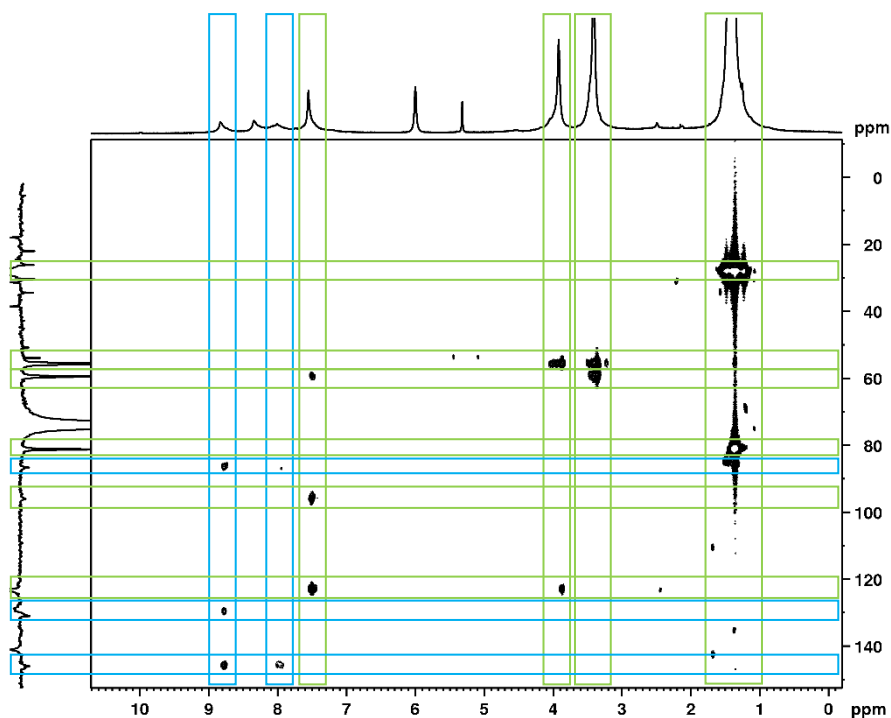
Appendix 2.10: ^{1}H-^{13}C correlation (HMBC) NMR spectrum (500 MHz, 1,1,2,2-tetrachloroethane-d_2) of **Ru-Alkyne-Metallostar-Ester** at 298 K. (Green lines = correlation on pyridine chelate, blue lines = correlation on phenanthroline ligand)

Appendix 2.11: Table of NMR assignments (500 MHz, D$_2$O, pD 4.38) for
Ru-Alkyne-Metallostar-Acid
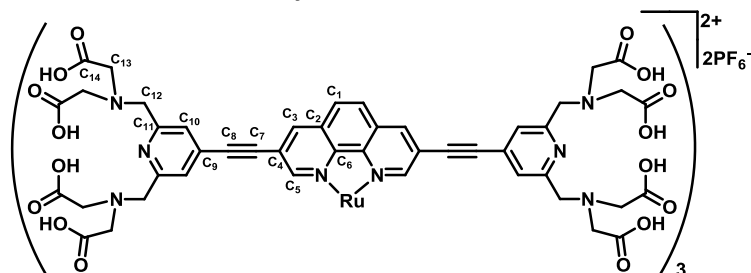
Carbon Number	Proton Shift (ppm)	Carbon Shift (ppm)
C1	8.06-8.45	154.4
C2		146.8
C3	8.81	140.9
C4		163.3
C5	8.06-8.45	129.2
C6		132.7
C7		90.1
C8		92.3
C9		170.1
C10	7.54	126.8
C11		150.5
C12	4.57	58.1
C13	3.82	57.2
C14		208.3
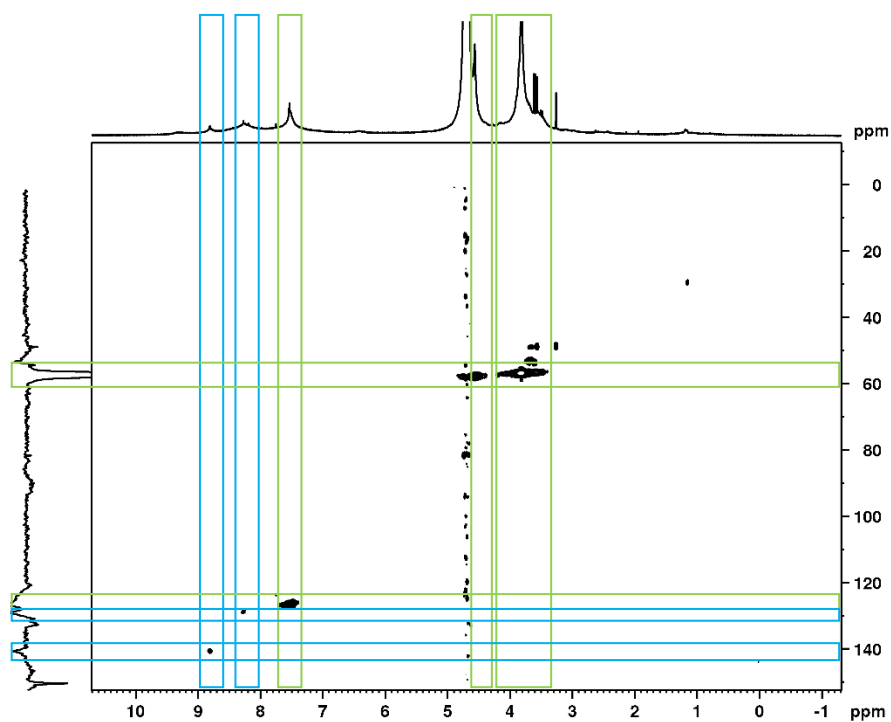
Appendix 2.12: ^{1}H-^{13}C correlation (HSQC) NMR spectrum (500 MHz, D$_2$O, pD 4.38) of **Ru-Alkyne-Metallostar-Acid** at 298 K. (Green lines = correlation on pyridine chelate, blue lines = correlation on phenanthroline ligand)
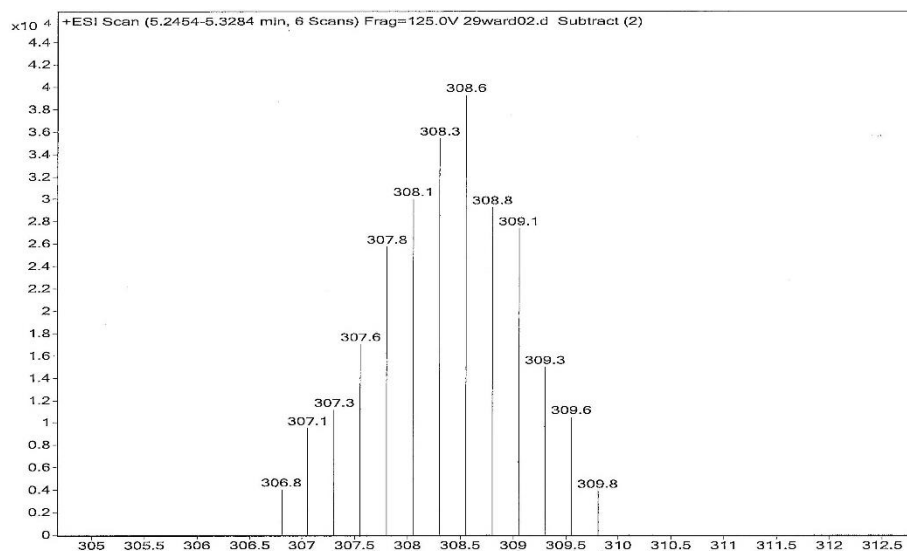
Appendix 2.13: Mass spectrum of the Glaser-coupled product from the synthetic route to **Ru-Triazole-Dyad-Ester**
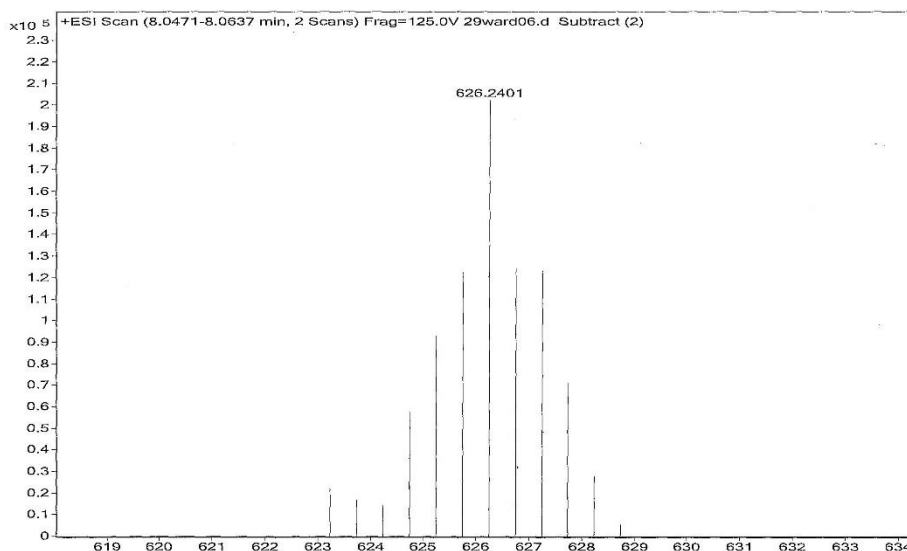
Appendix 2.14: High-resolution mass spectrum of **Ru-Triazole-Dyad-Ester**. Calculated for $[C_{65}H_{74}N_{12}O_8{}^{102}Ru]^{2+}$, 626.2393.
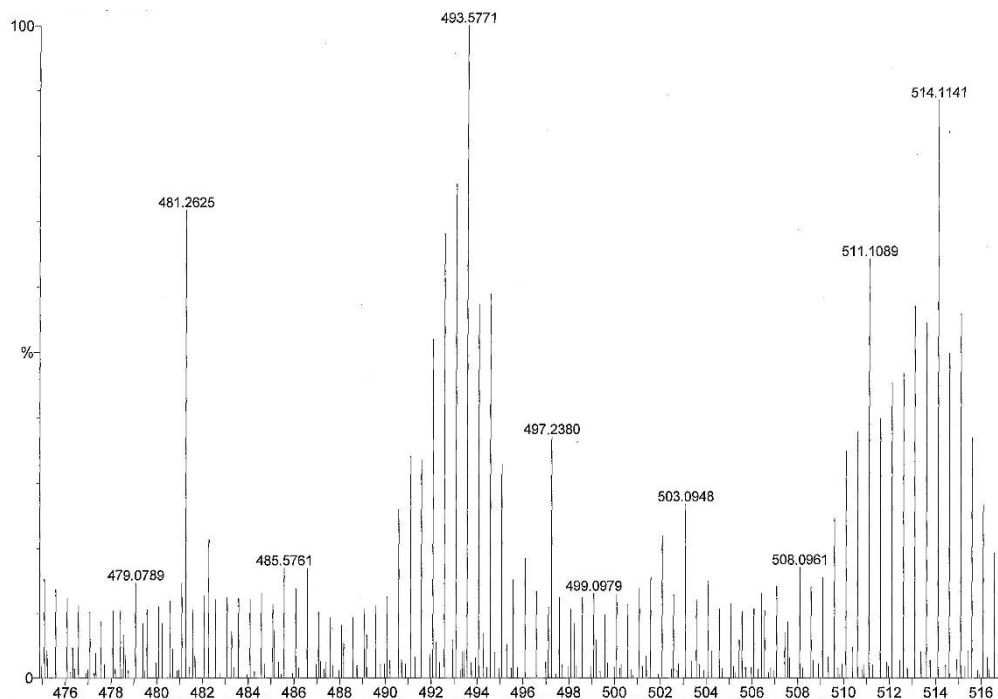
Appendix 2.15: High-resolution mass spectrum of **Ru-Triazole-Dyad-Acid**. Calculated for $[C_{49}H_{42}N_{12}O_8Ru]^{2+}$, 514.1162.

Chapter 3

Ru^{II}-Gd^{III} Complexes as Dual-Modal Optical/MRI Contrast Agents

3.1) Previous Work in the Ward Group

As was previously discussed in this thesis, the dinuclear **IrGd** (**26**) and trinuclear **IrGd₂** (**27**) acetylene-bridged complexes, previously published by the Ward group, demonstrated excellent potential as prototypical dual-modal optical/MR imaging agents (section **2.1**). Unusually high relaxivity values for the Gd^{III} centres of $r_1 = 14.0$ mM^{-1} s^{-1} and $r_1 = 12.6$ mM^{-1} s^{-1} (H$_2$O/DMSO (95:5, *v:v*), 20 MHz, 37 °C) were measured for **IrGd** and **IrGd₂**, respectively, which are comparable values to those observed for other d-f hybrids that contain three or four Gd^{III} centres[1].

In further studies, the suitability of the two complexes as probes for optical microscopy was assessed. Cellular imaging studies and toxicity assays were undertaken with the dinuclear **IrGd** complex in both MCF-7 and HeLa cell lines[2,3]. The staining detected in both cases was similar, with emission from the photoluminescent Ir^{III} centre observable in the cell cytosol, with additional punctate staining. Co-incubation experiments with the commercial nuclear stain DAPI in MCF-7 cells, and the commercial lysosomal stain Lysotracker® Red in HeLa cells (figure **3.01**), revealed that the complex does not cross the cell membrane, but does localise in the lysosomes, albeit not exclusively. Manders coefficients (obtained using the Coloc2 plugin in *ImageJ*) were used to quantify the extent of the co-localisation between **IrGd** and Lysotracker® Red, with convincing values of M1/M2 = 0.91/0.87 being observed. Cell viability after staining with **IrGd** at concentrations between 25-100 μM, and for incubation times between 4-24h, was tested by MTT toxicity assay in both cell lines. In both cases, it was observed that as the incubation time and the **IrGd** concentration increased, the cell viability decreased; however, at the optimum imaging conditions (50 μM, 4h) the cell survival fraction was similar to the control experiments in 0.5-1 % DMSO (0.8).

In contrast, the trinuclear **IrGd₂** complex, when incubated with HeLa cells, performed poorly as a luminescent imaging agent when compared to its dinuclear **IrGd** counterpart[3]. A similar staining pattern to the dinuclear probe was observed; however, due to the trinuclear probe's poor solubility in water, larger size and difference in charge (anionic compared to the neutral **IrGd**), the cellular uptake was found to be poorer for **IrGd₂**. This observation was reflected in the MTT toxicity data for this complex: surprisingly, at high concentrations and incubation times (100 μM, 18h), the survival fractions for the HeLa cells were comparable to

those observed for the 1 % DMSO control experiments. In view of the lower cell viabilities measured for the dinuclear **IrGd** complex under these conditions, the measured survival fractions were unusually high for **IrGd$_2$** considering the complex has an additional toxic Gd^{III} metal centre. This suggests that poor internalisation of **IrGd$_2$** into the cells is the cause of the low cytotoxicity measured, rather than the trinuclear complex being uncharacteristically much less toxic.
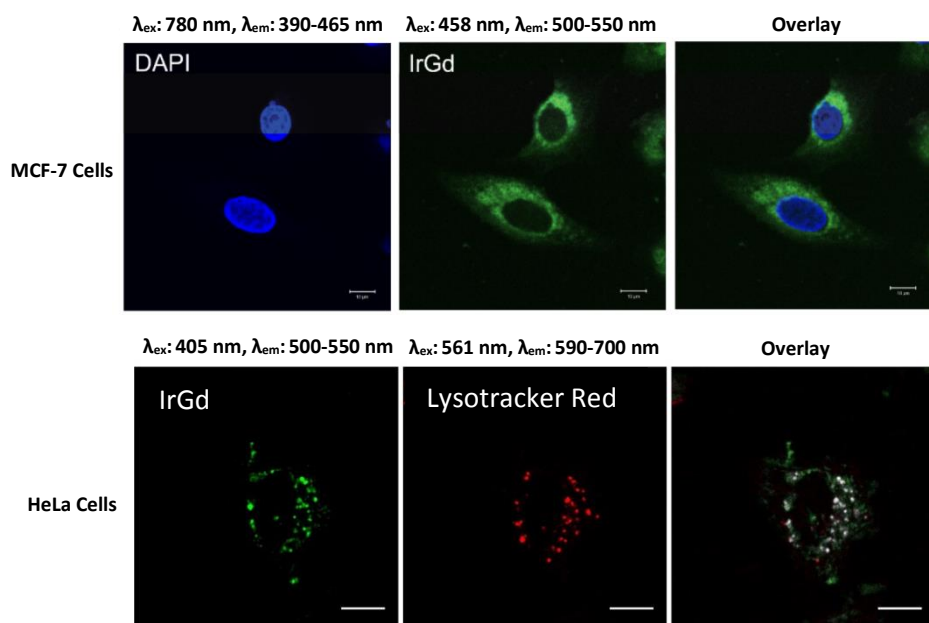
Figure 3.01: Steady-state confocal images of **IrGd** and commercial stains DAPI and Lysotracker® Red. Top) MCF-7 cells stained with DAPI (λ_{ex} = 780 nm, λ_{em} = 390-465 nm) and **IrGd** (50 µM, 4h, λ_{ex} = 458 nm, λ_{em} = 500-550 nm). Scale bar = 10 µm.
(Reproduced with permission from ref. 2. Copyright (2015) Royal Society of Chemistry).
Bottom) Live HeLa cells stained with **IrGd** (50 µM, 18h, λ_{ex} = 405 nm, λ_{em} = 500-550 nm) and Lysotracker® Red (λ_{ex} = 561 nm, λ_{em} = 590-700 nm) Scale bar = 10 µm.
(Reproduced with permission from ref. 3. Copyright (2016) American Chemical Society).

As **IrGd** demonstrated high solubility in aqueous media and low toxicity in two different cell lines, the probe was considered an ideal candidate for additional cellular imaging studies. The probe has a triplet-based luminescent lifetime in the order of hundreds of nanoseconds, which is sensitive to quenching by molecular oxygen, and so further luminescence-based oxygen sensing experiments were conducted in the HeLa cell line. Two-photon-phosphorescence lifetime imaging (2P-PLIM) of **IrGd** under increasing concentrations of oxygen in oxygen/nitrogen mixtures demonstrated that the Ir^{III}-based emission lifetime was sensitive to changes in the oxygen partial pressure, even when fixed inside a HeLa cell

(figure **3.02**). Lifetime maps with a varying colour scale from orange to blue in accordance with the increase of the average luminescence lifetime measured (0-1000 ns) were used to depict this sensitivity to oxygen. A clear change in lifetime plot colour from primarily orange (low lifetime value, 100 % oxygen) to primarily blue (high lifetime value, 0 % oxygen) can be observed with a decrease in oxygen concentration. This increase in luminescence lifetime compared to decrease in oxygen concentration is also depicted as a histogram, demonstrating a change in the average Ir^{III}-based lifetime from τ = 435 ns (100 % oxygen) to τ = 644 ns (0 % oxygen). Although this difference in emission lifetime is modest between the two extremes of oxygen concentration, there is scope to make further modifications to the Ir^{III} chromophore's structure in the future to improve upon this sensitivity to oxygen.
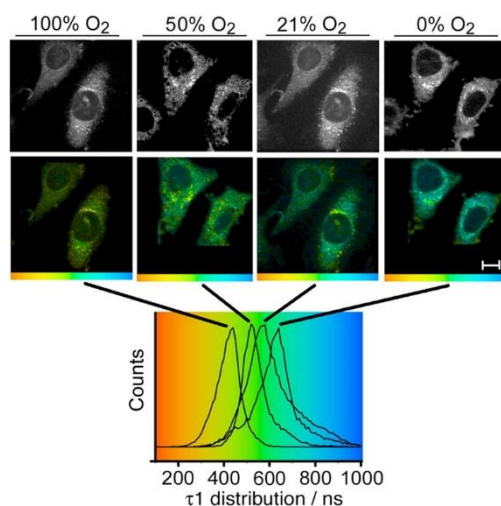
Figure 3.02: Two-photon PLIM imaging of fixed HeLa cells stained with **IrGd** (50 µM, 18h, λ_{ex} = 760 nm) under varying concentrations of oxygen. Scale bar = 10 µm. (Reproduced with permission from ref. 3. Copyright (2016) American Chemical Society)

These results illustrate the excellent promise that the dinuclear **IrGd** complex shows as a potential dual-modal optical/MR imaging agent. It exhibited a high relaxivity value compared to other mononuclear Gd^{III} complexes, and localised lysosomal staining was confirmed in two different cell lines, coupled with high cell viabilities (> 80 %). The emission from the Ir^{III}-based centre was also shown to be sensitive to oxygen concentration, further establishing the complex as a potential probe for hypoxic conditions. The trinuclear **IrGd₂** counterpart, however, exhibited flaws in its abilities as both an MRI contrast agent and as a luminescent imaging agent due to its poor solubility in aqueous media.

This chapter will present the synthesis of *water-soluble* ruthenium(II) bis(2,2'-bipyridine)-based analogues of the previously-reported dinuclear and trinuclear iridium complexes (**Ru-Alkyne-Dyad-Gd** and **Ru-Alkyne-Triad-Gd**, figure **3.03**), and their assessment as potential dual-modal optical/MR imaging agents. The relaxivity values for the two new **RuGd$_n$** (n = 1, 2) complexes were measured in D$_2$O at 400 MHz and 298 K, and cellular imaging studies were undertaken using the HeLa cell line, with cytotoxicity being evaluated through clonogenic assay.
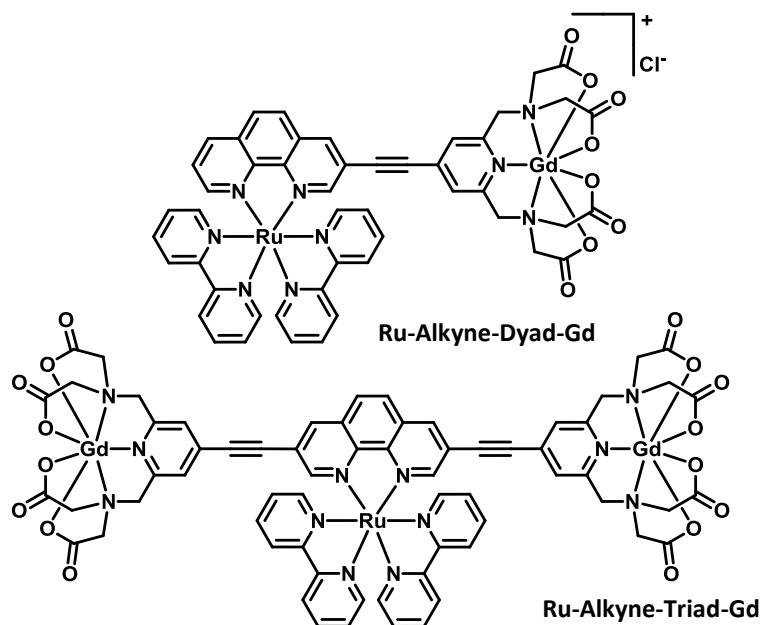
Figure 3.03: Structures of the newly synthesised, water-soluble **RuGd$_n$** (n = 1, 2) complexes

The synthesis of a larger, acetylene-bridged 'metallostar' complex (**RuGd$_6$**, figure **2.04**) was also attempted, although issues with water solubility were an unfortunate barrier to this complex's application as a dual-modal imaging agent. Progress towards a bimetallic probe with a triazole linking unit separating the Ru^{II} core from the pendant binding site for Gd^{III} (**Ru-Triazole-Dyad-Gd**, figure **2.04**) was better, as this probe showed excellent solubility in water; however, in this case, time restrictions were an obstacle to the complex's appraisal as a dual-modal imaging agent.

3.2) Synthesis and Characterisation

3.2.1) Alkyne-Bridged Dinuclear, Trinuclear and 'Metallostar' Ru^{II}-Gd^{III} Compounds

The syntheses of dinuclear (**Ru-Alkyne-Dyad-Gd**) and trinuclear (**Ru-Alkyne-Triad-Gd**) water-soluble, acetylene-bridged complexes were achieved in a similar manner, starting from the corresponding monosubstituted and disubstituted phenanthroline carboxylic acid scaffolds, **Ru-Alkyne-Dyad-Acid** and **Ru-Alkyne-Triad-Acid**, respectively (sections **2.2** and **2.3**, respectively).

The dinuclear complex, **Ru-Alkyne-Dyad-Gd**, was synthesised in 84 % yield by stirring 1.1 equivalents of GdCl$_3$.6H$_2$O with **Ru-Alkyne-Dyad-Acid** at room temperature in water (pH 5-6), for eighteen hours (scheme **3.01**). Purification of the compound was achieved by size-exclusion chromatography on Sephadex® LH-20 in methanol, before counterion exchange from a hexafluorophosphate ion to a chloride ion using Dowex® 1x2 chloride form (100-200 mesh) was used to improve the solubility of **Ru-Alkyne-Dyad-Gd** in water.

Scheme 3.01: Synthetic route to **Ru-Alkyne-Dyad-Gd**. i) H$_2$O (pH 5-6), GdCl$_3$.6H$_2$O, rt, 18h

The trinuclear complex, **Ru-Alkyne-Triad-Gd**, was synthesised in 69 % yield in a similar manner to its dinuclear counterpart (scheme **3.02**); 2.6 equivalents of GdCl$_3$.6H$_2$O were stirred with **Ru-Alkyne-Triad-Acid** in this case to account for the additional pendant metal binding site, and as the resulting trinuclear compound is neutral, no counterion exchange was necessary.

Scheme 3.02: Synthetic route to **Ru-Alkyne-Triad-Gd**. i) H$_2$O (pH 5-6), GdCl$_3$.6H$_2$O, rt, 18h

As Gd^{III} is paramagnetic, characterisation of **Ru-Alkyne-Dyad-Gd** and **Ru-Alkyne-Triad-Gd** using ^{1}H NMR spectroscopy was not a practical option; however, as the precursor carboxylic acid scaffolds showed excellent purity in their ^{1}H NMR spectra (figure **2.06** and figure **2.11**, respectively) it can be assumed that the two Gd^{III}-substituted compounds also exhibited a similar level of purity.

In order to provide direct evidence for the successful synthesis of the target heteronuclear **RuGd$_n$** (n = 1, 2) complexes, high-resolution mass spectrometry was employed. A high-resolution mass spectrum of **Ru-Alkyne-Dyad-Gd** (appendix **3.01**) confirms successful isolation of the dinuclear species, as the observed *m/z* value for the [*M* − Cl + H]$^{2+}$ ion (570.0562) matches the calculated *m/z* value (570.0558) well. Successful isolation of the trinuclear species was also confirmed using HRMS (appendix **3.02**) with the calculated and observed *m/z* values for the [*M* + 2H]$^{2+}$ species tallying well (842.5530 and 842.5664, respectively). In both cases, the correct isotope pattern for the Gd^{III} ion is clear in the spectra.

Synthesis of the heptanuclear complex **Ru-Alkyne-Metallostar-Gd** (**RuGd$_6$**) proved to be more difficult than syntheses of the dinuclear and trinuclear analogues, due to the low solubility of the carboxylic acid precursor **Ru-Alkyne-Metallostar-Acid** (section **2.4**) in water, and the insolubility of the resulting **RuGd$_6$** complex in all solvents. **Ru-Alkyne-Metallostar-Acid** was stirred with GdCl$_3$.6H$_2$O (6.6 equivalents) at room temperature in water at pH 5-6 (scheme **3.03**). After 18 hours, a rusty brown precipitate formed, which was unique to the 'metallostar' species, as the dinuclear, **Ru-Alkyne-Dyad-Gd**, and trinuclear, **Ru-Alkyne-Triad-Gd**, analogues had remained in solution upon binding of the Gd^{III} centres. This resulting precipitate was insoluble in all solvents and at all pH values where it was assumed that the chelation of the Gd^{III} centres had not been compromised.
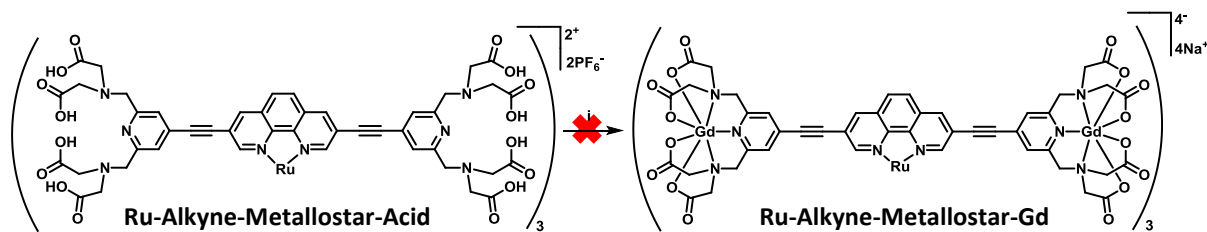
Scheme 3.03: Unsuccessful method for the synthesis of **Ru-Alkyne-Metallostar-Gd**.
i) H_2O (pH 5-6), $GdCl_3.6H_2O$, rt, 18h

To characterise the insoluble precipitate, inductively coupled plasma-mass spectrometry (ICP-MS) was employed to quantify the masses of the Ru^{II} and Gd^{III} ions in the sample, and elemental analysis was used to quantify the percentage of carbon, hydrogen and nitrogen present (table **3.01**). However, neither analytical technique afforded measured values that tallied well with the expected results. This may be as a result of excess water being present in the sample (we would expect that the hydrophilic exterior surface containing the carboxylate oxygen atoms would hydrogen-bond to water molecules). Alternatively, it could indicate that the target **Ru-Alkyne-Metallostar-Gd** compound was not successfully synthesised, with a partially-substituted entity precipitating out of solution before full incorporation of all six Gd^{III} centres was achieved. Due to the lack of definite evidence for the compound's successful synthesis, and the insolubility of the resulting precipitate in all solvents, unfortunately, **Ru-Alkyne-Metallostar-Gd** was not considered a successful candidate to be a dual-modal optical/MR imaging agent and was not tested further.

Table 3.01: ICP-MS and elemental analysis results for **Ru-Alkyne-Metallostar-Gd**

Analytical Technique	Analyte	Expected Value	Measured Value
ICP-MS	Ru	25,449 mg kg^{-1}	10,200 mg kg^{-1}
	Gd	236,646 mg kg^{-1}	292,000 mg kg^{-1}
Elemental Analysis	C	41.4 %	26.44 %
	H	2.57 %	3.00 %
	N	8.40 %	4.74 %

3.2.2) A Triazole-Bridged Dinuclear Ru^{II}-Gd^{III} Compound

A dinuclear **Ru-Triazole-Dyad-Gd** compound, in which the spacer unit separating the [Ru(bipy)$_2$(phen)]$^{2+}$ core from the Gd^{III} binding site is a triazole entity rather than an alkyne-bridge, was synthesised from the monosubstituted, triazole-bridged phenanthroline carboxylic acid scaffold (section **2.5**) in excellent yield (97 %). **Ru-Triazole-Dyad-Acid** was stirred with 1.3 equivalents of GdCl$_3$.6H$_2$O at room temperature in water (pH 5-6) for eighteen hours (scheme **3.04**), before purification was achieved by size-exclusion chromatography on Sephadex® LH-20. In an identical manner to the alkyne-bridged dinuclear compound, counterion exchange to a chloride ion was performed using Dowex® 1x2 chloride form (100-200 mesh) to improve the solubility of **Ru-Triazole-Dyad-Gd** in water.

Characterisation of **Ru-Triazole-Dyad-Gd** was achieved using HRMS (appendix **3.03**), with the calculated and observed *m/z* values for the [*M* − Cl + H]$^{2+}$ species tallying well (591.5644 and 591.5642, respectively), and the correct isotope pattern for the Gd^{III} ion being clear.

Ru-Triazole-Dyad-Acid   **Ru-Triazole-Dyad-Gd**
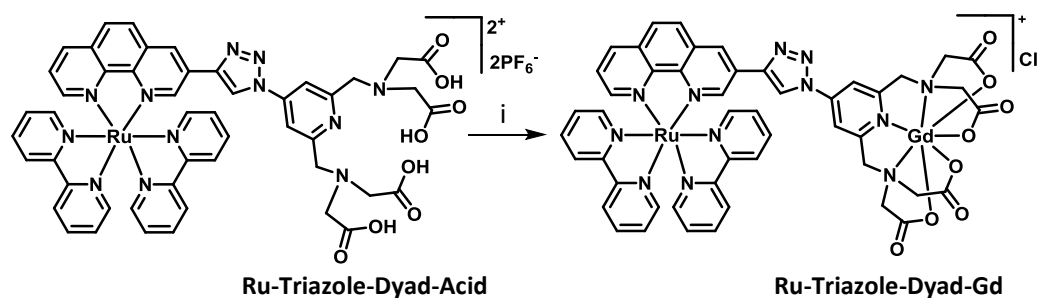
Scheme 3.04: Synthetic route to **Ru-Triazole-Dyad-Gd**. i) H$_2$O (pH 5-6), GdCl$_3$.6H$_2$O, rt, 18h

3.3) Photophysical Properties

UV/Vis absorption spectra were recorded in several solvents for **Ru-Alkyne-Dyad-Gd**, **Ru-Alkyne-Triad-Gd** and **Ru-Triazole-Dyad-Gd**, and extinction coefficients were measured for all compounds in water. Emission profiles and lifetimes of emission were recorded for all compounds (including as a frozen glass at 77 K for **Ru-Alkyne-Dyad-Gd** and **Ru-Triazole-Dyad-Gd**), and the quantum yield of emission was measured for all compounds against $[Ru(bipy)_3]Cl_2.6H_2O$ in aerated water. Finally, excitation spectra were measured in each solvent. Due to the insolubility of the **Ru-Alkyne-Metallostar-Gd** precipitate, no luminescence studies were carried out on this compound.

3.3.1) UV/Vis Absorption

UV/Vis absorption profiles for **Ru-Alkyne-Dyad-Gd**, **Ru-Alkyne-Triad-Gd** and **Ru-Triazole-Dyad-Gd** were recorded in several solvents (table **3.02**), but spectra in water will be reviewed for comparison purposes (figure **3.04**).

Figure 3.04: UV/Vis absorption spectra in H_2O at 298 K. **Ru-Alkyne-Dyad-Gd** (red), **Ru-Triazole-Dyad-Gd** (green) and **Ru-Alkyne-Triad-Gd** (blue)

The spectra for the three different **RuGd_n** (n = 1, 2) complexes have similar features, although the absorption bands associated with the phenanthroline ligand vary slightly in energy for each complex depending on the ligand substitution. There is a high energy absorption band (λ_{abs} = 285 nm) appearing in all of the spectra, which represents the $\pi \rightarrow \pi^*$ transitions on the 2,2'-bipyridine ligands, but the absorption bands for the $\pi \rightarrow \pi^*$ transitions

on the phenanthroline ligands differ in energy for each complex. The trinuclear **Ru-Alkyne-Triad-Gd** compound has a distinct, intense peak centred around λ_{abs} = 350 nm, compared to **Ru-Alkyne-Dyad-Gd** and **Ru-Triazole-Dyad-Gd**, which have less intense shoulder peaks at higher energy (λ_{abs} = 325 nm and λ_{abs} = 310 nm, respectively). The [1]MLCT absorption bands are present in the range λ_{abs} = 375-550 nm for all of the compounds, but again, there are differences in the energies of the absorptions depending on the phenanthroline ligand substitution. Both of the dinuclear **RuGd** compounds display a broad [1]MLCT absorption band with a maximum centred at λ_{abs} = 440 nm, which is a combination of the [1]MLCT absorptions associated with both the 2,2'-bipyridine ligands and the 1,10-phenanthroline ligands, overlapping in energy. The [1]MLCT absorption bands for the two different N^N ligands in **Ru-Alkyne-Triad-Gd**, on the other hand, are completely distinct, with the [1]MLCT absorption involving the 1,10-phenanthroline ligand (λ_{abs} = 485 nm) appearing as a red-shifted shoulder peak on the [1]MLCT absorption for the 2,2'-bipyridine ligands (λ_{abs} = 435 nm). This is due to the extended conjugation along the phenanthroline ligand in **Ru-Alkyne-Triad-Gd** stabilising the LUMO and lowering the energy of the [1]MLCT absorption for that ligand, in comparison to the [1]MLCT absorption for the 2,2-bipyridine ligands.

Table 3.02: UV/Vis absorption data for **Ru-Alkyne-Dyad-Gd**, **Ru-Alkyne-Triad-Gd** and **Ru-Triazole-Dyad-Gd** at 298 K. [a]Data taken from ref. 4**.**

Compound	Solvent	λ_{abs} (nm) [ε (x 10^3 M^{-1} cm^{-1})]
[a]**[Ru₂Gd] (11)**	H₂O	287 [272], 320 (sh) [46], 425 (sh) [39], 456 [48]
Ru-Alkyne-Dyad-Gd	EtOH/MeOH (4:1, *v:v*)	286, 327 (sh), 440 (br)
	MeOH	286, 327 (sh), 440 (br)
	H₂O	286 [56], 326 (sh) [25], 443 (br) [7.5]
	MeCN	286, 326 (sh), 440 (br)
	DMF	288, 327 (sh), 445 (br)
Ru-Alkyne-Triad-Gd	MeOH	286, 350, 435, 486 (sh)
	H₂O	286 [99], 350 [74], 435 [11], 486 (sh) [5.9]
Ru-Triazole-Dyad-Gd	EtOH/MeOH (4:1, *v:v*)	285, 311 (sh), 437, 451 (sh)
	MeOH	285, 313 (sh), 437, 452 (sh)
	H₂O	284 [42], 309 (sh) [14], 440 [6.1], 452 (sh) [6.3]
	DMF	287, 314 (sh), 441, 454 (sh)

When comparing the spectra for the three synthesised **RuGd$_n$** (n = 1, 2) complexes to that of a similarly-structured, previously published **Ru$_2$Gd** compound (**11**, figure **1.22**)[4], it can be seen that the complexes have similar features (table **3.02**).

3.3.2) Emission

Luminescence profiles and the lifetime of the luminescence decay for **Ru-Alkyne-Dyad-Gd**, **Ru-Alkyne-Triad-Gd** and **Ru-Triazole-Dyad-Gd** were recorded in several aerated solvents (table **3.03**), but profiles in aerated water at 298 K will be reviewed for comparison purposes (figure **3.05**).

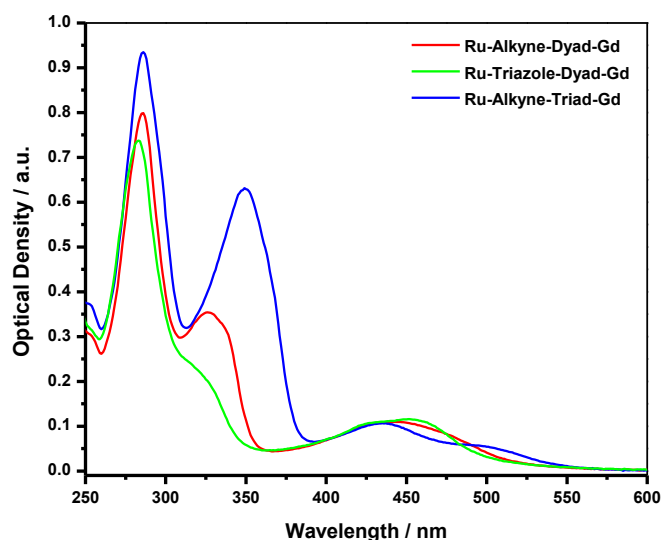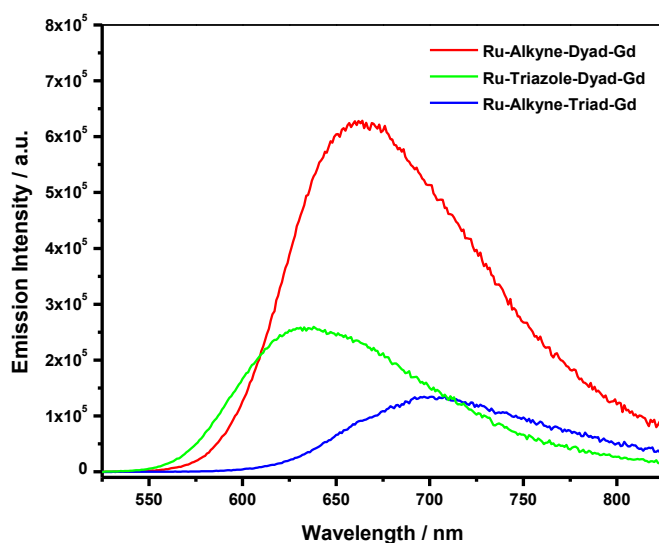**Figure 3.05:** Corrected emission spectra in aerated H$_2$O at 298 K.
Ru-Alkyne-Dyad-Gd (red), **Ru-Triazole-Dyad-Gd** (green) and **Ru-Alkyne-Triad-Gd** (blue) (λ_{ex} = 440 nm for all spectra, slit width = 3 nm)

Upon excitation in to the ^{1}MLCT absorption band at λ_{ex} = 440 nm, all three **RuGd$_n$** (n = 1, 2) complexes produce broad and featureless emission profiles at 298 K indicating spin-forbidden ^{3}MLCT {Ru^{II}→π*$_{(N^N)}$} transitions. The emission is centred around λ_{em} = 665 nm for **Ru-Alkyne-Dyad-Gd**, which is red-shifted when compared to **Ru-Triazole-Dyad-Gd** (λ_{em} = 635 nm). This increase in the maximum emission energy for **Ru-Triazole-Dyad-Gd** compared to **Ru-Alkyne-Dyad-Gd** must be as a result of exchanging the bridging unit along the phenanthroline ligand, as the two dinuclear complexes are otherwise isostructural. The maximum emission energy is red-shifted even further for **Ru-Alkyne-Triad-Gd** (λ_{em} = 700 nm) compared to the two dinuclear **RuGd** complexes, as the increase in conjugation along the

phenanthroline backbone by the addition of a second pendant metal chelate stabilises the LUMO energy level more than in the monosubstituted scaffolds.

Table 3.03: Luminescence data for **Ru-Alkyne-Dyad-Gd**, **Ru-Alkyne-Triad-Gd** and **Ru-Triazole-Dyad-Gd** in aerated solvents. [a]Data taken from ref. 4**.**

Compound	Solvent	$\lambda_{em}^{298\,K}$ (nm) [$\lambda_{em}^{77\,K}$ (nm)]	$\tau_1, \tau_2^{298\,K}$ (ns) [$\tau_1, \tau_2, \tau_3^{77\,K}$ (ns)]	A_1, A_2 (%)
[a]**[Ru₂Gd]** (11)	H_2O	620	540	--
Ru-Alkyne-Dyad-Gd	EtOH/MeOH (4:1, *v:v*)	654 [612, 662 (sh) 706 (sh)]	304 [5280]	--
	MeOH	654	258	--
	H_2O	664	351	--
	MeCN	665	239	--
	DMF	671	275	--
Ru-Alkyne-Triad-Gd	MeOH	690	237, 72	97, 3
	H_2O	699	402, 164	20, 80
Ru-Triazole-Dyad-Gd	EtOH/MeOH (4:1, *v:v*)	625 [584, 631]	219, 20 [5520, 462, 23]	[b]
	MeOH	627	220, 34	[b]
	H_2O	636	536, 52	[b]
	DMF	635	229, 25	[b]

[b]The luminescence lifetime decay curves for **Ru-Triazole-Dyad-Gd** were fitted by a sum of two exponentials, corresponding to the bound complex and to a small amount of dissociated complex in solution. The lifetime component ratios are insignificant, therefore, due to the different luminescence quantum yield values for the bound and dissociated complexes, respectively.

To directly compare the emission intensities of the three **RuGd_n** (n = 1, 2) probes, excitation wavelengths were chosen where all of the complexes have the same optical density in the UV/Vis spectra (0.1 a.u.). It can be seen in the resulting luminescence profiles that the emission intensity from **Ru-Triazole-Dyad-Gd** is lower by a factor of 2 compared to the intensity of the emission from **Ru-Alkyne-Dyad-Gd**, with luminescence quantum yield values of φ = 0.011 and φ = 0.021 being measured for the dinuclear triazole-bridged and alkyne-bridged entities, respectively. Previously, however, the quantum yield values for the two carboxylic acid precursor complexes, **Ru-Triazole-Dyad-Acid** and **Ru-Alkyne-Dyad-Acid**, were measured to be φ = 0.023 and φ = 0.020, respectively. As the quantum yield value has halved for **Ru-Triazole-Dyad-Gd** when compared to **Ru-Triazole-Dyad-Acid**, it suggests that exchanging the alkyne-bridge for a triazole unit along the phenanthroline scaffold has a quenching effect, but only when the Gd^{III} centre is bound. This may also account for the

existence of two lifetime components in the luminescence decay trace for **Ru-Triazole-Dyad-Gd**, compared to only one for **Ru-Alkyne-Dyad-Gd**. The alkyne-bridged dinuclear complex displays long-lived luminescence in aerated water (τ = 351 ns), whereas the triazole-bridged analogue exhibits both a long-lived lifetime component (τ_1 = 536 ns) and a shorter-lived component (τ_2 = 52 ns). The longer-lived component for **Ru-Triazole-Dyad-Gd** is most likely from a small portion of dissociated complex in solution, as it is the same (within experimental error) as the unquenched emission lifetime from **Ru-Triazole-Dyad-Acid** (τ = 543 ns), whilst the shorter lifetime component represents the genuine partially-quenched emission from the *bound* complex. The luminescence of **Ru-Alkyne-Triad-Gd** is quenched even further in comparison to the dinuclear complexes (ϕ = 0.006), suggesting that the presence of a second Gd^{III} chelate is the source of this effect.

Excitation spectra recorded in aerated water at 298 K for **Ru-Alkyne-Dyad-Gd** (λ_{em} = 645 nm), **Ru-Alkyne-Triad-Gd** (λ_{em} = 680 nm) and **Ru-Triazole-Dyad-Gd** (λ_{em} = 635 nm) were overlaid with UV/Vis absorption spectra recorded in the same solvent (figure **3.06**). A good match between the spectra can be seen, which is a clear indication that the emission observed for all complexes occurs as a result of absorption into the ^{1}MLCT band.
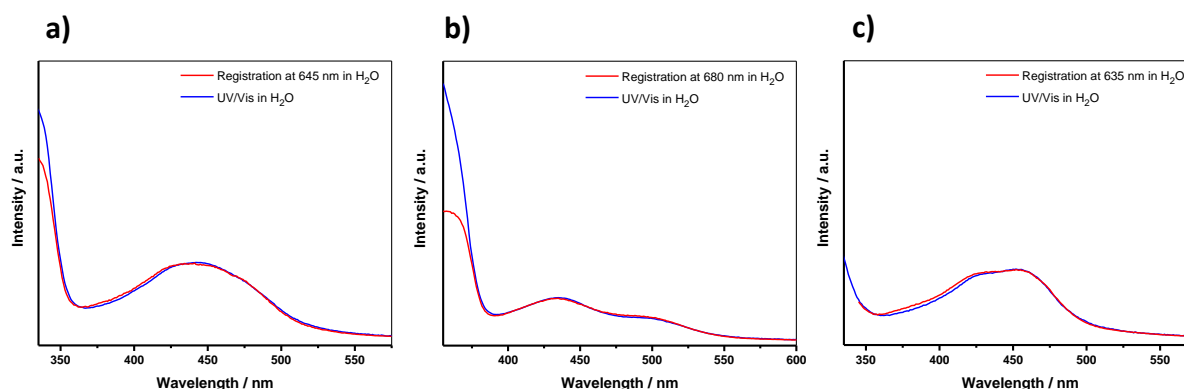
Figure 3.06: Normalised (at λ = max intensity) spectra in aerated H_2O at 298 K. Corrected excitation spectra (red) and UV/Vis spectra (blue) of a) **Ru-Alkyne-Dyad-Gd** (λ_{em} = 645 nm), b) **Ru-Alkyne-Triad-Gd** (λ_{em} = 680 nm) and c) **Ru-Triazole-Dyad-Gd** (λ_{em} = 635 nm)

3.4) Dual-Modal Imaging

Assessment of the two new water-soluble, acetylene-bridged ruthenium(II) bis(2,2'-bipyridine)-based complexes (**Ru-Alkyne-Dyad-Gd** and **Ru-Alkyne-Triad-Gd**) as dual-modal optical/MR imaging agents was undertaken. As was discussed previously, the heptanuclear probe, **Ru-Alkyne-Metallostar-Gd**, was not sufficiently water-soluble to be appraised as a dual-modal probe, and unfortunately, due to time restrictions, the evaluation of **Ru-Triazole-Dyad-Gd** was not accomplished either.

3.4.1) MRI Relaxivity Measurements

MRI relaxivity experiments for **Ru-Alkyne-Dyad-Gd** and **Ru-Alkyne-Triad-Gd** were carried out at 400 MHz and 298 K in D_2O, alongside the commercial MRI contrast agent Magnevist® ($[Gd(DTPA)]^{2-}$, figure **1.02**) for comparison purposes. Solutions of each of the probes were prepared at five different concentrations (0 – 2.0 mM) and the longitudinal relaxation time (T_1) for the residual H_2O peak in each sample was measured using a standard inversion-recovery pulse sequence. Concentration-normalised longitudinal relaxivity values (r_1) for each of the probes were then determined from a linear plot of longitudinal relaxation time against contrast agent concentration, in accordance with equation **3.01**.

$$\left(\frac{1}{T_1}\right)_{obs} = \left(\frac{1}{T_1}\right)_0 + r_1[M]$$

Equation 3.01: Equation used to calculate the relaxation rate of a contrast agent in solution. T_1 = longitudinal relaxation time, obs = observed T_1 values in the presence of contrast agent, 0 = observed T_1 value in the absence of contrast agent, r_1 = relaxivity value, [M] = concentration of contrast agent

It can be seen from linear plots for the three different contrast agents (figure **3.07**), that when measured at 400 MHz and 298 K, the two **RuGd$_n$** (n = 1, 2) probes have increased relaxivity values in comparison to the commercial contrast agent (table **3.04**). Under these conditions, Magnevist® has a relaxivity value of r_1 = 4.6 $mM^{-1} s^{-1}$, whereas **Ru-Alkyne-Dyad-Gd** and **Ru-Alkyne-Triad-Gd** have measured values of r_1 = 6.2 $mM^{-1} s^{-1}$ and r_1 = 13.6 $mM^{-1} s^{-1}$, respectively. This increase in the measured relaxivity value for the two **RuGd$_n$** (n = 1, 2) probes may arise from a number of factors, previously discussed in this thesis (section **1.2.1.1**).
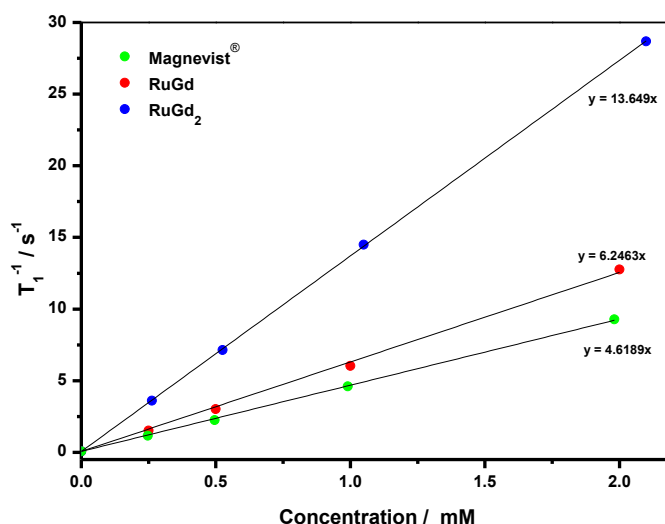
Figure 3.07: Plot of concentration (mM) versus relaxation rate of water protons (s^{-1}) to determine the concentration-normalised longitudinal relaxivity value (r$_1$, mM^{-1} s^{-1}) for **Ru-Alkyne-Dyad-Gd** (red), **Ru-Alkyne-Triad-Gd** (blue) and the commercial MRI contrast agent Magnevist® (green)

Table 3.04: Concentration-normalised longitudinal relaxivity values per Gd^{III} ion (r$_1$) for **Ru-Alkyne-Dyad-Gd**, **Ru-Alkyne-Triad-Gd** and the commercial MRI contrast agent Magnevist® measured at 400 MHz and 298 K in D$_2$O

Compound	Relaxivity Value per Gd^{III} ion (mM^{-1} s^{-1})
Magnevist®	4.6
Ru-Alkyne-Dyad-Gd	6.2
Ru-Alkyne-Triad-Gd	6.8

Firstly, the hydration state of each of the Gd^{III} ions (q value) is larger for **Ru-Alkyne-Dyad-Gd** and **Ru-Alkyne-Triad-Gd** (q = 1.6 ± 0.5)[2] compared to Magnevist® (q = 1)[5]. This means that more protons on water molecules can be relaxed in a shorter space of time, increasing the relaxivity value for the **RuGd$_n$** (n = 1, 2) probes. In the future, measurement of the mean residence time of the bound water molecules in the first coordination sphere (τ$_M$), and the water co-ligand exchange rate (k$_{ex}$) for the probes, would confirm this.

The number of water molecules coordinated to each of the Gd^{III} ions (q) in **Ru-Alkyne-Dyad-Gd** and **Ru-Alkyne-Triad-Gd** can be inferred to be the same as the previously tested analogous Ir^{III}-based compounds (**IrGd** and **IrGd$_2$**), due to the identical polyaminocarboxylate Ln^{III} chelation in all of the complexes. The q value was calculated by measuring the lifetime of the Eu^{III}-based emission in both H$_2$O and D$_2$O for the dinuclear **IrEu** compound (**26**)[2] and

substituting the values in to the Horrocks equation[6] (equation **3.02**). The calculated value of q = 1.6 ± 0.5 for each Gd^{III} centre suggests that there is an equilibrium present in solution between the mono(aqua) complex and the bis(aqua) complex.

The kinetic and thermodynamic stability of the Gd^{III} polyaminocarboxylate complex units in aqueous media was also inferred to be comparable to the previously tested Ir^{III}-based compounds (section **2.1**), with one equivalent of a competing DOTA ligand unable to strip the Ln^{III} ion from the heptadentate chelate.

$$q = A \times \left(\frac{1}{\tau_{H_2O}} - \frac{1}{\tau_{D_2O}} - B \right)$$

Equation 3.02: Equation used to calculate the number of water molecules coordinated to the Gd^{III} ions in the series of **RuGd_n** (n = 1, 2) complexes, q = number of coordinated water molecules, A = 'inner sphere' correction factor, B = 'outer sphere' correction factor, τ = Eu^{III}-based lifetime in each solvent

The increased hydration state of each of the Gd^{III} ions in **Ru-Alkyne-Dyad-Gd** and **Ru-Alkyne-Triad-Gd** cannot be the only contributing factor to the improved relaxivity values measured for the complexes compared to Magnevist®, however. Although **Ru-Alkyne-Triad-Gd** contains double the number of Gd^{III} ion binding sites, and hence double the number of vacant water coordination sites, compared to **Ru-Alkyne-Dyad-Gd**, the relaxivity value per Gd^{III} ion measured for **Ru-Alkyne-Triad-Gd** (r_1 = 6.8 mM^{-1} s^{-1}) was larger than the value measured for **Ru-Alkyne-Dyad-Gd** (r_1 = 6.2 mM^{-1} s^{-1}). This discrepancy can be accounted for by the increased size of **Ru-Alkyne-Triad-Gd** compared to **Ru-Alkyne-Dyad-Gd**.

The larger size and rigidity of both of these complexes compared to mononuclear Magnevist® has a slowing effect on the rotational correlation time (τ_R) of the probes in solution. This in turn increases the rate at which the water protons relax back to their ground state (aligned with the applied magnetic field), as the oscillating magnetic field generated by the slower tumbling rate of the larger, highly paramagnetic complexes in solution has components closer to the specific frequency of resonance (the Larmor frequency) for hydrogen. This allows absorption of another photon more quickly compared to the smaller complexes, and hence the relaxivity value for the larger complexes is increased in comparison, with the relaxivity value for the largest complex, **Ru-Alkyne-Triad-Gd**, benefitting from this

reduced rotational correlation time the most. In the future, direct measurement of the rotational correlation time (τ_R) of the probes in solution will confirm this.

3.4.2) Cellular Imaging Studies

Evaluation of the **RuGd$_n$** (n = 1, 2) complexes as probes for optical microscopy was undertaken in HeLa cells, with the cytotoxicity of the potential imaging agents being assessed through clonogenic assay in the same cell line.

Cells were initially incubated with either **Ru-Alkyne-Dyad-Gd** or **Ru-Alkyne-Triad-Gd** at concentrations of 25 µM, 50 µM and 75 µM for six or sixteen hours in fully-supplemented Dulbecco's modified eagle medium (DMEM). Cells stained with either of the probes for the longer incubation time (16h) at all concentrations were visually unhealthy when viewed under the microscope, and cells stained with the lowest concentration of the probes (25 µM) demonstrated weak Ru^{II}-based emission even at the longer incubation times. These preliminary results suggested, therefore, that shorter incubation times and higher concentrations would be closer to the optimum imaging conditions for both of the stains.

Further cellular staining was conducted with HeLa cells incubated with probe concentrations of 50 µM, 75 µM and 100 µM for four hours, or with an increased probe concentration (75 µM, 100 µM and 150 µM) over a shorter incubation period (two hours). In this instance, all of the cells stained for each incubation time, and at each concentration for both probes, were visually healthy when viewed under the microscope, apart from the cells incubated with a probe concentration of 150 µM, which were not very confluent and were beginning to detach from the sterile coverslip.

Ru^{II}-based emission was observed from all of the healthy cells when imaged with a confocal microscope (λ_{ex} = 405 nm, λ_{em} = 570-620 nm); however, the emission from the cells incubated with each of the probes for only two hours was weak, suggesting lower cellular uptake. Those cells incubated for four hours displayed brighter emission, but the images were still weak unless the laser power was increased, which may be a consequence of the low luminescence quantum yield values measured for each of the **RuGd$_n$** (n = 1, 2) probes. Changing the excitation wavelength to λ_{ex} = 457 nm or λ_{ex} = 488 nm proved an unsuccessful remedy to this issue, as no emission was observed from either of the **RuGd$_n$** (n = 1, 2) probes between λ_{em} = 570-620 nm or λ_{em} = 663-738 nm when excited at either of these wavelengths

(even at a high laser power), and no emission was observed between λ_{em} = 663-738 nm when the probes were excited at λ_{ex} = 405 nm either.

The optimum imaging conditions for each of the probes was taken to be an incubation time of four hours at a concentration of 50 µM, as this allowed for reasonable cellular uptake, without high levels of cytotoxicity being observed. Increasing the incubation time and probe concentration to levels higher than this did not improve upon the low Ru^{II}-based emission intensity observed from each of the probes. Example images of HeLa cells incubated with **Ru-Alkyne-Dyad-Gd** (figure **3.08a**-**b**) and **Ru-Alkyne-Triad-Gd** (figure **3.08c**-**d**) show that each of the **RuGd_n** (n = 1, 2) probes exhibits punctate cytoplasmic staining, with this observation more obvious in a 2.37x zoomed image.

The observed staining pattern suggests that both of the probes localise in a specific organelle within the HeLa cells, such as the lysosomes or the mitochondria. Co-localisation studies were carried out, therefore, with the commercial lysosomal and mitochondrial stains LysoTracker® Red and MitoTracker® Red to confirm this. These particular commercial stains were chosen as they have low absorbance values at the excitation wavelength for **Ru-Alkyne-Dyad-Gd** and **Ru-Alkyne-Triad-Gd** (λ_{ex} = 405 nm), and therefore, emission should not have been detectable in the range λ_{em} = 570-620 nm, where the Ru^{II}-based emission is observed. This should have allowed the luminescence from the organelle stains to be easily distinguished from that of **Ru-Alkyne-Dyad-Gd** and **Ru-Alkyne-Triad-Gd**. However, due to the low luminescence quantum yield values of the Ru^{II}-based probes, the laser power needed to produce a bright image of **Ru-Alkyne-Dyad-Gd** and **Ru-Alkyne-Triad-Gd** was increased to a level at which the LysoTracker® Red and MitoTracker® Red probes still weakly absorbed at λ_{ex} = 405 nm and produced observable emission in the range λ_{em} = 570-620 nm. As **Ru-Alkyne-Dyad-Gd** and **Ru-Alkyne-Triad-Gd** only produce observable emission under these conditions, the co-localisation studies with these particular commercial organelle stains were unsuccessful.

In future experiments, the commercial lysosomal and mitochondrial stains LysoTracker® Deep Red and MitoTracker® Deep Red that have *no* absorbance at λ_{ex} = 405 nm rather than *low* absorbance values, could be used to track the localisation of **Ru-Alkyne-Dyad-Gd** and **Ru-Alkyne-Triad-Gd** in cells. Commercial organelle stains that absorb at the same excitation wavelength as the **RuGd_n** (n = 1, 2) probes, but luminesce in a *different emission range* could also be used to track the specificity of the **RuGd_n** (n = 1, 2) probes. LysoTracker®

Blue may be a candidate for this as it exhibits no luminescence in the range λ_{em} = 570-620 nm when excited at λ_{ex} = 405 nm.
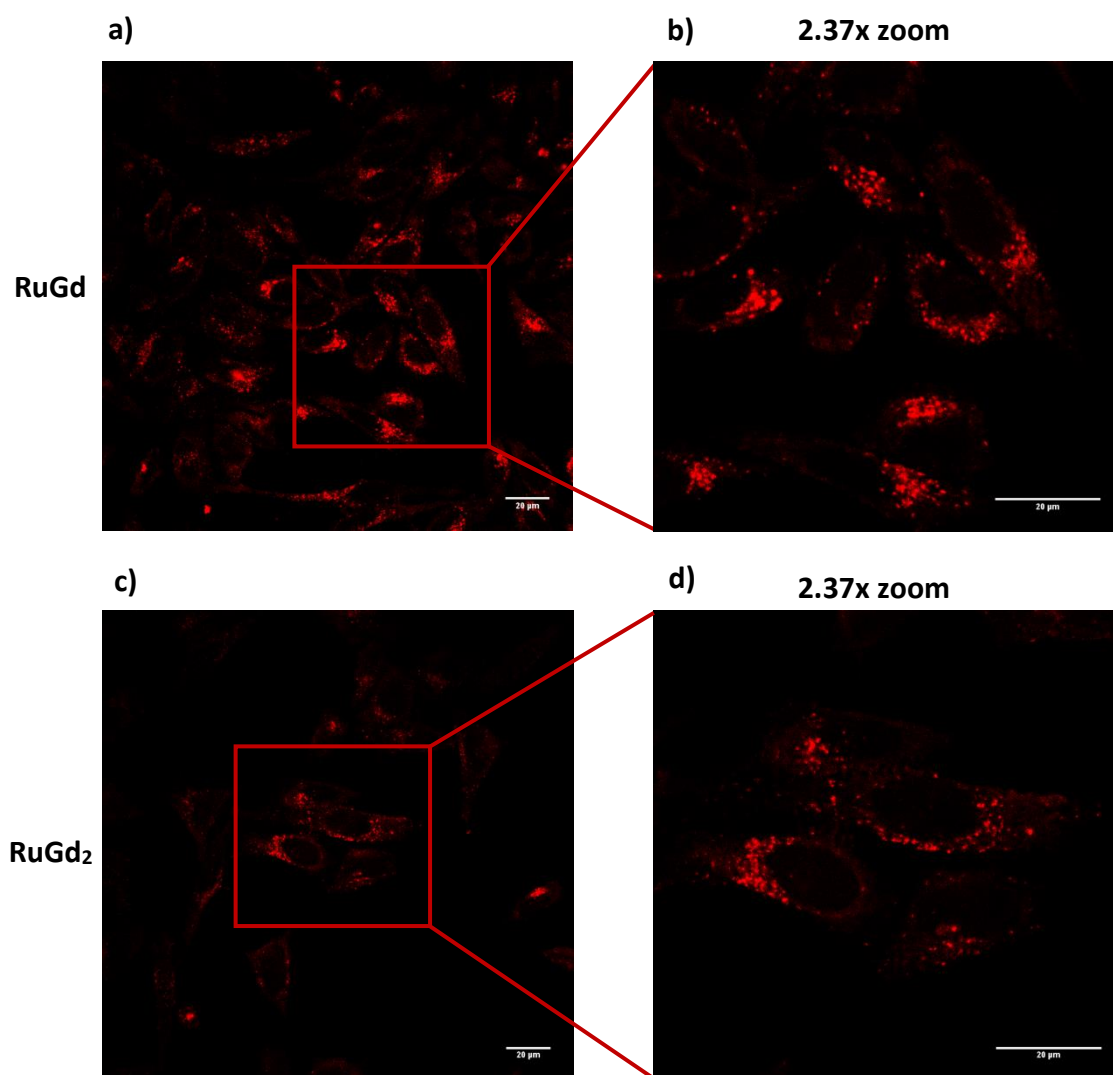
Figure 3.08: Confocal images of HeLa cells incubated with a) **Ru-Alkyne-Dyad-Gd** (50 µM, 4h); b) 2.37x zoom; c) **Ru-Alkyne-Triad-Gd** (50 µM, 4h); d) 2.37x zoom. λ_{ex} = 405 nm and λ_{em} = 570-620 nm for all images. Scale bars = 20 µm.

The cytotoxicity of **Ru-Alkyne-Dyad-Gd** and **Ru-Alkyne-Triad-Gd** towards the HeLa cell line under the optimum imaging conditions (50 µM, 4h), and at an increased probe concentration (200 µM, 4h), was assessed by clonogenic assay (figure **3.09**). It can be seen that both of the **RuGd$_n$** (n = 1, 2) probes exhibited low toxicity under the conditions used to image the cells, with survival fractions of > 0.85 being observed in both cases. Increasing the probe concentration four-fold to 200 µM had the expected effect of lowering the cell survival fraction in comparison to the lower probe concentration, but good viability levels were still

observed for both probes (> 0.8). The trinuclear probe **Ru-Alkyne-Triad-Gd** exhibited lower cell survival fractions at both probe concentrations when compared to the dinuclear **Ru-Alkyne-Dyad-Gd** counterpart. Again, this result is to be expected considering that there is an extra Gd^{III} binding site in the trinuclear species compared to the dinuclear species.
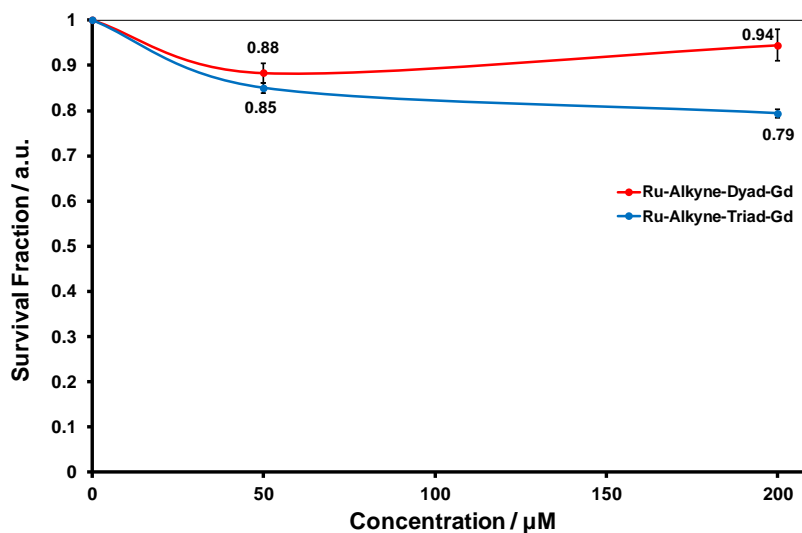
Figure 3.09: Clonogenic toxicity assay of HeLa cells incubated with **Ru-Alkyne-Dyad-Gd** and **Ru-Alkyne-Triad-Gd** at concentrations of 50 µM and 200 µM for 4 hours. Incubations were carried out in full DMEM at 37 °C under a 5 % CO_2 : 95 % air (*v:v*) environment for seven to ten days until visible cell colonies had formed. Error bars represent the standard deviation of six data points (three repeats of a duplicate data set).

3.5) Summary

The two new water-soluble, ruthenium(II) bis(2,2'-bipyridine)-based complexes, **Ru-Alkyne-Dyad-Gd** and **Ru-Alkyne-Triad-Gd**, exhibited excellent promise when evaluated as potential dual-modal optical/MR imaging agents. The **RuGd$_n$** (n = 1, 2) probes demonstrated high relaxivity values compared to the commercial contrast agent, Magnevist®, when measured at 400 MHz and 298 K in D$_2$O, owing to their larger size and rigidity, and to the increased hydration state of the Gd^{III} centres. The relaxivity values per Gd^{III} ion were measured to be r_1 = 6.2 mM^{-1} s^{-1} and r_1 = 6.8 mM^{-1} s^{-1} for **Ru-Alkyne-Dyad-Gd** and **Ru-Alkyne-Triad-Gd**, respectively.

Both of the **RuGd$_n$** (n = 1, 2) probes also exhibited punctate cytoplasmic staining when incubated with HeLa cells (50 µM, 4h), however, co-localisation studies with the commercial lysosomal and mitochondrial stains Lysotracker® Red and Mitotracker® Red were unsuccessful as the emission from the **RuGd$_n$** (n = 1, 2) probes was too weak and could not be successfully isolated from the highly luminescent commercial stains. Clonogenic toxicity assays of HeLa cells incubated with the two **RuGd$_n$** (n = 1, 2) probes at concentrations of 50 µM and 200 µM for four hours demonstrated that **Ru-Alkyne-Dyad-Gd** and **Ru-Alkyne-Triad-Gd** exhibited low cytotoxicity, with cell survival fractions of > 0.8 being measured.

3.6) Future Work

To continue this work further, it would be interesting to assess the effectiveness of **Ru-Triazole-Dyad-Gd** as a dual-modal optical/MR imaging agent to compare it to the results for the dinuclear acetylene-bridged complex. It would also be interesting to analyse the MRI functionality of the new water-soluble, acetylene-bridged **RuGd$_n$** (n = 1, 2) probes in more detail. Measurement of the mean residence time of the bound water molecules in the first coordination sphere (τ_M), the water co-ligand exchange rate (k_{ex}) and the rotational correlation time (τ_R), would provide insight in to the increased relaxivity values measured for each of the probes compared to the commercial MRI contrast agent, Magnevist®. Measuring the r_1 values for the **RuGd$_n$** (n = 1, 2) probes under different experimental conditions, such as in a 4 % solution of human serum albumin (HSA) and in PBS, would also aid the understanding of how the probes are likely to behave *in vivo*. Creating a nuclear magnetic relaxation dispersion (NMRD) profile for each of the **RuGd$_n$** (n = 1, 2) probes would also provide insight in to how the measured relaxivity values are likely to change depending on the magnet frequency.

With regards to the assessment of the **RuGd$_n$** (n = 1, 2) probes as luminescent imaging agents, further co-localisation experiments conducted with different commercial lysosomal and mitochondrial stains may help to elucidate which organelle the probes localise in, and to what extent they localise. Further to this, cell organelle extraction after staining with each of the **RuGd$_n$** (n = 1, 2) probes, followed by ICP-MS analysis, could be used to quantify the amount of each of the metals in the different cell compartments.

3.7) References

1   E. Debroye and T. N. Parac-Vogt, *Chem. Soc. Rev.*, 2014, **43**, 8178–8192.

2   A. Jana, E. Baggaley, A. Amoroso and M. D. Ward, *Chem. Commun.*, 2015, **51**, 8833–8836.

3   A. Jana, B. J. Crowston, J. R. Shewring, L. K. McKenzie, H. E. Bryant, S. W. Botchway, A. D. Ward, A. J. Amoroso, E. Baggaley and M. D. Ward, *Inorg. Chem.*, 2016, **55**, 5623–5633.

4   G. Dehaen, P. Verwilst, S. V. Eliseeva, S. Laurent, L. Vander Elst, R. N. Muller, W. M. De Borggraeve, K. Binnemans and T. N. Parac-Vogt, *Inorg. Chem.*, 2011, **50**, 10005–10014.

5   J. Costa, R. Ruloff, L. Burai, L. Helm and A. E. Merbach, *J. Am. Chem. Soc.*, 2005, **127**, 5147–5157.

6   A. Beeby, I. M. Clarkson, R. S. Dickins, S. Faulkner, D. Parker, L. Royle, A. S. de Sousa, J. A. G. Williams and M. Woods, *J. Chem. Soc., Perkin Trans. 2*, 1999, 493-503.

3.8) Appendices
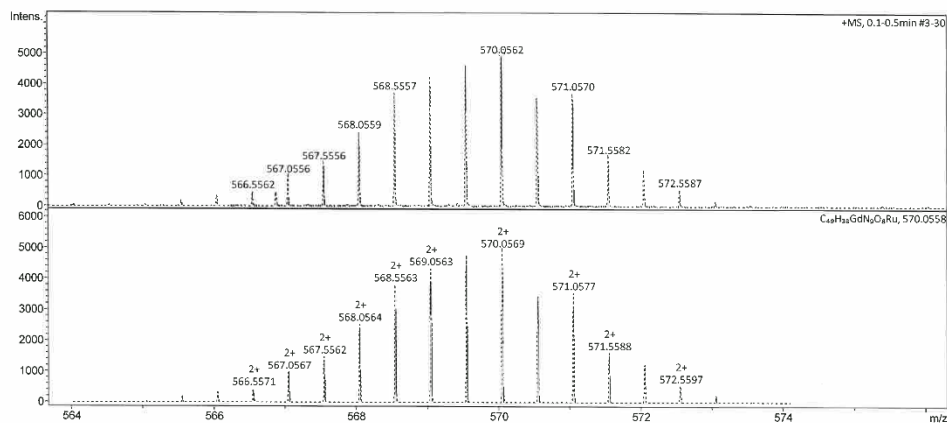
Appendix 3.01: High-resolution mass spectrum of **Ru-Alkyne-Dyad-Gd**.
Calculated for [C$_{49}$H$_{37}$N$_9$O$_8$RuGd + H]$^{2+}$, 570.0558.
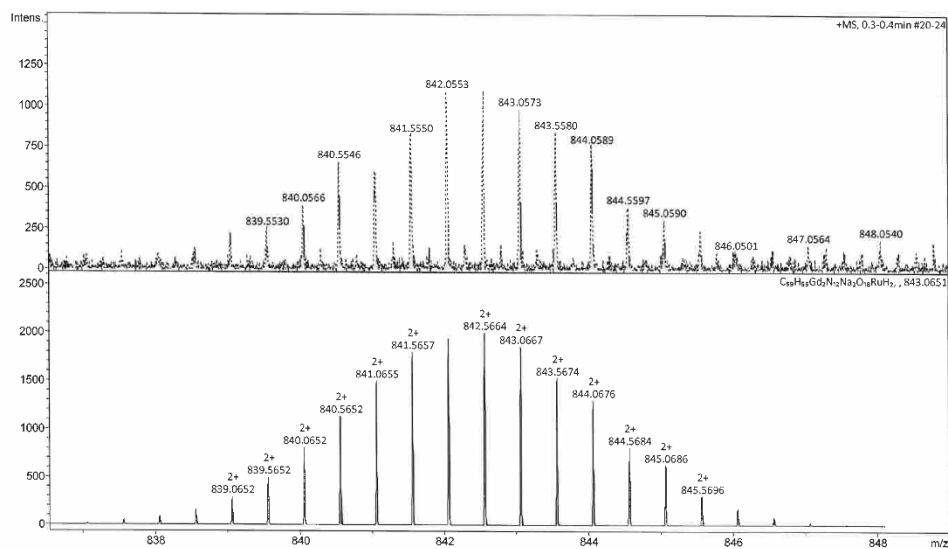
Appendix 3.02: High-resolution mass spectrum of **Ru-Alkyne-Triad-Gd**.
Calculated for [C$_{66}$H$_{50}$N$_{12}$O$_{16}$RuGd$_2$ + 2H]$^{2+}$, 842.5530.
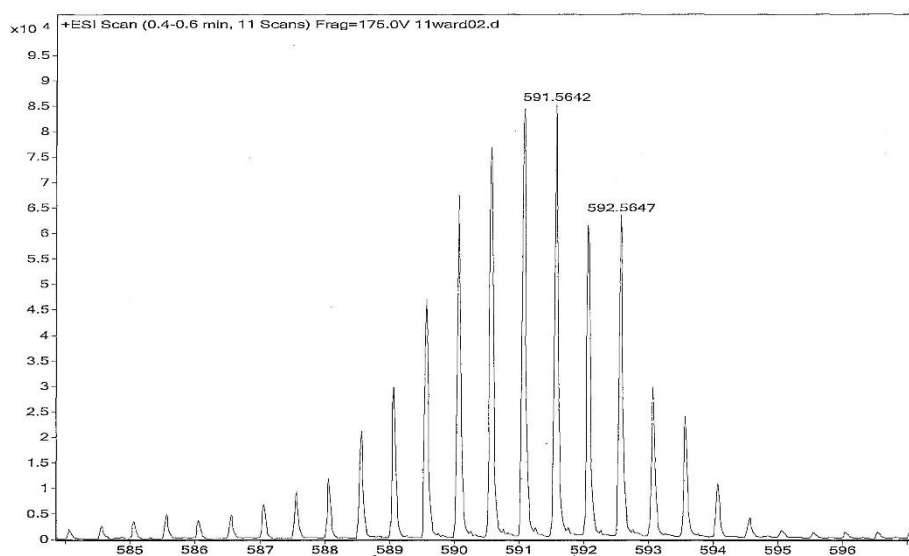
Appendix 3.03: High-resolution mass spectrum of **Ru-Triazole-Dyad-Gd**.
Calculated for $[C_{49}H_{38}N_{12}O_8RuGd + H]^{2+}$, 591.5644.

Chapter 4

Ru^{II}-Mn^{II} Complexes

4.1) Introduction

4.1.1) Ru^{II}-Mn^{II} Complexes as Dual-Modal Optical/MRI Contrast Agents

Recently, interest in utilising high spin Mn^{II} ions as alternative paramagnetic centres to Gd^{III} in T_1-weighted MRI contrast agents has grown, due to increasing concern for the *in vivo* toxicity of free Gd^{III} ions (section **1.2.2**). New ligand structures are beginning to be explored to incorporate Mn^{II} into probes used for MR imaging purposes; however, examples of dual-modal optical/MRI probes based on this metal are rare, with only one recent example of MnO_2 nanosheets integrated with $[Ru(bipy)_3][PF_6]_2$ being reported[1].

This chapter will present the synthesis and photophysical properties of two new water-soluble, heterometallic Ru^{II}-Mn^{II} complexes (**Ru-Alkyne-Dyad-Mn** and **Ru-Alkyne-Triad-Mn,** figure **4.01**) based on the 3- and 3,8-substituted phenanthroline scaffolds detailed previously (sections **2.2** and **2.3**, respectively), and their assessment as dual-modal optical/MR imaging agents. The relaxivity values for the new **RuMn_n** (n = 1, 2) probes were measured in D_2O at 400 MHz and 298 K, but unfortunately assessment of the probes for optical microscopy was not undertaken as the Ru^{II}-based luminescence was found to be quenched and, therefore, was not bright enough to produce an image. The reduced emission intensity was found to be a consequence of possible intramolecular electron-transfer between the Ru^{II} and Mn^{II} centres, in a similar process to that which occurs in photosystem II (PSII) during photosynthesis in green plants.
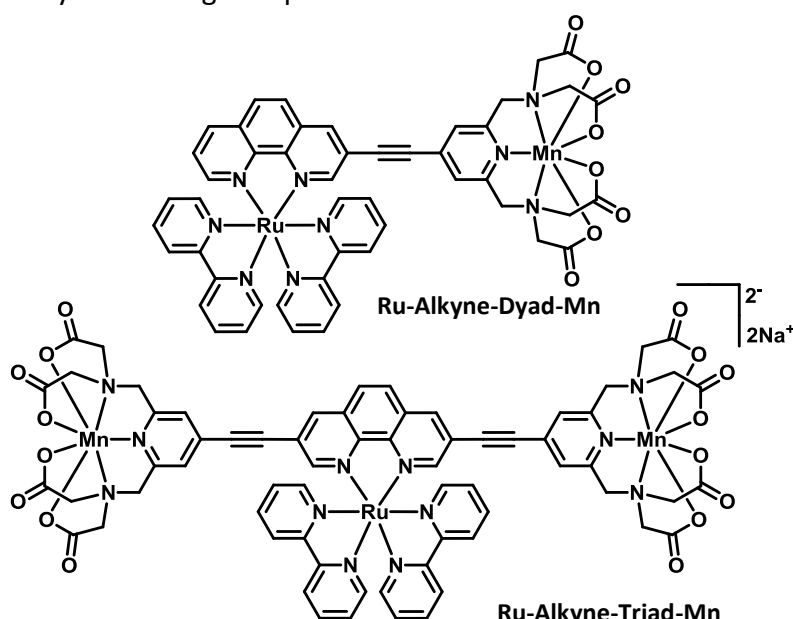
Figure 4.01: Structures of the newly synthesised, water-soluble **RuMn_n** (n = 1, 2) complexes

4.1.2) Photoinduced Electron-Transfer in Heterometallic Ru^{II}-Mn^{II} Complexes

During photosynthesis, solar energy (*hv*) is converted into chemical energy through the simultaneous reduction of carbon dioxide and the oxidation of water to molecular oxygen. This process is very complex and comprises two stages. Firstly, light-*dependent* reactions capture the solar energy and make energy-storage molecules, before light-*independent* reactions then use these molecules to capture and reduce carbon dioxide. The light-dependent reactions that capture the solar energy begin in the reaction centre of PSII, in which resides the primary photoelectron donor, P$_{680}$ (a chlorophyll dimer), surrounded by chlorophyll-binding proteins that absorb light. Upon absorption of one photon of sunlight, P$_{680}$ is promoted from the ground state to an excited-state, and a rapid cascade of electron-transfer processes is triggered; eventually funnelling the electron to an acceptor quinone molecule (Q$_A$). This produces a [P$_{680}$]$^+$ cation, which is reduced back to P$_{680}$ by electron-transfer from an electron donor (a tetramanganese cluster). After four electrons have been consecutively transferred, the manganese cluster recovers the four missing electrons by oxidising two water molecules, and in doing so produces molecular oxygen (figure **4.02**).
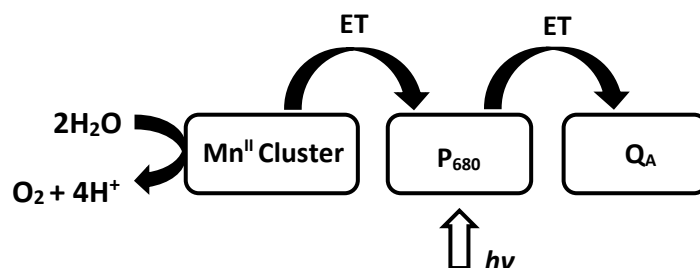
Figure 4.02: Simplified depiction of the photoinduced electron-transfer processes in PSII during photosynthesis in green plants. The chlorophyll dimer, P$_{680}$, absorbs a photon of light (*hv*), triggering electron-transfer (ET) to an electron-acceptor molecule (Q$_A$). An electron-donor molecule (a Mn^{II} cluster) then transfers an electron to reduce the [P$_{680}$]$^+$ cation back to P$_{680}$. The Mn cluster then recovers its electrons by oxidising two water molecules to produce molecular oxygen.

As the conversion of solar energy into fuel is an important part of sustainable energy production systems, heterometallic Ru^{II}-Mn^{II} complexes have been rationally designed in a bid to mimic the intramolecular photoinduced electron-transfer (PET) processes that occur during photosynthesis. Ruthenium polypyridyl complexes have been chosen as the photosensitising component of the PSII mimics, due to their well-studied photophysical and

photochemical properties, and due to the ease in which their structure can be synthetically modified. In each case, the [Ru^{II}(N^N)$_3$]$^{2+}$ complex is linked to a coordinated Mn^{II} ion through an organic spacer ligand (figure **4.03**)[2–4].

Figure 4.03: Examples of heterometallic Ru^{II}-Mn^{II} complexes studied as PSII mimics. (solv = a solvent molecule such as MeCN or H$_2$O)

The electron-transfer processes occurring in the Ru^{II}-Mn^{II} complexes can be described with a simplified Jablonksi diagram (figure **4.04**). Upon absorption of a photon, the Ru^{II}-Mn^{II} complex is promoted from the ground state to an excited MLCT state, [Ru^{III}-ligand$^-$-Mn^{II}]*, in which an electron has formally moved from the Ru^{II} centre to one of the surrounding ligands. The metal now has a formal charge of 3+ and a ligand radical has formed; (re-emission of the photon from the MLCT state at this point would produce characteristic Ru^{II}-based luminescence). If instead the Mn^{II} metal centre donates an electron to the Ru^{III} centre, a new charge-separated state is produced ([Ru^{II}-ligand$^-$-Mn^{III}]*) in which the Ru^{III} centre has been reduced back to Ru^{II} and the Mn^{II} centre has been oxidised to Mn^{III}; (similar to the process that occurs in PSII between P$_{680}$ and the manganese cluster). Non-radiative decay of this species through an oxidation process results in the complex returning to the electronic ground state, [Ru^{II}-ligand-Mn^{II}].

Figure 4.04: Simplified Jablonski diagram illustrating the electron-transfer processes in heterometallic Ru^{II}-Mn^{II} PSII mimics. The Ru^{II} metal centre absorbs a photon of light (*hv*) to produce an MLCT state i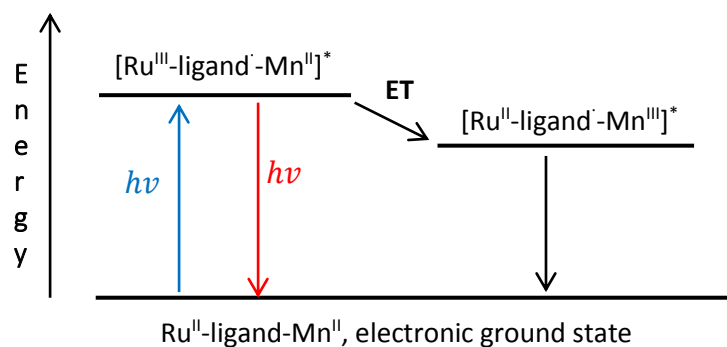n which the Ru^{II} centre has been photo-oxidised to Ru^{III}. The Mn^{II} centre then transfers an electron (ET) to reduce the Ru^{III} centre to Ru^{II}, oxidising to Mn^{III} in the process. The Mn^{III} ion then recovers its electron through an oxidation process and the whole molecule returns to the electronic ground state.

In order to observe whether electron-transfer processes are occurring in the newly synthesised dinuclear **Ru-Alkyne-Dyad-Mn** complex, femtosecond transient absorption (TA) spectroscopy was utilised. However, as neither the Mn^{II} or oxidised Mn^{III} species absorb light significantly in the UV/visible region of the electromagnetic spectrum, formation of the Mn^{III} species cannot be directly detected by TA spectroscopy. As a control experiment, therefore, a Ru^{II}-Zn^{II} analogue (**Ru-Alkyne-Dyad-Zn**) was also synthesised and studied by TA, as the resulting complex is isostructural with the Mn^{II}-based complex, but the Zn^{II} metal centre has a d^{10} electronic configuration and so is innocent with respect to the electron-transfer processes. Comparing the TA data for **Ru-Alkyne-Dyad-Mn** to **Ru-Alkyne-Dyad-Zn**, therefore, provides an efficient method to analyse whether electron-transfer processes are occurring in the Mn^{II}-based compound, as they definitely do not occur in the Zn^{II}-based compound.

4.2) Synthesis and Characterisation

4.2.1) Alkyne-Bridged Dinuclear Ru^{II}-Mn^{II} and Ru^{II}-Zn^{II} Compounds

Both bimetallic heteronuclear complexes, **Ru-Alkyne-Dyad-Mn** and **Ru-Alkyne-Dyad-Zn**, were synthesised from the monosubstituted, alkyne-bridged phenanthroline carboxylic acid scaffold **Ru-Alkyne-Dyad-Acid** (section **2.2**). One equivalent of **Ru-Alkyne-Dyad-Acid** was dissolved in water at pH 5-6 and stirred at room temperature with 1.3-1.6 equivalents of the appropriate metal chloride hydrate (M = Mn or Zn) for eighteen hours (scheme **4.01**). The excess metal salt was removed by size-exclusion chromatography on Sephadex® G-15 in water, to produce the pure, neutral compounds in good yields (80-95 %).

Ru-Alkyne-Dyad-Acid

Ru-Alkyne-Dyad-M
(M = Mn, Zn)
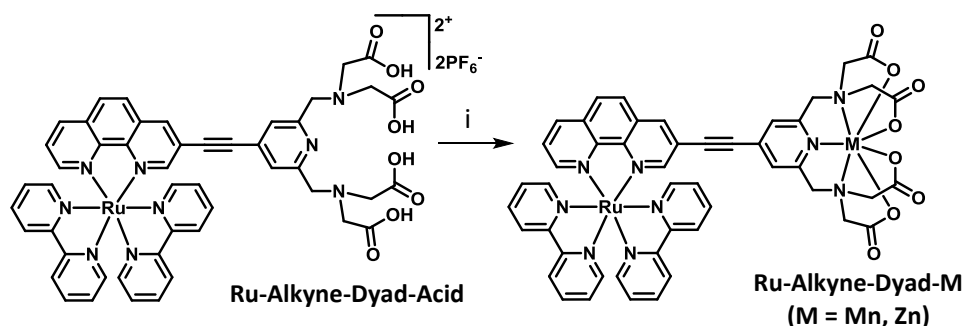
Scheme 4.01: Synthetic route to **Ru-Alkyne-Dyad-M (M = Mn, Zn)**
i) H_2O (pH 5-6), $MCl_2.XH_2O$ (M = Mn, Zn), rt, 18h

As Zn^{II} is diamagnetic, the successful synthesis and isolation of pure **Ru-Alkyne-Dyad-Zn** was confirmed by ^1H NMR spectroscopy (figure **4.05**). The aromatic region of the ^1H NMR spectrum (400 MHz, D_2O) integrates to the expected twenty-five protons, although there are four singlets at δ = 7.52 ppm, δ = 7.54 ppm, δ = 8.76 ppm and δ = 8.79 ppm that each integrate to half a proton. A two-dimensional ^1H-^1H NMR correlation spectrum (400 MHz, D_2O) (appendix **4.01**) confirms that these peaks correlate to either a H^3 or H^5 pyridine proton (δ = 7.52 ppm and δ = 7.54 ppm) and the H^2 phenanthroline proton (δ = 8.76 ppm and δ = 8.79 ppm). These half integral values suggest the presence of two isomers in solution, which were not present in the ^1H NMR spectrum (d_6-DMSO, 500 MHz) of the starting **Ru-Alkyne-Dyad-Acid** compound (figure **2.06**). As the protons in question are close to the metal chelation centre and are only inequivalent in **Ru-Alkyne-Dyad-Zn**, it would suggest that the two isomers are brought about by the chelation of the Zn^{II} ion in the polyaminocarboxylate binding site. This is further corroborated by the multiplet at δ = 3.34-3.52 ppm, which integrates as eight

protons, and represents protons on the 'arms' of the metal chelate. In the ^{1}H NMR spectrum for the starting **Ru-Alkyne-Dyad-Acid** compound, the protons are equivalent and are represented by a singlet at δ = 3.94 ppm; however, once the Zn^{II} ion is bound in **Ru-Alkyne-Dyad-Zn**, the protons are inequivalent and manifest as a multiplet due to the presence of the isomers. The remaining signals in the aliphatic region of the ^{1}H NMR spectrum represent the four protons closest to the pyridine ring on the metal chelate 'arms' (δ = 4.15 ppm), the residual water peak (δ = 4.79 ppm) and a small amount of unknown impurity (δ = 3.64-3.71 ppm).
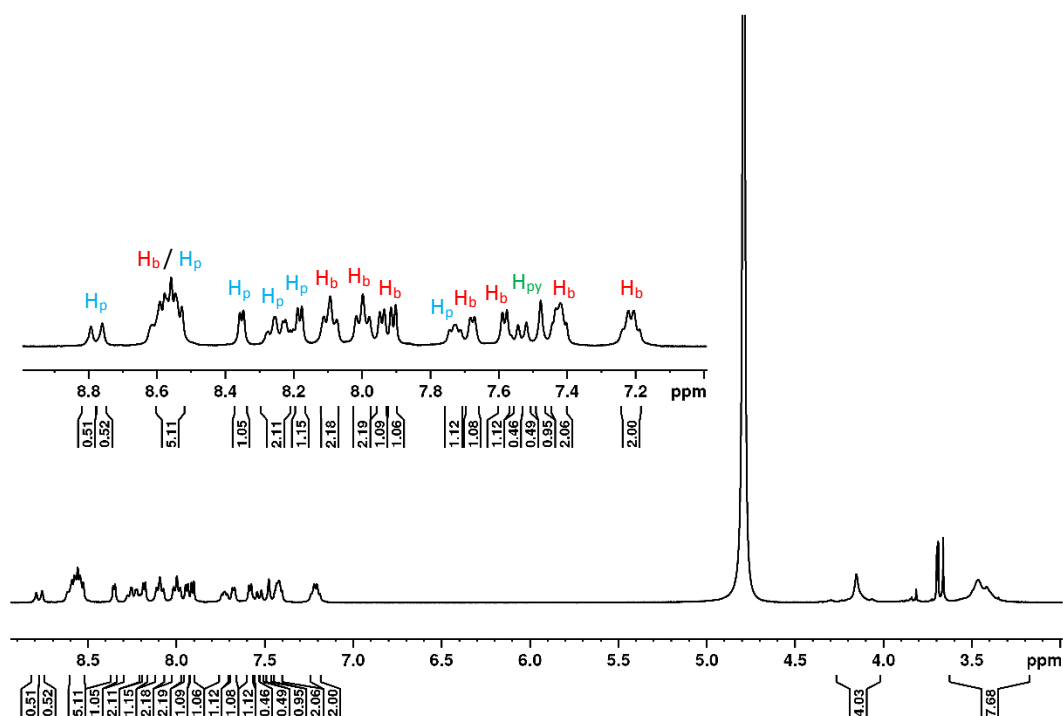
Figure 4.05: ^{1}H NMR spectrum (400 MHz, D$_2$O) of **Ru-Alkyne-Dyad-Zn** at 298 K.
(H$_b$ = proton on bipyridine ligand, H$_p$ = proton on phenanthroline ligand,
H$_{py}$ = proton on pyridine ring)

As **Ru-Alkyne-Dyad-Mn** contains a paramagnetic metal centre (Mn^{II}), characterisation by ^{1}H NMR spectroscopy was not practical; however, a high-resolution mass spectrum (appendix **4.02**) confirmed the successful synthesis of the complex, as the calculated and observed *m/z* values for the [*M* + 2H]$^{2+}$ ion tallied well (519.0667 and 519.0658, respectively). Further characterisation of **Ru-Alkyne-Dyad-Zn** was also achieved with HRMS (appendix **4.03**), with the calculated *m/z* value for the [*M* + 2H]$^{2+}$ ion (523.5623) matching the *m/z* value found (523.5632).

4.2.2) Alkyne-Bridged Trinuclear Ru^{II}-Mn$^{II}_2$ and Ru^{II}-Zn$^{II}_2$ Compounds

Both trinuclear, acetylene-bridged compounds (**Ru-Alkyne-Triad-Mn** and **Ru-Alkyne-Triad-Zn**) were synthesised in an analogous manner to their dinuclear counterparts (**Ru-Alkyne-Dyad-Mn** and **Ru-Alkyne-Dyad-Zn**) (scheme **4.02**). The starting alkyne-bridged, phenanthroline carboxylic acid scaffold in this case was the disubstituted complex, **Ru-Alkyne-Triad-Acid** (section **2.3**), and 2.4-4.8 equivalents of the appropriate metal chloride hydrate (M = Mn or Zn) was added to the reaction mixture to account for the extra vacant metal binding site. The pure compounds were produced in good yields (67-82 %), however, they were lower than the yields achieved for the dinuclear analogues. This was a consequence of incomplete incorporation of both of the metal centres, affording small amounts of the monosubstituted products.
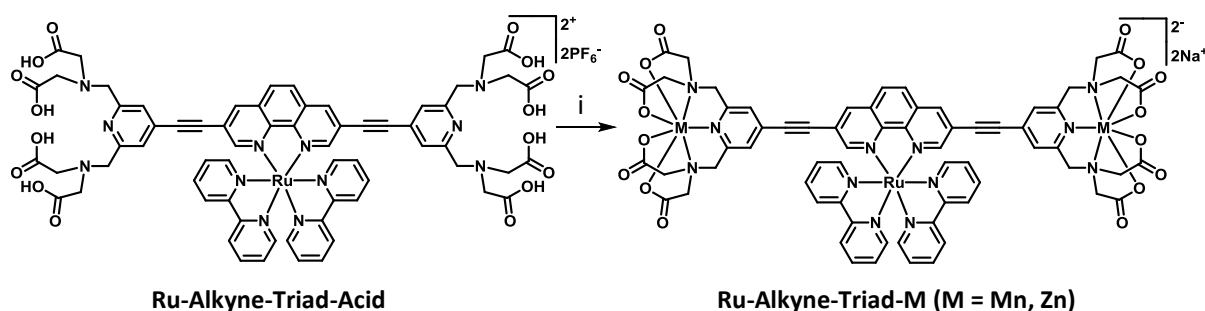
Scheme 4.02: Synthetic route to **Ru-Alkyne-Triad-M (M = Mn, Zn)**.
i) H$_2$O (pH 5-6), MCl$_2$.XH$_2$O (M = Mn, Zn), rt, 18h

Again, ^{1}H NMR spectroscopy (400 MHz, D$_2$O) was used to confirm the successful synthesis and isolation of pure **Ru-Alkyne-Triad-Zn** (figure **4.06**). When compared to the ^{1}H NMR spectrum (400 MHz, D$_2$O) of the starting **Ru-Alkyne-Triad-Acid** complex (figure **2.11**), it can be seen that the aromatic region for **Ru-Alkyne-Triad-Zn** is almost identical to that of the starting carboxylic acid compound. The signal integrals tally to the expected twenty-six protons; however, the four H^3/H^5 pyridine protons, which are equivalent in the starting **Ru-Alkyne-Triad-Acid** complex and are represented by a singlet at δ = 7.69 ppm, are inequivalent in **Ru-Alkyne-Triad-Zn** and are represented by two broad singlets between δ = 7.55-7.83 ppm (corroborated by a two-dimensional ^{1}H-^{1}H NMR correlation spectrum (400 MHz, D$_2$O, appendix **4.04**)). Similar to the dinuclear **Ru-Alkyne-Dyad-Zn** complex, this suggests the presence of isomers in the sample brought about by the chelation of the Zn^{II} ions in the polyaminocarboxylate binding sites. Further evidence for this lies in the aliphatic region of the

¹H NMR spectrum for **Ru-Alkyne-Triad-Zn**. Unlike the two distinct singlet peaks at δ = 4.16 ppm and δ = 4.74 ppm that represent the metal chelate 'arms' in the ¹H NMR spectrum of the **Ru-Alkyne-Triad-Acid** complex, there are a number of broad peaks whose integrals together add up to the twenty-four metal chelate protons in the spectrum for **Ru-Alkyne-Triad-Zn**. This suggests that the protons are no longer equivalent once the Zn^{II} ions are bound. The remaining signals in the spectrum are for the residual water peak (δ = 4.79 ppm) and a small amount of methanol (δ = 3.34 ppm) in the sample.
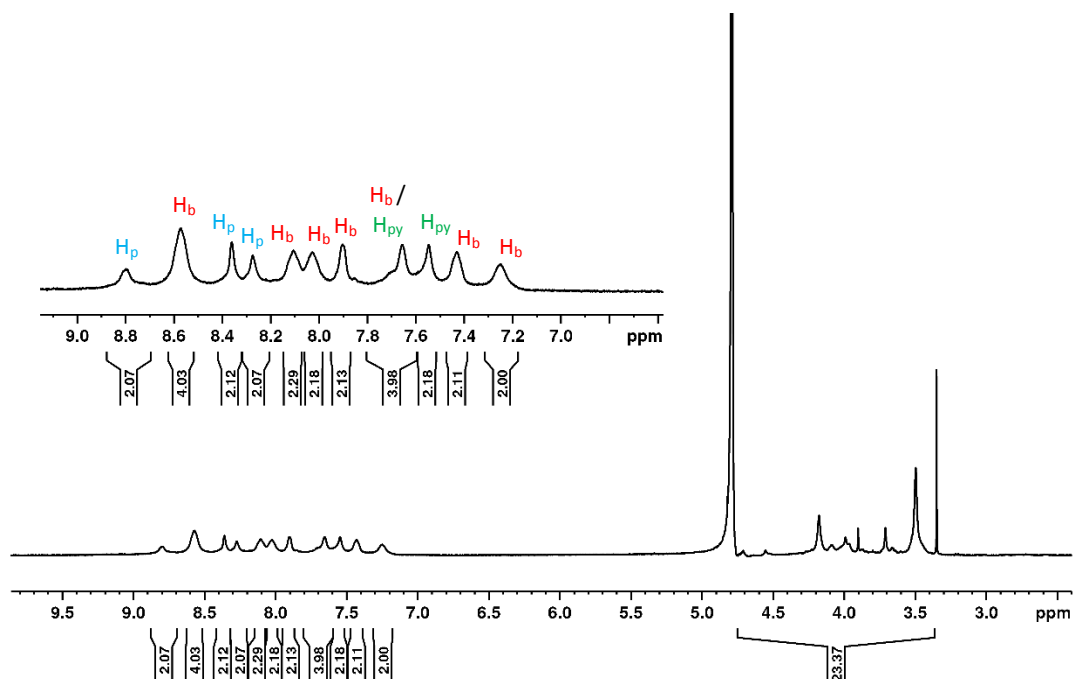
Figure 4.06: ¹H NMR spectrum (400 MHz, D₂O) of **Ru-Alkyne-Triad-Zn** at 298 K.
(H_b = proton on bipyridine ligand, H_p = proton on phenanthroline ligand,
H_py = proton on pyridine ring)

High-resolution mass spectra were recorded for both **Ru-Alkyne-Triad-Zn** and **Ru-Alkyne-Triad-Mn** (appendices **4.05** and **4.06**, respectively). In both cases the calculated and observed *m/z* values for the [*M* − 2Na]²⁻ ion agreed well (748.0553 and 748.0532 for **Ru-Alkyne-Triad-Zn**, respectively, and 739.0631 and 739.0598 for **Ru-Alkyne-Triad-Mn**, respectively).

4.3) MRI Relaxivity

MRI relaxivity experiments for **Ru-Alkyne-Dyad-Mn** and **Ru-Alkyne-Triad-Mn** were carried out in D_2O at 400 MHz and 298 K, alongside the commercial Gd^{III}-based MRI contrast agent, Magnevist® ($[Gd(DTPA)]^{2-}$, figure **1.02**), for comparison purposes. Solutions of each of the probes were prepared at five different concentrations (0 – 2.0 mM) and the longitudinal relaxation time (T_1) for the residual H_2O peak in each sample was measured using a standard inversion-recovery pulse sequence. Concentration-normalised longitudinal relaxivity values (r_1) for each of the probes were then determined from a linear plot of longitudinal relaxation time against contrast agent concentration, in accordance with equation **3.01**.

From linear plots of the two **RuMn$_n$** (n = 1, 2) complexes (figure **4.07**) it can be seen that when measured at 400 MHz and 298 K, **Ru-Alkyne-Dyad-Mn** and **Ru-Alkyne-Triad-Mn** have respectable relaxivity values of r_1 = 3.7 mM^{-1}s^{-1} and r_1 = 4.8 mM^{-1}s^{-1}, respectively. Under the same experimental conditions, the commercial Gd^{III}-based MRI contrast agent, Magnevist®, has a similar relaxivity value of r_1 = 4.6 mM^{-1}s^{-1}, and the previously synthesised Gd^{III}-based analogues, **Ru-Alkyne-Dyad-Gd** and **Ru-Alkyne-Triad-Gd**, have larger relaxivity values of r_1 = 6.2 mM^{-1}s^{-1} and r_1 = 13.6 mM^{-1}s^{-1}, respectively (table **4.01**).
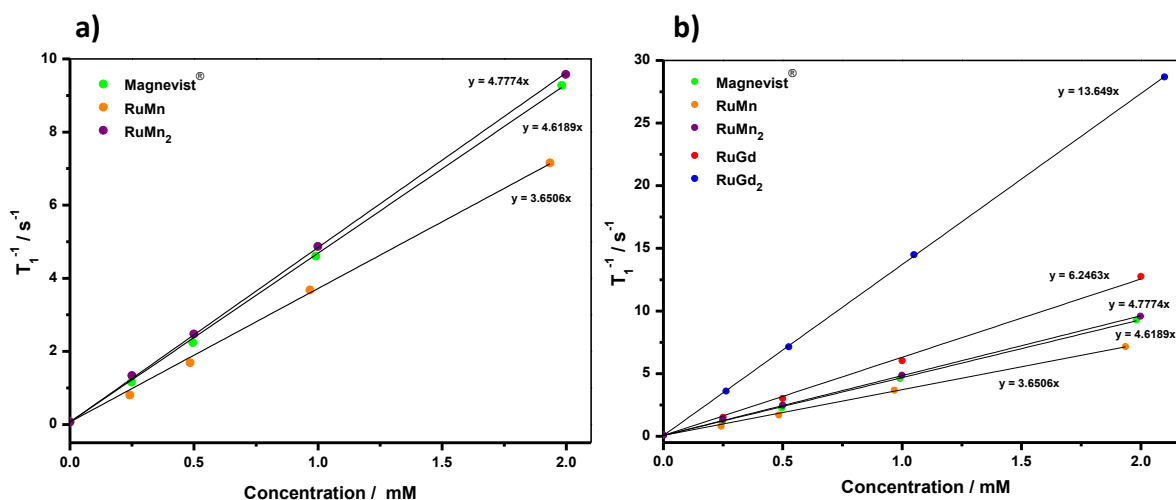

Figure 4.07: Plot of concentration (mM) versus relaxation rate of water protons (s^{-1}) to determine the concentration-normalised longitudinal relaxivity value (r_1, mM^{-1}s^{-1}) for **Ru-Alkyne-Dyad-Mn** (orange), **Ru-Alkyne-Triad-Mn** (purple), **Ru-Alkyne-Dyad-Gd** (red), **Ru-Alkyne-Triad-Gd** (blue) and the commercial MRI contrast agent, Magnevist®

Table 4.01: Concentration-normalised longitudinal relaxivity values (r$_1$) for
Ru-Alkyne-Dyad-Mn, **Ru-Alkyne-Triad-Mn, Ru-Alkyne-Dyad-Gd**, **Ru-Alkyne-Triad-Gd** and the commercial Gd^{III}-based MRI contrast agent, Magnevist®, measured in D$_2$O at 400 MHz and 298 K

Compound	Relaxivity Value (mM^{-1} s^{-1})
Magnevist®	4.6
Ru-Alkyne-Dyad-Mn	3.7
Ru-Alkyne-Triad-Mn	4.8
Ru-Alkyne-Dyad-Gd	6.2
Ru-Alkyne-Triad-Gd	13.6

The lower relaxivity values measured for the two **RuMn$_n$** (n = 1, 2) complexes in comparison to their Gd^{III}-based analogues is to be expected, as high spin Mn^{II} ions have less unpaired electrons compared to Gd^{III} ions (five and seven, respectively). This means that Mn^{II} has a lower magnetic moment (5.92 μ_B) than Gd^{III} (7.94 μ_B), and so the relaxivity values achievable by Mn^{II}-based complexes are lower than those achievable by the analogous complexes based on Gd^{III} ions. The d-block Mn^{II} ion also has a much smaller ionic radius compared to the lanthanide ion, Gd^{III}. This results in the Mn^{II} ion being able to make fewer coordination bonds than the Gd^{III} ion, and so the number of vacant coordination sites for water molecules to bind will be reduced in the **RuMn$_n$** (n = 1, 2) complexes compared to the analogous **RuGd$_n$** (n = 1, 2) complexes. This in turn will have a reducing effect on the relaxivity value measured for the Mn^{II}-based probes, as less protons on water molecules can be relaxed over a period of time.

The hydration state of each of the Gd^{III} ions (q value) in **Ru-Alkyne-Dyad-Gd** and **Ru-Alkyne-Triad-Gd** was previously reported to be (q = 1.6 ± 0.5)[5], which suggests that there may be an equilibrium present in solution between the mono(aqua) complex and the bis(aqua) complex. Determining the q value for the analogous Mn^{II}-based probes is not a straightforward undertaking, however; as, unlike the Ln^{III}-based complexes, using time-resolved luminescence measurements is not an option. Instead, the Caravan group have devised a method to estimate the hydration state of various Mn^{II} complexes using ^{17}O NMR line widths[6]. High spin Mn^{II} ions bound in different chelating ligands were found to have variable q values depending on their coordination environment. Mn^{II} ions bound in trans-1,2-diaminocyclohexane-N,N,N',N'-tetraacetic acid (CDTA) were shown to make 6 coordination

bonds to the chelate, with one vacant coordination site available for a water coligand (q = 0.9) (**29**, figure **4.08**), whereas Mn^{II} ions bound in DTPA (the same ligand as Gd^{III}-based Magnevist®, which has q = 1) (**30**, figure **4.08**) made seven to eight coordination bonds and had no water coligands (q = 0). As the polyaminocarboxylate chelate(s) in the newly synthesised **RuMn_n** (n = 1, 2) complexes are similar to these structures, it can be tentatively assumed that the Mn^{II} ion(s) bound in **Ru-Alkyne-Dyad-Mn** and **Ru-Alkyne-Triad-Mn** behave in a similar manner and have inner-sphere hydration states between q = 0 – 0.9. In the future, measurement of the Mn^{II} hydration state of the polyaminocarboxylate chelate in **Ru-Alkyne-Dyad-Mn** and **Ru-Alkyne-Triad-Mn** would confirm this.
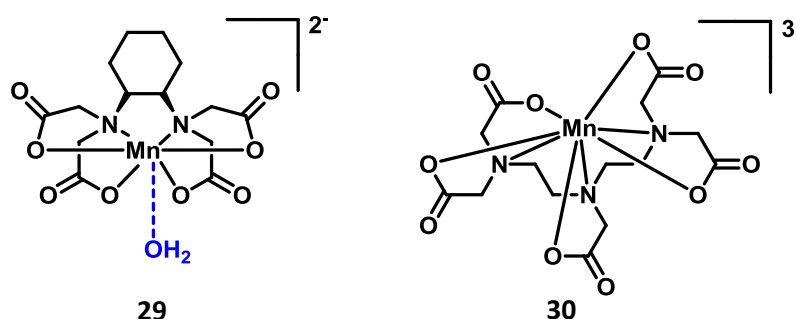

Figure 4.08: Examples of Mn^{II}-based complexes studied for their hydration values. 29) $[Mn(CDTA)(H_2O)]^{2-}$, 30) $[Mn(DTPA)]^{3-}$

As was previously discussed for the Gd^{III}-based analogues, **Ru-Alkyne-Dyad-Gd** and **Ru-Alkyne-Triad-Gd** (section **3.4.1**), the increased size of **Ru-Alkyne-Dyad-Mn** and **Ru-Alkyne-Triad-Mn** compared to Magnevist® will also have had an effect on the measured relaxivity values. The larger size and rigidity of both of the **RuMn_n** (n = 1, 2) complexes will have had a slowing effect on the rotational correlation time (τ_R) of the probes in solution, which in turn will have increased the r_1 value. The water protons will have relaxed back to their ground state (aligned with the applied magnetic field) at an increased rate, as the oscillating magnetic field generated by the slower tumbling rate of the larger, paramagnetic complexes in solution will have had components closer to the specific frequency of resonance (the Larmor frequency) for hydrogen. This will have allowed absorption of another photon more quickly for **Ru-Alkyne-Dyad-Mn** and **Ru-Alkyne-Triad-Mn** compared to the smaller complex, Magnevist®. In the future, measurement of the rotational correlation time (τ_R) of the probes in solution will confirm this.

4.4) Photophysical Properties

UV/Vis absorption spectra were recorded in several solvents for **Ru-Alkyne-Dyad-Mn**, **Ru-Alkyne-Dyad-Zn**, **Ru-Alkyne-Triad-Mn** and **Ru-Alkyne-Triad-Zn**, and extinction coefficients were measured for all compounds in water. Emission profiles and lifetimes of emission were recorded for all compounds (including as a frozen glass at 77 K for **Ru-Alkyne-Dyad-Mn** and **Ru-Alkyne-Dyad-Zn**), and the quantum yield of emission was measured for all compounds against $[Ru(bipy)_3]Cl_2.6H_2O$ in aerated water. Finally, excitation spectra were measured in each solvent.

4.4.1) UV/Vis Absorption

UV/Vis absorption profiles for **Ru-Alkyne-Dyad-Mn**, **Ru-Alkyne-Dyad-Zn**, **Ru-Alkyne-Triad-Mn** and **Ru-Alkyne-Triad-Zn** were recorded in several solvents (table **4.02**), but spectra in water will be reviewed for comparison purposes (figure **4.09**).
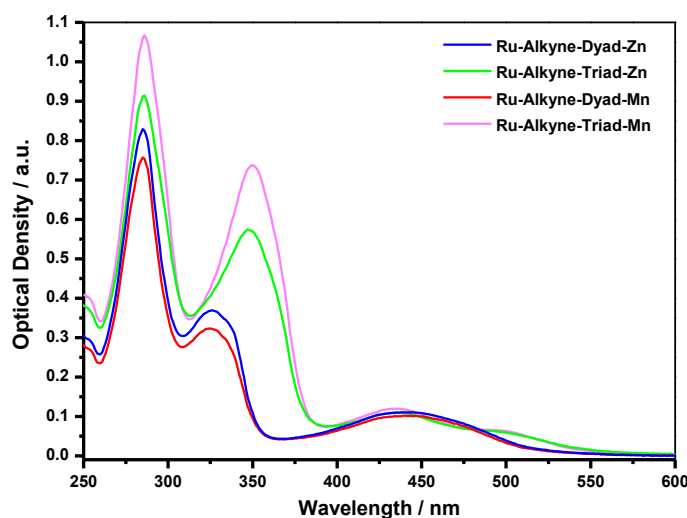

Figure 4.09: UV/Vis absorption spectra in aerated H_2O at 298 K.
Ru-Alkyne-Dyad-Zn (blue), **Ru-Alkyne-Triad-Zn** (green),
Ru-Alkyne-Dyad-Mn (red) and **Ru-Alkyne-Triad-Mn** (pink)

The spectra for the dinuclear **Ru-Alkyne-Dyad-Mn** and **Ru-Alkyne-Dyad-Zn** complexes are consistent with those measured for the monosubstituted phenanthroline carboxylic acid scaffold (section **2.2.2.1**) and for the dinuclear **Ru-Alkyne-Dyad-Gd** complex (section **3.3.1**), and the spectra for the trinuclear **Ru-Alkyne-Triad-Mn** and **Ru-Alkyne-Triad-Zn** complexes are consistent with those measured for the disubstituted phenanthroline carboxylic acid scaffold (section **2.3.2.1**) and for the trinuclear **Ru-Alkyne-Triad-Gd** complex (section **3.3.1**).

There are high energy absorption bands (λ_{abs} = 285 nm) representing the π→π* transitions on the 2,2'-bipyridine ligands in the spectra for all four complexes. The π→π* transitions on the phenanthroline ligands lie in the range λ_{abs} = 300-350 nm, with the absorption band for the disubstituted phenanthroline ligand in **Ru-Alkyne-Triad-Mn** and **Ru-Alkyne-Triad-Zn** having a maximum at lower energy (λ_{abs} = 350 nm) than the monosubstituted phenanthroline scaffold in **Ru-Alkyne-Dyad-Mn** and **Ru-Alkyne-Dyad-Zn** (λ_{abs} = 325 nm), due to the extended conjugation in the disubstituted scaffold stabilising the LUMO more than in the monosubstituted ligand. The ^{1}MLCT absorption bands are in the range λ_{abs} = 375-550 nm for all of the compounds, and parallel to their **RuGd$_n$** (n = 1, 2) counterparts, the ^{1}MLCT absorption band for the phenanthroline ligand either overlaps in energy (λ_{abs} = 440 nm) with that of the 2,2'-bipyridine ligands (in **Ru-Alkyne-Dyad-Mn** and **Ru-Alkyne-Dyad-Zn**) or manifests as a red-shifted shoulder peak (λ_{abs} = 480 nm) in **Ru-Alkyne-Triad-Mn** and **Ru-Alkyne-Triad-Zn**. Again, this is due to the extra stabilisation of the LUMO from the extended conjugation in the disubstituted phenanthroline ligand lowering the absorption energy.

When comparing the spectra for the four synthesised **RuM$_n$** (M = Mn, Zn, n = 1, 2) complexes to that of a similarly-structured, previously published **Ru.Mn** compound (**28b**, figure **4.03**)[2], it can be seen that the complexes have similar features (table **4.02**).

Table 4.02: UV/Vis absorption data for **Ru-Alkyne-Dyad-Mn**, **Ru-Alkyne-Dyad-Zn**, **Ru-Alkyne-Triad-Mn** and **Ru-Alkyne-Triad-Zn** at 298 K. [a]Data taken from ref. 2.

Compound	Solvent	λ_{abs} (nm) [ε (x 10^3 M^{-1}cm^{-1})]
[a]**Ru.Mn (28b)**	MeCN	245, 253, 287, 453
Ru-Alkyne-Dyad-Mn	EtOH/MeOH (4:1, *v:v*)	286, 325 (sh), 440 (br)
	MeOH	286, 325 (sh), 440 (br)
	H$_2$O	285 [80], 325 (sh) [34], 441 (br) [10]
	DMF	288, 327 (sh), 444 (br)
Ru-Alkyne-Dyad-Zn	EtOH/MeOH (4:1, *v:v*)	286, 326 (sh), 440 (br)
	MeOH	286, 326 (sh), 440 (br)
	H$_2$O	285 [30], 326 (sh) [13], 440 (br) [3.9]
	DMF	289, 328 (sh), 447 (br)
Ru-Alkyne-Triad-Mn	MeOH	287, 351, 435, 481 (sh)
	H$_2$O	286 [86], 350 [59], 435 [7.9], 481 (sh) [4.4]
Ru-Alkyne-Triad-Zn	MeOH	286, 349, 435, 478 (sh)
	H$_2$O	285 [88], 348 [55], 435 [9.2], 478 (sh) [5.3]

4.4.2) Emission

Luminescence profiles and the lifetime of the luminescence decay for **Ru-Alkyne-Dyad-Mn**, **Ru-Alkyne-Dyad-Zn**, **Ru-Alkyne-Triad-Mn** and **Ru-Alkyne-Triad-Zn** were recorded in several aerated solvents (table **4.03**), but profiles in aerated water at 298 K will be reviewed for comparison purposes (figure **4.10**). To directly compare the emission intensities of the four **RuM$_n$** (M = Mn, Zn, n = 1, 2) compounds, excitation wavelengths were chosen where all of the complexes have the same optical density in the UV/Vis spectra (0.1 a.u.). It can be seen in the resulting luminescence profiles that upon excitation in to the ^{1}MLCT absorption bands at λ_{ex} = 430-440 nm, all of the complexes produce broad and featureless emission profiles at 298 K indicating spin-forbidden ^{3}MLCT {Ru^{II}→π*$_{(N^\wedge N)}$} transitions; however, the maximum emission energy and emission intensity varies depending on the phenanthroline ligand substitution and the metal ion bound within the polyaminocarboxylate chelate.
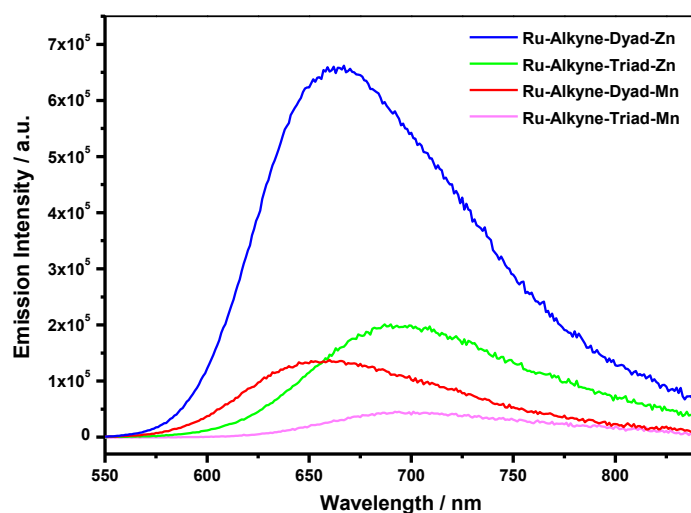

Figure 4.10: Corrected emission spectra in aerated H$_2$O at 298 K. **Ru-Alkyne-Dyad-Zn** (blue, λ_{ex} = 440 nm), **Ru-Alkyne-Triad-Zn** (green, λ_{ex} = 435 nm), **Ru-Alkyne-Dyad-Mn** (red, λ_{ex} = 430 nm) and **Ru-Alkyne-Triad-Mn** (pink, λ_{ex} = 435 nm) (Slit width = 3 nm)

As was recorded previously for the monosubstituted and disubstituted phenanthroline carboxylic acid scaffolds (sections **2.2.2.2** and **2.3.2.2**) and the analogous **RuGd$_n$** (n = 1, 2) complexes (section **3.3.2**), extending the conjugation along the phenanthroline backbone by the addition of a second pendant metal chelate in **RuM$_2$** (M = Mn, Zn), lowers the maximum emission energy of the ^{3}MLCT transition from λ_{em} = 660 nm for the dinuclear complexes (**Ru-Alkyne-Dyad-Mn** and **Ru-Alkyne-Dyad-Zn**), to λ_{em} = 700 nm for

the trinuclear complexes (**Ru-Alkyne-Triad-Mn** and **Ru-Alkyne-Triad-Zn**), and also significantly reduces the quantum yield values (ϕ = 0.019 and ϕ = 0.006, for **Ru-Alkyne-Dyad-Zn** and **Ru-Alkyne-Triad-Zn**, respectively and ϕ = 0.004 and ϕ = 0.0008, for **Ru-Alkyne-Dyad-Mn** and **Ru-Alkyne-Triad-Mn**, respectively).

Table 4.03: Luminescence data for **Ru-Alkyne-Dyad-Mn**, **Ru-Alkyne-Dyad-Zn**, **Ru-Alkyne-Triad-Mn** and **Ru-Alkyne-Triad-Zn** in aerated solvents. [a]Data taken from ref. 2.

Compound	Solvent	$\lambda_{em}^{298\,K}$ (nm) [$\lambda_{em}^{77\,K}$ (nm)]	$\tau_1, \tau_2, \tau_3^{298\,K}$ (ns) [$\tau_1, \tau_2^{77\,K}$ (µs)]	A_1, A_2 (%)
[a]**Ru.Mn** (**28b**)	MeCN	640	2.2	--
Ru-Alkyne-Dyad-Gd	H$_2$O	664	351	--
Ru-Alkyne-Dyad-Mn	EtOH/MeOH (4:1, *v:v*)	652 [612, 660 (sh), 709 (sh)]	275, 54 [1.8, 0.45, 0.05]	[b]
	MeOH	652	241, 58	[b]
	H$_2$O	657	410, 91	[b]
	DMF	666	284, 29	[b]
Ru-Alkyne-Dyad-Zn	EtOH/MeOH (4:1, *v:v*)	654 [617, 668 (sh), 720 (sh)]	266 [5.6]	--
	MeOH	658	234	--
	H$_2$O	666	329	--
	DMF	673	277	--
Ru-Alkyne-Triad-Gd	H$_2$O	699	402, 164	20, 80
Ru-Alkyne-Triad-Mn	MeOH	694	225, 59, 2	[b]
	H$_2$O	700	456, 164, 21	[b]
Ru-Alkyne-Triad-Zn	MeOH	688	231, 95	89, 11
	H$_2$O	695	301, 117	55, 45

[b]The luminescence lifetime decay curves for **Ru-Alkyne-Dyad-Mn** and **Ru-Alkyne-Triad-Mn** were fitted by a sum of two or three exponentials, corresponding to the bound complex and to a small amount of dissociated complex in solution. The lifetime component ratios are insignificant, therefore, due to the different luminescence quantum yield values for the bound and dissociated complexes, respectively.

Binding of the two different metal ions (Mn[II] and Zn[II]) in the polyaminocarboxylate chelate also has a profound effect on the Ru[II]-based emission intensity measured for each of the complexes. When comparing the spectra for the two dinuclear complexes (**Ru-Alkyne-Dyad-Mn** and **Ru-Alkyne-Dyad-Zn**) it can be seen that the intensity of the emission is lower by a factor of 5 when the metal ion is Mn[II] compared to Zn[II]; a result supported by the measured luminescence quantum yield values (ϕ = 0.004 and ϕ = 0.019, for **Ru-Alkyne-Dyad-Mn** and **Ru-Alkyne-Dyad-Zn**, respectively). This observation is mirrored in the emission

spectra for the trinuclear complexes (**Ru-Alkyne-Triad-Mn** and **Ru-Alkyne-Triad-Zn**) in which the luminescence is partially quenched for the **Ru-Alkyne-Triad-Mn** complex compared to **Ru-Alkyne-Triad-Zn**. Again, the measured quantum yield values reflect the diminished luminescence in the Mn^{II}-based complex (ϕ = 0.0008 and ϕ = 0.006, for **Ru-Alkyne-Triad-Mn** and **Ru-Alkyne-Triad-Zn**, respectively). When comparing the quantum yield values for the four **RuM_n** (M = Mn, Zn, n = 1, 2) compounds to the starting carboxylic acid complexes, **Ru-Alkyne-Dyad-Acid** and **Ru-Alkyne-Triad-Acid** (ϕ = 0.020 and ϕ = 0.006, respectively), it can be seen that the values for the Zn^{II}-based complexes are the same within experimental error. This indicates, therefore, that the Ru^{II}-based luminescence is only partially quenched when Mn^{II} ion(s) are bound in the polyaminocarboxylate chelate(s).

A possible explanation for the observed partial quenching of the Ru^{II}-based luminescence could be that coordination of the Mn^{II} ion(s) induces a change in the electronic properties of the [Ru(bipy)$_2$(phen)]$^{2+}$ centre. However, as there are no significant differences between the absorption and emission spectra for the starting carboxylic acid complexes and the **RuMn_n** (n = 1, 2) complexes, this suggests that the excited-state energy and the electronic structure are not affected by the Mn^{II} ion(s). Instead, the partial quenching of the Ru^{II}-based luminescence in the **RuMn_n** (n = 1, 2) complexes is most likely a result of photoinduced energy-transfer (PEnT) between the two different metal centres, as has been reported for previous heterometallic Ru^{II}-Mn^{II} complexes[8]. Mn^{II}-based complexes possess low-energy excited-states, but population of these states from the ground state is spin-forbidden and, therefore, the transitions are not observed in the absorption spectra. Instead population of these low-energy excited-states can occur as a result of PEnT from the excited [Ru(bipy)$_2$(phen)]$^{2+}$ centre, which has a main (0-0) emission band between λ_{em} = 610-645 nm.

The lifetimes of the Ru^{II}-based luminescence decay were measured for each of the four **RuM_n** (M = Mn, Zn, n = 1, 2) complexes (table **4.03**), with the results corroborating the trends observed with regards to the partial quenching of the emission in the Mn^{II}-based complexes. The curves for the dinuclear **Ru-Alkyne-Dyad-Zn** complex were fitted as monoexponential decays in each of the different solvents, with the lifetime values extracted ($\tau \approx$ 250-350 ns) approximately matching those of the analogous dinuclear **Ru-Alkyne-Dyad-Gd** complex (within experimental error), in which the luminescence is not partially quenched. The decay traces for the dinuclear **Ru-Alkyne-Dyad-Mn** complex were fitted by a sum of two exponentials, however; with a longer-lived component ($\tau_1 \approx$ 250-350 ns) and a shorter-lived

component (τ_2 < 100 ns) being observed. As the longer-lived component has the same magnitude as the lifetime for the unquenched emission in the **Ru-Alkyne-Dyad-Zn** and **Ru-Alkyne-Dyad-Gd** compounds, it is assumed that this value corresponds to a small amount of dissociated complex in solution (the starting carboxylic acid complex), as a result of the Mn^{II} ion leaching out of the chelate in a competitive solvent. The shorter-lived component, therefore, can be assigned as the lifetime of the partially quenched Ru^{II}-based decay from the non-dissociated **Ru-Alkyne-Dyad-Mn** complex.

The trinuclear complexes follow a similar pattern to the dinuclear complexes. The lifetime values for the Ru^{II}-based luminescence in **Ru-Alkyne-Triad-Zn** were extracted from a biexponential decay curve and are similar (within experimental error) to those of the unquenched emission observed for **Ru-Alkyne-Triad-Gd** in each of the solvents ($\tau_1 \approx$ 300 ns and $\tau_2 \approx$ 100 ns). The Ru^{II}-based emission from the **Ru-Alkyne-Triad-Mn** complex, however, has three lifetime components, with two matching those of the unquenched dissociated carboxylic acid complex ($\tau_1 \approx$ 300 ns and $\tau_2 \approx$ 100 ns) and one very short-lived lifetime (τ_3 < 21 ns) representing the Ru^{II}-based decay from the bound **Ru-Alkyne-Triad-Mn** complex.

If we take the shorter-lived lifetime components for each of the **RuMn$_n$** (n = 1, 2) complexes (τ_q = 91 ns for **Ru-Alkyne-Dyad-Mn**, and τ_q = 21 ns for **Ru-Alkyne-Triad-Mn**, which we assume represent the partially quenched Ru^{II}-based luminescence), and the lifetime values for the unquenched emission in the **RuZn$_n$** (n = 1, 2) complexes (τ = 329 ns for **Ru-Alkyne-Dyad-Zn**, and τ = 117 ns for **Ru-Alkyne-Triad-Zn**), the rate of the emission quenching (k_q) in aerated water for each of the complexes can be calculated using equation **4.01**. For **Ru-Alkyne-Dyad-Mn** this gives a value of k_q = 7.9 x 10^6 s^{-1} and for **Ru-Alkyne-Triad-Mn** a rate of k_q = 3.9 x 10^7 s^{-1}.

$$k_q = \frac{1}{\tau_q} - \frac{1}{\tau}$$

Equation 4.01: Equation used to calculate the rate constant for the Ru^{II}-based emission quenching (k_q) in **RuMn$_n$** (n = 1, 2) complexes. τ and τ_q are the unquenched (**M = Zn**) and quenched (**M = Mn**) lifetimes, respectively.

In order to ascertain that the quenching of the Ru^{II}-based emission was due to an *intra*molecular process rather than an *inter*molecular interaction, i.e. occurs between metal centres in the same molecule not on different molecules, time-resolved luminescence measurements were carried out on increasing concentrations of **Ru-Alkyne-Dyad-Mn** in

aqueous solution. The Ru^{II}-based emission lifetime values measured were constant across increasing concentrations of **Ru-Alkyne-Dyad-Mn**, demonstrating that the Ru^{II}-based emission quenching is independent of concentration and, therefore, occurs as a result of interaction *within* the molecules of **Ru-Alkyne-Dyad-Mn**.

Excitation spectra recorded in aerated water at 298 K for **Ru-Alkyne-Dyad-Mn** (λ_{em} = 640 nm)**, Ru-Alkyne-Dyad-Zn** (λ_{em} = 645 nm), **Ru-Alkyne-Triad-Mn** (λ_{em} = 675 nm) and **Ru-Alkyne-Triad-Zn** (λ_{em} = 690 nm) were overlaid with UV/Vis absorption spectra recorded in the same solvent (figure **4.11**). A good match between the spectra can be seen, which is a clear indication that the emission observed for all complexes occurs as a result of absorption into the ^1MLCT band.
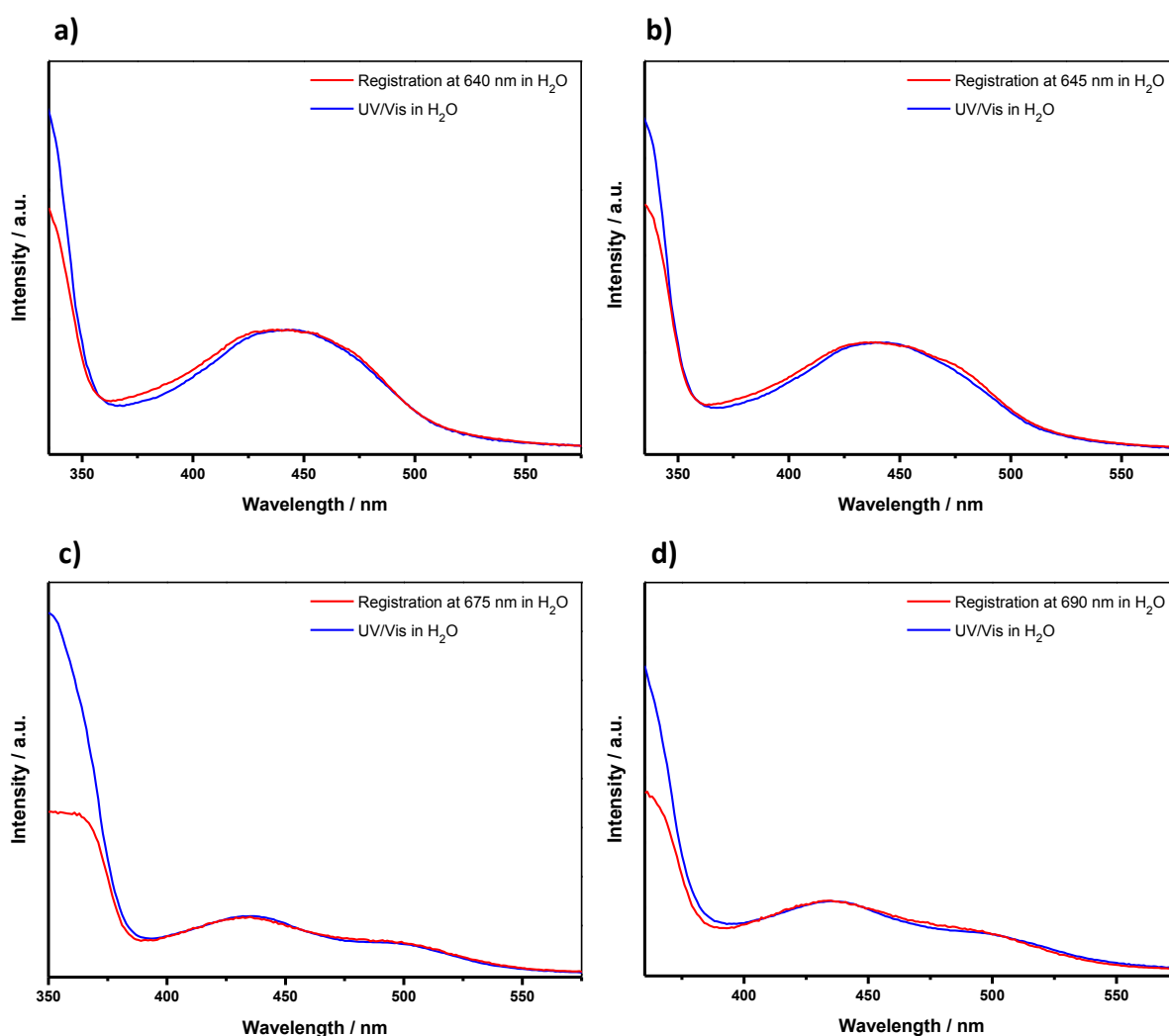

Figure 4.11: Normalised (at λ = 440 nm) spectra in aerated H$_2$O at 298 K. Corrected excitation spectra (red) and UV/Vis spectra (blue) of a) **Ru-Alkyne-Dyad-Mn** (λ_{em} = 640 nm)**,** b) **Ru-Alkyne-Dyad-Zn** (λ_{em} = 645 nm), c) **Ru-Alkyne-Triad-Mn** (λ_{em} = 675 nm) and d) **Ru-Alkyne-Triad-Zn** (λ_{em} = 690 nm)

4.4.3) Stability Experiment

The thermodynamic and kinetic stability of the d-block metal ions (Mn^{II} and Zn^{II}) bound within the polyaminocarboxylate chelate was measured by luminescence spectroscopy (figure **4.12**), as there was evidence of complex dissociation in aqueous solution from the time-resolved luminescence measurements. **Ru-Alkyne-Dyad-Mn** was dissolved in aerated water at a concentration of 1×10^{-5} M in the presence of one equivalent of the competing ligand EDTA (the hexadentate acyclic ligand ethylenediaminetetraacetic acid, used to sequester metal ions). The Ru^{II}-based emission intensity was then monitored by measuring a luminescence spectrum ($\lambda_{ex} = 440$ nm) at various time intervals.
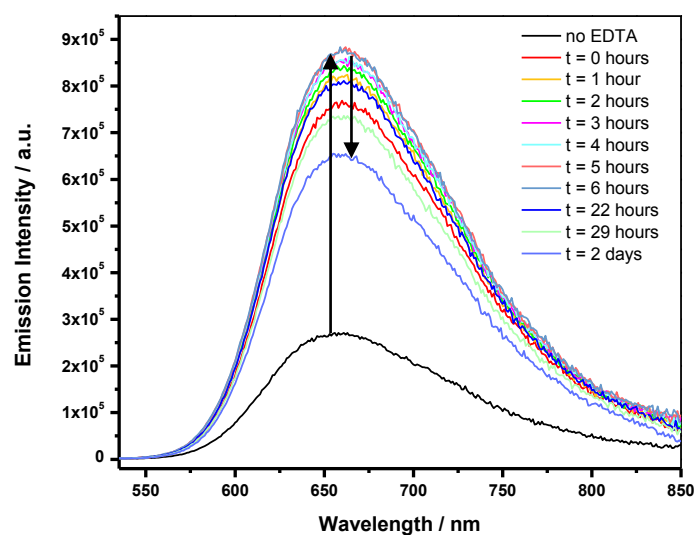

Figure 4.12: Kinetic stability experiment of **Ru-Alkyne-Dyad-Mn** (1×10^5 M) with EDTA (1:1) in aqueous solution ($\lambda_{ex} = 440$ nm)

It can be seen in the initial luminescence spectrum, in which there is no EDTA present in the solution, that the emission intensity is partially quenched (2.5×10^5 a.u.) as the Mn^{II} ions are bound within the chelate. Upon the addition of the metal scavenging ligand EDTA (at t = 0), there is an immediate increase in the Ru^{II}-based emission intensity by a factor of 3 (7.5×10^5 a.u.). This suggests that a portion of the kinetically labile Mn^{II} ions have been stripped from the **Ru-Alkyne-Dyad-Mn** complex, and an equilibrium has been established in solution between the unquenched emission from the dissociated **Ru-Alkyne-Dyad-Acid** starting complex and the partially quenched emission from the non-dissociated **Ru-Alkyne-Dyad-Mn** complex.

A steady increase in the Ru^{II}-based emission intensity is seen up to 6 hours after the initial addition of the EDTA ligand (8.5 x 10^5 a.u.), as more of the Mn^{II} ions are competitively leached out of the polyaminocarboxylate chelate. This is in contrast to the kinetic stability of a Ln^{III} ion bound within the chelate, which was discussed previously (section **2.1**). When one equivalent of a competing DOTA ligand was added to the dinuclear **IrEu** complex (**26**), there was no evidence to suggest that there was any significant leaching of the Eu^{III} ion out of the polyaminocarboxylate chelate over a similar time period. This is most likely due to the different number of stabilising coordination bonds that the metals can make to the chelate. Ln^{III} ions are larger than d-block metal ions and are known to make 8-9 coordination bonds, whereas high-spin Mn^{II} ions have been observed to make only 5-8 coordination bonds[6] and so are stabilised to a lesser extent. However, it is worth noting that the kinetics of Ln^{III}-complex formation with macrocyclic ligands such as DOTA is slow compared to complex formation with acyclic ligands such as EDTA, and so the results measured for the kinetic stability of each metal centre (Eu^{III} *vs.* Mn^{II}) cannot be absolutely compared.

After 22 hours, a steady decrease in the Ru^{II}-based emission intensity can be seen for **Ru-Alkyne-Dyad-Mn** (6 x 10^5 a.u.), which suggests that the EDTA ligand has now compromised the kinetically inert Ru^{II} metal centre as well.

4.5) Photoinduced Electron-Transfer

Femtosecond TA spectroscopy was utilised in order to probe whether photoinduced electron-transfer (PET) processes were occurring in the newly synthesised dinuclear **Ru-Alkyne-Dyad-Mn** complex. However, as neither the Mn^{II} or oxidised Mn^{III} species absorb light significantly in the UV/visible region of the electromagnetic spectrum, formation of the Mn^{III} species cannot be directly detected by TA spectroscopy. As a control experiment, therefore, the dinuclear **Ru-Alkyne-Dyad-Zn** complex was also analysed under identical experimental conditions, as the Zn^{II} metal centre has a d^{10} electronic configuration and so is innocent with respect to the PET processes. Comparing the TA data for **Ru-Alkyne-Dyad-Mn** to **Ru-Alkyne-Dyad-Zn** provides an efficient method to analyse whether electron-transfer processes are occurring in the the Mn^{II}-based complex, as they definitely do not occur in the Zn^{II}-based complex. All transient absorption data was acquired in the Laser Laboratory in the Chemistry Department at the University of Sheffield and was analysed by PhD student James Shipp.

Excitation (λ_{ex} = 400 nm) of a solution of either **Ru-Alkyne-Dyad-Zn** or **Ru-Alkyne-Dyad-Mn** in aerated water with a 40 fs pulse, followed by measurement of the absorption spectra at a series of time delays up to seven nanoseconds, produced similarly shaped differential TA spectra for both **Ru-Alkyne-Dyad-Zn** (figure **4.13a**) and **Ru-Alkyne-Dyad-Mn** (figure **4.13b**). There are positive signals that have maxima at λ_{abs} = 367 nm and λ_{abs} = 456 nm present in both spectra, as well as a broad absorption in the range λ_{abs} = 500-700 nm with a maximum at λ_{abs} = 620 nm. These transient spectral features approximately resemble those of the [phen]$^{\cdot-}$ radical anion in other reduced metal complexes such as [Re^{I}Cl(CO)$_3$(phen$^{\cdot-}$)]$^{-}$[9]. There are also negative signals that have minima at λ_{abs} = 442 nm and λ_{abs} = 480 nm, which can be ascribed to bleaching of the ground state MLCT.

Analysis of the dynamics of the transient signals for each of the heteronuclear complexes reveals different decay kinetics for **Ru-Alkyne-Dyad-Zn** and **Ru-Alkyne-Dyad-Mn**, however. For the dinuclear **Ru-Alkyne-Dyad-Zn** complex (figure **4.13c**) two lifetime components were extracted; a long-lived component (blue trace) that does not completely decay over the pump-probe delay period, and a much shorter-lived component (green trace) with a lifetime of τ = 6 ps. This shorter-lived component can be ascribed to fast vibrational cooling within the complex, and the longer-lived component (which is much larger than the time-limit of the experiment) can be ascribed to the lifetime of the emission from the Ru-

based ^{3}MLCT state, which was previously measured to be τ = 329 ns in aerated water by time-resolved luminescence measurements (section **4.4.2**).
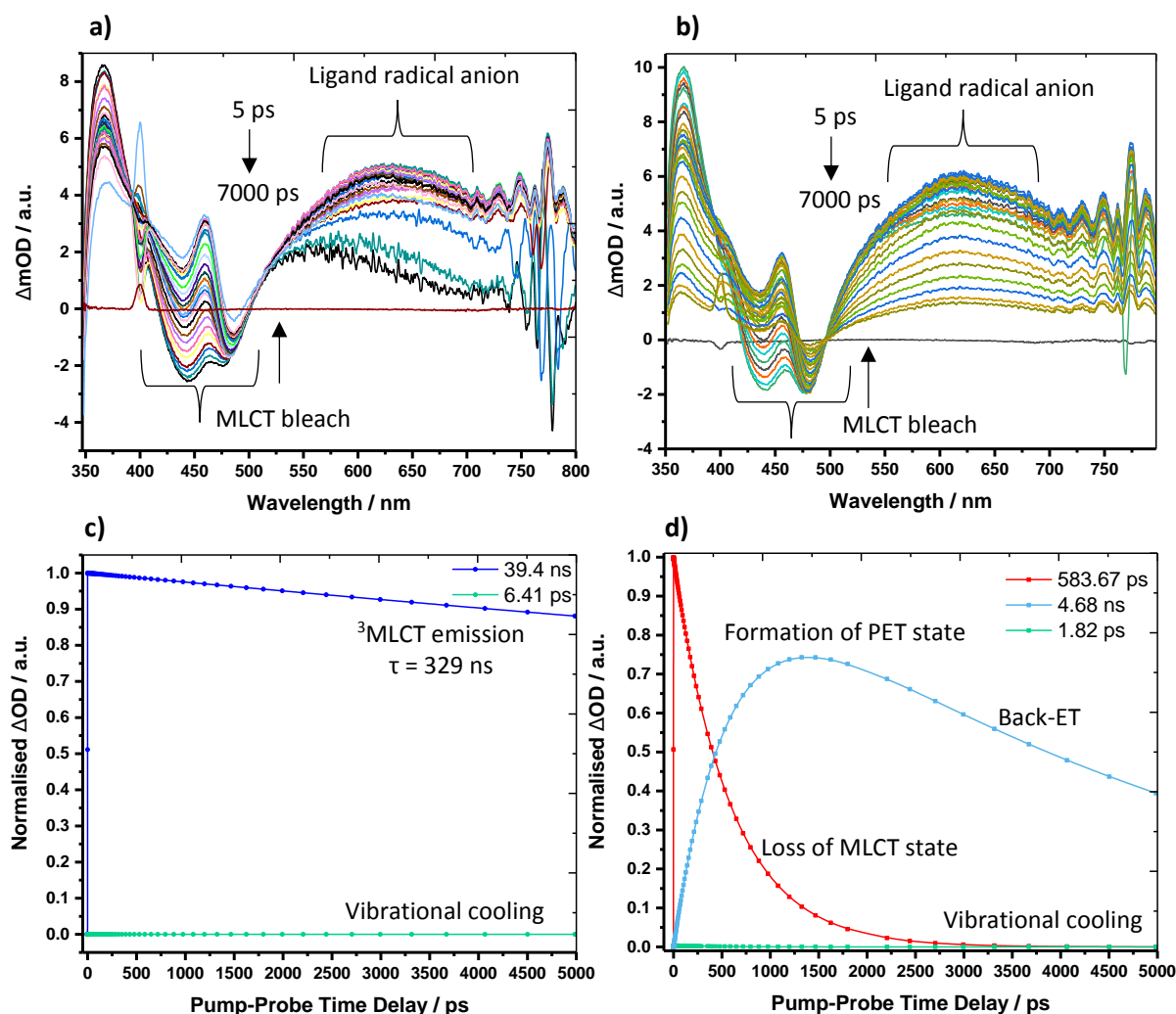

Figure 4.13: Differential transient absorption spectra in aerated H$_2$O at a series of time delays following excitation at λ_{ex} = 400 nm with a 40 fs pulse. a) **Ru-Alkyne-Dyad-Zn**; b) **Ru-Alkyne-Dyad-Mn**; c) dynamics of transient signals for **Ru-Alkyne-Dyad-Zn**; d) dynamics of transient signals for **Ru-Alkyne-Dyad-Mn.**

The dynamics of the transient absorption spectra for the dinuclear **Ru-Alkyne-Dyad-Mn** complex are more complicated than for **Ru-Alkyne-Dyad-Zn** (figure **4.13d**) and require three lifetime components to fit the decay profile satisfactorily. A shorter-lived component, with a lifetime of τ = 2 ps (green trace), is ascribed to fast vibrational cooling within the complex. A further decay process with a lifetime of τ = 584 ps (red trace) is synchronous with the grow-in for the component that subsequently decays with a lifetime of τ = 5 ns (blue trace). This indicates that the two components are associated, with one component decaying at the same rate that the other grows in. As the processes on these timescales are not present

in the dinuclear **Ru-Alkyne-Dyad-Zn** complex, it suggests that they may be a consequence of fast PET processes between the Ru^{II} and Mn^{II} metal centres in **Ru-Alkyne-Dyad-Mn**, which can be described using a simplified Jablonksi diagram (figure **4.14**).
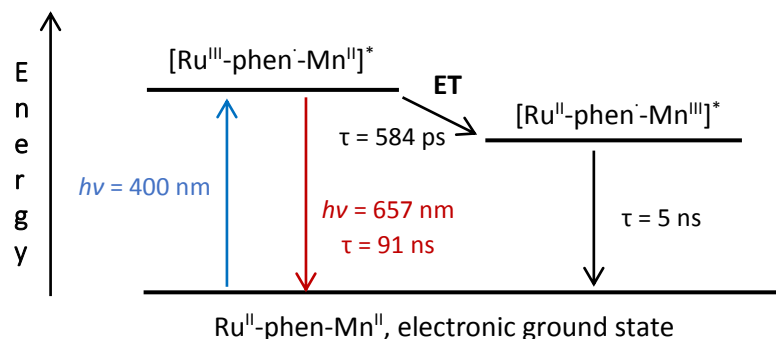

Figure 4.14: Simplified Jablonski diagram illustrating the possible PET processes in **Ru-Alkyne-Dyad-Mn**. The Ru^{II} metal centre absorbs a photon of light (hv = 400 nm) to produce an MLCT state in which the Ru^{II} centre has been photo-oxidised to Ru^{III}. The Mn^{II} centre then transfers an electron (ET) to reduce the Ru^{III} centre to Ru^{II} (τ = 584 ps), oxidising to Mn^{III} in the process. The Mn^{III} ion then recovers its electron through an oxidation process and the whole molecule returns to the electronic ground state (τ = 5 ns).

The observed τ = 584 ps decay process (red trace) is consistent with the decay of the initially-photogenerated MLCT state of the **Ru-Alkyne-Dyad-Mn** complex ([Ru^{III}-phen$^-$-Mn^{II}]*) to give the new charge-separated state ([Ru^{II}-phen$^-$-Mn^{III}]*) by PET from the Mn^{II} centre to the photogenerated Ru^{III} centre. This new charge-separated state decays with a τ = 5 ns lifetime, which can be tentatively ascribed to back-electron-transfer (BET). Note that direct luminescent decay from the Ru^{II}-based ^{3}MLCT state is not observed.

If we assume that the lifetime of the PET process is τ = 584 ps, this gives the rate of electron-transfer (k_{et}) between the Mn^{II} centre and the photogenerated Ru^{III} centre to be k_{et} = 1.71 x 10^9 s^{-1}. This rate of electron-transfer is much faster than previously reported Ru^{II}-Mn^{II} dyads (figure **4.03**)[2], that had values in the range k_{et} = 2 x 10^5 − 2 x 10^6 s^{-1}. This may be a consequence of a decreased intramolecular Ru-Mn distance in the newly synthesised **Ru-Alkyne-Dyad-Mn** complex compared to the previously reported complexes, or the extended conjugation in the newly synthesised complex facilitating more efficient inner-sphere PET than the previous saturated bridging ligands.

To probe the possible PET process from the Mn^{II} centre to the photogenerated Ru^{III} centre in **Ru-Alkyne-Dyad-Mn** further, the redox potentials for the Mn$^{II/III}$ and Ru$^{II/III}$ couples were measured by cyclic voltammetry. For comparison purposes, the Ru$^{II/III}$ couple in **Ru-**

Alkyne-Dyad-Zn was also measured. However, as both **Ru-Alkyne-Dyad-Mn** and **Ru-Alkyne-Dyad-Zn** only have high enough solubility in protic solvents such as water, the potential window limits for the voltammetry experiment prevented observation of the $Ru^{II/III}$ couples, which are masked in the voltammograms for both complexes by the high background current (appendix **4.07**). The $Mn^{II/III}$ couple in **Ru-Alkyne-Dyad-Mn** is also not obvious in the voltammogram at the expected redox potential value (0.80 – 0.90 V), which is an issue that has been reported for other Ru^{II}-Mn^{II} dyads where the $Mn^{II/III}$ couple redox potential was measured in anhydrous acetonitrile[2]. Attempts at measuring the redox potentials for the $Ru^{II/III}$ couple in **Ru-Alkyne-Dyad-Zn** and the $Mn^{II/III}$ and $Ru^{II/III}$ couples in **Ru-Alkyne-Dyad-Mn** in the anhydrous, aprotic solvent DMF also proved unsuccessful, as the solubility of both complexes in the solvent was too low to produce solutions of high enough concentration to probe.

4.6) Summary

The two new water-soluble, ruthenium(II) bis(2,2'-bipyridine)-based complexes, **Ru-Alkyne-Dyad-Mn** and **Ru-Alkyne-Triad-Mn**, exhibited mixed potential when evaluated as dual-modal optical/MR imaging agents. The probes demonstrated similar relaxivity values (r_1 = 3.7 mM^{-1}s^{-1} and r_1 = 4.8 mM^{-1}s^{-1}, respectively) to the commercial Gd^{III}-based contrast agent, Magnevist®, and reduced relaxivity values when compared to the analogous Gd^{III}-based complexes, **Ru-Alkyne-Dyad-Gd** and **Ru-Alkyne-Triad-Gd**, when measured in D$_2$O at 400 MHz and 298 K. However, considering that **RuMn$_n$** (n = 1, 2) complexes have a lower number of unpaired electrons compared to the **RuGd$_n$** (n = 1, 2) analogues, and hence lower magnetic moments, as well as reduced numbers of water coligands due to the smaller ionic radius of the Mn^{II} ion compared to the Gd^{III} ion, these relaxivity values can be considered respectable. Evaluation of the probes for optical microscopy was not undertaken, however, as the Ru^{II}-based emission was significantly quenched. This was possibly due to both photoinduced *energy*-transfer from the excited [Ru(bipy)$_2$(phen)]$^{2+}$ centre to the low-energy excited states on the Mn^{II} metal centre(s), and photoinduced *electron*-transfer from the Mn^{II} centre to the photogenerated Ru^{III} centre.

Transient absorption (TA) spectroscopy was utilised to probe whether photoinduced electron-transfer (PET) processes were occurring in the newly synthesised dinuclear **Ru-Alkyne-Dyad-Mn** complex, as well as in a **Ru-Alkyne-Dyad-Zn** analogue for comparison purposes. The dynamics of the transient signals for the dinuclear **Ru-Alkyne-Dyad-Zn** complex revealed only two lifetime components; a very short-lived decay (τ = 6 ps) for vibrational cooling, and a very long-lived decay (τ > 7 ns) for the decay of the Ru-based ^{3}MLCT state. The dynamics of the transient signals for the dinuclear **Ru-Alkyne-Dyad-Mn** complex were more complicated, however, with a fast component (τ = 584 ps) possibly representing ET between the Mn^{II} centre and the photogenerated Ru^{III} centre. This gave a rate of inner-sphere electron-transfer to be k_{et} = 1.71 x 10^9 s^{-1}, which is much faster than previously reported Ru^{II}-Mn^{II} dyads that had values in the range k_{et} = 2 x 10^5 – 2 x 10^6 s^{-1}.

Overall, the newly synthesised **RuMn$_n$** (n = 1, 2) complexes are not ideal candidates for dual-modal optical/MR imaging agents due to the Ru^{II}-based emission being significantly quenched. The possible ET processes occurring between the two different metal centres

mimic those that occur in PSII during photosynthesis in green plants, however, and so the new complexes may be useful as artificial models for PSII.

4.7) Future Work

To continue this work further, it would be interesting to analyse the MRI functionality of the new water-soluble **RuMn$_n$** (n = 1, 2) complexes in more detail. Measurement of the Mn^{II} hydration state in the polyaminocarboxylate chelate and the rotational correlation time (τ_R) for each of the **RuMn$_n$** (n = 1, 2) complexes would provide insight into the relaxivity values observed. Measuring the r_1 values for the **RuMn$_n$** (n = 1, 2) complexes under different experimental conditions, such as in a 4 % solution of human serum albumin (HSA) and in PBS, would also aid the understanding of how the complexes are likely to behave *in vivo*. Creating a nuclear magnetic relaxation dispersion (NMRD) profile for each of the complexes would also provide insight into how the measured relaxivity values are likely to change depending on the magnet frequency.

With regards to the possible PET observed in the Mn^{II}-based complexes, it would be appealing to assess whether the complexes can oxidise water molecules to produce molecular oxygen, in a similar process to that which occurs in PSII during photosynthesis in green plants.

4.8) References

1   W. Shi, B. Song, W. Shi, X. Qin, Z. Liu, M. Tan, L. Wang, F. Song and J. Yuan, *ACS Appl. Mater. Interfaces*, 2018, **10**, 27681–27691.

2   K. E. Berg, A. Tran, M. K. Raymond, M. Abrahamsson, J. Wolny, S. Redon, M. Andersson, L. Sun, S. Styring, L. Hammarström, H. Toftlund and B. Åkermark, *Eur. J. Inorg. Chem.*, 2001, **2001**, 1019–1029.

3   E. A. Karlsson, B.-L. Lee, R.-Z. Liao, T. Åkermark, M. D. Kärkäs, V. S. Becerril, P. E. M. Siegbahn, X. Zou, M. Abrahamsson and B. Åkermark, *Chempluschem*, 2014, **79**, 936–950.

4   A. G. Tebo, S. Das, R. Farran, C. Herrero, A. Quaranta, R. Fallahpour, S. Protti, M.-F. Charlot and W. Leibl, *Comptes Rendus Chim.*, 2017, **20**, 323–332.

5   A. Jana, E. Baggaley, A. Amoroso and M. D. Ward, *Chem. Commun.*, 2015, **51**, 8833–8836.

6   E. M. Gale, J. Zhu and P. Caravan, *J. Am. Chem. Soc.*, 2013, **135**, 18600–18608.

7   G. Dehaen, P. Verwilst, S. V. Eliseeva, S. Laurent, L. Vander Elst, R. N. Muller, W. M. De Borggraeve, K. Binnemans and T. N. Parac-Vogt, *Inorg. Chem.*, 2011, **50**, 10005–10014.

8   H. Berglund-Baudin, L. Sun, R. Davidov, M. Sundahl, S. Styring, B. Åkermark, M. Almgren and L. Hammarström, *J. Phys. Chem. A*, 1998, **102**, 2512–2518.

9   S. Záliš, C. Consani, A. El Nahhas, A. Cannizzo, M. Chergui, F. Hartl and A. Vlček, *Inorganica Chim. Acta*, 2011, **374**, 578–585.
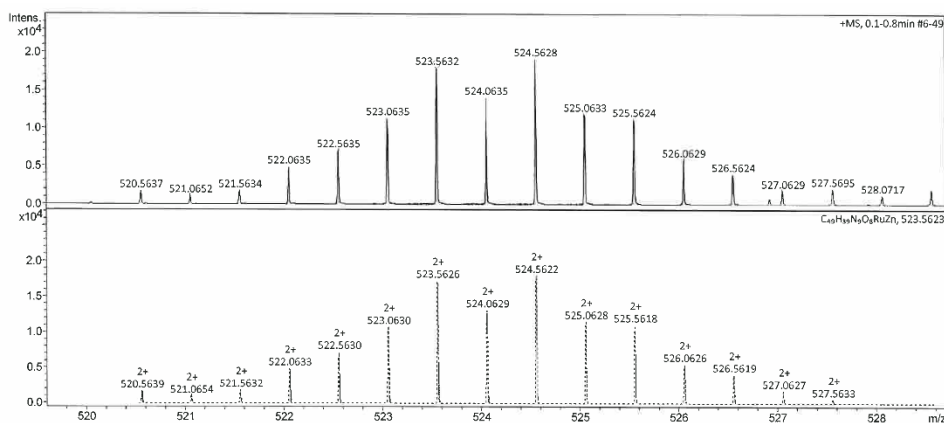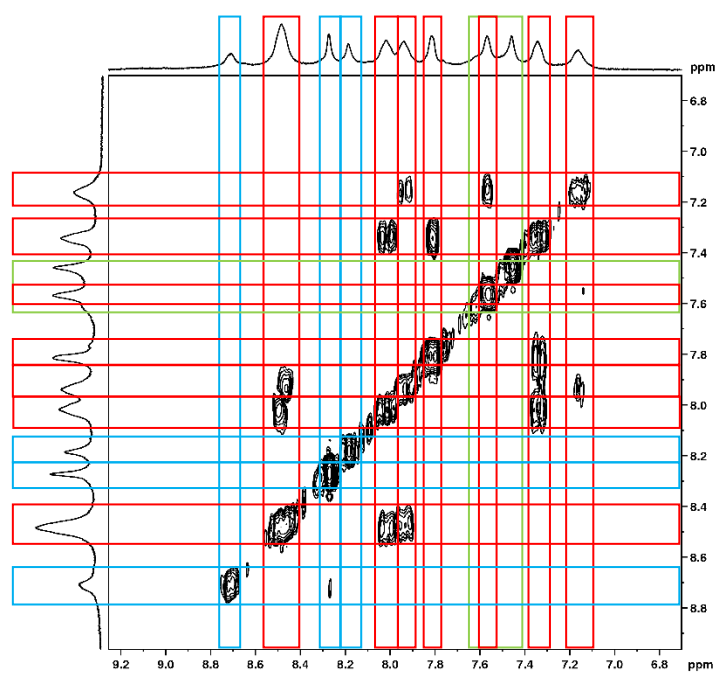
4.9) Appendices
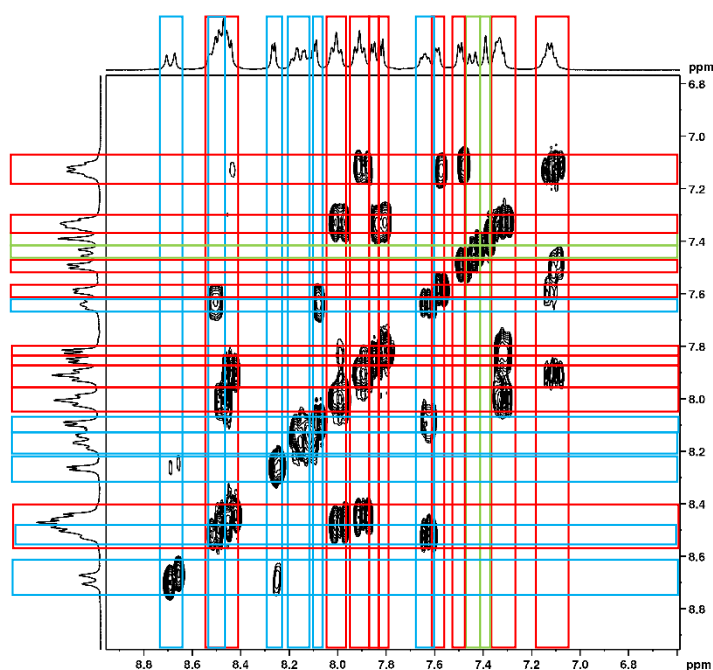
Appendix 4.01: The aromatic region of an annotated ^{1}H-^{1}H correlation NMR spectrum (400 MHz, D$_2$O) for **Ru-Alkyne-Dyad-Zn** at 298 K. (Red lines = protons on bipyridine ligand, blue lines = protons on phenanthroline ligand, green lines = protons on pyridine ligand)
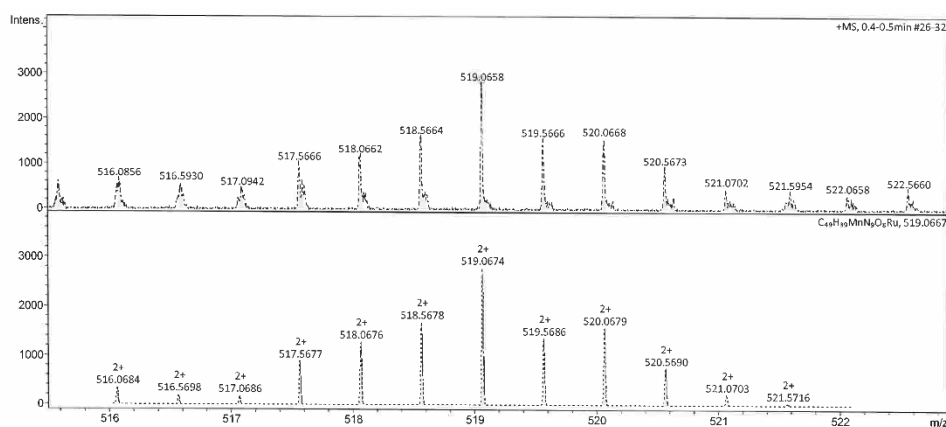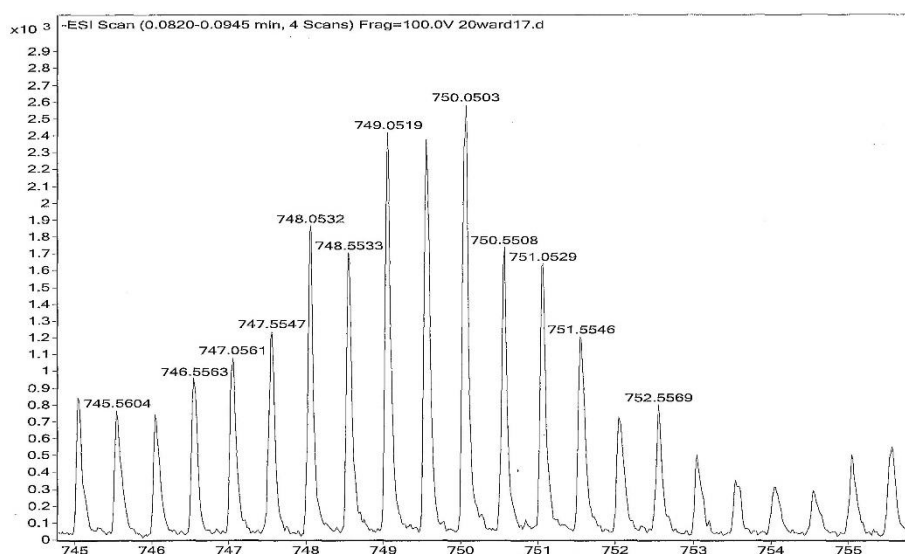

Appendix 4.02: High-resolution mass spectrum of **Ru-Alkyne-Dyad-Mn**. Calculated for [C$_{49}$H$_{37}$N$_9$O$_8$RuMn + 2H]$^{2+}$, 519.0667.

Appendix 4.03: High-resolution mass spectrum of **Ru-Alkyne-Dyad-Zn**.
Calculated for [C$_{49}$H$_{37}$N$_9$O$_8$RuZn + 2H]$^{2+}$, 523.5623.


Appendix 4.04: The aromatic region of an annotated ^{1}H-^{1}H correlation NMR spectrum (400 MHz, D$_2$O) for **Ru-Alkyne-Triad-Zn** at 298 K. (Red lines = protons on bipyridine ligand, blue lines = protons on phenanthroline ligand, green lines = protons on pyridine ligand)

Appendix 4.05: High-resolution mass spectrum of **Ru-Alkyne-Triad-Zn**.
Calculated for $[C_{66}H_{50}N_{12}O_{16}{}^{102}Ru^{64}Zn_2]^{2-}$, 748.0553.
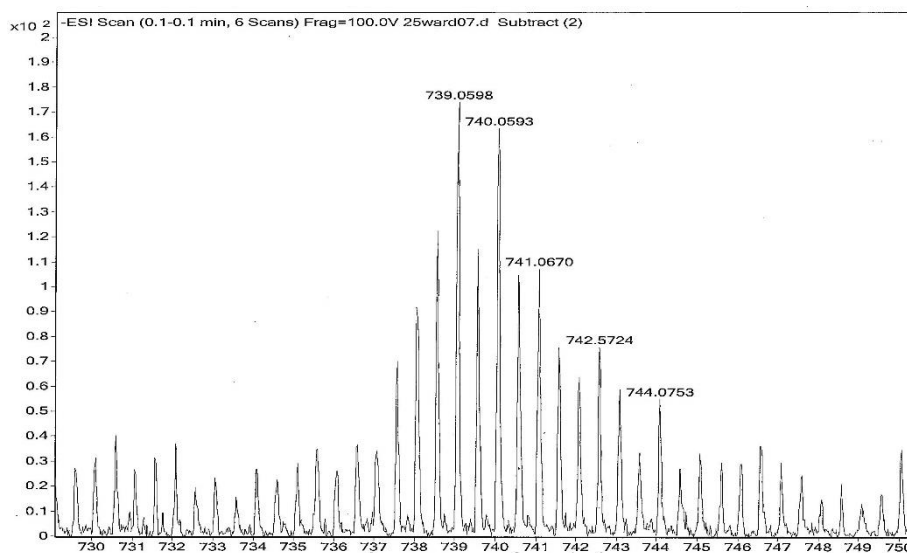
Appendix 4.06: High-resolution mass spectrum of **Ru-Alkyne-Triad-Mn**.
Calculated for $[C_{66}H_{50}N_{12}O_{16}{}^{102}RuMn_2]^{2-}$, 739.0631.
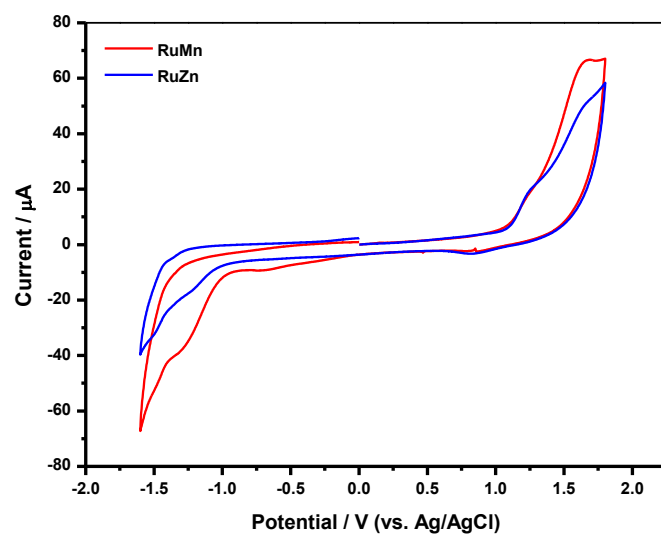
Appendix 4.07: Cylic voltammograms of **Ru-Alkyne-Dyad-Mn** (2.0 mM) and **Ru-Alkyne-Dyad-Zn** (1.4 mM) in 0.2 M Bu_4NPF_6/H_2O at a glassy-carbon electrode *vs*. Ag/AgCl. (Scan rate = 100 mV s^{-1})

Chapter 5

Ru^{II}-Nd^{III} and Ru^{II}-Yb^{III} Complexes as Dual-Modal Optical/NIR Imaging Agents

5.1) Introduction

5.1.1) Luminescence from Lanthanide Ions

The lanthanide (Ln) elements have been an appealing topic of research for some time now due to the wealth of interesting properties that they possess; especially in terms of their interactions with light. Much of their chemistry is dominated by the trivalent cationic species (Ln^{III}) with the electronic configuration [Xe]4f^n (where n = 0-14), as these ions demonstrate distinctive photophysical behaviour, which can be attributed to the 4f orbitals being both highly contracted and shielded by the filled outer orbitals. On absorption of a photon, an electron on the Ln^{III} ion is promoted to an f-f excited state, but this stored energy is not easily dissipated by molecular vibrations (in contrast to transition-metal d-d excited states) due to weak coupling between the buried f-orbitals and their surrounding environment. Instead the energy is more likely to be re-emitted as a photon in the process of luminescence, producing a sharp, monochromatic emission band.

Overall, the group of elements has a broad range of emission energies across the ultraviolet (UV), visible and near-infrared regions (NIR) of the electromagnetic spectrum, with each Ln^{III} ion having its own uniquely identifying spectrum of closely-spaced multiple emission lines (figure **5.01**). This is due to the energy levels being further subdivided into many electronic levels, as a consequence of the different possible arrangements of electrons within the 4f orbitals arising from spin-orbit coupling. Emission of a photon originates from a single excited-state down to the many electronic levels of the ground state, with each transition being of a slightly different energy. Ions such as Eu^{III}, Tb^{III}, Sm^{III} and Tm^{III} mainly emit in the visible region of the electromagnetic spectrum (red, green, orange and blue, respectively), whereas ions such as Nd^{III}, Yb^{III}, Er^{III}, and Pr^{III} have their main emission bands in the NIR region.

The practicality of exploiting luminescence from Ln^{III} ions is hindered, however, because of their low absorption coefficients (typically $\varepsilon < 10$ M^{-1} cm^{-1}). This is due to f-f transitions being Laporte forbidden, which makes generation of the excited-state by direct absorption of light difficult. This selection rule has the potential to be circumvented in a number of ways, such as coupling the electronic excited-state of the Ln^{III} ion to the vibrational states of the surrounding ligands, or by mixing the f-orbitals with those of opposite parity such as the 5d or 6s orbitals. However, both methods rely on the overlap of the f-orbitals with their surrounding environment, which does not occur satisfactorily due to the 4f orbitals being

highly contracted. Direct excitation of a Ln^{III} ion is, therefore, very inefficient (producing particularly low emission intensities), and as a result, lanthanide salts are very pale in colour or have no colour at all. To produce strong emission from a Ln^{III} ion, sensitisation has to occur through the use of an intense light source such as a laser, or more commonly *via* an indirect manner using a light-harvesting antenna group (known as the 'antenna effect').
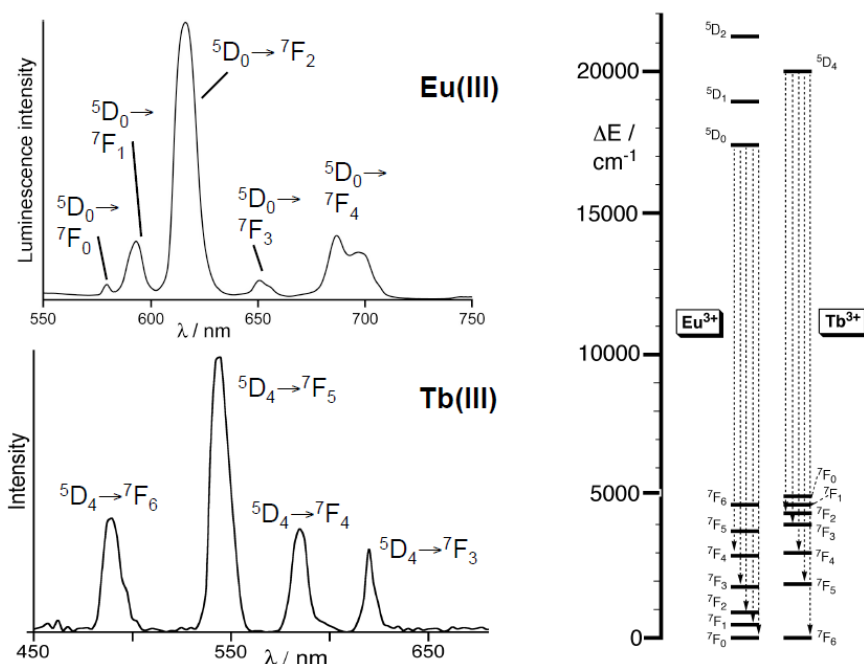

Figure 5.01: Emission spectra for the lanthanide ions Eu^{III} and Tb^{III} showing the various f-f transitions from a single excited state to the many electronic levels of the ground state

5.1.2) Sensitising Luminescence from Lanthanide Ions *via* d→f Energy-Transfer

The use of intramolecular photoinduced energy-transfer (PEnT) to sensitise luminescence from Eu^{III} (and other Ln^{III} ions) was first pioneered by Weissman in 1942[1]. Since then Lehn[2] has reported of a 'two-component light-conversion molecular device', from which dual luminescence was observed. The chromophore was selectively excited at one wavelength; the excited-state energy was funnelled *via* partial PEnT through an organic bridging ligand to a Ln^{III} luminophore; and then the luminophore re-emitted the energy at a longer wavelength (figure **5.02**). Luminescence from the chromophore was also observed due to incomplete PEnT.
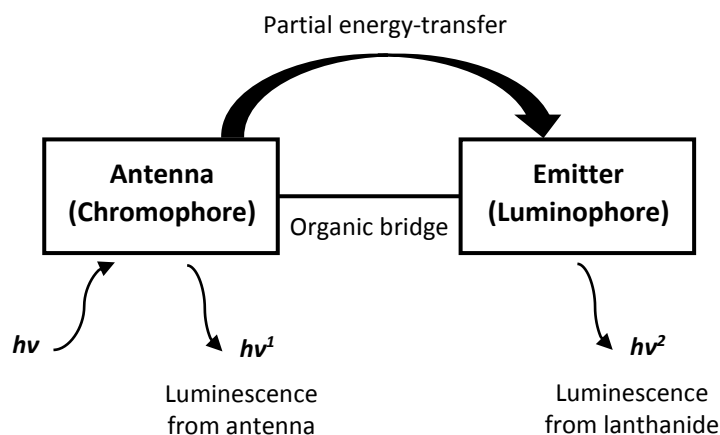
Figure 5.02: Schematic to show the 'antenna effect' used to sensitise luminescence from a Ln^{III} ion. The incident light absorbed by the chromophore is emitted at a different wavelength by the Ln^{III} luminophore due to partial PEnT across an organic bridge

The mechanism by which this sensitisation process works is complex, and more than one possible pathway has been observed (direct EnT pathways and a photoinduced electron-transfer-initiated EnT pathway)[3]. The direct EnT pathway is considered to be the more conventional of the two and is the one most often observed in sensitisation of Ln^{III} luminescence. The overall process can be described with a simplified Jablonski diagram (figure **5.03**).

On absorption of a photon, an electron in the chromophore is promoted into a higher energy orbital taking the molecule from the ground state (S_0) to an excited singlet state (S^*). From the many electronic levels of this excited-state the chromophore undergoes inter-system crossing (ISC) to an excited triplet state (T^*) still centred on the chromophore. From the T^* energy level on the chromophore, partial ligand-to-metal EnT occurs across to the many electronic levels of the excited-state on the lanthanide luminophore (Ln^*). Depending on the level of conjugation in the organic bridge between the chromophore and the luminophore, and the EnT mechanism (through-bond [Dexter] or through-space [Förster]), the timescale of this process can vary from nanoseconds to microseconds. Internal conversion (IC) from the higher energy electronic levels on the Ln^{III} ion to the lowest energy electronic level occurs at this point, before a photon is emitted from the Ln^* excited state, which collapses to one of the various electronic levels of the Ln ground state. Emission can be in the form of fluorescence (τ = ns) or phosphorescence (τ = µs or longer) depending on the nature of the emissive level.
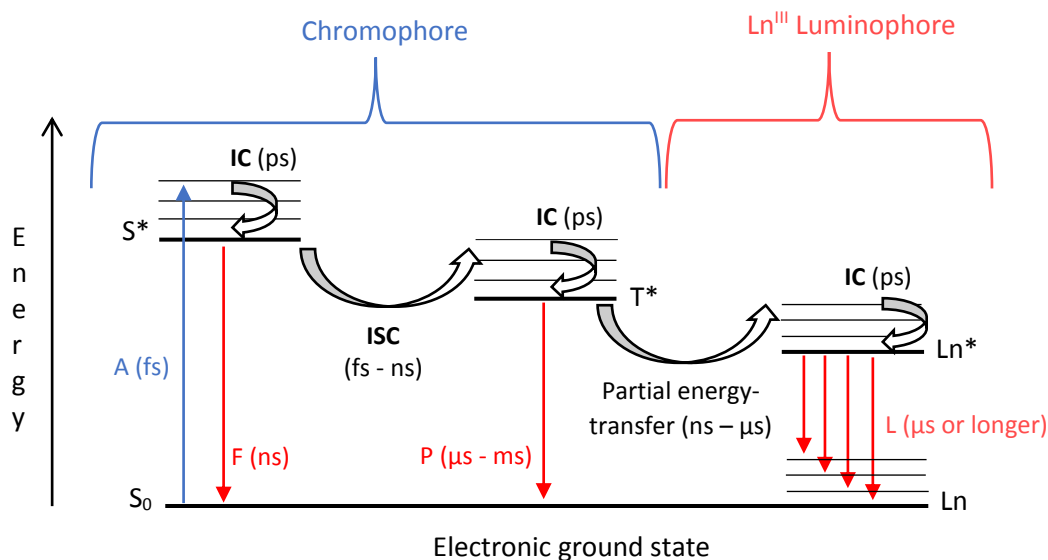
Figure 5.03: A simplified Jablonski diagram illustrating the transitions between electronic states of a metal complex during the 'antenna effect' used to sensitise emission from a Ln^III ion. S_0 = singlet ground state, A = absorption, S* = singlet excited state, IC = internal conversion, F = fluorescence, ISC = inter-system crossing, T* = excited triplet state, P = phosphorescence, Ln* = excited lanthanide state, L = luminescence, Ln = lanthanide ground state, fs, ps, ns, μs, ms = femto-, pico-, nano-, micro- and milli-second respectively. Coloured and block arrows represent radiative and non-radiative processes respectively.

5.1.3) Previous Work in the Ward Group

Sensitised luminescence from Ln^III ions was recently reported in heteronuclear Ir^III-Nd^III and Ir^III-Yb^III dyads by the Ward group[4]. The dinuclear complexes are based on the monosubstituted phenanthroline ligand previously discussed in this thesis (section **2.2**), with an identical polyaminocarboxylate binding site for the Ln^III ions; however, the d-block metal centre acting as the 'antenna group' in this case is [Ir(ppy)$_2$(phen)]^+ (where 'ppy' denotes the ligand phenylpyridine) (**31**, figure **5.04**).

Following photoexcitation (λ_{ex} = 355 nm), both **IrYb** and **IrNd** produced an Ir^III-based emission band (λ_{em} = 640 nm), which corresponds to luminescence from the ^{3}MLCT/^{3}LLCT excited-state. Luminescence from the Ln^III ions was observed in the NIR region of the emission spectra for each of the complexes, which had to be a result of sensitisation through d→f PEnT, as the excitation wavelength at λ_{ex} = 355 nm was into the Ir^III-based absorption band. In the spectrum for the dinuclear **IrYb** complex, a weak emission feature at λ_{em} = 980 nm was observed, which is the $^2F_{5/2} \rightarrow {}^2F_{7/2}$ transition on the Yb^III ion. Time-resolved luminescence measurements at this wavelength revealed a long-lived lifetime component (τ = 7.4 μs), which

is characteristic of Yb^{III}-based decay. There was no detectable loss of the Ir^{III}-based emission in this complex, however, and so the rate of Ir→Yb PEnT was low. In the spectrum for the dinuclear **IrNd** complex, sensitisation of the Nd^{III}-based luminescence was observed as two emission bands at λ_{em} = 1060 nm and λ_{em} = 1330 nm, which are the $^4F_{3/2}{\rightarrow}^4I_n$ transitions (n = 11/2, 13/2, respectively). Time-resolved luminescence measurements at these wavelengths revealed shorter-lived lifetime components of τ = 170 ns, which corresponds to the Nd^{III}-based decay, as the Ir^{III}-based decay lifetime is much shorter (τ = 33 ns). Quenching of the Ir^{III}-based luminescence was more pronounced for this complex, with the rate of Ir→Nd PEnT calculated to be k_{EnT} = 1.0 x 10^7 s^{-1}.

Mixed d/f metal complexes of this kind, in which there are two different metal centres, each with distinct photophysical properties, have recently begun to be explored as dual-modal optical/optical imaging agents. A dinuclear **IrEu** compound (**25**, figure **2.02**) displayed both Ir^{III}-based luminescence and Eu^{III}-based emission after excitation at λ_{ex} = 780 nm, as a consequence of partial Ir→Eu PEnT[5]. As the decay lifetimes for the individual metals were different by orders-of-magnitude, they could be identified by time-gated detection, as the shorter-lived luminescence from the Ir^{III} component could be rejected. When applied to cellular imaging, this enabled autofluorescence-free sensing of two different analytes, simultaneously and independently, and as the metals are tethered together through chemical bonds, in the same regions of a cell.
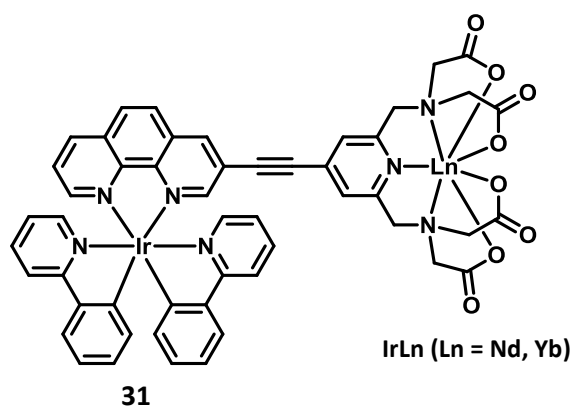

Figure 5.04: Examples of previously prepared dinuclear Ir^{III}-Ln^{III} complexes (Ln = Nd, Yb)

To expand upon this work, ruthenium(II) bis(2,2'-bipyridine)-based analogues of the dinuclear acetylene-bridged **IrLn** (Ln = Nd, Yb) complexes have been synthesised (**Ru-Alkyne-Dyad-Ln** (Ln = Nd, Yb), figure **5.05**). To extend the series of acetylene-bridged, heteronuclear d/f complexes further, the synthesis of trinuclear complexes has also been undertaken (**Ru-Alkyne-Triad-Ln** (Ln = Nd, Yb), figure **5.05**). Emission spectra and time-resolved luminescence measurements were recorded for all of the complexes across the visible and NIR regions, with sensitised d→f PEnT recorded in all cases. For each of the four **RuLn_n** (Ln = Nd, Yb, n = 1, 2) complexes, the rate of Ru→Ln PEnT has been calculated.
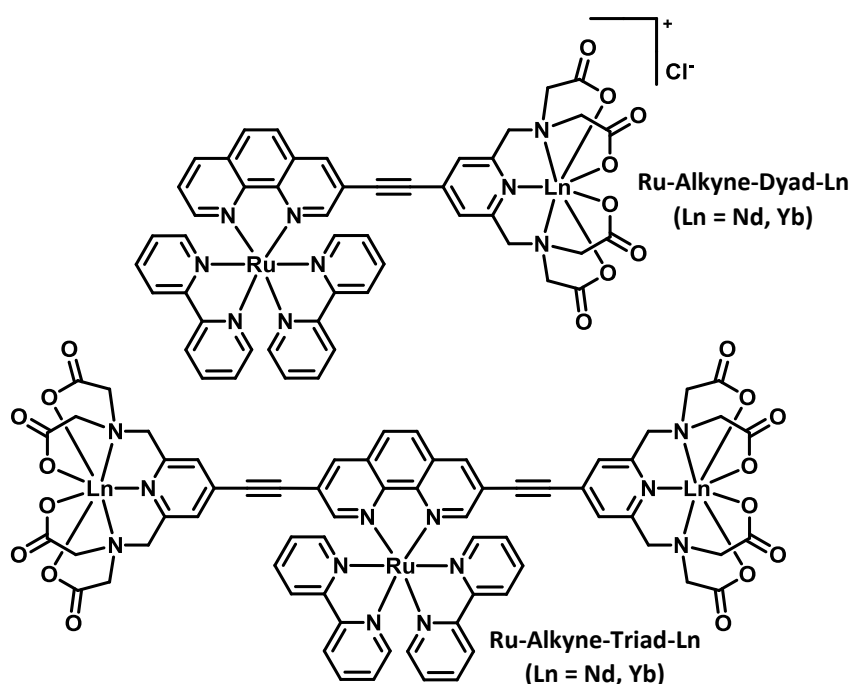

Figure 5.05: Structures of the newly synthesised, water-soluble **Ru-Alkyne-Dyad-Ln** and **Ru-Alkyne-Triad-Ln** (Ln = Nd, Yb) complexes

5.2) Synthesis and Characterisation

5.2.1) Alkyne-Bridged Dinuclear Ru^{II}-Nd^{III} and Ru^{II}-Yb^{III} Compounds

The two heterodinuclear complexes, **Ru-Alkyne-Dyad-Nd** and **Ru-Alkyne-Dyad-Yb**, were synthesised in good yields (83-95 %) from the monosubstituted phenanthroline carboxylic acid scaffold, **Ru-Alkyne-Dyad-Acid** (section **2.2**). One equivalent of the acid was dissolved in water at pH 5-6 and stirred at room temperature with 1.6 equivalents of the appropriate lanthanide triflate salt (Ln = Nd or Yb) for eighteen hours (scheme **5.01**). To improve the solubility of the resulting **Ru-Alkyne-Dyad-Ln** (Ln = Nd, Yb) complexes in water, counterion exchange to a chloride ion was performed using Dowex® 1x2 chloride form (100-200 mesh). To remove the excess lanthanide salt, the complexes were purified by size-exclusion chromatography on Sephadex® G-15 in water.
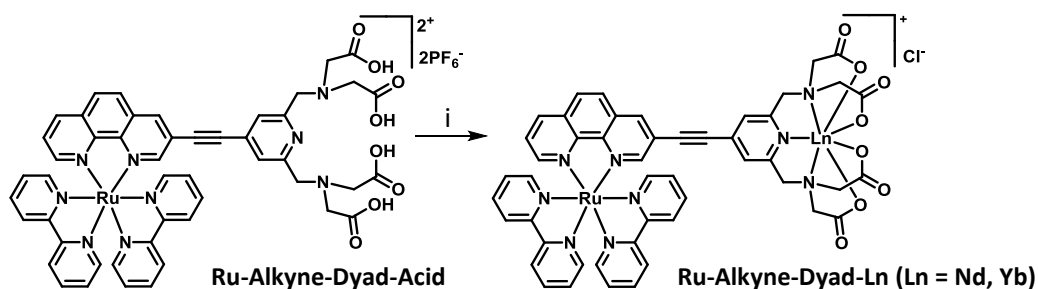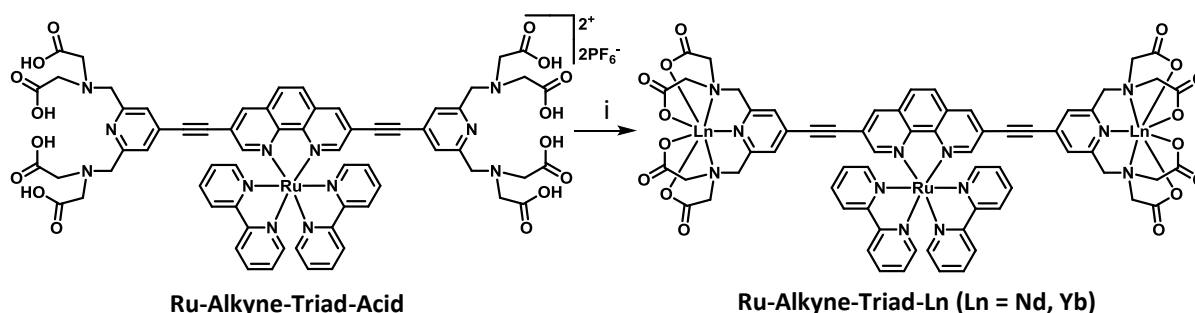

Scheme 5.01: Synthetic route to **Ru-Alkyne-Dyad-Ln (Ln = Nd, Yb)**.
i) H$_2$O (pH 5-6), Ln(OTf)$_3$ (Ln = Nd, Yb), rt, 18h

High-resolution mass spectra were recorded for both **Ru-Alkyne-Dyad-Nd** and **Ru-Alkyne-Dyad-Yb** (appendices **5.01** and **5.02**, respectively). In both cases the calculated and observed *m/z* values for the [*M* – Cl + H]$^{2+}$ ion agreed well (563.0488 and 563.0497 for **Ru-Alkyne-Dyad-Nd**, respectively, and 578.0632 and 578.0632 for **Ru-Alkyne-Dyad-Yb**, respectively), and the distinct isotope pattern observed in each case matched that expected for the different lanthanide ions.

5.2.2) Alkyne-Bridged Trinuclear Ru^{II}-Nd$^{III}_2$ and Ru^{II}-Yb$^{III}_2$ Compounds

The trinuclear compounds, **Ru-Alkyne-Triad-Nd** and **Ru-Alkyne-Triad-Yb**, in which two lanthanide metal chelates surround the central Ru^{II} metal complex, were synthesised in high yields (97-99 %) in an analogous manner to their dinuclear counterparts (scheme **5.02**). The starting alkyne-bridged, phenanthroline carboxylic acid scaffold in this case was the disubstituted complex, **Ru-Alkyne-Triad-Acid** (section **2.3**), and 2.4-2.8 equivalents of the appropriate lanthanide triflate salt (Ln = Nd or Yb) was added to the reaction mixture to account for the extra vacant metal binding site. As the resulting trinuclear compounds are neutral, no counterion exchange was necessary.

Ru-Alkyne-Triad-Acid   **Ru-Alkyne-Triad-Ln (Ln = Nd, Yb)**

Scheme 5.02: Synthetic route to **Ru-Alkyne-Triad-Ln (Ln = Nd, Yb)**.
i) H$_2$O (pH 5-6), Ln(OTf)$_3$ (Ln = Nd, Yb), rt, 18h

Again, HRMS was used to confirm the successful synthesis and isolation of the target trinuclear complexes, **Ru-Alkyne-Triad-Nd** and **Ru-Alkyne-Triad-Yb** (appendices **5.03** and **5.04**, respectively). In both cases the observed m/z value for the $[M + 2H]^{2+}$ ion agreed well with the calculated value (829.0404 and 829.0429, respectively, for **Ru-Alkyne-Triad-Nd**, and 858.0683 and 858.0710, respectively, for **Ru-Alkyne-Triad-Yb**), and the isotope patterns were as expected for each of the different lanthanide ions.

5.3) Photophysical Properties

UV/Vis absorption spectra were recorded in several solvents for **Ru-Alkyne-Dyad-Nd**, **Ru-Alkyne-Dyad-Yb**, **Ru-Alkyne-Triad-Nd** and **Ru-Alkyne-Triad-Yb**, and extinction coefficients were measured for all compounds in water. Emission profiles and lifetimes for the Ru^{II}-based emission were recorded for all compounds (including as a frozen glass at 77 K for **Ru-Alkyne-Dyad-Nd** and **Ru-Alkyne-Dyad-Yb**), and the quantum yield of the Ru^{II}-based emission was measured for all compounds against [Ru(bipy)$_3$]Cl$_2$.6H$_2$O in aerated water. Ln^{III}-based emission profiles and luminescence decay lifetimes were measured in deuterium oxide and deuterated methanol for **Ru-Alkyne-Dyad-Nd** and **Ru-Alkyne-Dyad-Yb** and in deuterium oxide for **Ru-Alkyne-Triad-Nd** and **Ru-Alkyne-Triad-Yb**. Finally, excitation spectra were measured at two different emission wavelengths (one corresponding to Ru^{II}-based emission and one to sensitised Ln^{III}-based emission) for each complex.

5.3.1) UV/Vis Absorption

UV/Vis absorption profiles for **Ru-Alkyne-Dyad-Nd**, **Ru-Alkyne-Dyad-Yb**, **Ru-Alkyne-Triad-Nd** and **Ru-Alkyne-Triad-Yb** were recorded in several solvents (table **5.01**), but spectra in water will be reviewed for comparison purposes (figure **5.06**).
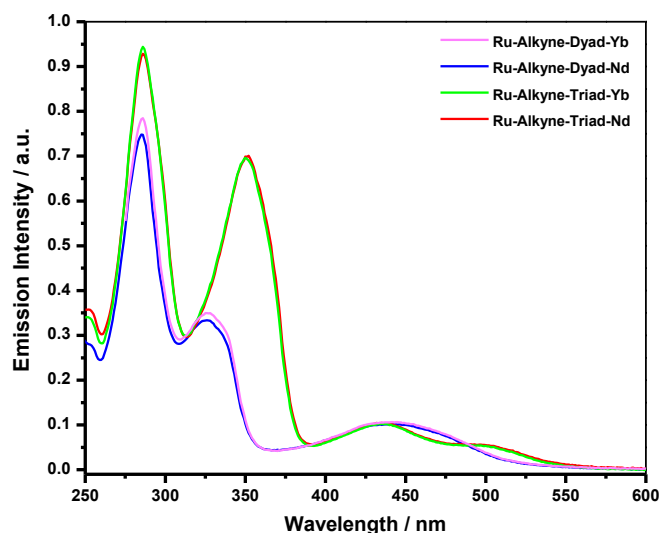

Figure 5.06: UV/Vis absorption spectra in aerated H$_2$O at 298 K.
Ru-Alkyne-Dyad-Yb (pink), **Ru-Alkyne-Dyad-Nd** (blue), **Ru-Alkyne-Triad-Yb** (green) and **Ru-Alkyne-Triad-Nd** (red)

The spectra for the dinuclear **Ru-Alkyne-Dyad-Ln** (Ln = Nd, Yb) complexes are consistent with those measured for the monosubstituted phenanthroline carboxylic acid scaffold (section **2.2.2.1**) and for the dinuclear **Ru-Alkyne-Dyad-Gd** and **Ru-Alkyne-Dyad-M** (M = Mn, Zn) complexes (sections **3.3.1** and **4.4.1**, respectively), and the spectra for the trinuclear **Ru-Alkyne-Triad-Ln** (Ln = Nd, Yb) complexes are consistent with those measured for the disubstituted phenanthroline carboxylic acid scaffold (section **2.3.2.1**) and for the trinuclear **Ru-Alkyne-Triad-Gd** and **Ru-Alkyne-Triad-M** (M = Mn, Zn) complexes (sections **3.3.1** and **4.4.1**, respectively). There are typical absorption bands in the high energy region of the spectra for the π→π* transitions on the 2,2'-bipyridine ligands (λ_{abs} = 285 nm) and the 1,10-phenanthroline ligands (λ_{abs} = 300-350 nm), and the ^{1}MLCT absorption bands are as usual in the range λ_{abs} = 375-550 nm. The absorption bands associated with the phenanthroline ligand have shifted to lower energy for the disubstituted phenanthroline scaffold (**Ru-Alkyne-Triad-Nd** and **Ru-Alkyne-Triad-Yb**) compared to the monosubstituted complexes (**Ru-Alkyne-Dyad-Nd** and **Ru-Alkyne-Dyad-Yb**), due to the extended conjugation in the disubstituted scaffold stabilising the LUMO more than in the monosubstituted ligand.

Table 5.01: UV/Vis absorption data for **Ru-Alkyne-Dyad-Nd**, **Ru-Alkyne-Dyad-Yb**, **Ru-Alkyne-Triad-Nd** and **Ru-Alkyne-Triad-Yb** at 298 K.

Compound	Solvent	λ_{abs} (nm) [ε (x 10^3 M^{-1} cm^{-1})]
Ru-Alkyne-Dyad-Gd	H_2O	286 [56], 326 (sh) [25], 443 (br) [7.5]
Ru-Alkyne-Dyad-Nd	EtOH/MeOH (4:1, *v:v*)	286, 326 (sh), 442 (br)
	MeOH	286, 326 (sh), 441 (br)
	H_2O	285 [37], 326 (sh) [16], 440 (br) [4.8]
	DMF	288, 328 (sh), 446 (br)
Ru-Alkyne-Dyad-Yb	EtOH/MeOH (4:1, *v:v*)	287, 329 (sh), 441 (br)
	MeOH	286, 328 (sh), 439 (br)
	H_2O	286 [12], 327 (sh) [5.2], 442 (br) [1.6]
	DMF	289, 330 (sh), 444 (br)
Ru-Alkyne-Triad-Gd	H_2O	286 [99], 350 [74], 435 [11], 486 (sh) [5.9]
Ru-Alkyne-Triad-Nd	MeOH	287, 352, 435, 490 (sh)
	H_2O	286 [88], 351 [67], 435 [9.9], 490 (sh) [5.3]
Ru-Alkyne-Triad-Yb	MeOH	287, 351, 435, 485 (sh)
	H_2O	286 [70], 350 [50], 435 [7.2], 488 (sh) [3.9]

5.3.2) Emission

Luminescence profiles and the lifetime of the decay for the Ru^{II}-based emission for **Ru-Alkyne-Dyad-Nd**, **Ru-Alkyne-Dyad-Yb**, **Ru-Alkyne-Triad-Nd** and **Ru-Alkyne-Triad-Yb** were recorded in several aerated solvents (table **5.02**), but profiles in aerated water at 298 K will be reviewed for comparison purposes (figure **5.07**). To directly compare the emission intensities of the four **RuLn$_n$** (Ln = Nd, Yb, n = 1, 2) complexes to the isostructural **RuGd$_n$** (n = 1, 2) compounds, excitation wavelengths were chosen where all of the complexes have the same optical density in the UV/Vis spectra (0.1 a.u.). It can be seen in the resulting luminescence profiles that upon excitation into the ^{1}MLCT absorption bands at λ_{ex} = 430 nm, the four **RuLn$_n$** (Ln = Nd, Yb, n = 1, 2) complexes produce broad and featureless emission profiles at 298 K indicating spin-forbidden ^{3}MLCT {Ru^{II}→π*$_{(N^N)}$} transitions; however, the maximum emission energy and emission intensity varies depending on the phenanthroline ligand substitution and the nature of the lanthanide ion bound within the polyaminocarboxylate chelate.
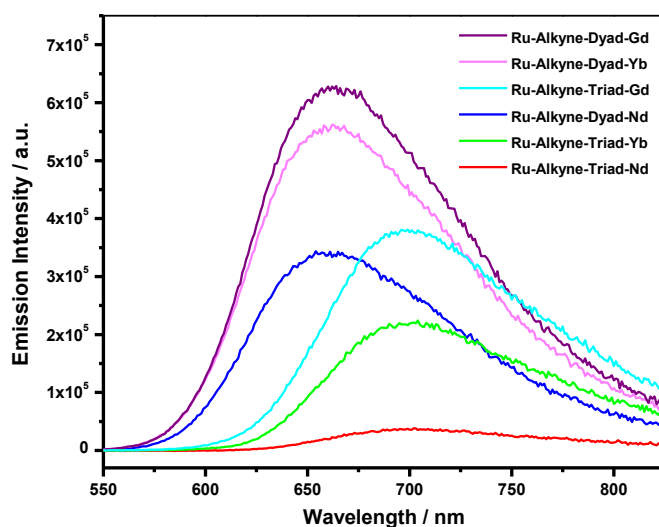

Figure 5.07: Corrected emission spectra in aerated H$_2$O at 298 K showing Ru^{II}-based luminescence. **Ru-Alkyne-Dyad-Gd** (purple, λ_{ex} = 440 nm), **Ru-Alkyne-Dyad-Yb** (pink, λ_{ex} = 430 nm), **Ru-Alkyne-Triad-Gd** (cyan, λ_{ex} = 425 nm), **Ru-Alkyne-Dyad-Nd** (blue, λ_{ex} = 430 nm), **Ru-Alkyne-Triad-Yb** (green, λ_{ex} = 430 nm) and **Ru-Alkyne-Triad-Nd** (red, λ_{ex} = 430 nm) (Slit width = 3 nm for all spectra)

Table 5.02: Luminescence data for **Ru-Alkyne-Dyad-Nd**, **Ru-Alkyne-Dyad-Yb**, **Ru-Alkyne-Triad-Nd** and **Ru-Alkyne-Triad-Yb** in aerated solvents.
All values are for the Ru^{II}-based luminescence unless otherwise stated.

Compound	Solvent	$\lambda_{em}^{298\,K}$ (nm) [$\lambda_{em}^{77\,K}$ (nm)]	$\tau_1, \tau_2, \tau_3^{298\,K}$ (ns)[b] [$\tau_1, \tau_2^{77\,K}$ (µs)]
Ru-Alkyne-Dyad-Gd	H$_2$O	664	351
Ru-Alkyne-Dyad-Nd	EtOH/MeOH (4:1, *v:v*)	649 [613, 664 (sh), 709 (sh)]	260, 26 [5.6, 0.7]
	MeOH	653	245, 29
	H$_2$O	662	358, 22
	DMF	670	296, 28
	D$_2$O[a]	1060	782
		1380	1390
	CD$_3$OD[a]	1060	911
		1380	596
Ru-Alkyne-Dyad-Yb	EtOH/MeOH (4:1, *v:v*)	660 [612, 662 (sh), 701 (sh)]	201, 98 [3.5, 0.7]
	MeOH	660	229, 125
	H$_2$O	663	242, 73
	DMF	674	233, 115
	D$_2$O[a]	980	13043
	CD$_3$OD[a]	980	16000
Ru-Alkyne-Triad-Gd	H$_2$O	699	402, 164
Ru-Alkyne-Triad-Nd	MeOH	697	214, 23
	H$_2$O	703	408, 18
	D$_2$O[a]	1060	704
		1380	481
Ru-Alkyne-Triad-Yb	MeOH	693	195, 108
	H$_2$O	700	223, 88
	D$_2$O[a]	980	10529, 302

[a]Lanthanide-based luminescence. [b]The luminescence lifetime decay curves for the **RuLn$_n$** (Ln = Nd, Yb, n = 1, 2) complexes were fitted by a sum of two exponentials, corresponding to the bound complex and to a small amount of dissociated complex in solution. The lifetime component ratios are insignificant, therefore, due to the different luminescence quantum yield values for the bound and dissociated complexes, respectively.

As was observed for the **RuGd$_n$** (n = 1, 2) (section **3.3.2**) and **RuM$_n$** (M = Mn, Zn, n = 1, 2) (section **4.4.2**) analogues, extending the conjugation along the phenanthroline backbone by the addition of a second pendant metal chelate to form trinuclear complexes (**Ru-Alkyne-Triad-Nd** and **Ru-Alkyne-Triad-Yb**), has a two-fold effect on the luminescence properties compared to the complexes based on monosubstituted phenanthroline scaffolds (**Ru-Alkyne-Dyad-Nd** and **Ru-Alkyne-Dyad-Yb**). The Ru^{II}-based luminescence is partially quenched in **Ru-Alkyne-Triad-Ln** (Ln = Nd, Yb) compared to **Ru-Alkyne-Dyad-Ln** (Ln = Nd, Yb), and the maximum emission energy of the ^{3}MLCT transition is lowered from λ_{em} = 660 nm for the dinuclear complexes (**Ru-Alkyne-Dyad-Ln** (Ln = Nd, Yb)) to λ_{em} = 700 nm for the trinuclear complexes (**Ru-Alkyne-Triad-Ln** (Ln = Nd, Yb)). Changing the lanthanide ion from Gd^{III} to Nd^{III} and Yb^{III} also has a quenching effect on the emission intensities observed. Luminescence profiles for **Ru-Alkyne-Dyad-Acid** and **Ru-Alkyne-Triad-Ester** recorded as a frozen glass at 77 K (figure **5.08**) reveal the ^{3}MLCT excited-state energies of the monosubstituted and disubstituted phenanthroline scaffolds to be 16,400 cm^{-1} and 15,500 cm^{-1}, respectively. Therefore, the excited-states on both scaffolds are high enough in energy to sensitise emission from the NIR-emitting Yb^{III} and Nd^{III} ions *via* partial Ru→Ln (Ln = Nd, Yb) PEnT, which causes the Ru^{II}-based emission to be partially quenched.
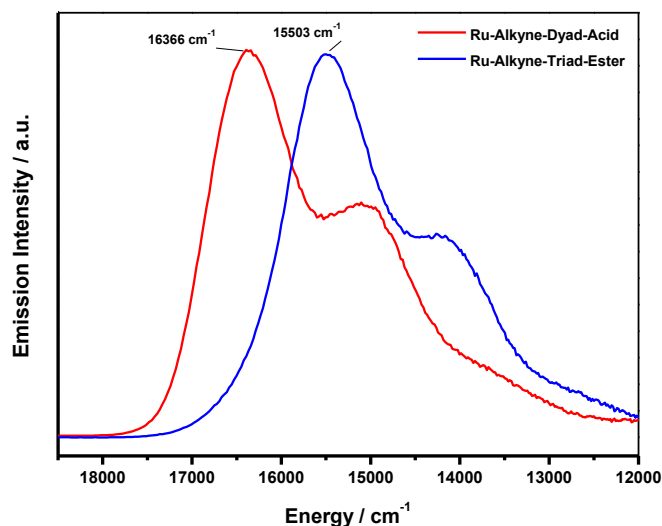

Figure 5.08: Normalised (at λ_{em} = max intensity), corrected emission spectra in aerated EtOH/MeOH (4:1, *v:v*) as a glass at 77 K. **Ru-Alkyne-Dyad-Acid** (red) and **Ru-Alkyne-Triad-Ester** (blue)

5.3.3) Photoinduced Energy-Transfer

When comparing the luminescence spectra for the three dinuclear complexes (**Ru-Alkyne-Dyad-Ln** (Ln = Gd, Nd, Yb)), a clear decrease in the Ru^{II}-based emission intensity can be observed along the series. **Ru-Alkyne-Dyad-Gd** demonstrates unquenched Ru^{II}-based emission, as the lowest excited state for the Gd^{III} ion ($^6P_{7/2} \approx 32,000$ cm^{-1}) is too high in energy to be directly populated by Ru→Gd PEnT. **Ru-Alkyne-Dyad-Yb** and **Ru-Alkyne-Dyad-Nd**, on the other hand, display partially quenched Ru^{II}-based emission due to partial Ru→Ln (Ln = Nd, Yb) PEnT, with the Ru^{II}-based emission from **Ru-Alkyne-Dyad-Nd** quenched to a greater extent than that of **Ru-Alkyne-Dyad-Yb**.

Luminescence quantum yield values and time-resolved luminescence measurements for the three complexes confirm this trend. The luminescence quantum yield value for **Ru-Alkyne-Dyad-Gd** was measured previously to be ɸ = 0.021 (section **3.3.2**), whilst the values for **Ru-Alkyne-Dyad-Yb** and **Ru-Alkyne-Dyad-Nd** are both lower at ɸ = 0.011 and ɸ = 0.010, respectively. The Ru^{II}-based luminescence lifetime curve for **Ru-Alkyne-Dyad-Gd** was fitted as a monoexponential decay in aerated water (τ = 351 ns), whereas **Ru-Alkyne-Dyad-Yb** and **Ru-Alkyne-Dyad-Nd** both exhibit two lifetime components (τ_1 = 242 ns, τ_2 = 73 ns for **Ru-Alkyne-Dyad-Yb**, τ_1 = 358 ns, τ_2 = 22 ns for **Ru-Alkyne-Dyad-Nd**) in the same solvent. The longer-lived component in both cases is most likely from a small portion of dissociated complex in solution, as the values extracted approximately match those of the dinuclear **Ru-Alkyne-Dyad-Gd** complex (within experimental error), in which the luminescence is not partially quenched. The shorter-lived components can, therefore, be assigned as the lifetimes of the partially quenched Ru^{II}-based decay from the non-dissociated **Ru-Alkyne-Dyad-Ln** (Ln = Nd, Yb) complexes. **Ru-Alkyne-Dyad-Yb** has slightly longer-lived luminescence than **Ru-Alkyne-Dyad-Nd**, which matches the results observed from the luminescence spectra (that the Ru^{II}-based emission from **Ru-Alkyne-Dyad-Nd** is quenched to a greater extent than that of **Ru-Alkyne-Dyad-Yb**).

If we take the shorter-lived lifetime component representing the partially quenched Ru^{II}-based decay in each of the **Ru-Alkyne-Dyad-Ln** (Ln = Nd, Yb) complexes, the rate of PEnT in aerated water in each case can be calculated using equation **5.01**, where τ is the unquenched Ru^{II}-based lifetime (τ = 351 ns in **Ru-Alkyne-Dyad-Gd**) and τ_q is the partially quenched lifetime (τ_q = 73 ns for **Ru-Alkyne-Dyad-Yb**, τ_q = 22 ns for **Ru-Alkyne-Dyad-Nd**). For

Ru-Alkyne-Dyad-Yb this gives the rate of Ru→Yb PEnT to be k_{EnT} = 1.1 x 10^7 s^{-1}, and for **Ru-Alkyne-Dyad-Nd** the rate of Ru→Nd PEnT to be k_{EnT} = 4.2 x 10^7 s^{-1}, which are similar values to the rate of Ir→Nd PEnT measured for the previously synthesised **IrNd** complex (**31**).

$$k_{EnT} = \frac{1}{\tau_q} - \frac{1}{\tau}$$

Equation 5.01: Equation used to calculate the rate of energy-transfer (k_{EnT}) in **RuLn$_n$** (Ln = Nd, Yb, n = 1, 2) complexes. τ and τ$_q$ are the unquenched (**Ln = Gd**) and quenched (**Ln = Nd**, **Yb**) lifetimes, respectively.

This trend in reduced Ru^{II}-based emission intensity observed along the series of **Ru-Alkyne-Dyad-Ln** (Ln = Gd, Yb, Nd) complexes is also mirrored in the trinuclear complexes (**Ru-Alkyne-Triad-Ln** (Ln = Gd, Yb, Nd)). Again, the **Ru-Alkyne-Triad-Gd** complex demonstrates unquenched Ru^{II}-based emission, whereas the **Ru-Alkyne-Triad-Yb** and **Ru-Alkyne-Triad-Nd** complexes both display partially quenched emission, with the luminescence from **Ru-Alkyne-Triad-Nd** being quenched to a greater extent than that from **Ru-Alkyne-Triad-Yb**. This is reflected in the measured luminescence quantum yield values for **Ru-Alkyne-Triad-Yb** and **Ru-Alkyne-Triad-Nd** (ɸ = 0.0039 and ɸ = 0.0007, respectively) when compared to **Ru-Alkyne-Triad-Gd** (ɸ = 0.0062).

The Ru^{II}-based luminescence from **Ru-Alkyne-Triad-Gd** in aerated water was previously found to decay to a sum of two exponentials (τ$_1$ = 402 ns, τ$_2$ = 164 ns), with the shorter-lived lifetime being the major component (80 %). The Ru^{II}-based luminescence from **Ru-Alkyne-Triad-Yb** and **Ru-Alkyne-Triad-Nd** also decays biexponentially in aerated water, with both complexes displaying a longer-lived component and a much shorter-lived lifetime component. The longer-lived component in **Ru-Alkyne-Triad-Yb** and **Ru-Alkyne-Triad-Nd** is similar to the unquenched value in **Ru-Alkyne-Triad-Gd** (τ$_1$ = 223 ns, **Ru-Alkyne-Triad-Yb** and τ$_1$ = 408 ns, **Ru-Alkyne-Triad-Nd**), which is the lifetime of the emission from the dissociated complex due to partial leaching of the Ln^{III} ion out of the polyaminocarboxylate chelate in a competitive solvent. The shorter-lived component measured for each complex (τ$_2$ = 88 ns, **Ru-Alkyne-Triad-Yb** and τ$_2$ = 18 ns, **Ru-Alkyne-Triad-Nd**) is representative of the partially quenched emission from the non-dissociated complexes.

Again, if we take the value of the shorter-lived luminescence component representing the lifetime of the partially quenched emission from the intact complexes (τ$_q$ = 88 ns, **Ru-**

Alkyne-Triad-Yb and τ_q = 18 ns, **Ru-Alkyne-Triad-Nd**), the rate of PEnT in aerated water for each of the complexes can be calculated using equation **5.01**, where τ = 164 ns for the unquenched emission from **Ru-Alkyne-Triad-Gd**. For **Ru-Alkyne-Triad-Yb** this gives a value of k_{EnT} = 5.3 x 10^6 s^{-1} for the rate of Ru→Yb PEnT, which is slower than the rate calculated for the dinuclear **Ru-Alkyne-Dyad-Yb** complex. The rate of Ru→Nd PEnT in **Ru-Alkyne-Triad-Nd** on the other hand was calculated to be k_{EnT} = 4.9 x 10^7 s^{-1}, which is the same as the rate measured for the dinuclear **Ru-Alkyne-Dyad-Nd** complex, within experimental error.

The observation that the rates of Ru→Nd PEnT in the **RuNd$_n$** (n = 1, 2) complexes are much faster than the rates of Ru→Yb PEnT in the **RuYb$_n$** (n = 1, 2) complexes can be explained in terms of the spectroscopic overlap between the emission from the $[Ru(bipy)_2(phen)]^{2+}$ donor and absorption of the acceptor Ln^III^ ion(s), which is necessary for efficient PEnT. Yb^III^ only has one f-f transition (λ_{em} = 980 nm) with energy between 10,000-20,000 cm^{-1} available to populate (figure **5.09**), which overlaps poorly with the emissive $[Ru(bipy)_2(phen)]^{2+}$ donor state in both of the **RuYb$_n$** (n = 1, 2) complexes, as the Ru^II^-based emission has almost decayed to the baseline at this energy. In comparison to Yb^III^, Nd^III^ has a large density of energy levels (figure **5.09**), which overlap with the region where the luminescence from the $[Ru(bipy)_2(phen)]^{2+}$ donor is most intense, allowing for efficient Ru→Nd PEnT. As a consequence the rate of Ru→Nd PEnT is much faster than the rate of Ru→Yb PEnT[6], and the Ru^II^-based emission is quenched to a greater extent in the **RuNd$_n$** (n = 1, 2) complexes compared to the **RuYb$_n$** (n = 1, 2) complexes.
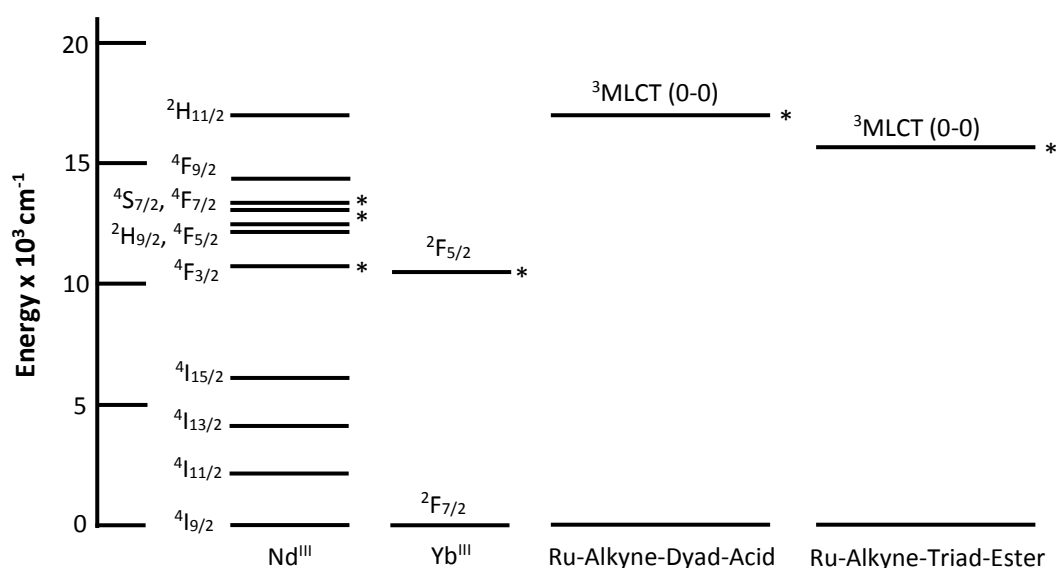

Figure 5.09: Partial energy level diagram for the Nd^III^ and Yb^III^ aqua ions, and the main 0-0 transitions for **Ru-Alkyne-Dyad-Acid** and **Ru-Alkyne-Triad-Ester**. *Luminescent energy level.

Direct evidence for the sensitised Ln^{III}-based emission can be seen in NIR luminescence spectra of the four **RuLn$_n$** (Ln = Nd, Yb, n = 1, 2) compounds in aerated D_2O. An emission feature at λ_{em} = 980 nm can be seen in the spectra for both **Ru-Alkyne-Dyad-Yb** (figure **5.10a**) and **Ru-Alkyne-Triad-Yb** (figure **5.10b**), which is the $^2F_{5/2}{\rightarrow}^2F_{7/2}$ transition. These emission bands must be a product of sensitised luminescence *via* Ru→Yb PEnT, as the excitation wavelength in both cases was into the Ru^{II}-based absorption band (λ_{ex} = 440 nm). Time-resolved luminescence measurements in aerated D_2O for both **Ru-Alkyne-Dyad-Yb** and **Ru-Alkyne-Triad-Yb** reveal characteristic long-lived decay lifetimes of τ = 13 µs and τ_1 = 11 µs, respectively, with an additional shorter-lived lifetime component of τ_2 = 320 ns measured for **Ru-Alkyne-Triad-Yb** being the long-wavelength tail of the residual Ru^{II}-based luminescence.

For both **Ru-Alkyne-Dyad-Nd** (figure **5.10a**) and **Ru-Alkyne-Triad-Nd** (figure **5.10b**) weak signals at λ_{em} = 1060 nm and λ_{em} = 1380 nm are present in the NIR luminescence spectra, which represent the $^4F_{3/2}{\rightarrow}^4I_n$ transitions (n = 11/2 and 13/2), respectively. Time-resolved luminescence measurements in aerated D_2O at these two wavelengths reveal lifetime values of $\tau_{(1060\ nm)}$ = 0.8 µs and $\tau_{(1380\ nm)}$ = 1.4 µs for **Ru-Alkyne-Dyad-Nd** and $\tau_{(1060\ nm)}$ = 0.7 µs and $\tau_{(1380\ nm)}$ = 0.5 µs for **Ru-Alkyne-Triad-Nd**. The much shorter lifetime values for the Nd^{III}-based decay compared to the Yb^{III}-based decay is characteristic for the Nd^{III} ion, as the lower-energy luminescence from Nd^{III}-substituted complexes is more easily quenched by molecular vibrations[6].
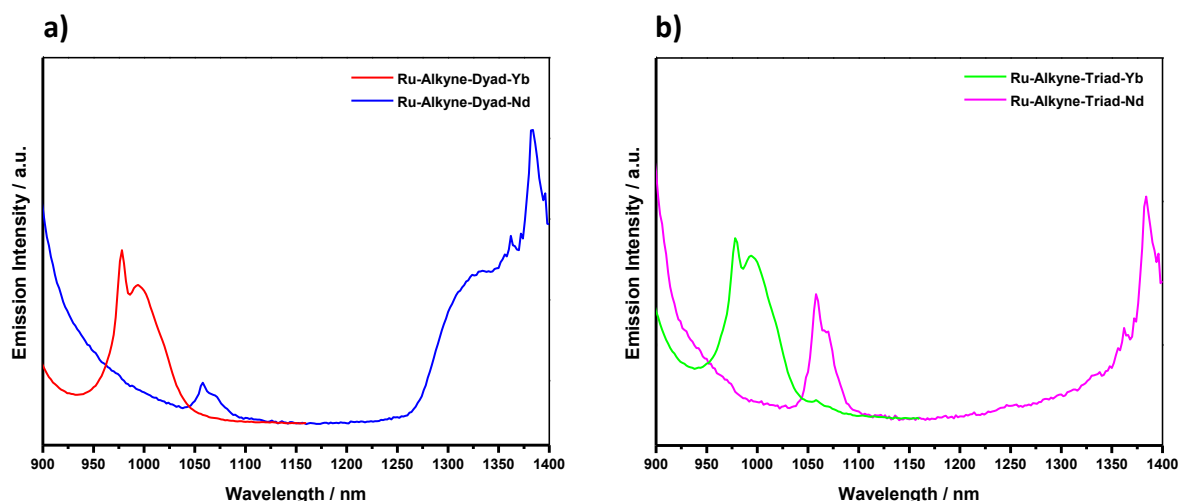

Figure 5.10: Normalised (at λ_{em} = max intensity), corrected emission spectra in aerated D_2O at 298 K showing sensitised lanthanide-based luminescence. a) **Ru-Alkyne-Dyad-Yb** (red) and **Ru-Alkyne-Dyad-Nd** (blue); b) **Ru-Alkyne-Triad-Yb** (green) and **Ru-Alkyne-Triad-Nd** (pink) (λ_{ex} = 440 nm for all spectra)

Excitation spectra recorded in aerated water at 298 K for **Ru-Alkyne-Dyad-Yb** (λ_{em} = 645 nm), **Ru-Alkyne-Dyad-Nd** (λ_{em} = 645 nm), **Ru-Alkyne-Triad-Yb** (λ_{em} = 680 nm) and **Ru-Alkyne-Triad-Nd** (λ_{em} = 680 nm) were overlaid with UV/Vis absorption spectra recorded in the same solvent (figure **5.11**). A good match between the spectra can be seen, which confirms that the Ru^{II}-based ^{3}MLCT emission observed for all four **RuLn$_n$** (Ln = Nd, Yb, n = 1, 2) complexes occurs as a result of absorption in to the ^{1}MLCT band.
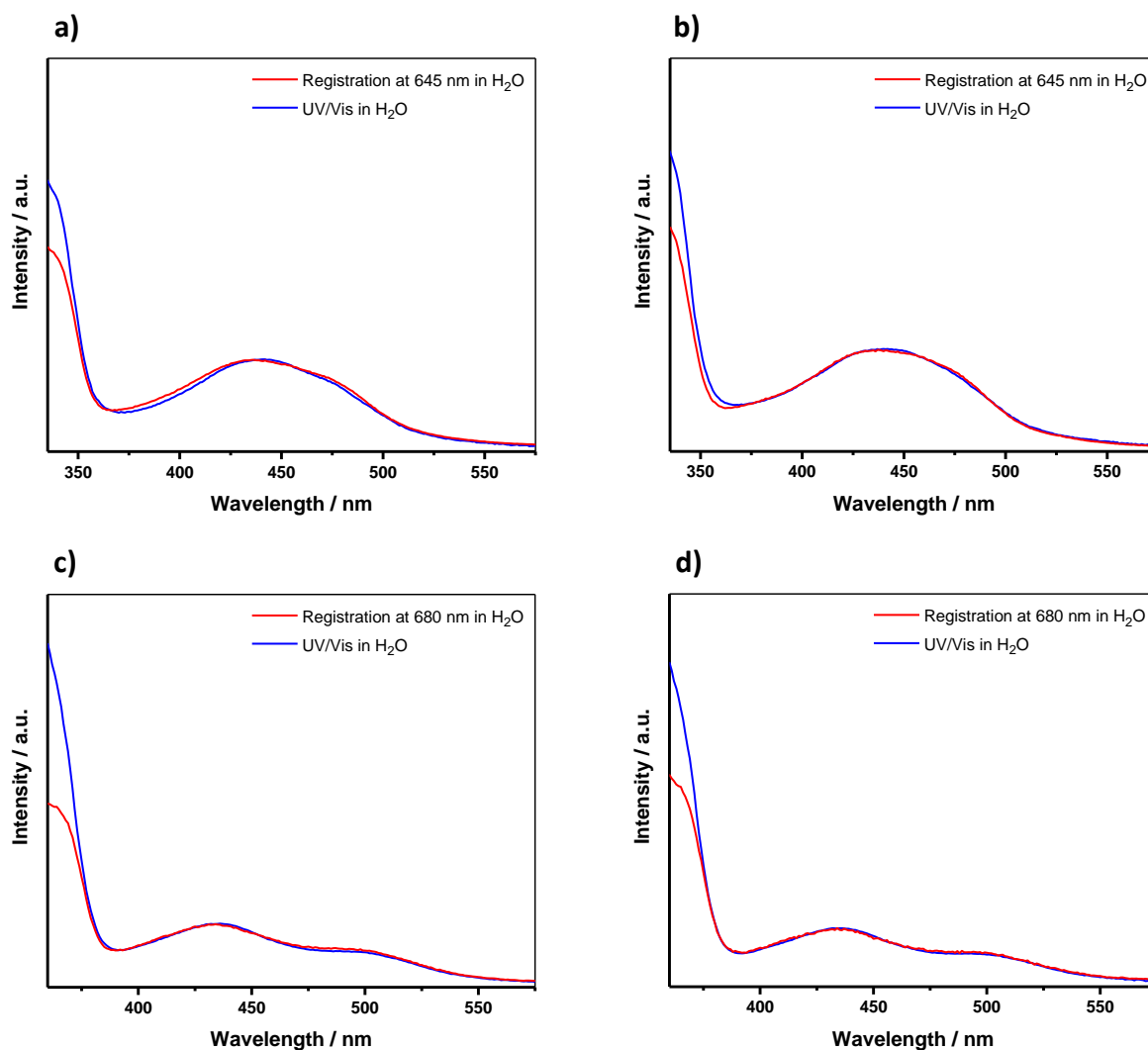

Figure 5.11: Normalised (at λ = 440 nm) spectra in aerated H$_2$O at 298 K. Corrected excitation spectra (red) and UV/Vis spectra (blue) of a) **Ru-Alkyne-Dyad-Yb** (λ_{em} = 645 nm), b) **Ru-Alkyne-Dyad-Nd** (λ_{em} = 645 nm), c) **Ru-Alkyne-Triad-Yb** (λ_{em} = 680 nm) and d) **Ru-Alkyne-Triad-Nd** (λ_{em} = 680 nm)

Similarly, excitation spectra recorded in aerated D$_2$O at 298 K for **Ru-Alkyne-Dyad-Yb** (λ_{em} = 980 nm), **Ru-Alkyne-Dyad-Nd** (λ_{em} = 1060 nm), **Ru-Alkyne-Triad-Yb** (λ_{em} = 980 nm) and **Ru-Alkyne-Triad-Nd** (λ_{em} = 1060 nm) were overlaid with UV/Vis absorption spectra recorded in the same solvent (figure **5.12**). A good match between the spectra can be seen, which is a clear indication that the emission observed in the NIR region for all four **RuLn$_n$** (Ln = Nd, Yb, n = 1, 2) complexes occurs as a result of absorption in to the ^{1}MLCT band followed by Ru→Ln PEnT.
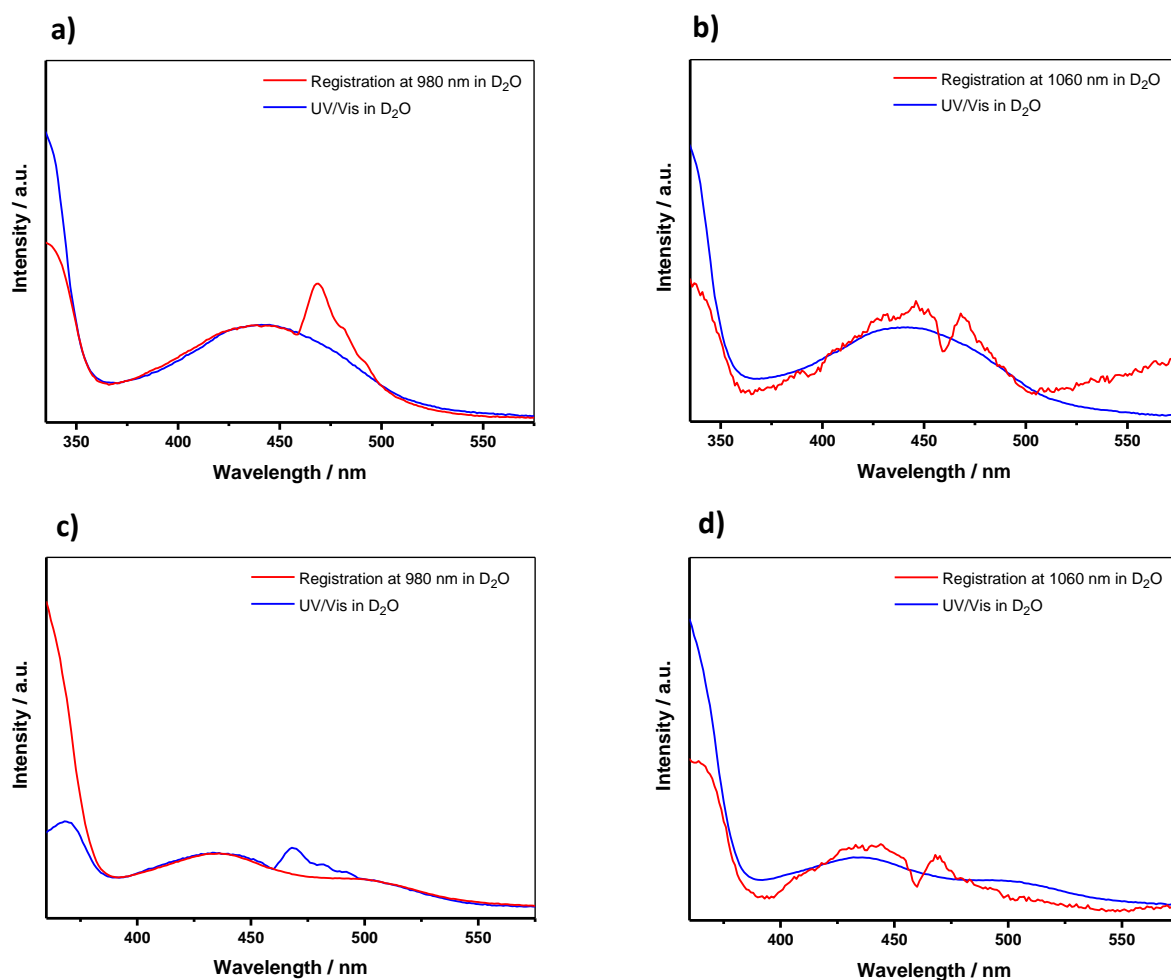

Figure 5.12: Normalised (at λ = 440 nm) spectra in aerated D$_2$O at 298 K. Corrected excitation spectra (red) and UV/Vis spectra (blue) of a) **Ru-Alkyne-Dyad-Yb** (λ_{em} = 980 nm), b) **Ru-Alkyne-Dyad-Nd** (λ_{em} = 1060 nm), c) **Ru-Alkyne-Triad-Yb** (λ_{em} = 980 nm) and d) **Ru-Alkyne-Triad-Nd** (λ_{em} = 1060 nm)

5.4) Summary

New water-soluble, ruthenium(II) bis(2,2'-bipyridine)-based complexes **Ru-Alkyne-Dyad-Yb**, **Ru-Alkyne-Dyad-Nd**, **Ru-Alkyne-Triad-Yb** and **Ru-Alkyne-Triad-Nd** were evaluated as dual-modal optical/NIR imaging agents. For all four of the **RuLn$_n$** (Ln = Nd, Yb, n = 1, 2) complexes, Ru^{II}-based luminescence was observed upon photoexcitation at λ_{ex} = 430 nm, as well as sensitised Ln^{III}-based emission as a consequence of Ru→Ln (Ln = Nd, Yb) photoinduced energy-transfer.

Both **RuNd$_n$** (n = 1, 2) complexes exhibited efficient Ru→Nd PEnT, with the rates calculated to be k_{EnT} = 4.2 x 10^7 s^{-1} and k_{EnT} = 4.9 x 10^7 s^{-1} for **Ru-Alkyne-Dyad-Nd** and **Ru-Alkyne-Triad-Nd**, respectively. In contrast, the rates of Ru→Yb PEnT were calculated to be slower in **Ru-Alkyne-Dyad-Yb** and in **Ru-Alkyne-Triad-Yb** (k_{EnT} = 1.1 x 10^7 s^{-1} and k_{EnT} = 5.3 x 10^6 s^{-1}, respectively) due to poorer spectroscopic overlap between the emission from the [Ru(bipy)$_2$(phen)]$^{2+}$ donor and absorption of the acceptor Ln^{III} ion(s) in the **RuYb$_n$** (n = 1, 2) complexes compared to the **RuNd$_n$** (n = 1, 2) complexes.

A sensitised emission feature at λ_{em} = 980 nm was recorded for both **RuYb$_n$** (n = 1, 2) complexes in aerated D$_2$O, which is the $^2F_{5/2}$→$^2F_{7/2}$ transition of Yb^{III}, and for both **RuNd$_n$** (n = 1, 2) complexes, sensitised emission features at λ_{em} = 1060 nm and λ_{em} = 1380 nm were observed, which represent the $^4F_{3/2}$→^4I_n transitions (n = 11/2 and 13/2) of Nd^{III}, respectively. The lifetimes of the Yb^{III}-based decay in **Ru-Alkyne-Dyad-Yb** and **Ru-Alkyne-Triad-Yb** were τ = 13 µs and τ = 11 µs, respectively, and the lifetimes of the Nd^{III}-based decay in **Ru-Alkyne-Dyad-Nd** and **Ru-Alkyne-Triad-Nd** were in the range τ = 0.5-1.4 µs. The Ru^{II}-based decay was orders-of-magnitude shorter for each of the four **RuLn$_n$** (Ln = Nd, Yb, n = 1, 2) complexes (τ = 18-88 ns) and so it should be possible to detect the luminescence from the Ln^{III} ions separately from the emission from the [Ru(bipy)$_2$(phen)]$^{2+}$ centre by time-gating the detection to reject the shorter-lived Ru^{II} component.

5.5) Future Work

To continue this work further, it would be interesting to assess the effectiveness of **Ru-Alkyne-Dyad-Yb**, **Ru-Alkyne-Dyad-Nd**, **Ru-Alkyne-Triad-Yb** and **Ru-Alkyne-Triad-Nd** as dual-modal optical/NIR imaging agents for cellular imaging.

5.6) References

1   S. I. Weissman, *J. Chem. Phys.*, 1942, **10**, 214–217.

2   J.-M. Lehn, *Angew. Chemie Int. Ed.*, 1990, **29**, 1304–1319.

3   M. D. Ward, *Coord. Chem. Rev.*, 2010, **254**, 2634–2642.

4   A. Jana, S. J. A. Pope and M. D. Ward, *Polyhedron*, 2017, **127**, 390–395.

5   E. Baggaley, D.-K. Cao, D. Sykes, S. W. Botchway, J. A. Weinstein and M. D. Ward, *Chem. Eur. J.*, 2014, **20**, 8898–8903.

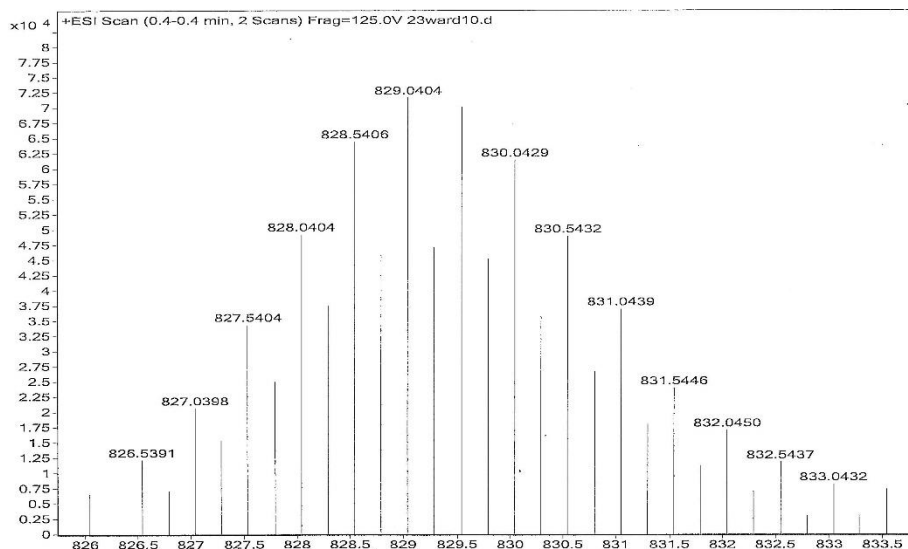6   G. M. Davies, S. J. A. Pope, H. Adams, S. Faulkner and M. D. Ward, *Inorg. Chem.*, 2005, **44**, 4656–4665.

5.7) Appendices
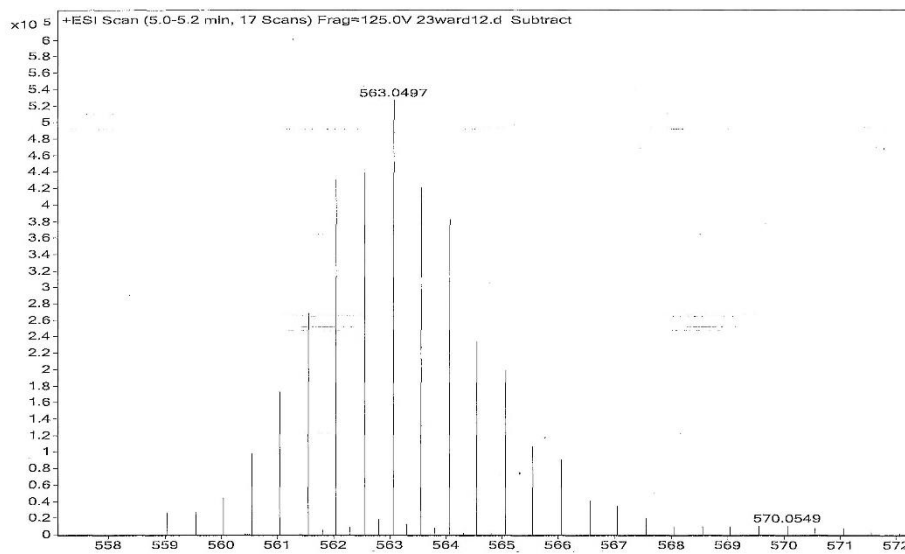
Appendix 5.01: High-resolution mass spectrum of **Ru-Alkyne-Dyad-Nd**.
Calculated for $[C_{49}H_{37}N_9O_8{}^{102}Ru^{144}Nd + H]^{2+}$, 563.0488.
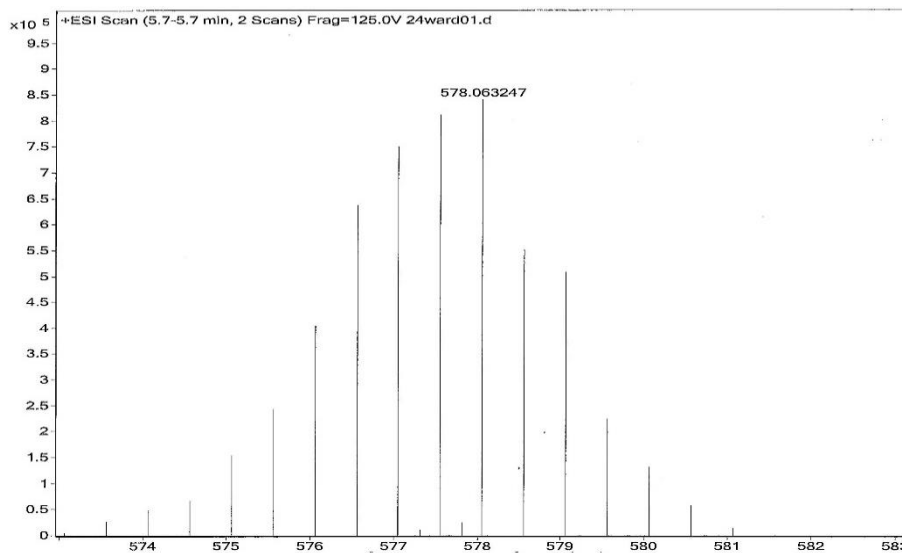
Appendix 5.02: High-resolution mass spectrum of **Ru-Alkyne-Dyad-Yb**.
Calculated for $[C_{49}H_{37}N_9O_8{}^{102}Ru^{173}Yb + H]^{2+}$, 578.0632.

Appendix 5.03: High-resolution mass spectrum of **Ru-Alkyne-Triad-Nd**.
Calculated for $[C_{66}H_{50}N_{12}O_{16}{}^{102}Ru^{144}Nd_2 + 2H]^{2+}$, 829.0429.
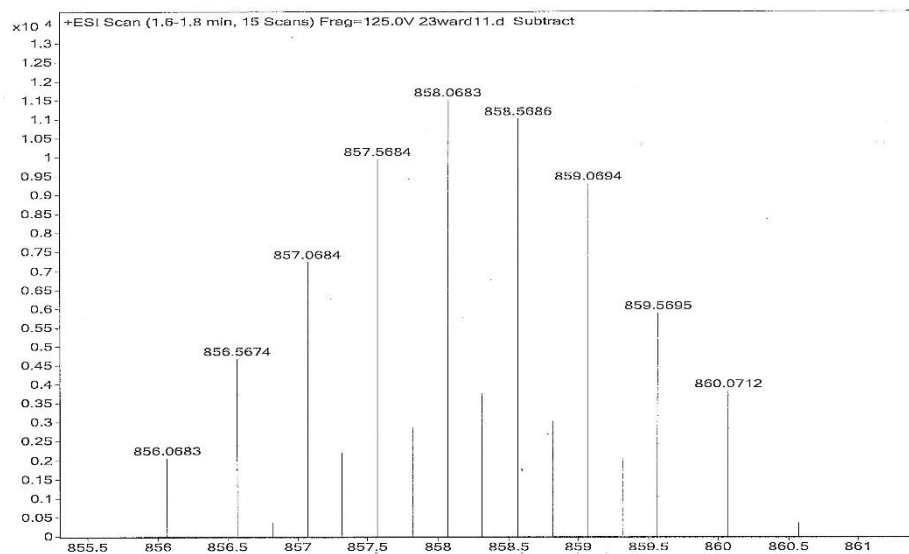
Appendix 5.04: High-resolution mass spectrum of **Ru-Alkyne-Triad-Yb**.
Calculated for $[C_{66}H_{50}N_{12}O_{16}{}^{102}Ru^{173}Yb_2 + 2H]^{2+}$, 858.0710.

Chapter 6

Experimental Methods

6.1) Characterisation and Reagents

6.1.1) Materials

All reagents, unless otherwise stated, were purchased from commercial sources (Sigma-Aldrich, Alfa Aesar, Fluorochem) and used as received. All solvents were of HPLC grade quality and were obtained from Fisher, excluding deuterated solvents (Sigma-Aldrich, Acros Organics, VWR). Dry solvents were obtained from the Grubbs dry solvent system at the University of Sheffield.

6.1.2) Nuclear Magnetic Resonance Spectroscopy

One-dimensional ^{1}H and ^{13}C NMR spectra and two-dimensional COSY, HMBC and HSQC spectra were recorded using either a Bruker Avance III HD 400 spectrometer or a Bruker Avance III HD 500 spectrometer. Spectra for **Ru-Alkyne-Dyad-Acid** and **Ru-Alkyne-Metallostar-Ester** were acquired by Dr Sandra van Meurs and spectra for **Ru-Alkyne-Metallostar-Acid** were acquired by Dr Craig Robertson. Spectroscopic grade deuterated solvents were used and all spectra were calibrated using residual protonated solvent peaks[1]. All measurements were taken at room temperature, unless otherwise stated. All chemical shifts are quoted in ppm and the following abbreviations are used when reporting the spectra; *br* – broad, s – singlet, d – doublet, dd – doublet of doublets, ddd – doublet of double doublets, t – triplet, td – triplet of doublets, tt – triplet of triplets, m – multiplet, phen = 1,10-phenantholine and bipy = 2,2-bipyridine.

6.1.3) Mass Spectrometry

Mass spectra were obtained from the University of Sheffield Mass Spectrometry Service and were acquired by either Mr. Simon Thorpe or Ms. Sharon Spey, with the exception of **Ru-Alkyne-Dyad-Gd**, **Ru-Alkyne-Triad-Gd**, **Ru-Alkyne-Dyad-Mn** and **Ru-Alkyne-Dyad-Zn**, which were obtained from the University of Warwick Mass Spectrometry Service and were acquired by Dr Lijiang Song. Positive electrospray ionisation (ES$^+$) spectra, negative electrospray ionisation (ES$^-$) spectra and high-resolution spectra acquired by the University of Sheffield Mass Spectrometry Service were recorded on an Agilent Technologies 6530 Accurate-Mass Q-TOF LC/MS instrument. High-resolution spectra acquired by the University

of Warwick Mass Spectrometry Service were recorded on a Bruker MaXis plus instrument. All measurements were taken at room temperature.

6.1.4) Photophysical Measurements

All UV/Vis, emission, excitation and lifetime measurements were recorded from room temperature solutions, unless otherwise stated, using a quartz fluorescence cell with a path length of 1 cm. Compounds to be analysed were dissolved in an aerated solvent to the concentration at which the maximum optical density at the excitation wavelength was 0.1 a.u..

6.1.4.1) UV/Visible Absorption

UV/Vis spectra were measured on a Varian Cary 50 Bio UV-Visible Spectrophotometer and were baseline corrected. Extinction coefficients (ε) were calculated from a linear plot of optical density (at a particular wavelength) against concentration, in accordance with the Beer Lambert law (equation **6.01**). Typically, solution concentrations of 10^{-6} to 10^{-4} M were used for extinction coefficient determination.

$$A = \varepsilon l c$$

Equation 6.01: The Beer Lambert Law. A = absorbance (a.u.), ε = extinction coefficient ($M^{-1}\ cm^{-1}$), l = path length (cm), c = concentration (M)

6.1.4.2) Emission and Excitation

Photoluminescence spectra were recorded on a Horiba Jobin Yvon Fluoromax-4-Spectrofluorometer and were corrected using correction files included within the FluorEssence^{TM} software. Near-IR emission and excitation spectra were acquired by Dr Adam Woodward at the University of Manchester on an Edinburgh Instrument FP920 Phosphorescence Lifetime Spectrometer equipped with a 450 watt steady state xenon lamp; a 5 watt microsecond pulsed xenon flashlamp (with single 300 mm focal length excitation and emission monochromators in Czerny Turner configuration); a red sensitive photomultiplier in a Peltier (air cooled) housing (Hamamatsu R928P); and a liquid nitrogen cooled nIR photomultiplier (Hamamatsu), and were corrected using correction files included within the software. Near-IR emission spectra were recorded by using a 645 nm longpass filter. Low-

temperature emission spectra were measured in a mix of ethanol/methanol (4:1, *v:v*): the solution was transferred into an NMR tube and frozen in a quartz dewar filled with liquid nitrogen to form a glass at 77 K. Emission quantum yield values (ϕ) were calculated using equation **6.02**, and the reference standard used was [Ru(bipy)$_3$]Cl$_2$.6H$_2$O in aerated double-distilled water (ϕ = 0.028)[2].

$$\phi_s = \phi_r \times \left(\frac{I_s}{(1 - 10^{-A})_s} \right) \times \left(\frac{(1 - 10^{-A})_r}{I_r} \right) \times \left(\frac{\eta_s{}^2}{\eta_r{}^2} \right)$$

Equation 6.02: Equation used to calculate emission quantum yield. ϕ = quantum yield, s = sample under investigation, r = reference standard, I = integrated emission intensity, A = optical density (absorbance) at excitation wavelength, η = solvent refractive index

6.1.4.3) Emission Lifetime

The Ru^{II}-based emission lifetimes were measured using an Edinburgh Instruments Mini-τ instrument fitted with a 405 nm pulsed diode laser as an excitation source. Near-IR emission lifetimes were acquired by Dr Adam Woodward at the University of Manchester and were measured using an Edinburgh Instrument FP920 Phosphorescence Lifetime Spectrometer equipped with a 450 watt steady state xenon lamp; a 5 watt microsecond pulsed xenon flashlamp (with single 300 mm focal length excitation and emission monochromators in Czerny Turner configuration); a red sensitive photomultiplier in a Peltier (air cooled) housing (Hamamatsu R928P); and a liquid nitrogen cooled nIR photomultiplier (Hamamatsu). Lifetime data were recorded following excitation with the microsecond flashlamp using time-correlated single photon counting (PCS900 plug-in PC card for fast photon counting). Low-temperature emission lifetimes were measured in a mix of ethanol/methanol (4:1, *v:v*): the solution was transferred into an NMR tube and frozen in a quartz dewar filled with liquid nitrogen to form a glass at 77 K. Decay curves generated by single photon counting (SPC) were fitted using Origin® software and the quality of fit judged by minimization of reduced chi-squared and sum-of-residuals squared values.

6.1.5) Relaxation Rates of Contrast Agents in Solution

Relaxivity measurements for the four synthesised contrast agents (**Ru-Alkyne-Dyad-Gd**, **Ru-Alkyne-Triad-Gd**, **Ru-Alkyne-Dyad-Mn**, and **Ru-Alkyne-Triad-Mn**) and the commercial contrast agent, Magnevist®, were performed on a Bruker Avance III 400 spectrometer at 298

K. Each compound under investigation was dissolved in D_2O at five different concentrations (0 – 2.0 mM) and the longitudinal relaxation time (T_1) for the residual H_2O peak in each sample measured using a standard inversion-recovery pulse sequence, with 12 recovery times varying between 0.001-60 seconds for Magnevist® and 15 recovery times varying between 0.001-15 seconds for the four synthesised contrast agents. Concentration-normalised longitudinal relaxivity values were determined from a linear plot of longitudinal relaxation time (T_1) against contrast agent concentration (0 – 2.0 mM) in accordance with equation **6.03**.

$$\left(\frac{1}{T_1}\right)_{obs} = \left(\frac{1}{T_1}\right)_0 + r_1[M]$$

Equation 6.03: Equation used to calculate the relaxation rate of a contrast agent in solution. T_1 = longitudinal relaxation time, obs = observed T_1 values in the presence of contrast agent, 0 = observed T_1 value in the absence of contrast agent, r_1 = concentration-normalised longitudinal relaxivity value, [M] = concentration of contrast agent

6.1.6) Cell Culture

HeLa cells were cultured in Dulbecco's modified eagle medium (DMEM, high glucose with L-glutamine) purchased from Lonza (500 mL) and supplemented with 10 % (*v:v*) foetal bovine serum (FBS). Cultures were grown as monolayers in T-75 flasks at 37 °C in a 5 % CO_2 : 95 % air (*v:v*) environment. Once at 75-80 % confluency, cells were subcultured using trypsin-EDTA (2 mL). Subcultures for live cell staining were seeded on to sterile coverslips (15 mm x 15 mm) in 6-well plates (100,000/well) and those for clonogenic assays were seeded directly in to 6-well plates (200-400/well). All subcultures were incubated in DMEM at 37 °C in a 5 % CO_2 : 95 % air (*v:v*) environment overnight to allow for adhesion to the well-plate or coverslip.

6.1.7) General Cell Staining

Ru-Alkyne-Dyad-Gd and **Ru-Alkyne-Triad-Gd** were dissolved in sterile, double-distilled water to form stock solutions with a concentration of 1 mM. Further dilution to generate working solutions of 50-200 µM was achieved using DMEM (high glucose with L-glutamine) purchased from Lonza (500 mL) and supplemented with 10 % (*v:v*) foetal bovine serum (FBS).

6.1.7.1) Live Cell Staining

After removal of the growth media, cells were washed with sterilised phosphate-buffered saline (PBS, 3 x 2 mL/well) before being treated with a solution of the appropriate **RuGd$_n$** (n = 1, 2) complex at concentrations of 50-200 µM (2 mL/well). Cells were incubated for 2h or 4h at 37 °C in DMEM in a 5 % CO_2 : 95 % air (*v:v*) environment. After the desired incubation time, the media was removed, and the cells were washed with PBS (3 x 2 mL/well) to remove excess complex. The cells were then treated with paraformaldehyde solution (4 % in PBS, 1 mL/well) for 20 minutes, before being washed with PBS (3 x 2 mL/well) again. The coverslips were mounted onto microscope slides (Immu-Mount^{TM}, Thermo Scientific) and left to dry for a minimum time of 30 minutes before imaging.

6.1.8) Steady-State Imaging

Confocal images of fixed HeLa cells were recorded using an inverted Nikon A1 confocal microscope with a 60x lens (CFI Plan Apochromat VC 60x oil, NA 1.4). A diode laser (λ_{ex} = 405 nm) was used to excite the **RuGd$_n$** (n = 1, 2) complex and a λ_{em} = 570-620 nm emission filter was used.

6.1.9) Toxicity Assay - Clonogenic Survival

After removal of the growth media, live HeLa cells were treated with a solution of the appropriate **RuGd$_n$** (n = 1, 2) complex at both 50 µM and 200 µM (1 mL/well). Cells in four control wells were left untreated and immersed in DMEM (2 mL/well). Cells were incubated for 4h at 37 °C in a 5 % CO_2 : 95 % air (*v:v*) environment. Following incubation, the treatment solution was removed, and the cells immersed in fresh DMEM (2 mL/well) and incubated for seven to ten days at 37 °C in a 5 % CO_2 : 95 % air (*v:v*) environment until visible cell colonies had formed. The growth media was removed, and the cells were fixed and stained with methylene blue in methanol (4 g/L) for a minimum of 30 minutes. The staining solution was removed, and the number of colonies counted, with each colony representing a surviving cell. The survival fraction for cells treated with the **RuGd$_n$** (n = 1, 2) complexes was calculated using equation **6.04**. Experiments were conducted in duplicate for seeding densities of 200 and 400 cells/well and repeated three times. Survival fractions quoted are averages of the three repeats.

$$\text{Survival Fraction} = \frac{\text{no. of colonies formed after treatment with } \mathbf{RuGd_n} \text{ (n = 1, 2)}}{\text{average no. of colonies formed in control wells}}$$

Equation 6.04: Equation used to calculate the survival fraction of cells treated with **RuGd$_n$** (n = 1, 2) complexes in a clonogenic assay

6.1.10) Transient Absorption Measurements

All transient absorption data was acquired by James Shipp in the Laser Laboratory in the Department of Chemistry at the University of Sheffield. A Ti:Sapphire regenerative amplifier (Spitfire ACE PA-40, Spectra-Physics) provided λ_{ex} = 800 nm, 1.2 mJ pulses (40 fs fwhm, 10 kHz, 1.2 mJ) as the excitation source. λ_{ex} = 400 nm sample excitation was provided by doubling a portion of the λ_{ex} = 800 nm output, in a β-barium borate crystal within a commercially available doubler/tripler (TimePlate, Photop Technologies). λ_{ex} = 525 nm excitation pulses were provided by a commercially available UV/Vis optical parametric amplifier with a wavelength range of λ = 240 – 1160 nm (TOPAS, Light Conversion). White light, supercontinuum, probe pulses were generated *in situ* using a portion of the Ti:Sapphire amplifier output, focused onto a CaF$_2$ crystal, allowing for the generation of light spanning λ = 340 – 790 nm. Detection was achieved using a commercial transient absorption spectrometer (Helios, Ultrafast Systems) and was performed by a CMOS sensor for the UV/Vis spectral range. The relative polarisation of the pump and probe pulses was set to the magic angle of 54.7° for anisotropy free measurements.

6.2) Synthesis of Compounds in Chapter 2

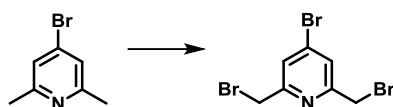### 6.2.1) 4-Bromo-2,6-dimethylpyridine
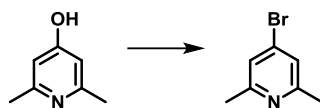
4-Bromo-2,6-dimethylpyridine was prepared by a modified literature procedure[3]. 4-Hydroxy-2,6-dimethylpyridine (7.2 g, 0.058 mol) and phosphorus pentabromide (25.0 g, 0.058 mol) were suspended in anhydrous $CHCl_3$ (30 mL) and heated at reflux. After 3 hours, the solvent was removed under reduced pressure and the resulting residue heated as a melt at 120 °C for 16 hours. Once cooled, the product was extracted into ethyl acetate (30 mL), washed with a solution of NaOH (1.25 M, 30 mL) and water (2 x 30 mL) and then dried ($MgSO_4$). The solvent was removed under reduced pressure to yield **4-bromo-2,6-dimethylpyridine** (3.1 g, 30 %) as a yellow oil.

Molecular Formula: C_7H_8NBr, **RMM:** 185.0
^{1}H NMR (400 MHz, $CDCl_3$): δ = 2.45 (s, 6H) 7.10 (s, 2H)
ES$^+$MS: m/z = 186.0 $[M + H]^+$

6.2.2) 4-Bromo-2,6-bis(bromomethyl)pyridine

4-Bromo-2,6-bis(bromomethyl)pyridine was prepared by a modified literature procedure[4]. 4-Bromo-2,6-dimethylpyridine (3.09 g, 17 mmol), NBS (5.94 g, 37 mmol) and benzoyl peroxide (catalytic amount) were suspended in $CHCl_3$ (30 mL) and heated at reflux under UV irradiation. The reaction was monitored by TLC (silica, petroleum ether: ethyl acetate, 9:1, $v:v$) every four hours and additional NBS (5.94 g, 37 mmol) and benzoyl peroxide (catalytic amount) were added until the complete consumption of both the starting material and monosubstituted product was seen. The reaction was then cooled and filtered. The filtrate was washed with a solution of $NaHCO_3$ (5 %, 30 mL), brine (30 mL) and water (30 mL), dried ($MgSO_4$) and the solvent removed under reduced pressure to yield a mixture of over-brominated products as a yellow oil. The oil was dissolved in anhydrous THF (30 mL) in a flask charged with argon and cooled to 0 °C. Diethyl phosphite (10 mL, 78 mmol) and N,N-

diisopropylethylamine (17 mL, 98 mmol) were added and the reaction stirred at room temperature. The reaction was monitored by TLC (silica, petroleum ether: ethyl acetate, 9:1, *v:v*) every hour until only the desired product was present. After 5 hours the reaction was poured onto ice water (30 mL) and extracted with diethyl ether (3 x 30 mL). The combined organic extracts were then washed with brine (30 mL) and water (30 mL), dried ($MgSO_4$) and the solvent removed under reduced pressure. The resulting brown solid was purified by flash column chromatography on silica gel (200-300 mesh) with petroleum ether/ethyl acetate (9:1, *v:v*) as the eluent to afford **4-bromo-2,6-bis(bromomethyl)pyridine** (3.79 g, 66 %) as an off-white solid.

Molecular Formula: $C_7H_6NBr_3$, **RMM:** 342.8

^{1}H NMR (400 MHz, CDCl$_3$): δ = 4.48 (s, 4H) 7.55 (s, 2H)

ES$^+$MS: *m/z* = 343.8 [*M* + H]$^+$

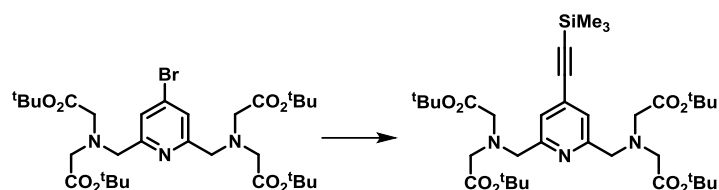### 6.2.3) 4-Bromo-2,6-disubstituted pyridine
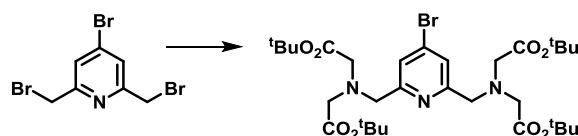
4-Bromo-2,6-disubstituted pyridine was prepared by a literature procedure[5]. 4-Bromo-2,6-bis(bromomethyl)pyridine (3.79 g, 11 mmol), di-tert-butyl iminodiacetate (5.42 g, 22 mmol) and sodium carbonate (11.70 g, 110 mmol) were added to anhydrous MeCN (45 mL) in a flask charged with argon. The mixture was stirred at room temperature for 24 hours and then filtered. The filtrate was evaporated under reduced pressure and the resulting yellow oil dissolved in CHCl$_3$ (50 mL), washed with water (2 x 30 mL) and dried ($MgSO_4$). The solvent was removed under reduced pressure to yield **4-bromo-2,6-disubstituted pyridine** (6.89 g, 93 %) as a yellow oil.

Molecular Formula: $C_{31}H_{50}N_3O_8Br$, **RMM:** 673.3

^{1}H NMR (400 MHz, CDCl$_3$): δ = 1.41 (s, 36H) 3.42 (s, 8H) 3.94 (s, 4H) 7.68 (s, 2H)

ES$^+$MS: *m/z* = 674.3 [*M* + H]$^+$, 696.3 [*M* + Na]$^+$

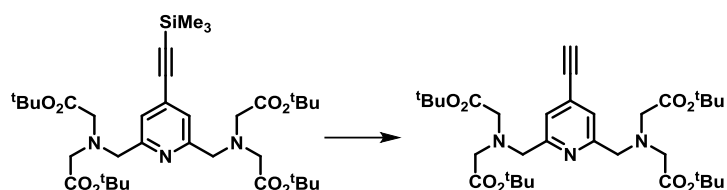### 6.2.4) 4-(Trimethylsilyl)ethynyl-2,6-disubstituted pyridine

4-Bromo-2,6-disubstituted pyridine (6.89 g, 10.2 mmol), Pd(PPh$_3$)$_2$Cl$_2$ (0.50 g, 0.712 mmol), CuI (0.30 g, 1.58 mmol) and PPh$_3$ (0.10 g, 0.381 mmol) were added to anhydrous ^{i}Pr$_2$NH (30 mL) and the mixture deoxygenated with argon for 30 minutes. TMSA (15 mL, 108 mmol) was added with vigorous stirring and the resulting mixture heated at 83 °C for 24 hours. Once cooled, the reaction was filtered through celite® with CH$_2$Cl$_2$ until the washings ran clear. The solvent was then removed under reduced pressure to afford a black residue, which was flash-filtered through silica gel (200-300 mesh) with CH$_2$Cl$_2$. The crude product was then purified further using column chromatography on silica gel (200-300 mesh) with petroleum ether/ethyl acetate (9:1 to 8:2, *v:v*) as the eluent to afford **4-(trimethylsilyl)ethynyl-2,6-disubstituted pyridine** (4.25 g, 60 %) as a dark yellow oil.

Molecular Formula: C$_{36}$H$_{59}$N$_3$O$_8$Si, **RMM:** 689.4
^{1}H NMR (400 MHz, CDCl$_3$): δ = 0.18 (s, 9H) 1.42 (s, 36H) 3.43 (s, 8H) 3.96 (s, 4H) 7.48 (s, 2H)
**ES$^+$MS:** *m/z* = 690.4 [*M* + H]$^+$, 712.4 [*M* + Na]$^+$

6.2.5) 4-Ethynyl-2,6-disubstituted pyridine

4-(Trimethylsilyl)ethynyl-2,6-disubstituted pyridine (0.75 g, 1.09 mmol) and TBAF (0.43 g, 1.63 mmol) were dissolved in THF (45 mL) and stirred at room temperature for 16 hours. The solvent was then removed under reduced pressure and the resulting residue dissolved in CH$_2$Cl$_2$ (30 mL), washed with water (2 x 30 mL) and dried (MgSO$_4$). The solvent was removed under reduced pressure to afford **4-ethynyl-2,6-disubstituted pyridine** (0.62 g, 92 %) as a dark yellow oil. Due to the instability of the alkyne substituent, **4-ethynyl-2,6-disubstituted pyridine** was generated and used immediately without characterisation.

6.2.6) 3-Bromo- and 3,8-dibromo-1,10-phenanthroline
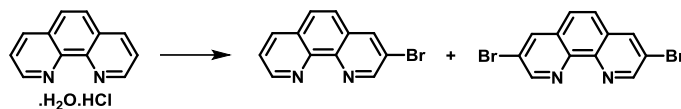
3-Bromo-1,10-phenanthroline and **3,8-dibromo-1,10-phenanthroline** were prepared by a literature procedure[6]. A solution of 1,10-phenanthroline monohydrochloride monohydrate (10 g, 43 mmol) in nitrobenzene (20 mL) was heated to 130 °C. A solution of bromine (3.3 mL, 65 mmol) in nitrobenzene (9.3 mL) was added to the slurry dropwise over a period of an hour and the resulting solution heated for 3 hours. Concentrated ammonium hydroxide solution (100 mL) was then slowly added in portions to the cooled reaction mixture before extraction with CH_2Cl_2 (3 x 50 mL). The combined organic layers were washed with water (3 x 50 mL) and dried ($MgSO_4$). Removal of the solvent under reduced pressure afforded a suspension of the products in nitrobenzene, which was removed *via* vacuum distillation at 100 °C. The resulting crude mixture was purified using flash column chromatography on silica gel (200-300 mesh) with CH_2Cl_2/MeOH (100:0 to 99.4:0.6, *v:v*) as the eluent to afford **3-bromo-1,10-phenanthroline** (3.5 g, 32 %) and **3,8-dibromo-1,10-phenanthroline** (2.4 g, 17 %) as white powders.

Molecular Formula: $C_{12}H_7N_2Br$, **RMM:** 258.0
^{1}H NMR (400 MHz, CDCl$_3$): δ = 7.67 (dd, 1H, *J* = 8.2 Hz, *J* = 5.2 Hz) 7.73 (d, 1H, *J* = 8.9 Hz) 7.84 (d, 1H, *J* = 8.9 Hz) 8.26 (dd, 1H, *J* = 8.2 Hz, *J* = 1.2 Hz) 8.41 (d, 1H, *J* = 1.8 Hz) 9.18 – 9.21 (m, 2H)
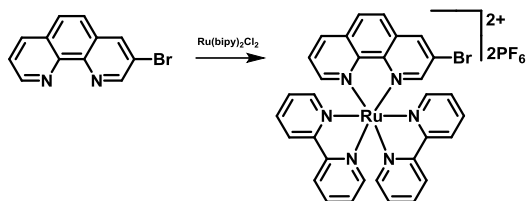**ES$^+$MS:** *m/z* = 259.0 [*M* + H]$^+$

Molecular Formula: $C_{12}H_7N_2Br_2$, **RMM:** 337.9
^{1}H NMR (400 MHz, CDCl$_3$): δ = 7.76 (s, 2H) 8.41 (d, 2H, *J* = 1.9 Hz) 9.19 (d, 2H, *J* = 1.9 Hz)
ES$^+$MS: *m/z* = 338.9 [*M* + H]$^+$

6.2.7) Bis(2,2'-bipyridine)(3-bromo-1,10-phenanthroline)Ru(II) hexafluorophosphate

3-Bromo-1,10-phenanthroline (0.95 g, 3.68 mmol) and *cis*-bis(2,2'-bipyridine)dichloro Ru(II) dihydrate[7] (1.90 g, 3.65 mmol) were dissolved in MeOH (30 mL) and refluxed for 16 hours. Once cooled, the solution was concentrated under reduced pressure and an excess of saturated $KPF_{6(aq)}$ solution (20 mL) was added. The solution was left at 4 °C for 16 hours and the resulting precipitate dissolved in CH_2Cl_2 (30 mL), separated and washed with water (3 x 25 mL). The combined aqueous layers were then washed with further portions of CH_2Cl_2 (2 x 25 mL) and the resulting organic extracts combined and dried ($MgSO_4$). The solvent was removed under reduced pressure to afford **bis(2,2'-bipyridine)(3-bromo-1,10-phenanthroline)Ru(II) hexafluorophosphate** (3.51 g) as a red solid in quantitative yield.

Molecular Formula: $[C_{32}H_{23}N_6BrRu]^{2+}[2PF_6^-]$, **RMM:** 962

^{1}H NMR (400 MHz, d_6-acetone): δ = 7.36 – 7.42 (m, 2H, bipy) 7.60 – 7.66 (m, 2H, bipy) 7.85 (dd, 1H, *J* = 1.5 Hz, *J* = 5.6 Hz, bipy) 7.94 (dd, 1H, *J* = 5.2 Hz, *J* = 8.2 Hz, phen) 8.04 (dd, 1H, *J* = 1.5 Hz, *J* = 5.6 Hz, bipy) 8.10 (dd, 1H, *J* = 1.5 Hz, *J* = 5.6 Hz, bipy) 8.12 – 8.18 (m, 2H, bipy) 8.19 (dd, 1H, *J* = 1.5 Hz, *J* = 5.6 Hz, bipy) 8.25 (tt, 2H, *J* = 1.5 Hz, *J* = 7.9 Hz, bipy) 8.35 (d, 1H, *J* = 8.9 Hz, phen) 8.44 (dd, 1H, *J* = 1.2 Hz, *J* = 5.2 Hz, phen) 8.45 (d, 1H, *J* = 8.9 Hz, phen) 8.47 (d, 1H, *J* = 1.9 Hz, phen) 8.78 – 8.87 (m, 5H, 4 x bipy,1 x phen) 9.06 (d, 1H, *J* = 1.9 Hz, phen)

ES$^+$MS: *m/z* = 337 $[M - 2PF_6]^{2+}$

HRMS ES$^+$: calculated for $[C_{32}H_{23}N_6BrRu]^{2+}$ 337.0099, found 337.0101

6.2.8) Ru(II)-Alkyne-Dyad-Ester hexafluorophosphate
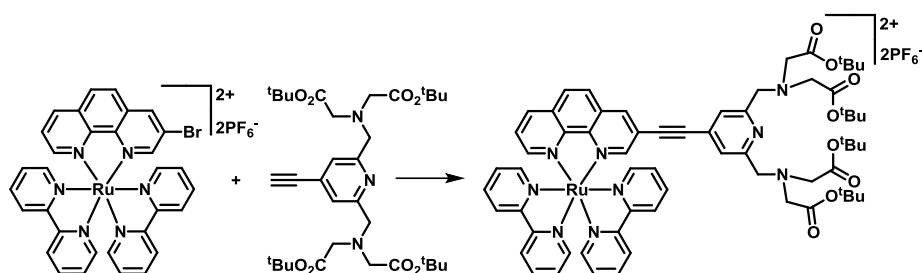
Ru(II)-Alkyne-Dyad-Ester hexafluorophosphate was prepared by a modified literature procedure[8]. Bis(2,2'-bipyridine)(3-bromo-1,10-phenanthroline)Ru(II) hexafluorophosphate (0.53 g, 0.55 mmol), (dppf)PdCl$_2$.CH$_2$Cl$_2$ (0.05 g, 0.06 mmol) and CuI (0.01 g, 0.05 mmol) were dissolved in a mixture of anhydrous DMF and ^{i}Pr$_2$NH (6 mL, 5:1, *v:v*) and deoxygenated with argon for 30 minutes. To this, a solution of 4-ethynyl-2,6-disubstituted pyridine (0.62 g, 1.00 mmol) in a deoxygenated mixture of anhydrous DMF and ^{i}Pr$_2$NH (3 mL, 5:1, *v:v*) was added dropwise. The solution was stirred at room temperature for 16 hours under argon, before removal of the solvent under reduced pressure. The resulting brown solid was purified by column chromatography on silica gel (200-300 mesh) with MeCN/H$_2$O/sat. KNO$_{3(aq)}$ (100:0:0 to 100:4:2, *v:v:v*) as the eluent. The solvent was then removed under reduced pressure and the solid dissolved in CH$_2$Cl$_2$ (30 mL), washed with an excess of saturated KPF$_{6(aq)}$ solution (20 mL) and separated. The aqueous layer was extracted with further portions of CH$_2$Cl$_2$ (2 x 15 mL) and the combined organic layers then washed with water (2 x 15 mL) and dried (MgSO$_4$). The solvent was removed under reduced pressure to afford **Ru(II)-Alkyne-Dyad-Ester hexafluorophosphate** (0.41 g, 50 %) as a dark red solid.

Molecular Formula: [C$_{65}$H$_{73}$N$_9$O$_8$Ru]$^{2+}$[2PF$_6^-$], **RMM:** 1499

^{1}H NMR (400 MHz, d_6-acetone): δ = 1.45 (s, 36H, ^{t}Bu) 3.49 (s, 8H, N–CH$_2$–ester) 4.00 (s, 4H, CH$_2$–pyridyl) 7.37 – 7.45 (m, 2H, bipy) 7.61 (s, 2H, pyridyl H^3/H^5) 7.62 – 7.67 (m, 2H, bipy) 7.88 (d, 1H, *J* = 5.6 Hz, bipy) 7.96 (dd, 1H, *J* = 5.2 Hz, *J* = 8.2 Hz, phen) 8.09 (d, 1H, *J* = 5.6 Hz, bipy) 8.13 (d, 1H, *J* = 5.6 Hz, bipy) 8.14 – 8.20 (m, 2H, bipy) 8.21 (d, 1H, *J* = 5.6 Hz, bipy) 8.26 (t, 2H, *J* = 7.9 Hz, bipy) 8.40 – 8.50 (m, 3H, phen) 8.67 (d, 1H, *J* = 1.9 Hz, phen) 8.79 – 8.88 (m, 5H, 4 x bipy, 1 x phen) 9.04 (d, 1H, *J* = 1.9 Hz, phen)

ES$^+$MS: *m/z* = 604.7 [*M* – 2PF$_6$]$^{2+}$

HRMS ES$^+$: calculated for [C$_{65}$H$_{73}$N$_9$O$_8$Ru]$^{2+}$ 604.7316, found 604.7318

6.2.9) Ru(II)-Alkyne-Dyad-Acid hexafluorophosphate
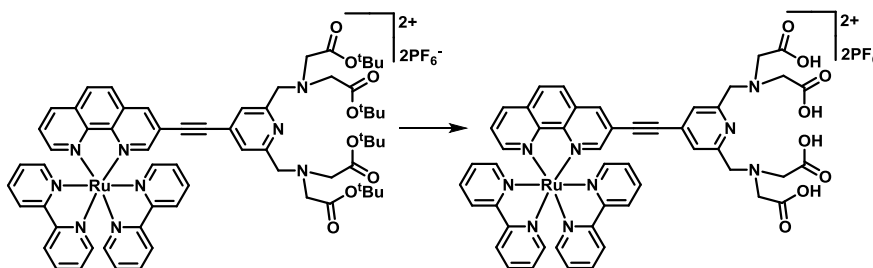
A solution of Ru(II)-Alkyne-Dyad-Ester hexafluorophosphate (73 mg, 0.049 mmol) in CH_2Cl_2 (3 mL) and TFA (3 mL) was stirred at room temperature for 18 hours. The solvent was then removed under reduced pressure to yield a red solid. To remove any residual TFA, the solid was dissolved in CH_2Cl_2 (10 mL) and the solvent removed under reduced pressure. This process was repeated ten times. The solid was then washed with MeOH (10 x 10 mL) following the same procedure. Finally, the red solid was dissolved in the minimum amount of MeOH and precipitated with an excess of diethyl ether. The solid was collected by centrifugation and dried under a stream of N_2 to yield **Ru(II)-Alkyne-Dyad-Acid hexafluorophosphate** (61 mg, 98 %) as a red solid.

Molecular Formula: $[C_{49}H_{41}N_9O_8Ru]^{2+}[2PF_6^-]$, **RMM:** 1275

^{1}H NMR (500 MHz, d_6-DMSO, 303 K): δ = 3.46 (s, 8H, N–CH$_2$–acid) 3.94 (s, 4H, CH$_2$–pyridyl) 7.33 − 7.38 (m, 2H, bipy) 7.53 (d, 1H, J = 5.3 Hz, bipy) 7.56 (s, 2H, pyridyl H^3/H^5) 7.56 − 7.62 (m, 2H, bipy) 7.75 (d, 2H, J = 5.3 Hz, bipy) 7.87 (d, 1H, J = 5.3 Hz, bipy) 7.90 (dd, 1H, J = 5.2 Hz, J = 8.2 Hz, phen) 8.07 − 8.16 (m, 3H, 2 x bipy, 1 x phen) 8.21 (t, 2H, J = 7.8 Hz, bipy) 8.29 (d, 1H, J = 1.0 Hz, phen), 8.35 (d, 1H, J = 8.8 Hz, phen), 8.44 (d, 1H, J = 8.8 Hz, phen), 8.78 − 8.90 (m, 5H, 4 x bipy, 1 x phen), 9.16 (d, 1H, J = 1.0 Hz, phen)

ES$^+$MS: m/z = 492.6 $[M - 2PF_6]^{2+}$, 328.7 $[M - 2PF_6 + H]^{3+}$

HRMS ES$^+$: calculated for $[C_{49}H_{41}N_9O_8Ru]^{2+}$ 492.6055, found 492.6056

6.2.10) Bis(2,2'-bipyridine)(3,8-dibromo-1,10-phenanthroline)Ru(II) hexafluorophosphate
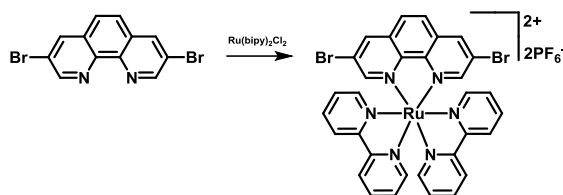
3,8-Dibromo-1,10-phenanthroline (0.33 g, 0.98 mmol) and *cis*-bis(2,2'-bipyridine) dichloro Ru(II) dihydrate[7] (0.51 g, 0.98 mmol) were dissolved in MeOH (30 mL) and refluxed for 16 hours. Once cooled, the solution was concentrated under reduced pressure and an excess of saturated $KPF_{6(aq)}$ solution (20 mL) was added. The solution was left at 4 °C for 16 hours and the resulting precipitate dissolved in CH_2Cl_2 (30 mL), separated and washed with water (3 x 25 mL). The combined aqueous layers were then washed with further portions of CH_2Cl_2 (2 x 25 mL) and the resulting organic extracts combined and dried ($MgSO_4$). The solvent was removed under reduced pressure to afford **bis(2,2'-bipyridine)(3,8-dibromo-1,10-phenanthroline)Ru(II) hexafluorophosphate** (1.02 g) as a red solid in quantitative yield.

Molecular Formula: $[C_{32}H_{22}N_6Br_2Ru]^{2+}[2PF_6^-]$, **RMM:** 1040

^{1}H NMR (400 MHz, *d*[6]-acetone): δ = 7.40 (ddd, 2H, *J* = 1.2 Hz, *J* = 5.6 Hz, *J* = 7.9 Hz, bipy) 7.63 (ddd, 2H, *J* = 1.2 Hz, *J* = 5.6 Hz, *J* = 7.9 Hz, bipy) 8.01 (dd, 2H, *J* = 1.5 Hz, *J* = 5.6 Hz, bipy) 8.12 (dd, 2H, *J* = 1.5 Hz, *J* = 5.6 Hz, bipy) 8.16 (td, 2H, *J* = 1.5 Hz, *J* = 7.9 Hz, bipy) 8.25 (td, 2H, *J* = 1.5 Hz, *J* = 7.9 Hz, bipy) 8.40 (s, 2H, phen) 8.48 (d, 2H, *J* = 1.9 Hz, phen) 8.79 (d, 2H, *J* = 7.9 Hz, bipy) 8.83 (d, 2H, *J* = 7.9 Hz, bipy) 9.07 (d, 2H, *J* = 1.9 Hz, phen)

ES[+]MS: *m/z* = 376.0 $[M - 2PF_6]^{2+}$

HRMS ES[+]: calculated for $[C_{32}H_{22}N_6Br_2Ru]^{2+}$ 375.9648, found 375.9650

6.2.11) Ru(II)-Alkyne-Triad-Ester hexafluorophosphate
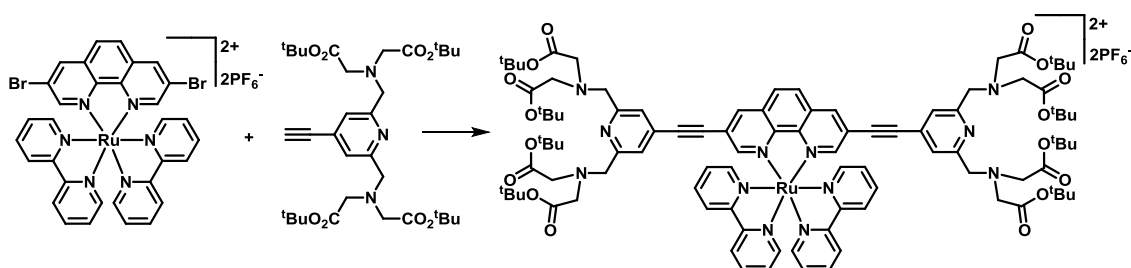
Bis(2,2'-bipyridine)(3,8-dibromo-1,10-phenanthroline)Ru(II) hexafluorophosphate (1.02 g, 0.98 mmol), (dppf)PdCl$_2$.CH$_2$Cl$_2$ (0.05 g, 0.06 mmol) and CuI (0.01 g, 0.05 mmol) were dissolved in a mixture of anhydrous DMF and ^{i}Pr$_2$NH (6 mL, 5:1, *v:v*) and deoxygenated with argon for 30 minutes. To this, a solution of 4-ethynyl-2,6-disubstituted pyridine (1.28 g, 2.07 mmol) in a deoxygenated mixture of anhydrous DMF and ^{i}Pr$_2$NH (3 mL, 5:1, *v:v*) was added dropwise. The solution was stirred at room temperature for 16 hours under argon before the addition of a further solution of 4-ethynyl-2,6-disubstituted pyridine (1.28 g, 2.07 mmol) in a deoxygenated mixture of anhydrous DMF and ^{i}Pr$_2$NH (3 mL, 5:1, *v:v*). The reaction was stirred under argon for 24 hours before the solvent was removed under reduced pressure. The resulting brown solid was purified by column chromatography on silica gel (200-300 mesh) with MeCN/H$_2$O/sat. KNO$_{3(aq)}$ (100:0:0 to 100:4:2, *v:v:v*) as the eluent. The solvent was then removed under reduced pressure and the solid dissolved in CH$_2$Cl$_2$ (30 mL), washed with an excess of saturated KPF$_{6(aq)}$ solution (20 mL) and separated. The aqueous layer was extracted with further portions of CH$_2$Cl$_2$ (2 x 15 mL) and the combined organic layers then washed with water (2 x 15 mL), dried (MgSO$_4$) and the solvent removed under reduced pressure. Further purification was then achieved by size exclusion chromatography on Sephadex® LH-20 in MeOH. The solvent was removed under reduced pressure to afford **Ru(II)-Alkyne-Triad-Ester hexafluorophosphate** (0.94 g, 45 %) as a dark red solid.

Molecular Formula: [C$_{98}$H$_{122}$N$_{12}$O$_{16}$Ru]$^{2+}$[2PF$_6^-$], **RMM:** 2115

^{1}H NMR (400 MHz, d_6-acetone): δ = 1.45 (s, 72H, ^{t}Bu) 3.49 (s, 16H, N–CH$_2$–ester) 3.99 (s, 8H, CH$_2$-pyridyl) 7.40 – 7.45 (m, 2H, bipy) 7.56 (s, 4H, pyridyl H^3/H^5) 7.60 – 7.66 (m, 2H, bipy) 8.05 (d, 2H, *J* = 5.6 Hz, bipy) 8.12 – 8.21 (m, 4H, bipy) 8.25 (t, 2H, *J* = 7.9 Hz, bipy) 8.48 (s, 2H, phen) 8.67 (d, 2H, *J* = 1.9 Hz, phen) 8.78 – 8.87 (m, 4H, bipy) 9.05 (d, 2H, *J* = 1.9 Hz, phen)

ES$^+$MS: *m/z* = 912.4 [*M* − 2PF$_6$]$^{2+}$, 608.6 [*M* − 2PF$_6$ + H]$^{3+}$

HRMS ES$^+$: calculated for [C$_{98}$H$_{122}$N$_{12}$O$_{16}$Ru]$^{2+}$ 912.4067, found 912.4073

6.2.12) Ru(II)-Alkyne-Triad-Acid hexafluorophosphate
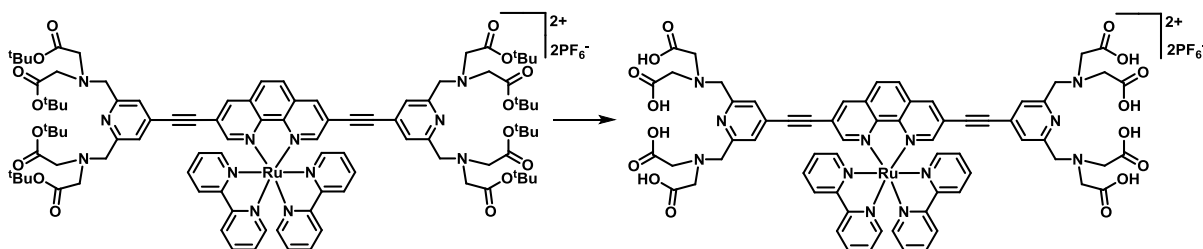
A solution of Ru(II)-Alkyne-Triad-Ester hexafluorophosphate (92 mg, 0.044 mmol) in CH_2Cl_2 (3 mL) and TFA (3 mL) was stirred at room temperature for 18 hours. The solvent was then removed under reduced pressure to yield a red solid. To remove any residual TFA, the solid was dissolved in CH_2Cl_2 (10 mL) and the solvent removed under reduced pressure. This process was repeated ten times. The solid was then washed with MeOH (10 x 10 mL) following the same procedure. Finally, the red solid was dissolved in the minimum amount of MeOH and precipitated with an excess of diethyl ether. The solid was collected by centrifugation and dried under a stream of N_2 to yield **Ru(II)-Alkyne-Triad-Acid hexafluorophosphate** (71 mg, 98 %) as a red solid.

Molecular Formula: $[C_{66}H_{58}N_{12}O_{16}Ru]^{2+}[2PF_6^-]$, **RMM:** 1666

^{1}H NMR (400 MHz, D_2O): δ = 4.16 (s, 16H, *br*, N–CH$_2$–acid) 4.74 (s, 8H, *br*, CH$_2$-pyridyl) 7.17 – 7.31 (m, 2H, *br*, bipy) 7.37 – 7.48 (m, 2H, *br*, bipy) 7.65 (d, 2H, *J* = 4.0 Hz, *br*, bipy) 7.69 (s, 4H, *br*, pyridyl H^3/H^5) 7.90 (d, 2H, *J* = 4.8 Hz, *br*, bipy) 7.98 – 8.06 (m, 2H, *br*, bipy) 8.06 – 8.16 (m, 2H, *br*, bipy) 8.25 (s, 2H, *br*, phen) 8.35 (s, 2H, *br*, phen) 8.51 – 8.63 (m, 4H, *br*, bipy) 8.74 (s, 2H, *br*, phen)

ES⁺MS: *m/z* = 688.2 $[M - 2PF_6]^{2+}$

HRMS ES⁺: calculated for $[C_{66}H_{58}N_{12}O_{16}Ru]^{2+}$ 688.1563, found 688.1568

6.2.13) Tris(3,8-dibromo-1,10-phenanthroline)Ru(II) hexafluorophosphate
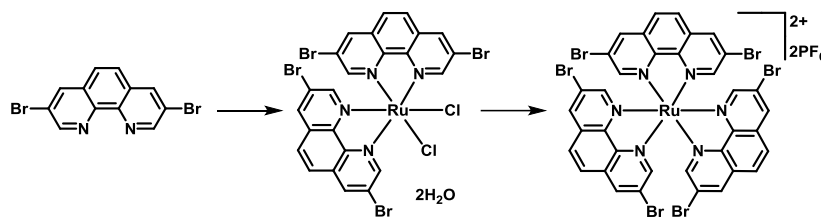
RuCl$_3$.3H$_2$O (0.135 g, 0.52 mmol), 3,8-dibromo-1,10-phenanthroline (0.350 g, 1.04 mmol) and LiCl (0.131 g, 3.12 mmol) were dissolved in DMF (30 mL) and heated to reflux for 7 hours. Once cooled, acetone (150 mL) was added and the reaction mixture left at 4 °C for 16 hours. The black precipitate was filtered, washed with ice cold acetone and dried under a stream of N$_2$ to yield crude ***cis*-bis(3,8-dibromo-1,10-phenanthroline)dichloro Ru(II) dihydrate** (0.262 g, 58 %) as a black solid. The solid was used without further purification.

Cis-bis(3,8-dibromo-1,10-phenanthroline)dichloro Ru(II) dihydrate (0.170 g, 0.19 mmol) and 3,8-dibromo-1,10-phenanthroline (0.069 g, 0.20 mmol) were dissolved in ethylene glycol (15 mL) and heated at 120 °C for 16 hours. Once cooled, CH$_2$Cl$_2$ (30 mL) and saturated KPF$_{6(aq)}$ solution (30 mL) were added and the reaction mixture separated. The compound was extracted with further portions of CH$_2$Cl$_2$ (2 x 30 mL) and the combined organic extracts washed with water (2 x 15 mL), dried (MgSO$_4$) and the solvent removed under reduced pressure. The resulting red solid was purified by column chromatography on silica gel (200-300 mesh) with MeCN/H$_2$O/sat. KNO$_{3(aq)}$ (100:0:0 to 100:4:2, *v:v:v*) as the eluent. The solvent was then removed under reduced pressure and the solid dissolved in CH$_2$Cl$_2$ (30 mL), washed with an excess of saturated KPF$_{6(aq)}$ solution (20 mL) and separated. The aqueous layer was extracted with further portions of CH$_2$Cl$_2$ (2 x 15 mL) and the combined organic layers then washed with water (2 x 15 mL) and dried (MgSO$_4$). The solvent was removed under reduced pressure to afford **tris(3,8-dibromo-1,10-phenanthroline)Ru(II) hexafluorophosphate** (0.270 g) as a red solid in quantitative yield.
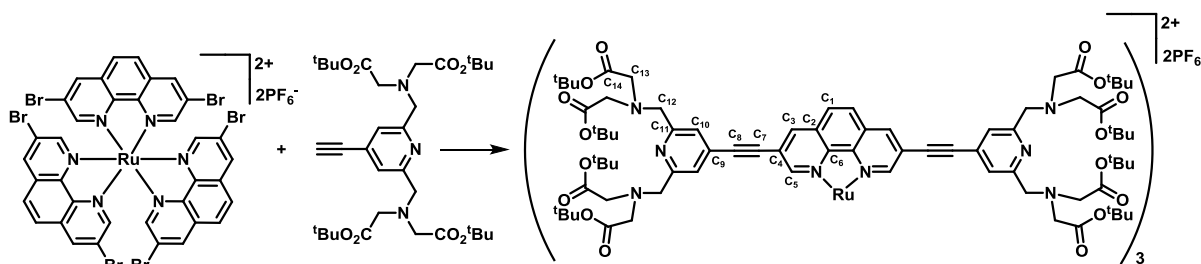
Molecular Formula: [C$_{36}$H$_{18}$N$_6$Br$_6$Ru]$^{2+}$[2PF$_6^-$], **RMM:** 1399
^{1}H NMR (400 MHz, *d$_6$*-acetone): δ = 8.39 (s, 6H) 8.53 (d, 6H, *J* = 1.9 Hz) 9.07 (d, 6H, *J* = 1.9 Hz)
ES$^+$MS: *m/z* = 557.8 [*M* − 2PF$_6$]$^{2+}$
HRMS ES$^+$: calculated for [C$_{36}$H$_{18}$N$_6$Br$_6$Ru]$^{2+}$ 557.7839, found 557.7823

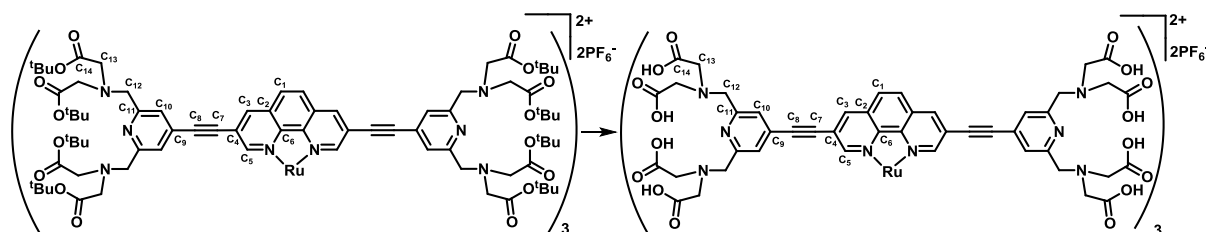### 6.2.14) Ru(II)-Alkyne-Metallostar-Ester hexafluorophosphate

Tris(3,8-dibromo-1,10-phenanthroline)Ru(II) hexafluorophosphate (0.270 g, 0.193 mmol), (dppf)PdCl$_2$.CH$_2$Cl$_2$ (0.033 g, 0.041 mmol) and CuI (0.005 g, 0.026 mmol) were dissolved in a mixture of anhydrous DMF and NEt$_3$ (6 mL, 5:1, *v:v*) and deoxygenated with argon for 30 minutes. To this, a solution of 4-ethynyl-2,6-disubstituted pyridine (1.42 g, 2.30 mmol) in a deoxygenated mixture of anhydrous DMF and NEt$_3$ (3 mL, 5:1, *v:v*) was added dropwise. The solution was stirred at room temperature for 16 hours before the addition of a further solution of 4-ethynyl-2,6-disubstituted pyridine (1.42 g, 2.30 mmol) in a deoxygenated mixture of anhydrous DMF and NEt$_3$ (3 mL, 5:1, *v:v*). The reaction was stirred for 7 days under argon before the solvent was removed under reduced pressure. The resulting brown solid was purified by column chromatography on silica gel (200-300 mesh) with MeCN/H$_2$O/sat. KNO$_{3(aq)}$ (100:0:0 to 200:6:2, *v:v:v*) as the eluent. The solvent was then removed under reduced pressure and the solid dissolved in CH$_2$Cl$_2$ (30 mL), washed with an excess of saturated KPF$_{6(aq)}$ solution (20 mL) and separated. The aqueous layer was extracted with further portions of CH$_2$Cl$_2$ (2 x 15 mL) and the combined organic layers then washed with water (2 x 15 mL) and dried (MgSO$_4$). Further purification was then achieved by size exclusion chromatography on Sephadex® LH-20 in MeOH. The solvent was removed under reduced pressure to afford **Ru(II)-Alkyne-Metallostar-Ester hexafluorophosphate** (0.135 g, 15 %) as a rusty brown solid.

Molecular Formula: [C$_{234}$H$_{318}$N$_{24}$O$_{48}$Ru]$^{2+}$[2PF$_6^-$], **RMM:** 4624

^{1}H NMR (400 MHz, *d$_6$*-acetone): δ = 1.41 (s, 216H, *br*, ^{t}Bu) 3.45 (s, 48H, *br*, N–CH$_2$–ester) 3.96 (s, 24H, *br*, CH$_2$-pyridyl) 7.55 (s, 12H, *br*, pyridyl H^3/H^5) 8.49 (s, 6H, *br*, phen) 8.81 (s, 6H, *br*, phen) 9.06 (s, 6H, *br*, phen)

^{13}C NMR (500 MHz, 1,1,2,2-tetrachloroethane-*d$_2$*, DEPTQ): δ = 28.2 (C(CH$_3$)$_3$) 55.6 (C$_{13}$) 59.4 (C$_{12}$) 81.2 (C(CH$_3$)$_3$) 86.6 (C$_7$) 96.0 (C$_8$) 123.1 (C$_{10}$) 128.7 (C$_5$) 131.0 (C$_6$) 141.0 (C$_3$) 145.9 (C$_2$) 153.6 (C$_1$) 159.3 (C$_{11}$) 166.7 (C$_4$) 170.3 (C$_9$) 207.8 (C$_{14}$) **ES$^+$MS:** *m/z* = 2168.6 [*M* − 2PF$_6$]$^{2+}$

### 6.2.15) Ru(II)-Alkyne-Metallostar-Acid hexafluorophosphate

A solution of Ru(II)-Alkyne-Metallostar-Ester hexafluorophosphate (0.10 g, 0.022 mmol) in CH_2Cl_2 (3 mL) and TFA (3 mL) was stirred at room temperature for 18 hours. The solvent was then removed under reduced pressure to yield a rusty brown solid. To remove any residual TFA, the solid was dissolved in CH_2Cl_2 (10 mL) and the solvent then removed under reduced pressure. This process was repeated ten times. The solid was then washed with MeOH (10 x 10 mL) following the same procedure. Finally, the rusty brown solid was dissolved in the minimum amount of MeOH and precipitated with an excess of diethyl ether. The solid was collected by centrifugation and dried under a stream of N_2 to yield **Ru(II)-Alkyne-Metallostar-Acid hexafluorophosphate** (0.07 mg, 99 %) as a rusty brown solid.

Molecular Formula: $[C_{138}H_{126}N_{24}O_{48}Ru]^{2+}[2PF_6^-]$, **RMM:** 3279

¹H NMR (500 MHz, D_2O, pD 4.38): δ = 3.82 (s, 48H, *br*, N–CH_2–acid) 4.57 (s, 24H, *br*, CH_2-pyridyl) 7.54 (s, 12H, *br*, pyridyl H^3/H^5) 8.06-8.45 (m, 12H, *br*, phen) 8.81 (s, 6H, *br*, phen)

¹³C NMR (500 MHz, D_2O, pD 4.38, DEPTQ): δ = 57.2 (C_{13}) 58.1 (C_{12}) 90.1 (C_7) 92.3 (C_8) 126.8 (C_{10}) 129.2 (C_5) 132.7 (C_6) 140.9 (C_3) 146.8 (C_2) 150.5 (C_{11}) 154.4 (C_1) 163.3 (C_4) 170.1 (C_9) 208.3 (C_{14})

### 6.2.16) 4-Azido-2,6-disubstituted pyridine
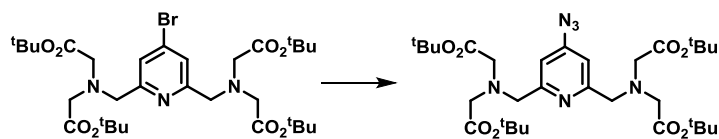
4-Azido-2,6-disubstituted pyridine was prepared by a modified literature procedure[9]. 4-Bromo-2,6-disubstituted pyridine (0.90 g, 1.3 mmol), sodium azide (0.87 g, 13.4 mmol) and tetrabutylammonium hydrogensulfate (0.09 g, 0.3 mmol) were added to anhydrous DMF (25 mL) in a flask charged with argon. The suspension was heated at 100 °C for 48 hours and then cooled to room temperature. Water (30 mL) was added and the compound extracted into di-isopropyl ether (3 x 50 mL). The combined organic layers were washed with water (2 x 20 mL) and dried (MgSO$_4$). The solvent was removed under reduced pressure to yield **4-azido-2,6-disubstituted pyridine** (0.62 g, 73 %) as a dark yellow oil.

Molecular Formula: C$_{31}$H$_{50}$N$_6$O$_8$, **RMM:** 634.4

^{1}H NMR (400 MHz, CDCl$_3$): δ = 1.45 (s, 36H) 3.46 (s, 8H) 3.98 (s, 4H) 7.23 (s, 2H)

ES$^+$MS: m/z = 635.4 [M + H]$^+$ 657.4 [M + Na]$^+$

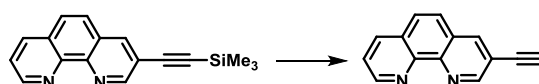### 6.2.17) 3-(Trimethylsilyl)ethynyl-1,10-phenanthroline
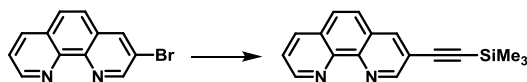
3-(Trimethylsilyl)ethynyl-1,10-phenanthroline was prepared by a literature procedure[10]. 3-Bromo-1,10-phenanthroline (0.40 g, 1.55 mmol), Pd(PPh$_3$)$_2$Cl$_2$ (0.06 g, 0.09 mmol) and CuI (0.04 g, 0.23 mmol) were dissolved in a mixture of THF and NEt$_3$ (15 mL, 2:1, *v:v*) and deoxygenated with argon for 30 minutes. TMSA (2.20 mL, 15.9 mmol) was added dropwise with vigorous stirring and the resulting mixture heated at 70 °C for 24 hours. Once cooled, the solvent was removed under reduced pressure to afford a black residue which was filtered through celite® with CH$_2$Cl$_2$ until the washings ran clear. The solvent was then removed under reduced pressure and the resulting solid filtered through celite® with hexane until the washings ran clear. The solvent was removed under reduced pressure and the crude product purified by column chromatography on silica gel (200-300 mesh) with CH$_2$Cl$_2$/MeOH (199:1, *v:v*) as the eluent to afford **3-(trimethylsilyl)ethynyl-1,10-phenanthroline** (0.05 g, 12 %) as a beige solid.

Molecular Formula: $C_{17}H_{16}N_2Si$, **RMM:** 276.1

^{1}H NMR (400 MHz, CDCl$_3$): δ = 0.30 (s, 9H) 7.60 (dd, 1H, *J* = 7.8 Hz, *J* = 4.4 Hz) 7.69 (d, 1H, *J* = 8.8 Hz) 7.76 (d, 1H, *J* = 8.8 Hz) 8.20 (dd, 1H, *J* = 7.8 Hz, *J* = 1.8 Hz) 8.29 (d, 1H, *J* = 1.8 Hz) 9.11 – 9.21 (m, 2H)

ES$^+$MS: *m/z* = 277.1 [*M* + H]$^+$

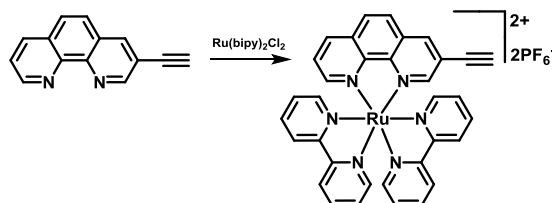### 6.2.18) 3-Ethynyl-1,10-phenanthroline

3-Ethynyl-1,10-phenanthroline was prepared by a modified literature procedure[11]. 3-(Trimethylsilyl)ethynyl-1,10-phenanthroline (56 mg, 0.20 mmol) was dissolved in a mixture of MeOH and THF (10 mL, 1:1, *v:v*). Potassium carbonate (38 mg, 0.28 mmol) was added and the resulting solution stirred at room temperature for 6 hours. The solvent was removed under reduced pressure and the solid dissolved in CH_2Cl_2 (20 mL), washed with water (2 x 20 mL) and dried (MgSO$_4$). The solvent was removed under reduced pressure to afford **3-ethynyl-1,10-phenanthroline** (17 mg, 40 %) as a beige solid.

Molecular Formula: $C_{14}H_8N_2$, **RMM:** 204.1

^{1}H NMR (400 MHz, CDCl$_3$): δ = 3.34 (s, 1H) 7.60 (dd, 1H, *J* = 8.0 Hz, *J* = 4.4 Hz) 7.69 (d, 1H, J = 8.8 Hz) 7.76 (d, 1H, J = 8.8 Hz) 8.20 (dd, 1H, *J* = 8.0 Hz, *J* = 1.8 Hz) 8.30 (d, 1H, *J* = 2.1 Hz) 9.16 (dd, 1H, *J* = 4.4 Hz, *J* = 1.8 Hz) 9.19 (d, 1H, *J* = 2.1 Hz)

ES$^+$MS: *m/z* = 205.1 [*M* + H]$^+$

6.2.19) Bis(2,2'-bipyridine)(3-ethynyl-1,10-phenanthroline)Ru(II) hexafluorophosphate

3-Ethynyl-1,10-phenanthroline (17 mg, 0.083 mmol) and *cis*-bis(2,2'-bipyridine)dichloro Ru(II) dihydrate[7] (41 mg, 0.079 mmol) were dissolved in MeOH (10 mL) and refluxed for 6 hours. Once cooled, the solvent was removed under reduced pressure and the resulting red solid purified by column chromatography on silica gel (200-300 mesh) with

MeCN/H$_2$O/sat. KNO$_{3(aq)}$ (100:0:0 to 100:10:5, *v:v:v*) as the eluent. The solvent was then removed under reduced pressure and the solid dissolved in CH$_2$Cl$_2$ (30 mL), washed with an excess of saturated KPF$_{6(aq)}$ solution (20 mL) and separated. The aqueous layer was extracted with further portions of CH$_2$Cl$_2$ (2 x 15 mL) and the combined organic layers then washed with water (2 x 15 mL) and dried (MgSO$_4$). The solvent was removed under reduced pressure to afford **bis(2,2'-bipyridine)(3-ethynyl-1,10-phenanthroline)Ru(II) hexafluorophosphate** (75 mg) as a red solid in quantitative yield.

Molecular Formula: [C$_{34}$H$_{24}$N$_6$Ru]$^{2+}$[2PF$_6$$^-$], **RMM:** 908

^{1}H NMR (400 MHz, *d*$_6$-acetone): δ = 4.18 (s, 1H) 7.40 (ddt, 2H, *J* = 1.4 Hz, *J* = 5.7 Hz, *J* = 7.8 Hz, bipy) 7.64 (ddd, 2H, *J* = 1.3 Hz, *J* = 5.7 Hz, *J* = 7.8 Hz, bipy) 7.88 (dd, 1H, *J* = 0.7 Hz, *J* = 5.7 Hz, bipy) 7.96 (dd, 1H, *J* = 5.3 Hz, *J* = 8.3 Hz, phen) 8.05 (dd, 1H, *J* = 0.7 Hz, *J* = 5.7 Hz, bipy) 8.13 – 8.19 (m, 3H, bipy) 8.21 (dd, 1H, *J* = 0.7 Hz, *J* = 5.7 Hz, bipy) 8.26 (tdd, 2H, *J* = 1.4 Hz, *J* = 2.7 Hz, *J* = 7.9 Hz, bipy) 8.39 (d, 1H, *J* = 8.8 Hz, phen) 8.44 – 8.48 (m, 3H, phen) 8.79 – 8.88 (m, 5H, 4 x bipy, 1 x phen) 8.92 (d, 1H, *J* = 1.6 Hz, phen)

ES$^+$MS: *m/z* = 309.1 [*M* − 2PF$_6$]$^{2+}$, 763 [*M* − PF$_6$]$^+$

HRMS ES$^+$: calculated for [C$_{34}$H$_{24}$N$_6$Ru]$^{2+}$ 309.0552, found 309.0556

6.2.20) Ru(II)-Triazole-Dyad-Ester hexafluorophosphate
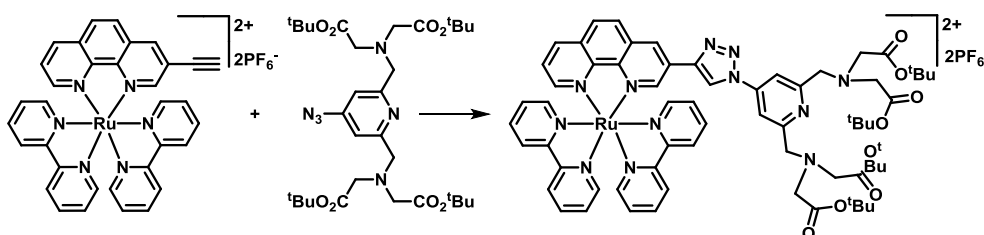
Ru(II)-Triazole-Dyad-Ester hexafluorophosphate was prepared by a modified literature procedure[9]. Bis(2,2'-bipyridine)(3-ethynyl-1,10-phenanthroline)Ru(II) hexafluorophosphate (75 mg, 0.083 mmol), 4-azido-2,6-disubstituted pyridine (0.11 g, 0.17 mmol) and CuI (0.01 g, 0.05 mmol) were dissolved in MeCN (20 mL) and deoxygenated with argon for 30 minutes. The solution was then refluxed for 24 hours under argon, before removal of the solvent under reduced pressure. The resulting orange solid was purified by column chromatography on silica gel (200-300 mesh) with MeCN/H$_2$O/sat. KNO$_{3(aq)}$ (100:0:0 to 100:2:1 to 100:4:2, *v:v:v*) as the eluent. The solvent was then removed under reduced

pressure and the solid dissolved in CH_2Cl_2 (30 mL), washed with an excess of saturated $KPF_{6(aq)}$ solution (20 mL) and separated. The aqueous layer was extracted with further portions of CH_2Cl_2 (2 x 15 mL) and the combined organic layers then washed with water (2 x 15 mL) and dried ($MgSO_4$). Further purification was then achieved by size exclusion chromatography on Sephadex® LH-20 in MeOH. The solvent was removed under reduced pressure to afford **Ru(II)-Triazole-Dyad-Ester hexafluorophosphate** (26 mg, 20 %) as an orange solid.

Molecular Formula: $[C_{65}H_{74}N_{12}O_8Ru]^{2+}[2PF_6^-]$, **RMM:** 1542

^{1}H NMR (400 MHz, d_6-acetone): δ = 1.44 (s, 36H, ^{t}Bu) 3.57 (s, 8H, N–CH_2–ester) 4.12 (s, 4H, CH_2-pyridyl) 7.36 – 7.44 (m, 2H, bipy) 7.66 (ddd, 1H, J = 1.1 Hz, J = 5.7 Hz, J = 7.8 Hz, bipy) 7.73 (ddd, 1H, J = 1.1 Hz, J = 5.7 Hz, J = 7.8 Hz, bipy) 7.93 – 7.99 (m, 2H, 1 x bipy, 1 x phen) 8.09 (s, 2H, pyridyl H^3/H^5) 8.11 (d, 1H, J = 5.7 Hz, bipy) 8.13 – 8.19 (m, 2H, bipy) 8.21 (d, 1H, J = 5.7 Hz, bipy) 8.25 – 8.32 (m, 2H, bipy) 8.36 (td, 1H, J = 1.1 Hz, J = 7.8 Hz, bipy) 8.43 – 8.50 (m, 3H, phen) 8.79 – 8.87 (m, 3H, 2 x bipy, 1 x phen) 8.90 (t, 2H, J = 8.4 Hz, bipy) 8.95 (d, 1H, J = 1.6 Hz, phen) 9.27 (d, 1H, J = 1.6 Hz, phen) 9.29 (s, 1H, triazole)

ES$^+$MS: m/z = 626.2 $[M - 2PF_6]^{2+}$

HRMS ES$^+$: calculated for $[C_{65}H_{74}N_{12}O_8{}^{102}Ru]^{2+}$ 626.2393, found 626.2401

6.2.21) Ru(II)-Triazole-Dyad-Acid hexafluorophosphate
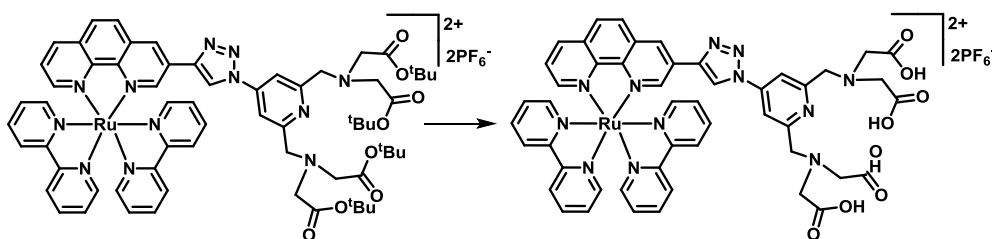
A solution of Ru(II)-Triazole-Dyad-Ester hexafluorophosphate (26 mg, 0.017 mmol) in CH_2Cl_2 (3 mL) and TFA (3 mL) was stirred at room temperature for 18 hours. The solvent was then removed under reduced pressure to yield a red solid. To remove any residual TFA, the solid was dissolved in CH_2Cl_2 (10 mL) and the solvent removed under reduced pressure. This process was repeated ten times. The solid was then washed with MeOH (10 x 10 mL) following the same procedure. Finally, the red solid was dissolved in the minimum amount of MeOH and precipitated with an excess of diethyl ether. The solid was collected by centrifugation and dried under a stream of N_2 to yield **Ru(II)-Triazole-Dyad-Acid hexafluorophosphate** (20 mg, 90 %) as an orange solid.

**Molecular Formula:** $[C_{49}H_{42}N_{12}O_8Ru]^{2+}[2PF_6^-]$, **RMM:** 1318

^{1}H NMR (400 MHz, *d*$_6$-DMSO, 373 K): δ = 3.53 (s, 8H, N–CH$_2$–acid) 4.09 (s, 4H, CH$_2$-pyridyl) 7.33 – 7.41 (m, 2H, bipy) 7.58 – 7.65 (m, 2H, bipy) 7.67 (t, 1H, *J* = 6.2 Hz, bipy) 7.77 (d, 1H, *J* = 3.9 Hz, bipy) 7.84 – 7.99 (m, 5H, 2 x bipy, 1 x phen, 2 x pyridyl H^3/H^5) 8.06 – 8.13 (m, 2H, bipy) 8.17 (d, 1H, *J* = 4.8 Hz, phen) 8.22 (t, 1H, *J* = 7.2 Hz, bipy) 8.29 (t, 1H, *J* = 7.2 Hz, bipy) 8.41 (s, 2H, phen) 8.59 (s, 1H, phen) 8.72 – 8.88 (m, 5H, 4 x bipy, 1 x phen) 9.23 (s, 1H, phen) 9.34 (s, 1H, triazole)

ES$^+$MS: *m/z* = 514 [*M* − 2PF$_6$]$^{2+}$

HRMS ES$^+$: calculated for $[C_{49}H_{42}N_{12}O_8Ru]^{2+}$ 514.1162, found 514.1141

6.3) Synthesis of Compounds in Chapter 3
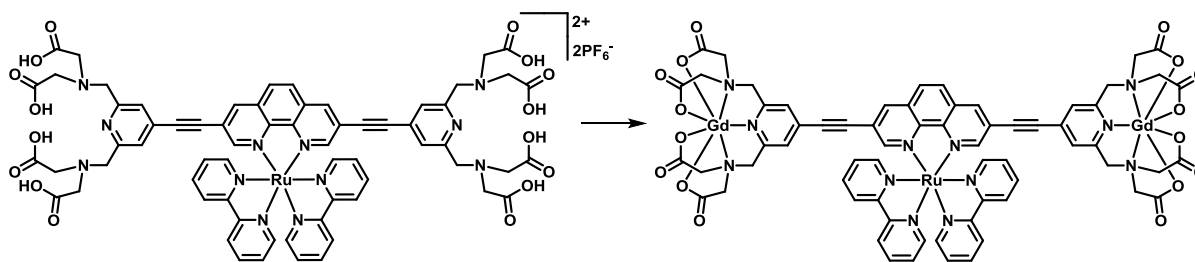
6.3.1) Ru(II)-Alkyne-Dyad-Gd(III) chloride
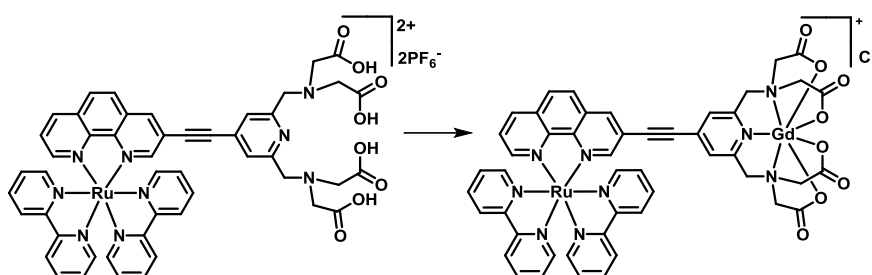
Ru(II)-Alkyne-Dyad-Acid hexafluorophosphate (45 mg, 0.035 mmol) was dissolved in water (3 mL) and cooled to 0 °C. A solution of $GdCl_3.6H_2O$ (14 mg, 0.038 mmol) in water (0.5 mL) was added dropwise and the mixture stirred at room temperature. After one hour, the solution was taken to pH 5-6 using a solution of $NaOH_{(aq)}$ (1M) and left to stir at room temperature for 18 hours. Saturated $KPF_{6(aq)}$ solution was then added to produce a red precipitate which was filtered and washed with water. The red solid was then dissolved in the minimum amount of MeOH and precipitated with an excess of diethyl ether. The precipitate was collected by centrifugation and purified further using Sephadex® LH-20 in MeOH. The solvent was removed under reduced pressure and the resulting red solid dried under a stream of N_2. Counterion exchange was then achieved using Dowex® 1x2 chloride form (100-200 mesh) in water. The solution was filtered, the water removed under reduced pressure and the resulting red solid dried under a stream of N_2 to yield **Ru(II)-Alkyne-Dyad-Gd(III) chloride** (35 mg, 84 %) as a red solid.

Molecular Formula: $[C_{49}H_{37}N_9O_8RuGd]^+[Cl^-]$, **RMM:** 1174

ES$^+$MS: m/z = 570.1 $[M - Cl + H]^{2+}$, 380.4 $[M - Cl + 2H]^{3+}$

HRMS ES$^+$: calculated for $[C_{49}H_{37}N_9O_8RuGd + H]^{2+}$ 570.0558, found 570.0562

6.3.2) Ru(II)-Alkyne-Triad-Gd(III)

Ru(II)-Alkyne-Triad-Acid hexafluorophosphate (100 mg, 0.060 mmol) was dissolved in water (3 mL) and cooled to 0 °C. A solution of $GdCl_3.6H_2O$ (59 mg, 0.159 mmol) in water (0.5 mL) was added dropwise and the mixture stirred at room temperature. After one hour, the solution was taken to pH 5-6 using a solution of $NaOH_{(aq)}$ (1M) and left to stir at room temperature for 18 hours. The solution was then purified using Sephadex® LH-20 in water. The solvent was removed under reduced pressure and the resulting red solid dried under a stream of N_2 to yield **Ru(II)-Alkyne-Triad-Gd(III)** (70 mg, 69 %) as a red solid.

Molecular Formula: $C_{66}H_{50}N_{12}O_{16}RuGd_2$, **RMM:** 1683

ES⁺MS: m/z = 842.1 $[M + 2H]^{2+}$ 852.5 $[M + Na + H]^{2+}$ 864.6 $[M + 2Na]^{2+}$

HRMS ES⁺: calculated for $[C_{66}H_{50}N_{12}O_{16}RuGd_2 + 2H]^{2+}$ 842.5530, found 842.5664

6.3.3) Ru(II)-Alkyne-Metallostar-Gd(III) sodium
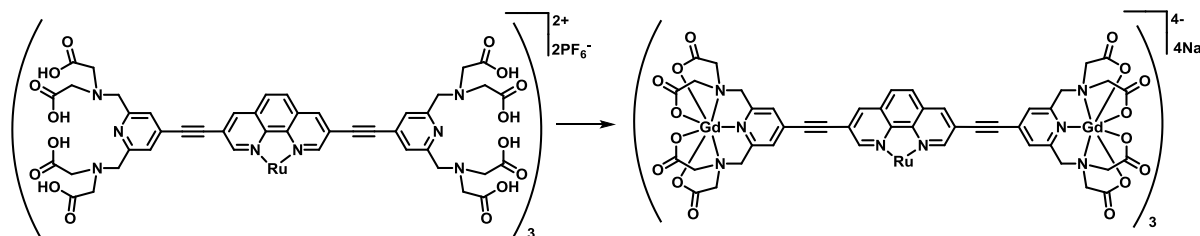
Ru(II)-Alkyne-Metallostar-Acid hexafluorophosphate (38 mg, 0.011 mmol) was dissolved in water (3 mL) and the pH of the solution adjusted to 5-6 using a solution of $NaOH_{(aq)}$ (0.1 M). With stirring, a solution of $GdCl_3.6H_2O$ (27 mg, 0.073 mmol) in water (0.5 mL) was added dropwise. The mixture was stirred at room temperature and the pH readjusted to 5-6 using $NaOH_{(aq)}$ (0.1 M) when necessary. After 18 hours, a rusty brown precipitate formed which was filtered and washed with water. Due to the resulting solid's insolubility in all solvents, however, no characterisation was achieved to ascertain successful synthesis of the target compound.

6.3.4) Ru(II)-Triazole-Dyad-Gd(III) chloride
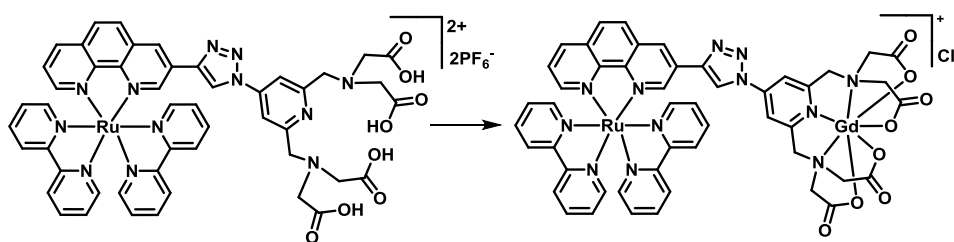
Ru(II)-Triazole-Dyad-Acid hexafluorophosphate (20 mg, 0.015 mmol) was dissolved in water (3 mL) and the pH of the solution adjusted to 5-6 using a solution of $NaOH_{(aq)}$ (0.1 M). With stirring, a solution of $GdCl_3.6H_2O$ (7 mg, 0.019 mmol) in water (0.5 mL) was added dropwise. The mixture was stirred at room temperature and the pH readjusted to 5-6 using $NaOH_{(aq)}$ (0.1 M) when necessary. After 18 hours, Dowex® 1x2 chloride form (100-200 mesh) was added and the solution was left stirring for a further 24 hours. The solution was filtered, concentrated under reduced pressure and purified on Sephadex® G-15. The solvent was removed under reduced pressure and the resulting orange solid dried under a stream of N_2 to yield **Ru(II)-Triazole-Dyad-Gd(III) chloride** (18 mg, 97 %) as an orange solid.
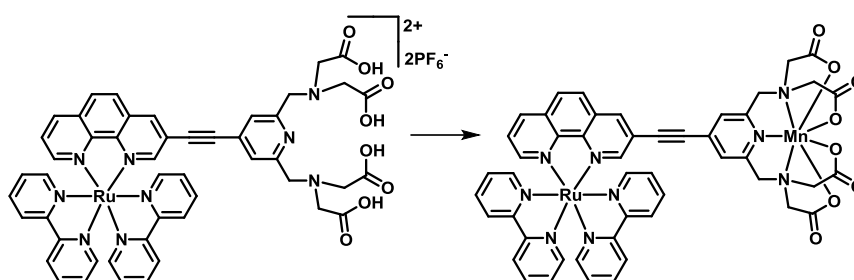
Molecular Formula: $[C_{49}H_{38}N_{12}O_8RuGd]^+[Cl^-]$, **RMM:** 1217

ES⁺MS: m/z = 591 $[M - Cl + H]^{2+}$, 1182 $[M - Cl]^+$

HRMS ES⁺: calculated for $[C_{49}H_{38}N_{12}O_8RuGd + H]^{2+}$ 591.5644, found 591.5642

6.4) Synthesis of Compounds in Chapter 4

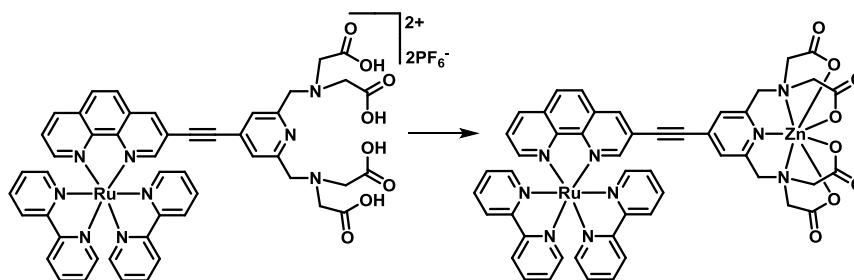### 6.4.1) Ru(II)-Alkyne-Dyad-Mn(II)

Ru(II)-Alkyne-Dyad-Acid hexafluorophosphate (130 mg, 0.102 mmol) was dissolved in water (3 mL) and the pH of the solution adjusted to 5-6 using a solution of $NaOH_{(aq)}$ (0.1 M). With stirring, a solution of $MnCl_2.4H_2O$ (26 mg, 0.131 mmol) in water (0.5 mL) was added dropwise. The mixture was stirred at room temperature and the pH readjusted to 5-6 using $NaOH_{(aq)}$ (0.1 M) when necessary. After 18 hours, the reaction mixture was concentrated under reduced pressure and purified on Sephadex® G-15. The solvent was removed under reduced pressure and the resulting red solid dried under a stream of N_2 to yield **Ru(II)-Alkyne-Dyad-Mn(II)** (100 mg, 95 %) as a red solid.

Molecular Formula: $C_{49}H_{37}N_9O_8RuMn$, **RMM:** 1036

ES$^+$MS: m/z = 519.1 $[M + 2H]^{2+}$

HRMS ES$^+$: calculated for $[C_{49}H_{37}N_9O_8RuMn + 2H]^{2+}$ 519.0667, found 519.0658

6.4.2) Ru(II)-Alkyne-Dyad-Zn(II)

Ru(II)-Alkyne-Dyad-Acid hexafluorophosphate (38 mg, 0.030 mmol) was dissolved in water (3 mL) and the pH of the solution adjusted to 5-6 using a solution of $NaOH_{(aq)}$ (0.1 M). With stirring, a solution of $ZnCl_2.XH_2O$ (10 mg, 0.049 mmol) in water (0.5 mL) was added dropwise. The mixture was stirred at room temperature and the pH readjusted to 5-6 using $NaOH_{(aq)}$ (0.1 M) when necessary. After 18 hours, the reaction mixture was concentrated

under reduced pressure and purified on Sephadex® G-15. The solvent was removed under reduced pressure and the resulting red solid dried under a stream of N_2 to yield **Ru(II)-Alkyne-Dyad-Zn(II)** (25 mg, 80 %) as a red solid.

Molecular Formula: $C_{49}H_{37}N_9O_8RuZn$, **RMM:** 1045

^{1}H NMR (400 MHz, D_2O): δ = 3.34 – 3.52 (m, 8H, N–CH$_2$–Zn) 4.15 (s, 4H, CH$_2$–pyridyl) 7.16 – 7.26 (m, 2H, bipy) 7.39 – 7.46 (m, 2H, bipy) 7.48 (s, 1H, pyridyl H^3 or H^5) 7.52 (s, 0.5H, pyridyl H^3 or H^5) 7.54 (s, 0.5H, pyridyl H^3 or H^5) 7.58 (d, 1H, *J* = 5.3 Hz, bipy) 7.68 (d, 1H, *J* = 5.3 Hz, bipy) 7.73 (t, 1H, *J* = 6.5 Hz, phen) 7.91 (d, 1H, *J* = 5.3 Hz, bipy) 7.94 (d, 1H, *J* = 5.3 Hz, bipy) 7.99 (t, 2H, *J* = 7.5 Hz, bipy) 8.09 (t, 2H, *J* = 7.5 Hz, bipy) 8.18 (d, 1H, *J* = 4.8 Hz, phen) 8.19 – 8.29 (m, 2H, phen) 8.35 (d, 1H, *J* = 4.5 Hz, phen) 8.50 – 8.64 (m, 5H, 4 x bipy, 1 x phen) 8.76 (s, 0.5H, phen) 8.79 (s, 0.5H, phen)

ES$^+$MS: *m/z* = 523.6 [*M* + 2H]$^{2+}$

HRMS ES$^+$: calculated for $[C_{49}H_{37}N_9O_8RuZn + 2H]^{2+}$ 523.5623, found 523.5632
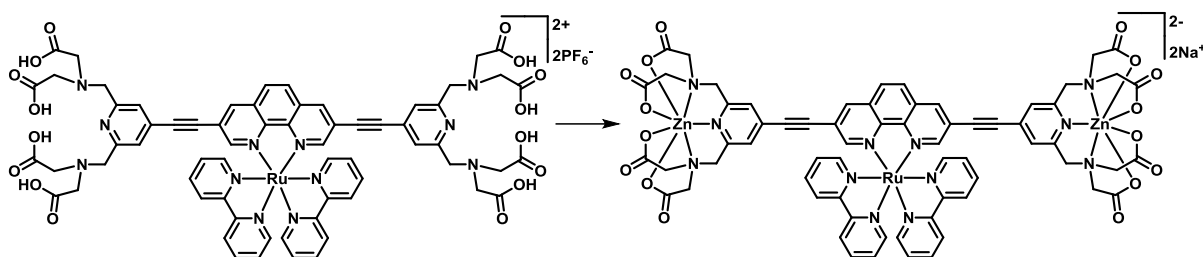
6.4.3) Ru(II)-Alkyne-Triad-Mn(II) disodium
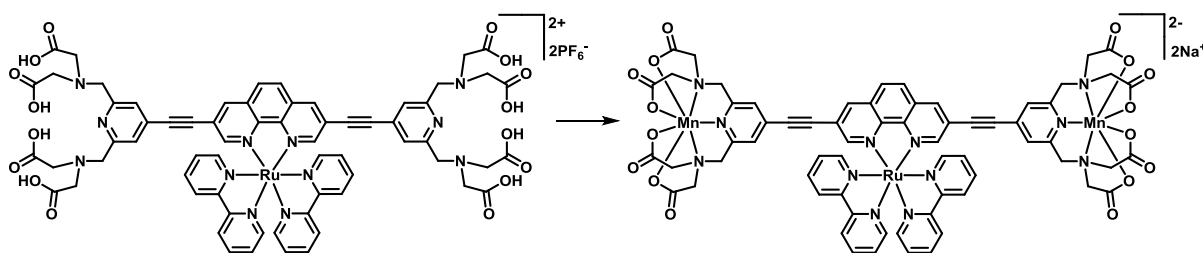
Ru(II)-Alkyne-Triad-Acid hexafluorophosphate (41 mg, 0.025 mmol) was dissolved in water (3 mL) and the pH of the solution adjusted to 5-6 using a solution of NaOH$_{(aq)}$ (0.1 M). With stirring, a solution of MnCl$_2$.4H$_2$O (12 mg, 0.061 mmol) in water (0.5 mL) was added dropwise. The mixture was stirred at room temperature and the pH readjusted to 5-6 using NaOH$_{(aq)}$ (0.1 M) when necessary. After 18 hours, the reaction mixture was concentrated under reduced pressure and purified on Sephadex® G-15. The solvent was removed under reduced pressure and the resulting red solid dried under a stream of N_2 to yield **Ru(II)-Alkyne-Triad-Mn(II) disodium** (25 mg, 67 %) as a red solid.

Molecular Formula: $[C_{66}H_{50}N_{12}O_{16}RuMn_2]^{2-}[2Na^+]$, **RMM:** 1523

ES$^-$MS: *m/z* = 739.1 [*M* − 2Na]$^{2-}$

HRMS ES$^-$: calculated for $[C_{66}H_{50}N_{12}O_{16}{}^{102}RuMn_2]^{2-}$ 739.0631, found 739.0598

6.4.4) Ru(II)-Alkyne-Triad-Zn(II) disodium

Ru(II)-Alkyne-Triad-Acid hexafluorophosphate (9 mg, 5.20 μmol) was dissolved in water (3 mL) and the pH of the solution adjusted to 5-6 using a solution of $NaOH_{(aq)}$ (0.1 M). With stirring, a solution of $ZnCl_2.XH_2O$ (5 mg, 25 μmol) in water (0.5 mL) was added dropwise. The mixture was stirred at room temperature and the pH readjusted to 5-6 using $NaOH_{(aq)}$ (0.1 M) when necessary. After 18 hours, the reaction mixture was concentrated under reduced pressure and purified on Sephadex® G-15. The solvent was removed under reduced pressure and the resulting red solid dried under a stream of N_2 to yield **Ru(II)-Alkyne-Triad-Zn(II) disodium** (7 mg, 82 %) as a red solid.

**Molecular Formula:** $[C_{66}H_{50}N_{12}O_{16}RuZn_2]^{2-}[2Na^+]$, **RMM:** 1542

^{1}H NMR (400 MHz, D$_2$O): δ = 3.50 (s, 16H, *br*, N–CH$_2$–Zn) 4.18 (s, 8H, *br*, CH$_2$–pyridyl) 7.14 – 7.36 (2H, *br*, bipy) 7.36 – 7.50 (2H, *br*, bipy) 7.55 (s, 2H, *br*, pyridyl H^3 or H^5) 7.60 – 7.83 (m, 4H, *br,* 2 x bipy, 2 x pyridyl H^3 or H^5) 7.84 – 7.95 (2H, *br*, bipy) 7.95 – 8.06 (m, 2H, *br*, bipy) 8.06 – 8.18 (m, 2H, *br*, bipy) 8.27 (s, 2H, *br*, phen) 8.36 (s, 2H, *br*, phen) 8.47 – 8.69 (m, 4H, *br*, bipy) 8.80 (s, 2H, *br*, phen)

ES⁻MS: *m/z* = 748.1 $[M – 2Na]^{2-}$

HRMS ES⁻: calculated for $[C_{66}H_{50}N_{12}O_{16}{}^{102}Ru^{64}Zn_2]^{2-}$ 748.0553, found 748.0532

6.5) Synthesis of Compounds in Chapter 5
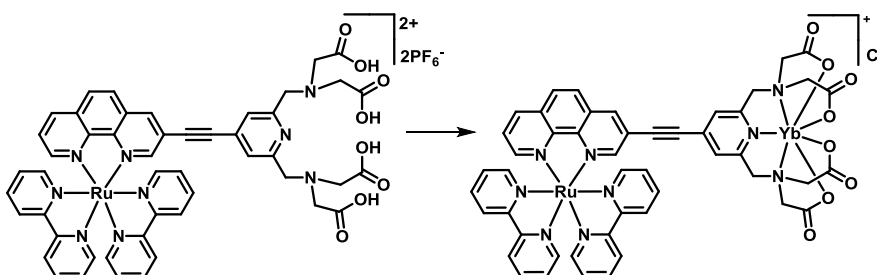
6.5.1) Ru(II)-Alkyne-Dyad-Nd(III) chloride
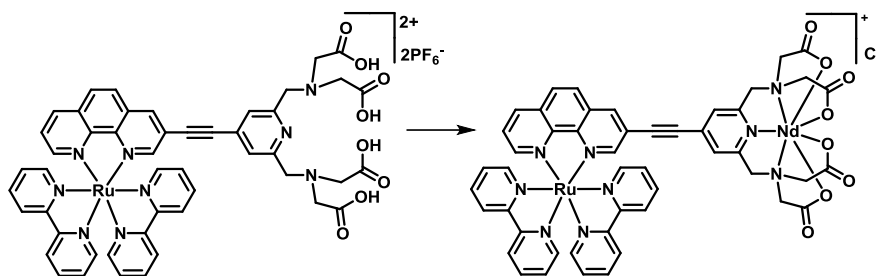
Ru(II)-Alkyne-Dyad-Acid hexafluorophosphate (15 mg, 0.012 mmol) was dissolved in water (3 mL) and the pH of the solution adjusted to 5-6 using $NaOH_{(aq)}$ (0.1 M). With stirring, a solution of $Nd(OTf)_3$ (11 mg, 0.019 mmol) in water (0.5 mL) was added dropwise. The mixture was stirred at room temperature and the pH readjusted to 5-6 using $NaOH_{(aq)}$ (0.1 M) when necessary. After 18 hours, a small portion of Dowex® 1x2 chloride form (100-200 mesh) was added and the mixture stirred at room temperature for a further 24 hours. The solution was then filtered, concentrated under reduced pressure and purified on Sephadex® G-15. The solvent was removed under reduced pressure and the resulting red solid dried under a stream of N_2 to yield **Ru(II)-Alkyne-Dyad-Nd(III) chloride** (13 mg, 95 %) as a red solid.

Molecular Formula: $[C_{49}H_{37}N_9O_8RuNd]^+[Cl^-]$, **RMM:** 1158

ES$^+$MS: m/z = 563.0 $[M - Cl + H]^{2+}$, 375.7 $[M - Cl + 2H]^{3+}$

HRMS ES$^+$: calculated for $[C_{49}H_{37}N_9O_8{}^{102}Ru^{144}Nd + H]^{2+}$ 563.0488, found 563.0497

6.5.2) Ru(II)-Alkyne-Dyad-Yb(III) chloride

Ru(II)-Alkyne-Dyad-Acid hexafluorophosphate (18 mg, 0.014 mmol) was dissolved in water (3 mL) and the pH of the solution adjusted to 5-6 using $NaOH_{(aq)}$ (0.1 M). With stirring, a solution of $Yb(OTf)_3$ (14 mg, 0.023 mmol) in water (0.5 mL) was added dropwise. The mixture was stirred at room temperature and the pH readjusted to 5-6 using $NaOH_{(aq)}$ (0.1 M) when necessary. After 18 hours, a small portion of Dowex® 1x2 chloride form (100-200 mesh) was
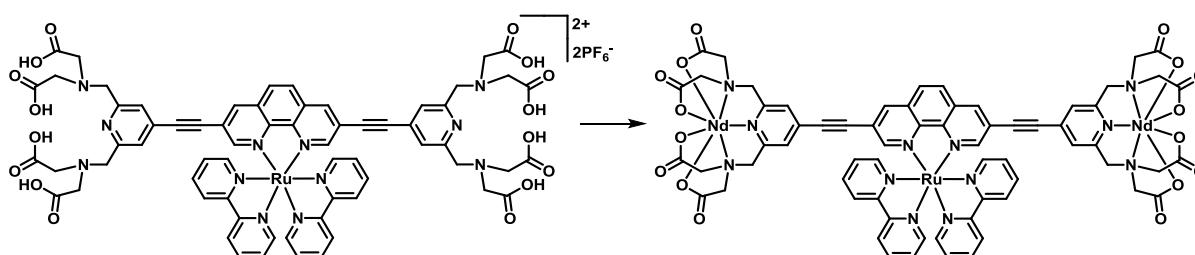
added and the mixture stirred at room temperature for a further 24 hours. The solution was then filtered, concentrated under reduced pressure and purified on Sephadex® G-15. The solvent was removed under reduced pressure and the resulting red solid dried under a stream of N_2 to yield **Ru(II)-Alkyne-Dyad-Yb(III) chloride** (14 mg, 83 %) as a red solid.

Molecular Formula: $[C_{49}H_{37}N_9O_8RuYb]^+[Cl^-]$, **RMM:** 1190

ES⁺MS: m/z = 578.1 $[M - Cl + H]^{2+}$

HRMS ES⁺: calculated for $[C_{49}H_{37}N_9O_8{}^{102}Ru^{173}Yb + H]^{2+}$ 578.0632, found 578.0632

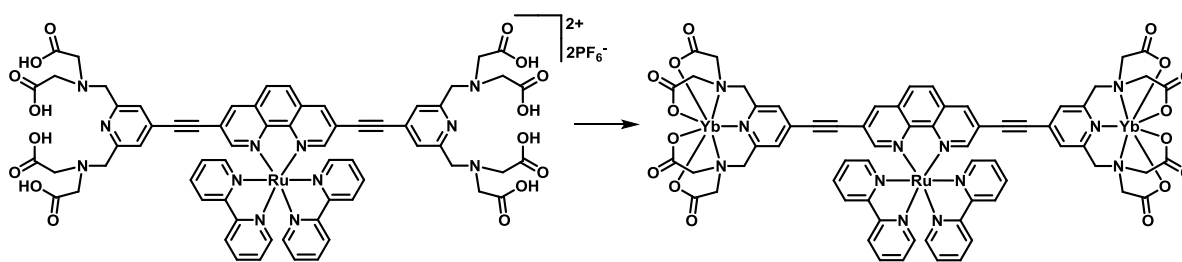### 6.5.3) Ru(II)-Alkyne-Triad-Nd(III)

Ru(II)-Alkyne-Triad-Acid hexafluorophosphate (11.4 mg, 0.007 mmol) was dissolved in water (3 mL) and the pH of the solution adjusted to 5-6 using $NaOH_{(aq)}$ (0.1 M). With stirring, a solution of $Nd(OTf)_3$ (10 mg, 0.017 mmol) in water (0.5 mL) was added dropwise. The mixture was stirred at room temperature and the pH readjusted to 5-6 using $NaOH_{(aq)}$ (0.1 M) when necessary. After 18 hours, the reaction mixture was concentrated under reduced pressure and purified on Sephadex® G-15. The solvent was removed under reduced pressure and the resulting red solid dried under a stream of N_2 to yield **Ru(II)-Alkyne-Triad-Nd(III)** (11 mg, 97 %) as a red solid.

Molecular Formula: $C_{66}H_{50}N_{12}O_{16}RuNd_2$, **RMM:** 1656

ES⁺MS: m/z = 829.0 $[M + 2H]^{2+}$, 553.0 $[M + 3H]^{3+}$, 415.0 $[M + 4H]^{4+}$

HRMS ES⁺: calculated for $[C_{66}H_{50}N_{12}O_{16}{}^{102}Ru^{144}Nd_2 + 2H]^{2+}$ 829.0429, found 829.0404

6.5.4) Ru(II)-Alkyne-Triad-Yb(III)

Ru(II)-Alkyne-Triad-Acid hexafluorophosphate (7.4 mg, 0.004 mmol) was dissolved in water (3 mL) and the pH of the solution adjusted to 5-6 using NaOH$_{(aq)}$ (0.1 M). With stirring, a solution of Yb(OTf)$_3$ (7 mg, 0.011 mmol) in water (0.5 mL) was added dropwise. The mixture was stirred at room temperature and the pH readjusted to 5-6 using NaOH$_{(aq)}$ (0.1 M) when necessary. After 18 hours, the reaction mixture was concentrated under reduced pressure and purified on Sephadex® G-15. The solvent was removed under reduced pressure and the resulting red solid dried under a stream of N$_2$ to yield **Ru(II)-Alkyne-Triad-Yb(III)** (7.5 mg, 99 %) as a red solid.

Molecular Formula: C$_{66}$H$_{50}$N$_{12}$O$_{16}$RuYb$_2$, **RMM:** 1714

ES$^+$MS: m/z = 858.1 [M + 2H]$^{2+}$, 572.4 [M + 3H]$^{3+}$, 429.5 [M + 4H]$^{4+}$

HRMS ES$^+$: calculated for [C$_{66}$H$_{50}$N$_{12}$O$_{16}$^{102}Ru^{173}Yb$_2$ + 2H]$^{2+}$ 858.0710, found 858.0683

6.6) References

1   H. E. Gottlieb, V. Kotlyar and A. Nudelman, *J. Org. Chem.*, 1997, **62**, 7512–7515.

2   K. Nakamaru, *Bull. Chem. Soc. Jpn.*, 1982, **55**, 2697–2705.

3   H. Li, J. Tatlock, A. Linton, J. Gonzalez, T. Jewell, L. Patel, S. Ludlum, M. Drowns, S. V Rahavendran, H. Skor, R. Hunter, S. T. Shi, K. J. Herlihy, H. Parge, M. Hickey, X. Yu, F. Chau, J. Nonomiya and C. Lewis, *J. Med. Chem.*, 2009, **52**, 1255–1258.

4   J.-L. Chen, X. Wang, F. Yang, C. Cao, G. Otting and X.-C. Su, *Angew. Chem. Int. Ed.*, 2016, **55**, 13744–13748.

5   H. Takalo, P. Pasanen, J. Kankare, K. Undheim, G. Wittman, L. Gera, M. Bartók, I. Pelczer and G. Dombi, *Acta Chem. Scand.*, 1988, 42b, 373–377.

6   D. Tzalis, Y. Tor, F. Salvatorre and S. Jay Siegel, *Tetrahedron Lett.*, 1995, **36**, 3489–3490.

7   B. P. Sullivan, D. J. Salmon and T. J. Meyer, *Inorg. Chem.*, 1978, **17**, 3334–3341.

8   D. Tzalis and Y. Tor, *J. Am. Chem. Soc.*, 1997, **119**, 852–853.

9   C. S. Bonnet, F. Buron, F. Caillé, C. M. Shade, B. Drahoš, L. Pellegatti, J. Zhang, S. Villette, L. Helm, C. Pichon, F. Suzenet, S. Petoud and É. Tóth, *Chem. Eur. J.*, 2012, **18**, 1419–1431.

10   Y. Fan, L.-Y. Zhang, F.-R. Dai, L.-X. Shi and Z.-N. Chen, *Inorg. Chem.*, 2008, **47**, 2811–2819.

11   J. Ponce, J. Aragó, I. Vayá, J. G. Magenti, S. Tatay, E. Ortí and E. Coronado, *Eur. J. Inorg. Chem.*, 2016, **2016**, 1851–1859.